SHEAR BEHAVIOR OF STEEL FIBER REINFORCED PRESTRESSED CONCRETE BEAMS WITHOUT SHEAR REINFORCEMENT

by

JAE-SUNG CHO

Presented to the Faculty of the Graduate School of

The University of Texas at Arlington in Partial Fulfillment

of the Requirements

for the Degree of

DOCTOR OF PHILOSOPHY

THE UNIVERSITY OF TEXAS AT ARLINGTON

December 2011

ACKNOWLEDGEMENTS

I would like to express his sincere gratitude to Dr. Shih-Ho Chao, supervising professor, for his support and mentor with love and care throughout the course of this research. I would also like to extend his doctoral committee, including Dr. Ali Abolmaali, Dr. John H. Matthys, Dr. Hai Huang, and Mr. Joe Lundy who are most appreciated and gratefully acknowledged.

I would like to express his sincere gratitude to the Hanson Pipe & Precast. This research would not have been possible without great help for the Hanson. Sincere and personal thanks are extended to our research group members and laboratory technicians in the Civil Engineering Department as well as my personal friends.

I wants to offer my sincerest thanks to parents for their encouragement and support with endless love.

And, I thanks to his lovely wife, Jae-Heon Kim. My study has been possible with her endless love and constant support.

November 8, 2011

ABSTRACT

SHEAR BEHAVIOR OF STEEL FIBER REINFORCED PRESTRESSED CONCRETE BEAMS WITHOUT SHEAR REINFORCEMENT

Jae-Sung Cho, PhD

The University of Texas at Arlington, 2011

Supervising Professor: Shih-Ho Chao

The ACI 318-08 building code allows to use the steel fiber reinforcement as alternative shear reinforcement with satisfying certain criteria when a beam is required minimum shear reinforcement. However, this provision applies to a nonprestressed and prestressed concrete beam such that it could be conservative since the shear strength of prestressed concrete beam is generally enhanced due to the prestressing force. This is due partially to the fact that the provision has been accepted based on researches, mostly conducted in nonprestressed concrete beam. Most of experiments conducted for prestressed concrete beam in small scale tests, with a height of specimens were less than 10 in. A larger scale of experiment is required due to concerns of size effect. In addition, in order to evaluate the qualification of a Steel Fiber Reinforced Concrete (SFRC) mixture used for structural applications, such as increasing shear resistance, a material evaluation method is essential. Currently ASTM or ACI Committee 544 (Fiber-

Reinforced Concrete) does not recommend any standardized test method for evaluating shear performance of a particular SFRC material. This study addresses the research gaps described above by testing large-scale Steel Fiber Reinforced Prestressed Concrete (SFRPC) beams as well as developing a simple laboratory test techniques.

A total 13 simply-supported beams for large-scale test with a shear span to effective depth ratio of 3.0 and a height of 24 in. were subjected to monotonically-increased, concentrated load. The test parameters were mainly included compressive strength, volume fraction of steel fibers, compressive reinforcement ratio. The results of large-scale test showed that the use of hooked steel fibers in a volume fraction greater than or equal to 0.50% volume fraction of steel fibers (67 lb per cubic yard), which is less than requirement by ACI 318-08 (0.75%, 100 lb per cubic yard), led to substantial enhancement of shear behaviors including the first cracking, the ultimate, and ductility. High compressive strength of SFRC, greater than 9000 psi, which is higher than ACI 318-08 requirement (less than 6000 psi) could be used as well. However, there was no significant effect from compressive reinforcement ratio.

A simply shear test method for SFRC was proposed in this study. The test apparatus is almost exactly the same as the conventional ASTM bending test with only minor modification, in addition, it could simulate a pure shear stress by adjusting loading and support positions. By introducing a proper reinforcement for bending stress, it was possible to evaluate shear performance of SFRC with clear and uncomplicated shear stress field in the critical section.

TABLE OF CONTENTS

LIST OF ILLUSTRATIONS

LIST OF TABLES

CHAPTER 1

INTRODUCTION

1.1 General

1.1.1 Shear Design

The design of a typical slender beam begins from determining the amount of longitudinal reinforcement needed based on flexure, then the shear capacity is checked and shear reinforcement is added, if necessary. This process is done to ensure that the beam will fail by flexure rather than shear if the beam is overloaded (Wight and MacGregor, 2009). Flexural failure is preferred because the nature of shear failure is brittle and generally undesired due to the fact that it does not give ample warning in terms of large deflections(ACI 318-08, 2008). Furthermore, the ultimate shear strength tends to be less predictable than flexural failure due to considerably more complex failure mechanisms.

The origin of shear design method can be traced back to the turn of the twentieth century. A shear design method called the "45-degree truss analogy" was proposed independently by Ritter, a Swiss engineer, in 1899 and Mörsch, a German engineer, in 1902. The action of a reinforced concrete beam with stirrups may be represented as that of a truss in which the concrete compression zone is the top chord, the tension reinforcement is the bottom chord, the stirrups or bent-up bars are the tension web

members, and portion of the concrete web of the beam are compression web members.. In this analogy, all inclined tensile stresses are assumed to be carried by the stirrups or bent-up bars such that the web concrete diagonal tension capacity is not considered. Consequently, this analogy underestimates the shear strength of the concrete beam (ACI-ASCE Committee 326, 1962).

Extensive research efforts were undertaken to determine the shear strength of concrete beam without shear reinforcement, leading to the derivation of the empirical equation, $v_c = 0.03f'_c$ (ACI 318-56, 1956). The equation was used to design numerous concrete beams in 1950's and early 1960's to determine the shear strength of the concrete beams without shear reinforcement (Sherwood, 2005). However, in 1955, considerable portion of the roof of the Wilkins Air Force Warehouse in Selby, Ohio collapsed suddenly due to shear failure (Anderson, 1957). The roof of the building was designed without stirrups because it was estimated that the shear force within the roof could be solely resisted by concrete based on the shear capacity obtained from the above equation. As a result of the collapse numerous research works had been conducted to derive better expression of shear resistance. These findings led to the equation,

$$V_c = 2\sqrt{f'_c}\, b_w d \qquad [1.1]$$

$$\text{or} \quad \frac{V_c}{b_w d} = 1.9\sqrt{f'_c} + 2500\left(\rho V d / M\right) < 3.5\sqrt{f'_c} \text{ (psi, units)} \qquad [1.2]$$

Equation 2.1 was suggested by ACI-ASCE Committee 326 (ACI-ASCE Committee 326, 1962). This equation remains unchanged and is specified in the latest version of ACI code (Section 11.2.2.1 ACI 318-08, 2008).

1.1.2 Steel Fibers

Fibers have been used to reinforce brittle material for millennia. The bible states in Exodus 5: 6-7 that "*And Pharaoh commanded the same day the task-masters of the people, and their officers, saying, 'Ye shall no more give the people straw to make bricks, as heretofore: let them go and gather straw for themselves.*" In the modern era however, metal types of fibers have been incorporated in Portland cement concrete since it has been in use as a building material. Discontinued and deformed shape fibers were first developed by Berard in 1874 by using granular waste iron (Naaman, 1985). At the time, no attempts were made to use metal fibers to enhance shear strength in concrete; this did not take place until 1970's. In 1972, the first scientific investigation regarding the use of steel fiber as shear reinforcement was conducted by Batson, Jenkins, and Spatney (1972). They conducted experimental programs with various fiber shapes (round, flat and crimped) and fiber amount (0%, 0.22%, 0.44%, 0.88% and 1.76% of volume fraction). As can be seen in Figure 1.1, the size of the specimen used in this study was 4×6×78 in. His study proved that the replacement of conventional shear reinforcement by steel fiber provides effective resistance against shear failure. For instance, the specimens having shear span to depth ratio of 4.8 and without steel fibers were failed in shear, while the specimens having same shear span to depth ratio and

with 1 inch length of crimped steel fibers were failed in the manner of flexure (Batson et al.1972).

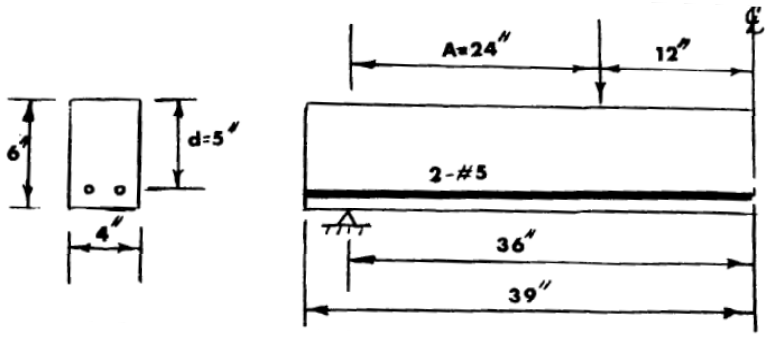

Figure 1.1 The dimensions of the tested beam (Batson et al., 1972)

Since then numerous research works have been conducted on steel fiber reinforcement and the results supported Baston's conclusion that steel fiber reinforced concrete (SFRC) can considerably enhance shear strength and ductility of plain concrete. Despite the obvious evidence from previous research results, the ACI building code did not accept steel fibers as alternative shear reinforcement until the 2008 code (ACI Committee 318, 2008). At this time the code states, "when $\phi 0.5v_c \leq v_u \leq \phi v_c$, steel fibers can be used to replace the minimum shear reinforcement for flexural members (prestressed and nonprestressed) constructed of steel fiber-reinforced concrete with f'_c compressive strength not exceeding 6000 psi, depth not greater than 24 inches, and shear stress v_u not greather than $\phi 2\sqrt{f'_c}$". The minimum amount of steel fiber is recommended as 0.75% volume fraction, which in turn corresponding to 100 lb of steel fibers per cubic yard of concrete (ACI 318-08 Section 5.6.6.2, 2008).

It should be noted that the provision is applied to prestressed and nonprestressed flexural members even though almost all prior investigations, which led to the new provision, were based on experimental tests on nonprestressed concrete beams such that enhancement of shear capacity induced by prestressing force is not accounted. It may lead to underestimate shear capacity of a prestressed beam with steel fibers.

1.2 Motivation

The efforts of the previous research finally prevailed and the ACI 318-08 building code finally accepted the use of steel fibers as alternative shear reinforcement if certain qualifications of SFRC are satisfied (ACI 318-08, 2008). However, this provision does not consider the contribution of prestressing force in shear due to the limited experimental results investigating shear behavior of Steel Fiber Reinforced Prestressed Concrete (SFRPC) beams. Furthermore, most of them were conducted in small scale tests, with a height of specimens were less than 10 in. A larger scale of experiment is required due to concerns of size effect.

In addition, in order to evaluate the qualification of an SFRC mixture used for structural applications, such as increasing shear resistance, a material evaluation method is essential. Currently ASTM or ACI Committee 544 does not recommend any standardized test method for evaluating shear performance of a particular SFRC material. ACI 318-08 Section 5.6.6.2 requires that ASTM C 1609 ["*Standard test method for flexural performance of fiber-reinforced concrete (using beam with third-poin loading)*"] (ASTM C 1609-10, 2010) as an evaluation method of SFRC material.

However this test method might not a suitable method for evaluating shear performance of SFRC since flexural and shear behaviors are distinctly different.

This study addresses the research gaps described above by testing large-scale steel fiber reinforced prestressed concrete (SFRPC) beams as well as developing a simple laboratory test technique for evaluating the performance of SFRC materials in shear. It is expected that the proposed experimental program would provide useful information on the shear transfer mechanisms and the essential shear properties of SFRC.

1.3 Objectives

The main objectives of the proposed researches are to;

(a) Investigate shear behavior of large scale steel fiber reinforced prestressed concrete beams, and determine the shear transfer and failure mechanisms.

(b) Develop a standard test method to evaluate shear performance of steel fiber reinforced concrete materials.

The depth of the large-scale beams was fixed as 24 in. in this study, which is the current upper limit for beams using SFRC as specified in the ACI 318-08 provisions (Section 11.4.6.1). A shear span to effective depth ratio of 3.0 was used, which places the beam within slender beam category. In general the shear failure mode is due to a major inclined shear crack after the appearance of initial flexural cracks (flexural-shear failure). Steel fibers used in this study have a hooked end shape, which is widely used in

industry. Two volume fractions of steel fibers, 0.5% and 0.75% were used. For comparison purposes, conventional prestressed concrete beams with and without web shear reinforcement were also tested. The overview of the research program is shown in Figure 1.1.

1.4 Organization of the Dissertation

This dissertation is organized into eight chapters. Details of each chapter are described as follows.

Chapter 1 – Introduction: This chapter contains general idea of shear design in concrete flexural member and steel fibers, as well as the motivation and objectives of the research.

Chapter 2 – Literature Review: This chapter reviews previous researches regarding shear design/behavior in concrete flexural members without web shear reinforcement including nonprestressed and prestressed members, history of steel fibers, material properties of steel fiber reinforced concrete (SFRC), and shear behavior of steel fiber reinforced nonprestressed and prestressed concrete beams.

Chapter 3 – Experimental Program: Large-scale experimental program is described in this chapter including design and fabrication of specimen, mix proportions for the concrete, test setup, and types of instrumentation used. In addition, the experimental

program for material shear test including shape of the specimen and test setup is also discussed.

Chapter 4 – Development of material testing method for evaluating shear resistance of SFRC: finite element analyses were conducted to investigate the suitability of various testing methods for shear resistance of SFRC. A new testing method is proposed and its performance is evaluated.

Chapter 5 – Experimental Result: The shear behavior of the test beams is discussed. Test results are reported including strength of beams, data from instrumentation, crack paths, and failure modes.

Chapter 6 – Special Topic: This chapter provides information of an advanced sensing technology, acoustic emission, which was used in the large-scale experimental program. General information and application of AE is reviewed. The locations of AE sensors and results of post analysis are also provided in this chapter.

Chapter 7 – Analysis of Experimental Results: Discussions of failure modes and crack patterns are presented. The enhanced shear resistance by using SFRC is explained by using a mechanical-based shear resistance mechanism.

Chapter 8 – Summary and Conclusions: This chapter presents a summary of the overall research study, main conclusions of the research, and suggested future study based on the findings from this study.

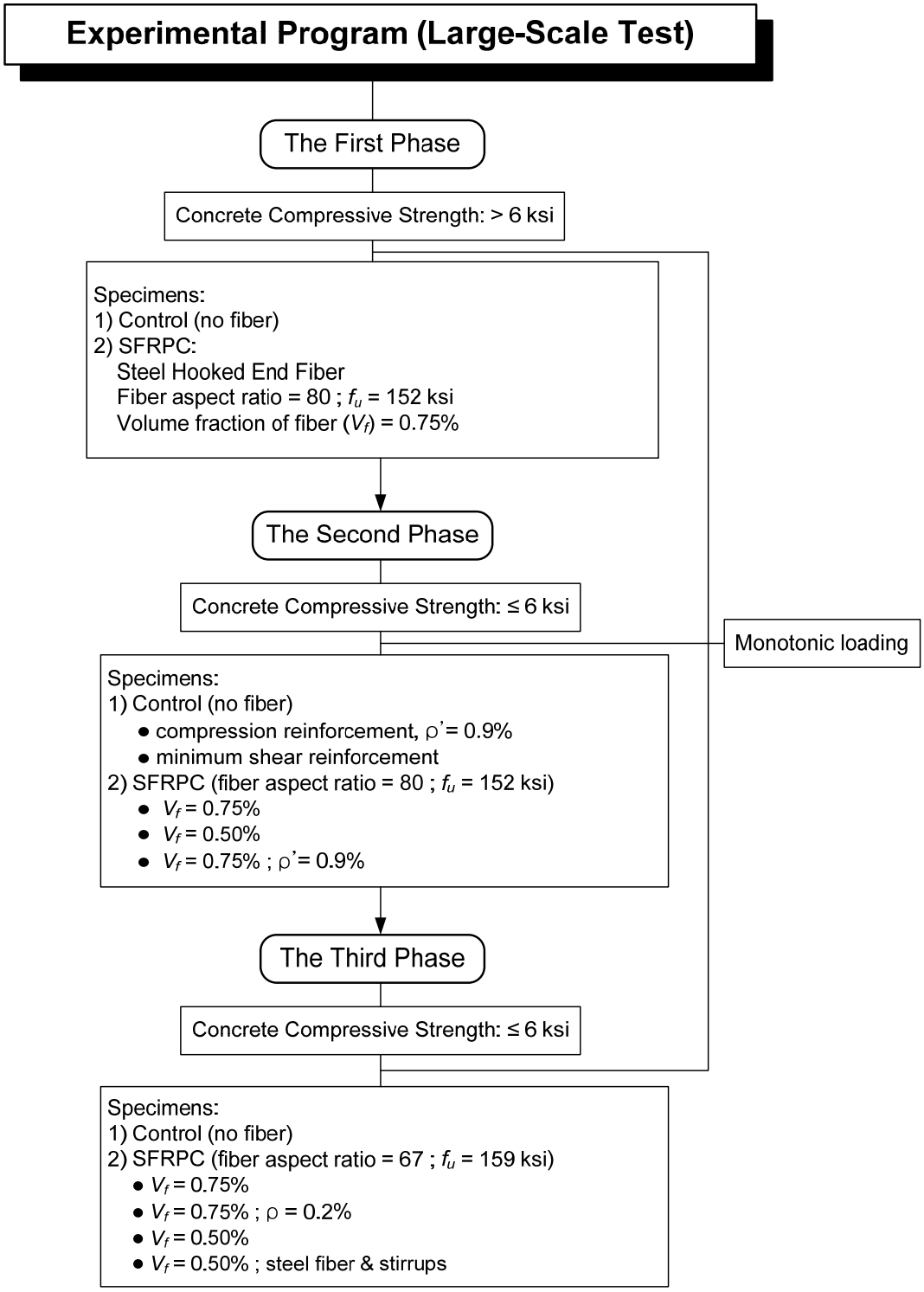

Figure 1.2 Flowchart of the experimental program for large-scale tests

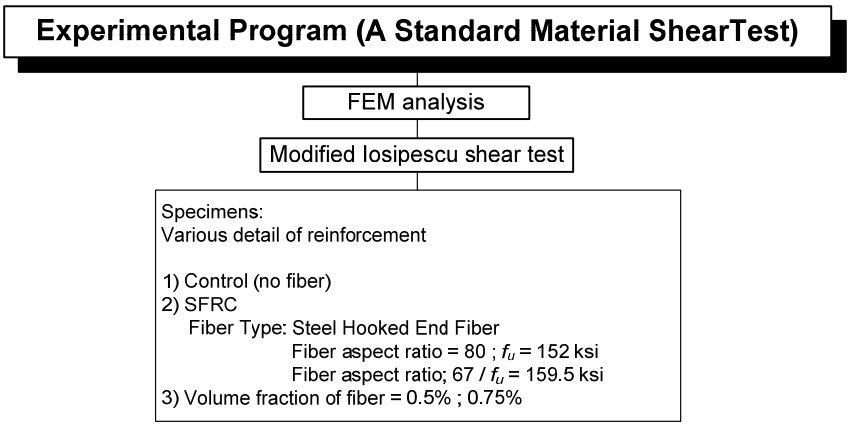

Figure 1.3 Flowchart for the development of a standard material shear test

CHAPTER 2

LITERATURE REVIEW

2.1 General

As mentioned in Chapter 1, a shear failure is undesirable due to the fact that the nature of shear failure is brittle and less predictable. One of the characteristics of shear failure in beams is the occurrence of inclined cracks, normally referred to as "diagonal shear cracks." Diagonal shear cracks are caused by excessive principal tensile stress in concrete. After the formation of diagonal shear cracks, shear resistance mechanism of a beam without shear reinforcement become uncertain. Currently, it is generally assumed that shear resistances are provided by aggregate interlock, dowel action, and uncracked compression region. In the case of deep beams, which are defined as shear span to depth ratio approximately less than 2.5 (Wight, 2009), arch action is one of primary shear resistance mechanism.

Steel fiber reinforced concrete (SFRC), a composite material with steel fibers and concrete, generally improves post-cracking behavior compared to plain concrete. The primary role of steel fibers is to bridge cracks after concrete cracks due to tensile stresses. Depending on bond strength between steel fibers and matrix and strength of steel fibers, the fibers can either fracture or be pulled out of the matrix as cracks open,

which in turn enhances the ultimate and/or post-cracking strength. A stable pullout process is a more preferred toughening mechanism, which generally provides greater energy dissipation along the post-cracking stage. Originally, steel fibers were used primarily for crack control to replace the secondary reinforcement often used in pavement and flat slabs (Bentur and Mindess, 2007). In recent year, the use of steel has been expanded into legitimate structural enhancements either to replace conventional reinforcement or to act in complimentary reinforcement fashion.

This chapter will review shear resistance mechanisms in concrete beams without web shear reinforcement for conventional nonprestressed and prestressed as well as researches related to steel fiber reinforcement. In this dissertation, the scope is limited to shear behavior of SFRC, though it is worth observing applications of steel fibers as other functions such as flexure in structural members.

2.2 Shear Models in Concrete Beams without Web Shear Reinforcement

2.2.1. ACI Shear Design Method in Nonprestressed Concrete Beam

In 1899, the Swiss engineer Ritter, and in 1902 the German engineer Mörch, proposed independently shear design method for concrete beams with web shear reinforcement known as 45 – degree truss. The model implies that web of the equivalent truss consists of stirrups acting as tension members and concrete struts running parallel to diagonal cracks, generally at 45° to beam axis. The compression zone and longitudinal reinforcement act like the top and the bottom chords of the truss system.

The forces in the truss members can only be determined by equilibrium. Its simplicity has attracted engineers so much that the model forms the basis of ACI building code expression for the shear resistance provided by stirrups. However, this model assumes that shear forces are resisted solely by the transverse reinforcement. This analogy ignores the contribution from concrete, meaning the shear capacity of a concrete beam was generally underestimated. Extensive research efforts had been undertaken to determine contribution in shear capacity, which led to the derivation of the empirical equation, $v_c = 0.03f'_c$ (ACI 318-51). This equation was used in designing numerous concrete beams in period of 1950's and early 1960's. However, in 1955, a considerable portion of the roof of the Wilkins Air Force Warehouse in Selby, Ohio collapsed suddenly due to shear failure. It was designed without stirrups and assumed that the shear force could be resisted solely by concrete itself based on the equation mentioned. This equation has led to unsafe design due to this underestimation of the shear capacity. As a result of the collapse, either new equation or design method was required for safe design. Numerous research works had been conducted to derive better expression of shear resistance in concrete itself.

In 1962, ACI-ASCE Committee 326 (now 426) published the state-of-art document contained concepts of "Diagonal Tension". The report presented following concepts to develop shear design criteria: 1) diagonal tension is a combined stresses problem in which horizontal tensile stresses due to bending as well as shear stresses must be considered; 2) failure due to shear may occur with the formation of the critical diagonal

crack or, if redistribution of internal forces is accompanied, failure may occur by shear-compression destruction in the compression zone at a higher load; 3) the load causing the formation of the critical diagonal tension crack must be considered in design as the ultimate load carrying capacity of a reinforced concrete member without web shear reinforcement; 4) distributions of shear and flexural stresses over a cross section of reinforced concrete are not well known. By evaluating available test data, which was plotted in the Figure 2.1, and the mathematical model based on the concept of principle stress, three major variables affecting diagonal cracking, shear span to effective depth ratio (M/Vd), longitudinal tensile reinforcement ratio (ρ), and 28-day compressive strength ($\sqrt{f'_c}$), were chosen, and concrete contribution in shear resistance was determined as following equation;

$$\begin{aligned} \frac{V_c}{b_w d} &= 1.9\lambda\sqrt{f_c'} + 2500\frac{\rho_w V d}{M} \le 3.5\sqrt{f_c'} && (psi) \\ \frac{V_c}{b_w d} &= \frac{1}{7}\lambda\sqrt{f_c'} + 17\frac{\rho_w V d}{M} \le 0.29\sqrt{f_c'} && (MPa) \end{aligned} \qquad [2.1]$$

where, V_c is shear carried by the concrete, b_w is the width of the beams, λ is the modification factor reflecting the reduced mechanical properties of lightweight concrete, d is the effective depth of the beams, $\sqrt{f'_c}$ is the 28-day compressive strength, V is the applied shear force at the considered section, and M is applied bending moment at considered section. ACI 318 building code (2008) accepted simplified version as following;

$$\begin{aligned} V_c &= 2\lambda\sqrt{f_c'}b_w d && (psi) \\ V_c &= 0.167\lambda\sqrt{f_c'}b_w d && (MPa) \end{aligned} \qquad [2.2]$$

Those equations remain unchanged and are specified in the latest ACI code (Section 11.2.2.2 ACI 318-08, 2011)

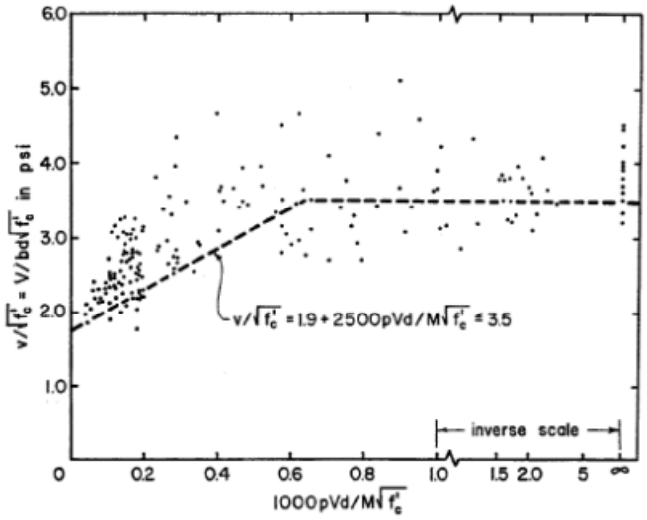

Figure 2.1 Deviation of shear design equation (ACI-ASCE Committee 326, 1962)

2.2.2. Mechanisms of Shear Resistance of Concrete Beams without Web Shear Reinforcement

The Committee 326 (now 426) works concluded that it could not yet clearly define the failure mechanism in shear, though numerous research works have been conducted and these outcomes were accepted by ACI 318 building code.

Mörch reported that diagonal cracking loading is close to the tensile strength of concrete (1907). That is because in biaxial stress state maximum principal tensile stress led to diagonal crack, which occurs perpendicular to the principal tension plane (Figure 2.2). It may be an indication of shear failure. This resistance coming from the tensile strength of concrete could be considered as concrete contribution in shear.

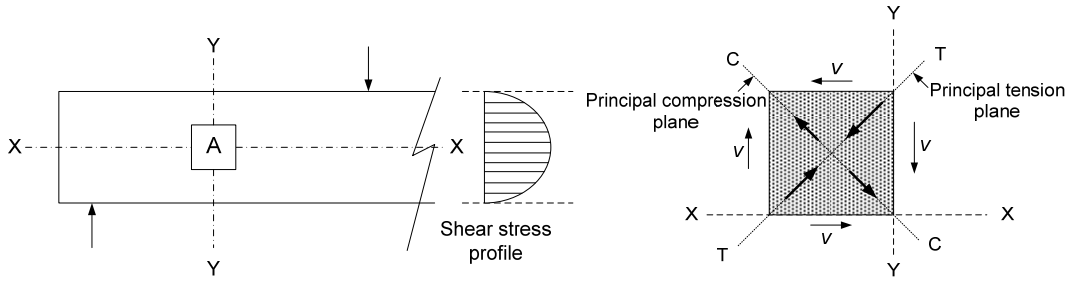

Figure 2.2 Stress state for an element taken along the neutral axis (Naaman, 2004)

Fenwick and Paulay (1968)stated that there are two main actions in shear span; beam action and arch action.

$$V = \frac{dM}{dx} = \frac{d}{dx}(Tjd) = jd\frac{dT}{dx} + T\frac{d(jd)}{dx} \qquad [2.3]$$

The first term in Equation 2.3 represents beam action and the second term represents arch action. It is well known that beam action is generally valid when a beam has shear span to effective depth ratio larger than 2.5, and in the opposite case arch action is normally the primary contribution in shear resistance. In beam action, after diagonal crack exists the they pointed out that shear force V might be resisted by following components (Figure 2.3); 1) the shear stresses across the compression zone, which sum up to V_c; 2) the transverse component V_g of the force G, which results from interlocking of aggregate particles across a crack; 3) the transverse force induced in the main flexural reinforcement by dowel action V_d.

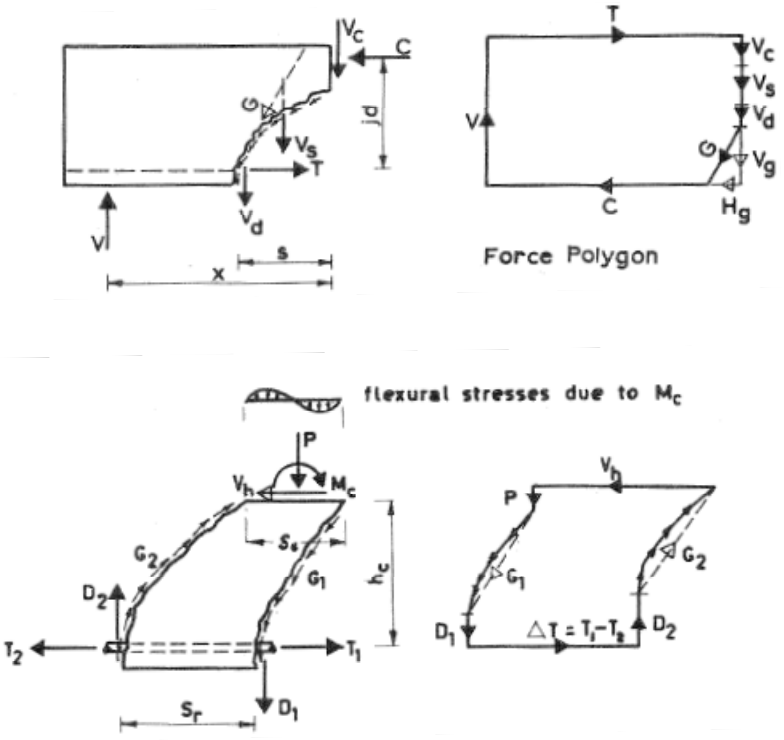

Figure 2.3 Forces acting in shear span of a beam (Fenwick and Paulay, 1968)

The shear transfer occurs in the uncracked portions of structural members is shown in Figure 2.3. The ability of the compression region to resist shear depends on the degree of penetration of the diagonal crack. Diagonal crack begins in the web and propagates rapidly toward the loading point, in turn, it could be considered that the area of compression zone is normally not sufficient to resist shear stress, though some portions of shear resistance could be provided by the compression zone but not a significant portion. Aggregate interlock derives its strength the crack surface bearing against the two protruding portion the beam providing resistance to sliding. The resistance coming from aggregate interlock decreases when width of crack increases, therefore, effect of aggregate interlock is only valid when the width of crack is relatively small (Walraven,

1981). In addition, the contribution of the aggregate interlocking was criticized since it objects the fundamental concrete properties; a crack develops when the maximum tensile stress exceeds its strength, propagates in perpendicular to the maximum principal tensile plane and opens in the orthogonal direction such that the friction on the cracked surface cannot be activated (Kotsovos, 1988). Longitudinal reinforcement carrying shear, known as dowel action, may prevent the beam from splitting the lower portion of the beam from the upper portion over a short length. Proportions of shear resistance provided by each component have been investigated and is presented in Figure 2.4.

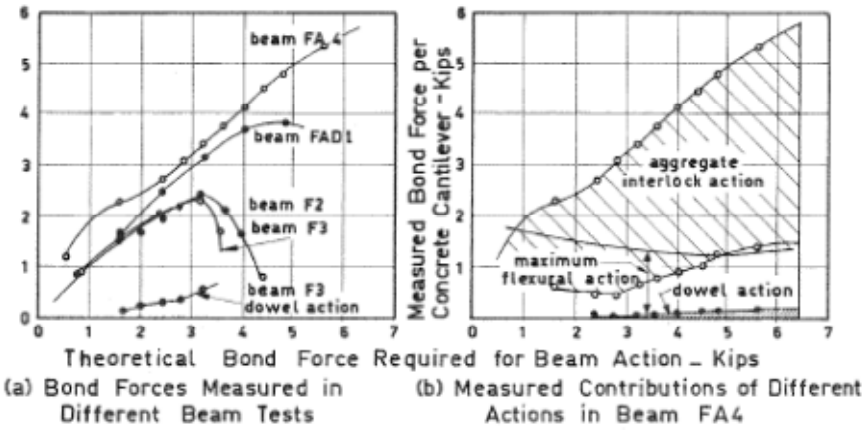

Figure 2.4 Bond forces measured in test beams (Fenwick and Paulay, 1968)

When for any reason the bond between concrete and rebar is destroyed the tensile force in rebar cannot be changed, hence, $dT/dx = 0$ (see Equation 2.3). As a consequence, the "beam action" as shown in the first term of Equation 2.3 is not valid. In this case, the external shear is mainly resisted by the inclined internal compression, as expressed by the second term in Equation 2.3. Here the internal tension, T, is replaced by the internal compression force C, to signify that it is the vertical component of a compression force,

with constant slope, which balances the external shear force. From the examination of equilibrium and compatibility conditions of the shear span of a reinforced concrete beam, it is apparent that arch action is limited to two regions of the span; one is the load point, and the other occurs above the last flexural crack adjacent to the support such that load is able to be transferred directly from the loading point to the supports. (Fenwick and Paulay,1968). To develop arch action over the complete span, these two regions must merge, and this can occur when the diagonal crack extends to the support, thus separating the compression and tension zones of the shear span and permitting the translation displacement, associated with the occurrence of arch action. Hence, diagonal cracking is a prerequisite to the development of appreciable arch action in the shear span (Fenwick and Paulay, 1968). Figure 2.5 shows the variation in shear capcity with a/d for rectangular beams in concrete beam without web shear reinforcement. It is apparently shown that smaller a/d (smaller shear span) increases shear capacity since it would make for line of thrust, illustrated in Figure 2.6, to be steeper so as to more area can resist compressive force, as the result, capacity of arch action would increase.

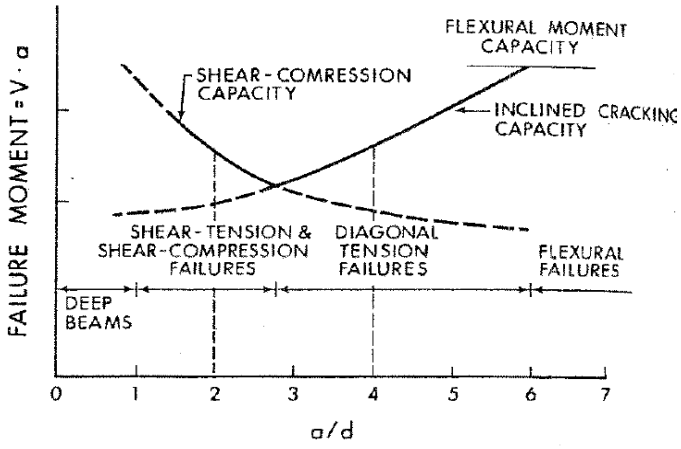

Figure 2.5 Variation in shear capacity with a/d for rectangular beams in concrete without web shear reinforcement (ASCE-ACI Committee 426, 1973)

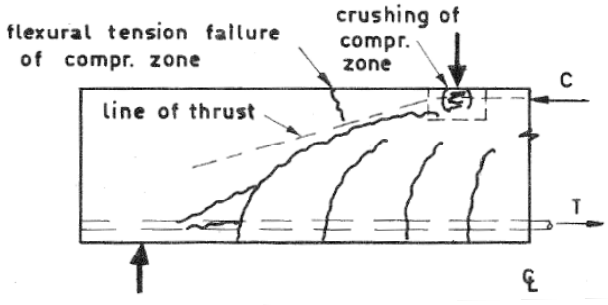

Figure 2.6 Failure modes for arch action (Fenwick and Paulay, 1968)

On the other hand, the failure in beam with higher ratios would occur as diagonal cracking because of the reduced size of compression zone causing a compression failure, or the eccentricity of the line of thrust causes a flexural tension failure of the compression zone above the diagonal crack. Strictly speaking, arch action is not a shear mechanism in the sense that it does not transmit a tangential force to a nearby parallel plane, however, arch action does permit the transfer of a vertical concentrated force to a reaction and thereby reduce the contribution of the other types of shear transfer but

increase shear capacity of a beam (ACSE-ACI Committee 426, 1973). For this reason, ASCE-ACI Committee 426 (1973) considered arch action as one of shear transfer mechanism.

2.2.3. Modified Compression Field Theory (MCFT)

Vecchio and Collins (1986) introduced the Modified Compression Field Theory, MCFT, which is based on the concept of average stress and strain in cracked concrete. In this theory, it is assumed that cracks are aligned in the principal directions such that the direction of principal stress coincides with that of principal strain. The crack width, w, is calculated assuming that small tensile strains in concrete between cracks can be neglected, meaning the crack width is the product of the crack spacing in the principal tensile direction, s_θ, and the principal tensile strain, ε_1 (Figure 2.7). The term s_θ is predicted to be a function of the ability of the reinforcement in the x and z-direction to control crack spacing in those directions. As shown in Figure 2.7, the terms s_x and s_z in equation 10, are the crack spacing that would occur if a member were subjected to pure longitudinal tension and pure transverse tension respectively, and are functions of the crack control characteristics of the reinforcing bars.

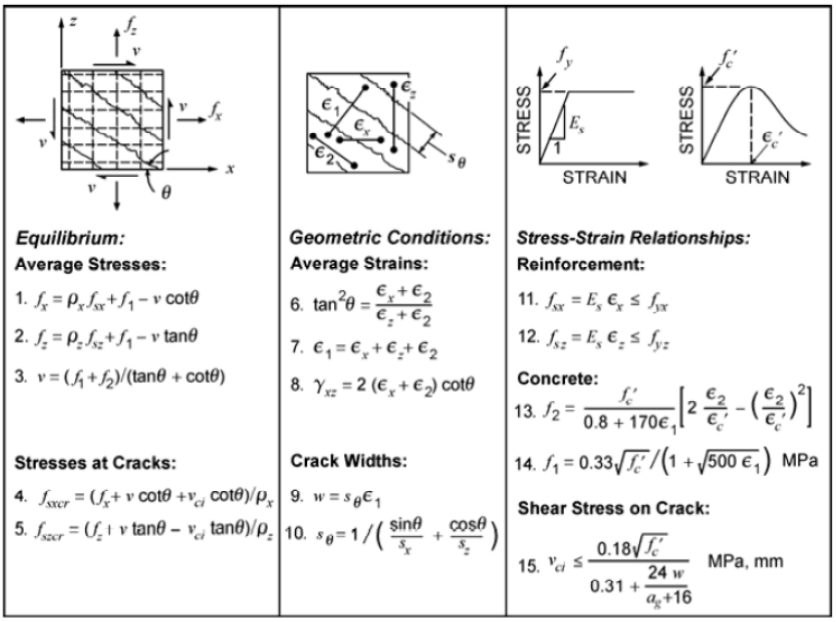

Figure 2.7 Relationships of the MCFT (Bentz et. al., 2006)

Experimental data by Walraven (1981) showed that the shear stress, v_{ci}, at a crack is related to the crack width, aggregate size, and compressive stress transmitted across the crack shown in Expression 15 in Figure 2.7. The following equation is for psi unit.

$$v_{ci} = \frac{2.16\sqrt{f_c'}}{0.3 + \frac{24w}{a + 0.63}} \qquad [2.4]$$

where w is the crack width (mm) and a is the aggregate size (mm).

By combining Expressions 9 and 15 shown in Figure 2.7, the capacity of cracks to transfer shear stresses due to aggregate interlock may limit the shear strength as indicated by Equation below.

$$v_{ci} = \frac{2.16\sqrt{f_c'}}{0.3 + \frac{24\varepsilon_1 s_\theta}{a + 0.63}} \qquad [2.5]$$

For beams without web shear reinforcement, only a single crack would occur if the elements were subjected to pure transverse tension, hence s_z in Expression 10 in Figure 2.7 equals infinity, and it reduced to;

$$s_\theta = \frac{s_x}{\sin\theta} \qquad [2.6]$$

The relationship between the average stress and strain is then obtained by an iterative calculation. The MCFT has been adopted in some design codes, for example Canadian Concrete Code (Technical Committee on Reinforced Concrete Design, 1994) and AASHTO LRFD Bridge Design Specifications (2010).

2.2.4. Different Perspectives

Despites of the classic studies, there are many attempts to explain the shear resistance after the inclined cracking. Drucker (1961) introduced the direct load transfer mechanism, which assumes that the applied load is transferred from the loading point to supports directly, and Kotsovos (1988) also introduced the compressive force path theory, which assumes that the load is transferred through compressive force path, which is uncracked section. Muttoni and Ruzi (2002) established the critical shear crack theory, which assumes that the applied load is transferred through a direct strut and further load can be resisted by aggregate interlocking in the strut even though cracks disrupt the strut. These theories will be treated in Chapter 7.

Tureyen and Frosh (2003) proposed that shear strength should be the function of neutral axis depth, *c* (that is, the depth of the compression zone), when members are analyzed with different reinforcement ratios and modulus. The free-body diagram and average shear stress distribution are shown in Figure 2.8. The authors assumed that shear would be carried by the uncracked section only. A basic form of their equation is similar to the one that is presented in ACI 318 building code (Section 11.2.2.2), in which the depth of neutral axis, *c*, was used instead of using effective depth, *d*.

$$V_c = K\sqrt{f_c'}b_w c$$

$$K = \sqrt{16 + \frac{4\sigma_m}{3\sqrt{f_c'}}} \qquad [2.7]$$

The coefficient, *K*, could be directly computed from experimental results, and "*K=5*" was recommended and provides reasonable outcome:

$$V_c = 5\sqrt{f_c'}b_w c \qquad [2.8]$$

The model could be applied to slender reinforced concrete beams and consider the tensile longitudinal reinforcement ratio, which can be accounted in term of "c".

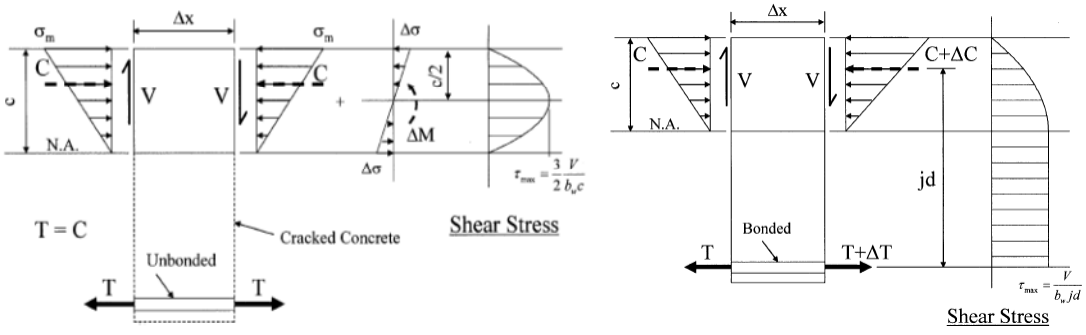

Figure 2.8 Free-body diagrams in cracked region and average shear stress distribution (Tureyen and Frosh, 2003)

2.3 Shear Models in Prestressed Concrete Beams without Web Shear Reinforcement

Prestressed concrete beams have two major advantages in terms of shear resistance over nonprestressed concrete beams (Naaman, 2004). Shear stress in prestressed concrete beams can be smaller due to slope of the prestressing force when the tendons are draped or harped. In this case the vertical component of the pre-compression counteract part of the shear stresses induced by the external loads, thus reducing the shear force and the diagonal tension.. In addition, as mentioned previously the diagonal crack will occur when the principal tensile stress exceeds tensile strength of concrete, however, the principal tensile stress (*TT*) becomes smaller in prestressed concrete than in reinforced concrete due to the compressive stress induced by the prestressing force as can be seen in Figure 2.9. Therefore, prestressed concrete beams generally have better shear resistance over nonprestressed concrete beams.

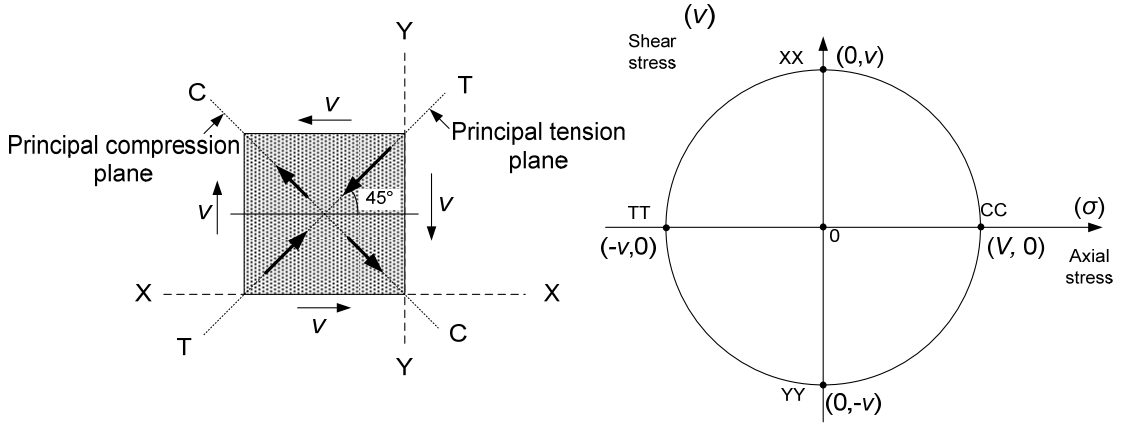

(a)

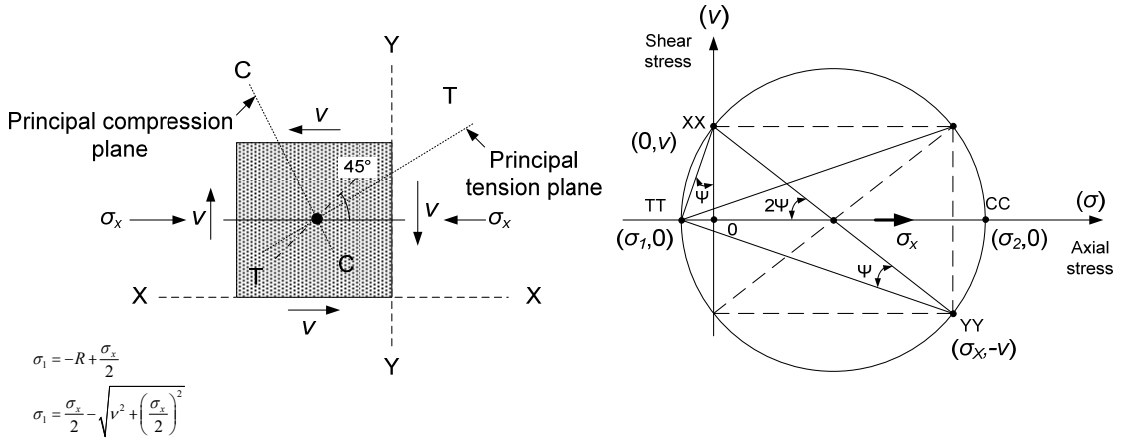

(b)

Figure 2.9 Mohr's circle for an element taken along the neutral axis; (a) Nonprestressed concrete; (b) prestressed concrete (Naaman, 2004)

In prestressed concrete beams, shear cracks can be mainly categorized with web shear and flexural-shear cracks. Web shear cracks normally occur when a higher prestressing force is applied in thin web or members have relative thin webs. A web shear crack is initiated when the principal tensile stress at some point in the uncracked beam exceeds the tensile strength of concrete. Web shear cracking load may be predicted with

reasonable accuracy from the use of Mohr's Failure Theory for concrete subjected to combined shear and normal stress. (kar, 1968)

From the Mohr's Circle, shear stress corresponding to reaching the tensile strength of the concrete at the neutral axis of a beam with an average axial stress could be calculated as the following equation:

$$V_{cw} = f_t \sqrt{1 + \frac{f_{pc}}{f_t}} + \frac{V_p}{b_w t} \qquad [2.9]$$

ACI code accepted simplified equation,

$$v_{cw} = 3.5\sqrt{f_c'} + 0.3 f_{pc} + \frac{V_p}{b_w d} \qquad [2.10]$$

where, v_{cw} is the web shear resistance in psi, f'_c is the compressive strength at 28 days, f_{pc} is the prestressing stress, V_p is the vertical component of prestressing force at the section considered, b_w is the width of beams, d is the effective depth.

Flexural-shear cracks occur due to the combined effects of flexure and shear. The corresponding cracks initiate as flexural cracks, and then those cracks deviate and propagate at inclined direction corresponding to the inclination of the diagonal tension plane due to the increased effect of diagonal tension at tip of cracks. In deriving flexural-shear resistance capacity (Naaman, 2002), it was assumed that the flexural-shear capacity is the sum of the shear required to cause a flexural crack and an additional increment of shear required to change a flexural crack to flexural-shear crack.

$$v_{ci} = 0.6\lambda\sqrt{f_c'} + \frac{V_G}{b_w d} + \left(\frac{\Delta V_u \times \Delta M_{cr}}{\Delta M_u}\right)\frac{1}{b_w d} \geq 1.7\lambda\sqrt{f_c'} \qquad [2.11]$$

where, v_{ci} is the flexure-shear stress resistance, psi, V_G is the shear force due to self-weight of member at section considered, ΔV_u is the factored shear force due to the superimposed dead load plus the live load at section considered under the same loading as ΔM_u , ΔM_u is the factored bending moment due to the superimposed dead load plus live load at the section considered, and ΔM_{cr} is the moment in excess of self-weight moment causing flexural cracking in the precompressed tensile fiber at the section being considered. In Equation [2.11], the first, second, and third terms indicate shear stress needed to transform a flexural crack into an inclined crack, shear stress due to self-weight, and shear stress that initially will cause a flexural crack to occur, respectively. When calculated the shear capacity of concrete itself, if the smaller values of the web shear cracking and flexural-shear cracking resistance, is less than the demand, stirrups should be provided according to the following equation, which is based on the 45 °analogy.

$$v_s = \frac{A_v f_y d}{s} \leq 8\sqrt{f_c'} b_w d \qquad (psi) \qquad [2.12]$$

where, v_s is the shear strength provided by the stirrups, A_v is the total areas of the stirrups, f_y is the nominal yield strength of the stirrups, d is the effective depth of a beam, and s is the spacing of stirrups. The term, $8\sqrt{f'_c} b_w d$, is to prevent a diagonal compression failure and to ensure good performance under service load levels. Finally, shear capacity in prestressed concrete becomes,

$$V_n = V_C + V_S \quad [2.13]$$

where V_n is the nominal shear strength of prestressed concrete beam, V_c is the nominal shear strength provided by the concrete, and V_s is the nominal shear strength provided by the stirrups.

2.4 Steel Fiber Reinforced Concrete (SFRC) Beams

Steel fibers are one of the most popular fiber types used in fiber reinforced concrete. Steel fibers have high elastic modulus and strength and can be easily dispersed into concrete mixtures. Steel fibers greatly improve material properties of concrete such as post-cracking strength, toughness, ductility, and many others. In early stage of their application, steel fibers have been used mainly for cracking control, and it has also been suggested for steel fibers to be used for a role in secondary reinforcement. Recently, numerous of studies have been investigating the behavior of steel fiber reinforced concrete, especially in shear, and have verified that steel fibers can partially or totally replace conventional shear reinforcement.

2.4.1. History of Steel Fiber

Attempts were made since long time ago to incorporate fibers in concrete to improve its performance in terms of toughness, tensile strength, and ductility. Several patents involved the invention of various types of metal fibers in late 1800s to now. Discontinued and deformed shape fibers were first developed by Berard in 1874 by using granular waste iron. In 1918, a French patent, Alfsen used small longitudinal

bodies (fibers) of iron, wood or other materials to improve tensile strength of concrete. He also suggested an idea of enhancing bonding strength between fibers and matrix by applying rough surface and end bents shapes in fibers. Weakly was granted patent in 1912 for using steel wire strip and Kleinlogel mixed a relatively large volume of iron particles with concrete (1920). In 1927 Martin and Meischke-Smith developed plain and crimped steel wires. In 1933, Etheridge proposed annulus types of fibers with varying size and diameters to improve crack control and fatigue performance of concrete. Constantinesco (1927) described fiber reinforcing parameters to enhance bond strength (i.e., coiled or helical shapes of fibers could enhance the bonding strength); this concept is similar to the one in use today. Some early patents on metallic fibers are shown in Figure 2.10. When fibers are used, the main considerations are not changed in recent; strength of fibers and bonding strength. Tensile strength of metallic fibers is approximately 150 ksi ~ 350 ksi with minimum strength as 80 ksi. If the fiber strength is too low, fiber will be broken upon small slips. Longer steel fibers normally lead to better composite behavior due to the greater bond action, but there is length limitation in terms of aspect ratio (length divided by diameter) due to difficulty of mixing. For this reason, ACI Committee 544, *Fiber Reinforced Concrete Committee*, recommends maximum aspect ratio of 100 in practice (1996). The geometries of commonly used steel fibers in recent are presented in Figure 2.11. The specifications for minimum requirements of steel fibers intended for use in fiber-reinforced concrete can be found in ASTM A820, "*Standard Specification for Steel Fibers for Fiber-Reinforced Concrete*."

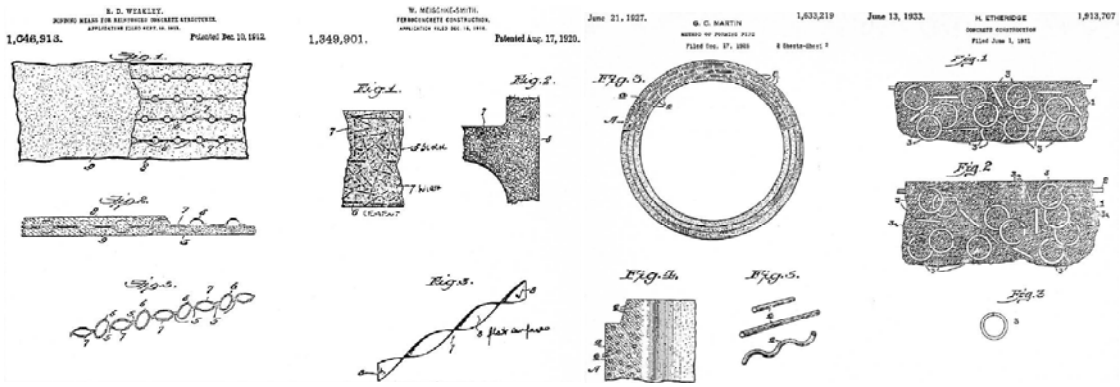

Figure 2.10 Some metal types of fibers in early stage (Naaman, 1985)

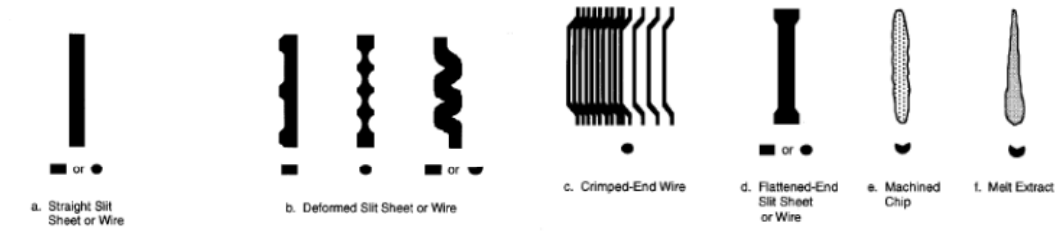

Figure 2.11 Various steel fiber geometries (ACI Committee 544, 1996)

2.4.2. Mechanical Properties of SFRC

In general steel fibers enhance the strength of the concrete by providing a means of transferring stresses or loads across cracks and the toughness by providing energy absorption mechanisms. Those mechanical properties are essentially related to the debonding and pull-out processes of the fibers after cracks occur. The overall behavior of an SFRC can be represented by either strain hardening or strain softening behavior.

2.4.2.1 Tensile Strength of SFRC

To evaluate shear strength of SFRC, tensile strength of SFRC is an important mechanical property because the shear strength of concrete is heavily dependent upon the tensile strength of concrete due to the fact that diagonal crack occurs when principal tensile stress reaches its capacity. However, currently there is no universal standard test method to assess tensile properties of SFRC. The most appropriate test method is apparently the direct tensile test. However several issues such as difficulty in the end grip of the fixtures (Chao, et al., 2011. The direct tensile test typically leads to scattered data and hinder the use of this method.

Shah (1978) performed direct tensile test using steel fiber reinforced mortar, and its typical results were reported in ACI Committee 544 and briefly summarized in Figure 2.12. The ascending part of the curve up to the first crack is similar to the unreinforced mortar, but unlike unreinforced mortar, those examples showed the considerable residual strengths after first cracking. It can be seen in Figure 2.12 that larger aspect ratio enhanced post-crack strength. It is important to note that enhancing bonding between matrix and fibers by introducing hooked-end and enlarged-end effectively increased the residual strength.

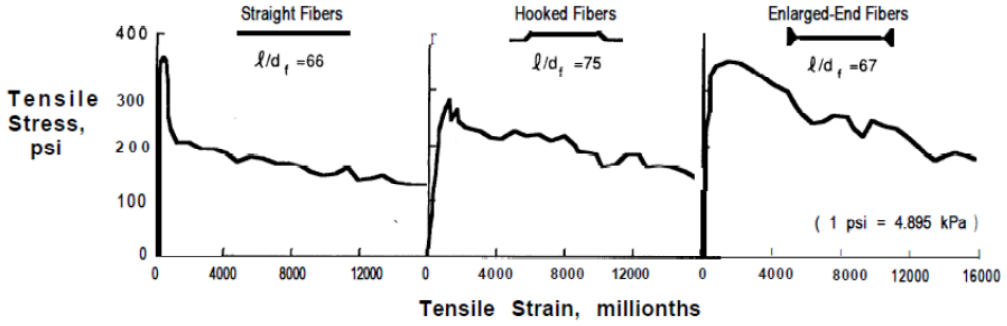

Figure 2.12 Direct tensile stress-strain curves for different types of SFRCs (Shah, 1978)

Dinh (2009) conducted direct tensile test with dog-bone shape specimens with 0.75% volume fraction fibers and varying aspect ratio (diameter/length) of steel fibers.

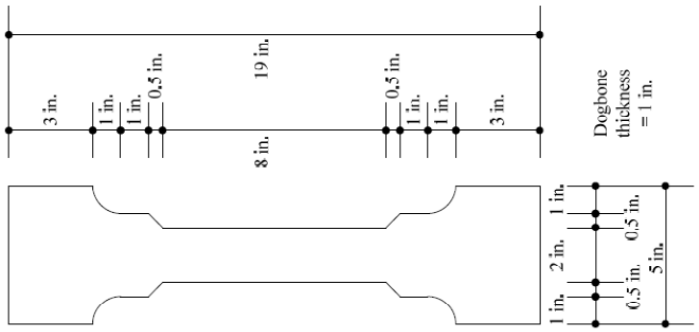

Figure 2.13 Dimensions of dog-bone specimen used by Dinh (2009)

The steel fibers used are RC80/60BN and ZP305 (see Figure 2.14 (a) and (b)), which have aspect ratio of 82 and 55, respectively but identical tensile strength of 152 ksi. As seen in Figure 2.14, It can be said that larger aspect ratio showed higher post-cracking strength, but there was no significant increment in peak strength.

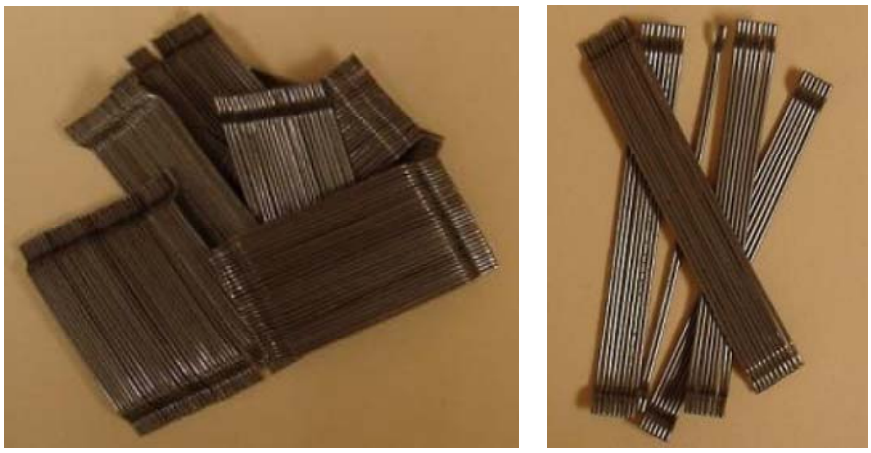

(a) (b)

Figure 2.14 Steel fibers; (a) Double end hooked, ZP 305; (b) Double end hooked, RC80/60BN

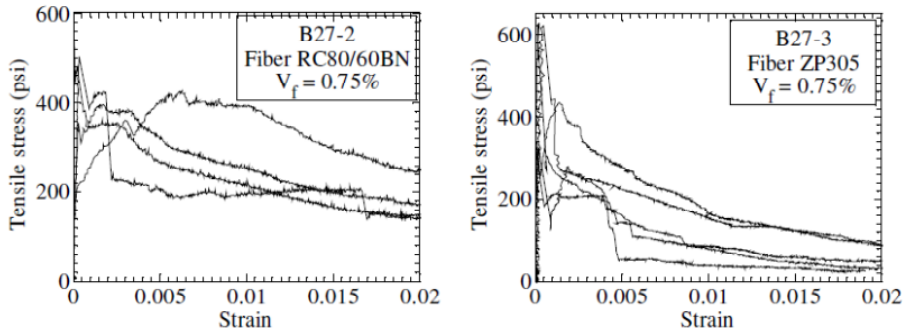

Figure 2.15 Typical results of dog-bone direct tensile test (Dinh, 2009)

Chao et al. (2011) conducted direct tensile test with dog-bone shape specimens. Their specimens, unlike Dinh's, have larger cross section. to avoid the alignment of fibers in one or two directions, as typically happened in a thin specimen. The test setup and mold are shown in Figure 2.16.

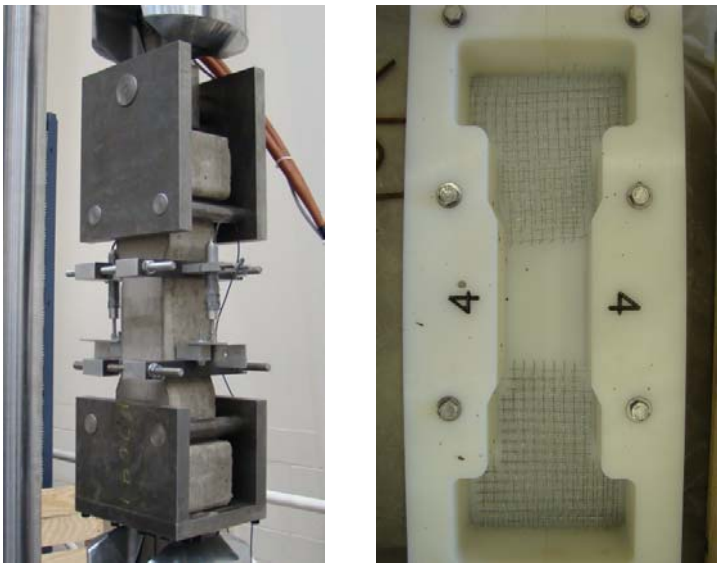

Figure 2.16 Test setup and mold of the direct tensile specimen (Chao et al., 2011)

To prevent failure at boundary due to stress concentration, four layers of mesh at each side were provided, as shown in Fig.2.16. This was done so that the cracks would occur within the gauge length. Steel fibers used in the experiment have hooked ends (see Figure 2.17), length and diameter of 1.55 and 0.038 in. , (aspect ratio is 40), respectively, and a tensile strength of 150 ksi. The concrete had an average compressive strength of 9.5 ksi and contained maximum aggregate size of ¾ in.

Figure 2.17 Single hooked ends steel fibers (Chao, et al., 2011)

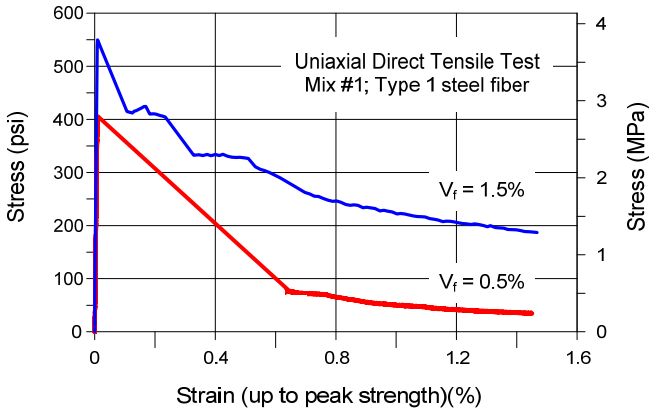

Figure 2.18 Typical direct tensile test result (Chao et al., 2011)

It can be seen from Figure 2.18 that higher volume contents of fibers enhanced not only peak strength but also residual strength. It is interesting to note that specimens with higher volume content of fibers led to greater enhancement in the residual strength than the peak strength.

There have been numerous attempts to predict overall behavior of tensile stress-strain relationship in FRC. The law of mixtures leads to the following expressions for FRC tensile strength and elastic modulus at first crack (Balaguru and Shah, 1992),

$$\sigma_{cc} = \sigma_f V_f + \sigma_{mu}\left(1 - V_f\right) \qquad [2.14]$$

where σ_{cc}, σ_f, V_f, σ_{mu} are respectively, the composite tensile strength, the fiber tensile strength, the volume fraction of fiber, and the matrix tensile strength. In addition, modulus of elasticity is expressed as followed (Balaguru and Shah, 1992),

$$E_c = E_f V_f + E_m\left(1 - V_f\right) \qquad [2.15]$$

where E_c, E_f, E_m are respectively, the elastic modulus of composite, fiber, and matrix. Those equations mentioned above are only valid if fibers are continuous and aligned in the loading direction, as well as if there is perfect bond between the matrix and the fibers, which are not easily achieved in practice. For discrete fibers, the fiber length, the orientation of the fibers, and fiber-matrix bond strength should be accounted for. Law (1971) suggested a concept of critical length parameter, l_c, saying there is insufficient embedded length to generate a stress equal to the fiber strength and the fiber is not utilized efficiently when length of fiber is less than the critical length (l_c).

$$l_c = \frac{\sigma_{fu} \cdot r}{\tau_{fu}} \qquad [2.16]$$

where σ_{fu}, r, and τ_{fu} are fiber strength, radius of fiber and bonding strength respectively. Using the concept of the critical length, the efficiency factor (η_l) at failure can be calculated as,

$$\eta_l = 1 - \frac{l_c}{2l}\frac{\varepsilon_{mu}}{\varepsilon_{fu}} \qquad [2.17]$$

where l_c, ε_{mu}, and ε_{fu} are the length of fiber, the strain in the matrix and the ultimate strain in the fiber respectively. In post-cracking zone, the efficiency factor can be calculated as,

$$\text{for } l << 2l_c \qquad \eta_l = \frac{1}{2l_c\left(2 - \tau_d / \tau_s\right)}$$

$$\text{for } l >> 2l_c \qquad \eta_l = 1 - \frac{l_c}{2l}\left(2 - \tau_d / \tau_s\right) \qquad [2.18]$$

where, τ_d and τ_s are the bonding strength by friction between the fiber and the matrix and the interfacial bond respectively. In order to achieve 90% strength efficiency in the post-cracking region, the fiber must be 5 ~ 10 times longer than its critical strength. This can be achieved alternatively by controlling the geometry of the fiber or by enhancing the fiber-matrix interaction.

It should be noted that combined effects for length and orientation cannot be simply calculated as the product of its efficiency factor (Laws, 1971). Laws derived the total efficiency factor considering the length and orientation as followed,

$$\begin{aligned} l << \frac{5}{3} l_c' \qquad & \eta = \frac{3}{8} \times \frac{3}{5} \left(\frac{l}{l_c \left(2 - \tau_d / \tau_s \right)} \right) \\ l >> \frac{5}{3} l_c' \qquad & \eta = \frac{3}{8} \left(1 - \frac{5 l_c}{6 l \left(2 - \tau_d / \tau_s \right)} \right) \end{aligned} \qquad [2.19]$$

$$\begin{aligned} l << \frac{10}{7} l_c' \qquad & \eta = \frac{1}{5} \times \frac{7}{10} \left(\frac{l}{l_c \left(2 - \tau_d / \tau_s \right)} \right) \\ l >> \frac{10}{7} l_c' \qquad & \eta = \frac{1}{5} \left(1 - \frac{5}{7} \frac{l_c}{2l} \left(2 - \tau_d / \tau_s \right) \right) \end{aligned} \qquad [2.20]$$

where, $l_c' = \frac{1}{2} l_c \left(2 - \tau_d / \tau_s \right)$

The Equations, 2.19 and 2.20 are the efficiency factors of length for 2-D and 3-D respectively. The total efficiency factors as function of the ratio of fiber length to critical length are plotted in Figure 2.20. As can be seen in Figure 2.19, the aligned

fibers showed higher efficiency factor, but randomly distributed fibers in three dimensions showed lower the factor.

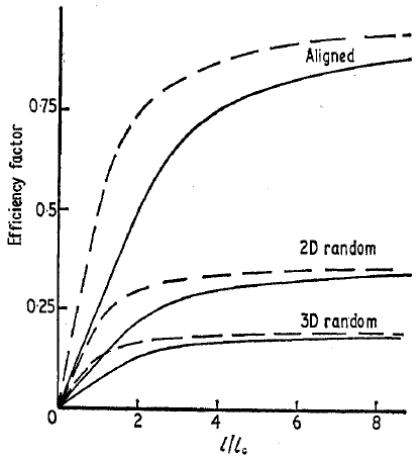

Figure 2.19 The total efficiency factor η as a function of the ratio of fiber length to critical fiber length, when $\tau_d = \tau_s$ (broken curve) and $\tau_d = 0$ (full curve), (Laws, 1971)

The rule of mixture can be used to predict the modulus of elasticity, E_c, and the first crack stress of the composite, σ_{mu}, in tension,

$$E_c = E_m V_m + \eta_l \eta_\theta E_f V_f$$
$$\sigma_{mu} = \sigma'_{mu} + \eta_l \eta_\theta \sigma'_f V_f \qquad [2.21]$$

where σ'_f is the stress in the fiber at the first crack strain and σ'_{mu} is the tensile strength of the matrix in the absence of fibers. Substituting typical properties of fibers in the equations ($V_f << 5\%$, $E_f \leq 30.5$ ksi), modulus of elasticity for a composite cannot be exceed 10~20% of modulus of elastic of plain concrete, which is not very significant in practical point of view. If there is sufficient amount fibers, stress can be transferred between fibers though the matrix cracks. This volume fraction of fibers can be defined as the critical volume fraction of fibers as defined in Equation 2.22. The mode of

fracture with the critical volume fraction of fibers can be characterized as multiple cracks rather than single crack, because the fibers can keep transferring force without significant degradation of fiber-matrix bond. . For continuous aligned fibers, the critical volume fraction can be calculated as followed,

$$V_{f(crit.)} = \frac{E_c}{E_m}\frac{\sigma_{mu}}{\sigma_{fu}} \qquad [2.22]$$

The critical volume calculated based on the equation is ranged from 0.3% to 0.8% for steel. However, for short and randomly distributed fibers, the critical fiber volume is generally ranged from 1% to 3% (Hannant, 1978).

2.4.2.2 Flexural Strength of SFRC

ASTM C1609, "*Standard test method for flexural performance of fiber-reinforced concrete* (Using beam with third-point loading),"(2010) is the specifications for flexural test method for FRC used in the U.S. This test method is the test for evaluation of SFRC in shear as required by ACI 318building code (2008).

Numerous researches have been conducted in the past a few decades regarding the flexural behavior of SFRC, a few of them are summarized as follows.

Ramakrishnan et al. (1979) investigated flexural behaviors of SFRC, which contained straight or deformed ends steel fibers. The dimensions of beams used in this study were 4 in. in height and width, and 14 in. long. Third point load was applied with span length of 12 in. From this investigation, SFRC increased not only modulus of rupture but also

toughness, which can be defined as the area under the load – deflection curve as shown in Figure 2.20. Plain concrete showed brittle failure. Once it reached peak (or cracking) strength, the beam was failed, in contrast, SFRC showed either deflection-hardening or deflection-softening behaviors after first cracking. It is interesting to note that fibers with hooked end (also called as deformed shape in their study) showed better performance in terms of peak and residual strength compared to straight steel fibers even though a dosage of hooked end shape steel fiber was less. They concluded that hooked end shape was superior to the straight one due to an excellent end anchorage (or bond).

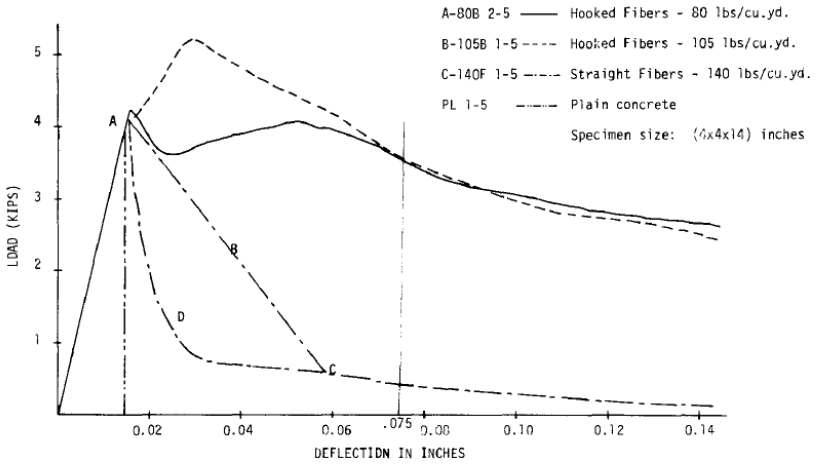

Figure 2.20 Load-deflection curves for static loading at 28 days
(Ramakrishnan et al., 1979)

Wafa and Ashour (1992) conducted experimental program to investigate flexural property in high strength SFRC, with compressive strength ranged from 13.7 ksi to 14.2 ksi. The steel fibers used in their study had hooked end and had a length of 2.36 in. and

diameter of 0.03 in., in turn, the aspect ratio was 75. The flexural test was performed based on ASTM C1018 (1997), which used to be applied to observe toughness index, however, it was withdrawn from the ASTM standards in 2006 due to lack of knowledge regarding with the concept of toughness index (ASTM C 1018, 2006). The sizes of specimen used were 6×6×21 in. and 4×4×14 in. They also concluded that increasing fiber contents increased both the peak and residual strength in flexure. It should be noted that the flexural strength of 6×6×21 in. specimens was approximately 91% of that of the 4×4×14 in. specimens, regardless of fiber contents (see Figure 2.21). This seemed to suggest the flexural strength of SFRCs is subjected to size effect.

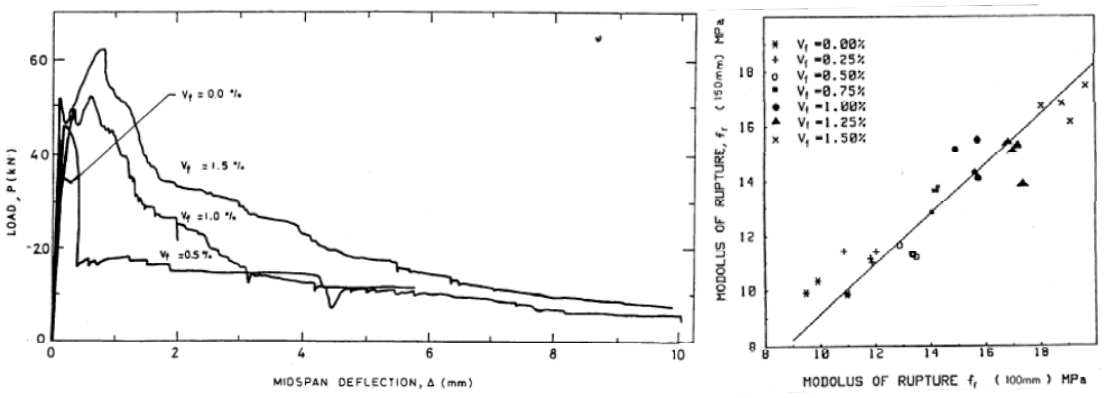

(a) (b)

Figure 2.21 Typical test results in flexural test (Wafa and Ashour, 1992); (a) Load-deflection curves for HSFRC beams; (b) Effect of specimen

In fact, the size effect in SFRCs was reported by Naaman and Reinhardt as well (2006). As can be seen in Figure 2.22, small dog-bone specimens generally showed better performances in terms of the peak and residual strengths over large dog-bone specimens.

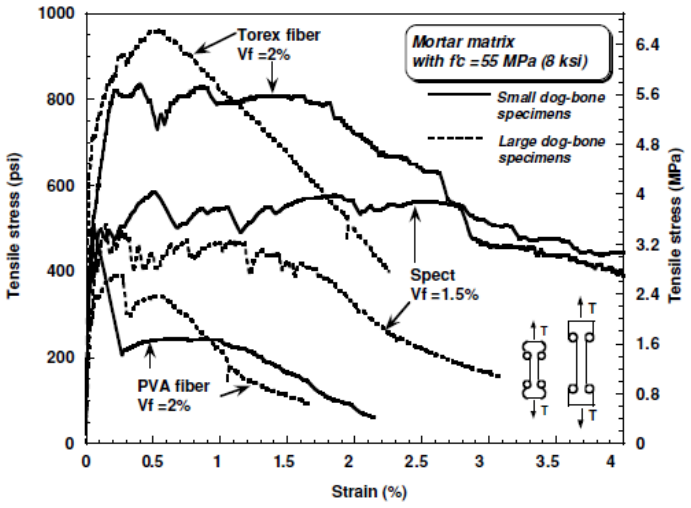

Figure 2.22 Tensile stress-strain curves of FRC curves illustrating size effect (Naaman and Reinhardt, 2006)

Gao et al.(1997) conducted tests to observe effects of aspect ratio of steel fibers on the flexural behavior. Unfortunately, they did mentioned the shape of steel fibers used. The specimens used in their study had a height and width of 4 inches and length of 14 inches. The steel fibers had a rectangular shape with varying lengths, producing a variation in aspect ratios. As shown in Figure 2.23, the SFRC beams showed an increase in peak and residual strengths compared plain concrete. It should be noted that the specimens with a higher aspect ratio showed better performances in flexure with same amount of fibers.

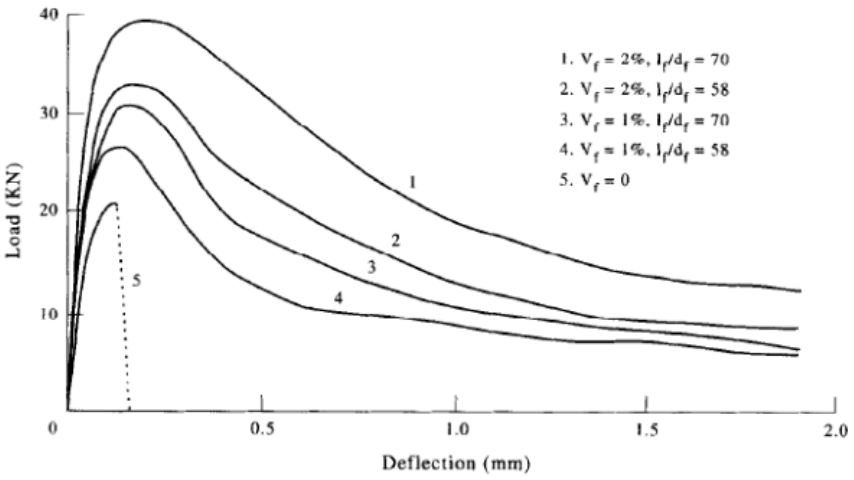

Figure 2.23 Typical flexural load-deflection curves of SFRC
(Gao et al.1997)

Sivakumar and Santhanam (2007) found flexural toughness index in FRC using JCI-SF4 "*Method of tests for flexural strength and flexural toughness of fiber reinforced concrete using beam with third-point load*" (year). The toughness index is defined as area under load-deflection curve up to 3 mm (0.12 inch.) deflection in JCI-SF4. They used steel and hybrid fibers concrete, which used both metallic and non-metallic fibers in one concrete mixture. It can be noted from Figure 2.24 that adding fibers increases flexural toughness. It is interesting to note that as contents of metallic fibers increased the specimens showed higher flexural toughness compared to specimens with higher contents of non-metallic and lower contents of metallic fibers. For stiff fibers such as steel ones, the strains (or crack width of the concrete) needed to develop full strength of fibers are relatively low compared to non-metallic or polymeric fibers, hence, for the same volume fraction, aspect ratio and shape of fibers, stiff fibers generally provide better composite behavior.

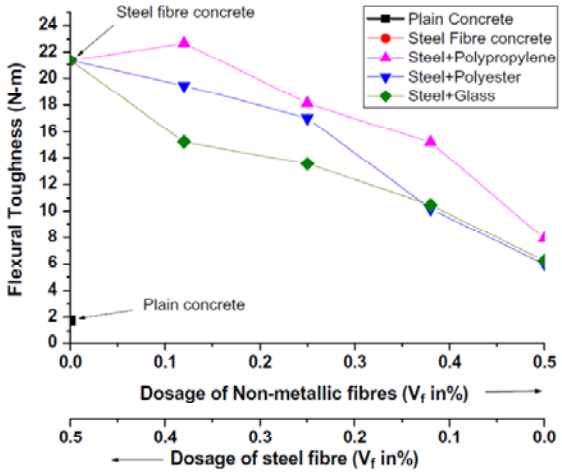

Figure 2.24 Flexural toughness of various hybrid fiber concretes (Sivakumar and Santhanam, 2007)

2.4.2.3 Compressive Strength of SFRC

Fanella and Naaman (1983) conducted compressive test on SFRC. They reported that there was slightly improvement in the compressive strength, ranging from 0 to 15 percent at best, with up to 2% of volume fraction of fibers. On the other hand, toughness, which can be defined by the area under stress – strain curve, was significantly improved as shown in Figure 2.25. It can be said that inclusion of fibers does not enhance the peak compressive strength significantly in practice, but does enhance ductility significantly.

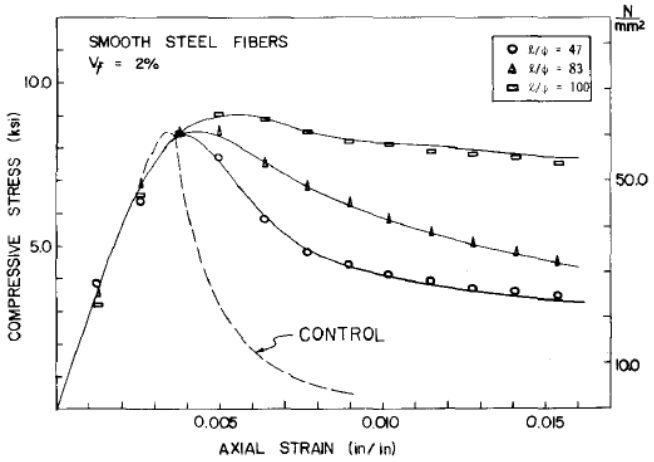

Figure 2.25 Influence of the aspect ratio of fibers on the stress-strain curve (Fanella and Naaman, 1983)

Gao et al. (1997)reported similar results; the compressive strength only reached a certain level of strength while fiber dosages increased, and the compressive strength did not benefit very much from the increased fiber amount. They stated that this might be because dispersion of fiber became very difficult when fiber volume fraction was further increased to 2.5%. For this reason, concrete was not fully compacted, thus inducing more defects.

Song and Hwang (2007) also showed that adding steel fibers in high strength concrete slightly increased compressive strength around 15.3% by using1.5% of volume fraction of fibers. However, 2.0% volume fraction of fibers only improved 12.9% of the peak strength. It can be explained by compact issue suggested by Gao et al. Shah and Rangan (1971) recommended use SFRC in a zone where toughness or ductility of concrete is critically important, such as compression zone of beams.

2.5 Shear Behavior of SFRC

2.5.1 Test of SFRC Beams without Stirrups

The first scientific investigation regarding the use of steel fibers as shear reinforcement was conducted by Batson et al. (1972). They conducted experimental programs to investigate shear behavior of SFRC with various fiber shapes (round, flat and crimped) and fiber amounts (0%, 0.22%, 0.44%, 0.88% and 1.76% by volume). The size of the specimen used in this study was 4×6×78 inch. The general conclusion was that the vertical stirrups could be replaced by round, flat, or crimped steel fibers. Figure 2.26 showed the shear stress as a function of the steel fiber content. The broken vertical line indicated a failure mode, i.e., left side was the shear failure, and right side was the flexural failure. As can be seen in Figure 2.26, the concrete beams with higher than 0.44% volume fraction of fibers showed the flexural failure rather than the shear failure indicating that the inclusion of steel fibers enhanced the shear capacity such that the failure mode was shifting to the flexure. In addition, a specimen that had shear span to effective depth ratio, *a/d*, less than 3 showed a greater increment of shear compared to a specimen that had *a/d* more than 3. They approached a result related to the effect of fiber shape as a concept of fiber spacing rather than bonding strength used in recent years. They believed that smaller size of steel fibers performed better than larger sized one because more fibers could be added with the same volume fraction of fibers, which provides smaller spacing between fibers.

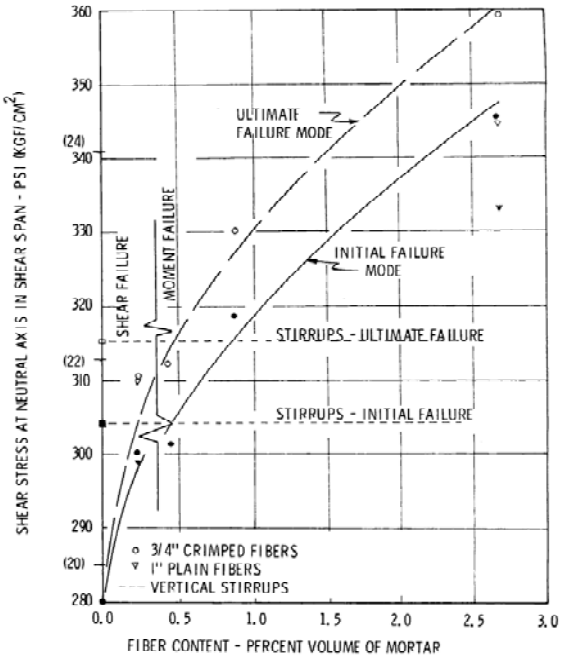

Figure 2.26 Shear stress at neutral axis (Batson et al., 1972)

Since then, numerous research works have been conducted and have verified that steel fibers are able to enhance the shear capacity of concrete beams, in addition, conventional vertical stirrups could be totally or partially replaced by steel fibers with proper mix design and selection of fiber types and contents.

Parra-Montesinos (2006) built a database comprising results from tests of 147 SFRC beams with deformed steel fibers and 45 companion beams without fibers. The parameters considered in the database were effective beam depths ranging 7 in. to 22.5 inch., shear span to effective depth ratios ranging from 1.0 to 6.0, concrete compressive strengths ranging from 2.6 ksi to 15.1 ksi, fiber volume fractions ranging from 0.25% to 2.0%, types of steel fiber (hooked end or crimped; in five of the beams a combination of

straight and hooked end fibers were used), fiber length to diameter ratios ranging from 50 to 100, and longitudinal tensile reinforcement ratios ranging from 0.37% to 4.58%. By analyzing the database (see Figure 2.27), he suggested that 0.75% volume fraction of deformed steel fibers can be used as lower bound of steel fiber content in order to completely replace conventional shear reinforcement. To evaluate material performance, ACI 318 building code (2008) adopted to use ASTM C1609 test method. The test is based on flexural tests, ASTM C1609 and the criteria require that the strengths at midspan deflections of 1/300 and 1/150 of the span length should be greater than or equal to 90 and 75% of the first peak strength, respectively, in *any* flexural test unit. It is interesting to note that flexural test method is required to evaluate the shear behavior of concrete beam even though shear and flexural behaviors are distinctly different. That is because there is no universal shear and direct tensile test methods for fiber reinforced concrete.

Based on clear evidence stated above, ACI 318-08 building code accepts the use of steel fibers as shear reinforcement to replace minimum required shear reinforcement with certain criteria (ACI 318-08 Section 11.2.2.1 and 5.6.6.2)

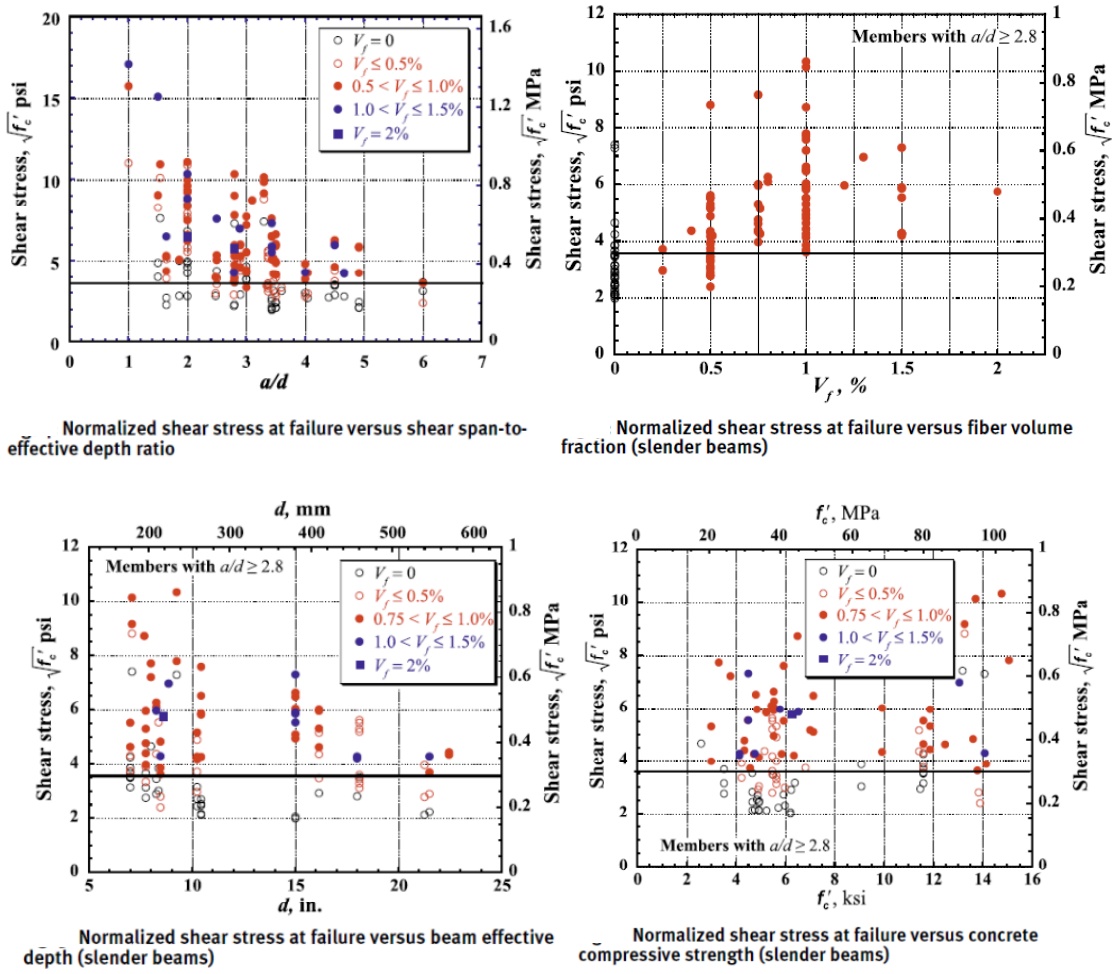

Figure 2.27 Shear strength of SFRC (Parra-Montesinos, 2006)

2.5.2 Prediction of Shear Strength of SFRC Beams

Sharma (1986) proposed an empirical expression to predict ultimate shear strength using the indirect tensile strength, f_{ct}, and the shear span to effective depth ratio, a/d.

$$v_u = \left(kf_t\right)\frac{d^{0.25}}{a} \qquad [2.23]$$

where k is a constant. The author adopted k=2/3, which was suggested by Wright (1955), which is a factor to revise indirect tensile strength to direct tensile strength. Sharma used the following relation recommended by the European Concrete Committee (Comité Euro-International du Béton, 1993) when tensile strength of concrete was not available.

$$f_{ct} = 9.5\sqrt{f_c'} \qquad [2.24]$$

He concluded that a reasonable estimation of shear strength of SFRC beam can be made by using the Equation [2.23].

Narayanan and Darwish (1987) have investigated the shear behavior of steel fiber reinforced concrete beams.. They considered that diagonal shear cracks develop and eventually cause failure of the concrete beam when principal tensile stresses exceed the tensile strength of the concrete. To evaluate tensile strengths of plain concrete and SFRC, they used splitting tensile strength, f_{spfc}, which is considered to be one of the major contributions of shear resistance. They attempted to use fiber pull-out forces along the inclined crack to postulate the contribution of steel fibers. Their proposed equation to predict the shear strength is shown below with units of N and mm;

$$v_u = e\left[0.24 f_{spfc} + 80\rho\frac{d}{a}\right] + v_b \qquad [2.25]$$

where, e is a non-dimensional factor that takes into account the effect of arch action. The coefficient, e, is 1.0 when $a/d > 2.8$ and 2.8 d/a when $a/d \leq 2.8$. f_{spfc} was derived from regression analysis.

$$f_{spfc} = \frac{f_{cuf}}{20 - \sqrt{F}} + 0.7 + \sqrt{F} \qquad [2.26]$$

where, f_{cuf} is the compressive strength from cube test and F is defined as follows;

$$F = \left(\frac{L}{D}\right) \cdot \rho_f \cdot d_f \qquad [2.27]$$

where, L/D is aspect ratio of the fibers, ρ_f is the volume fraction of the fibers, and d_f is the bond factor that accounts for differing bond characteristics of the fibers. They suggested d_f as 0.5 for round fiber, 0.75 for crimped fibers, and 1.0 for indented fibers. v_b represents pull-out force:

$$v_b = 0.41\frac{L}{D} \cdot \rho_f \cdot \tau \qquad [2.28]$$

where, τ is average fiber matrix interfacial bond stress. The authors adopted the value of τ as 4.15 N/mm^2, which was proposed by Swamy et al. (1974).

Swamy et al.(1993) proposed a simple method based on a truss model with variable inclination of compression chord and compression diagonals or struts for analysis of the fiber concrete beams as illustrated in Figure 2.28. The total resistance is:

$$V = V_w + V_c \qquad [2.29]$$

where, V_w is contribution of web reinforcement and V_c is contribution of inclined compression chord. In the case of SFRC beams, V_w can be given by

$$V_w = 0.9\sigma_{cu} \cdot b_w \cdot d \qquad [2.30]$$

where, σ_{cu} is post-cracking tensile strength, which can be calculated as

$$\sigma_{cu} = \eta_o \cdot \eta_L \cdot \sigma_{fu} \cdot V_f \qquad [2.31]$$

where, η_o and η_L are the orientation factor of fibers and length efficiency factor of fibers. The author used the orientation factor as 0.41 and the length efficiency factor based on the work of Laws (Eq. 2.17). σ_{fu} and V_f are the fiber fracture stress and volume fraction of fibers, respectively. V_c can be calculated as:

$$V_c = 3.75\tau_R \cdot b_w \cdot d \qquad [2.32]$$

where, τ_R is the concrete shear strength and depends on its compressive strength.

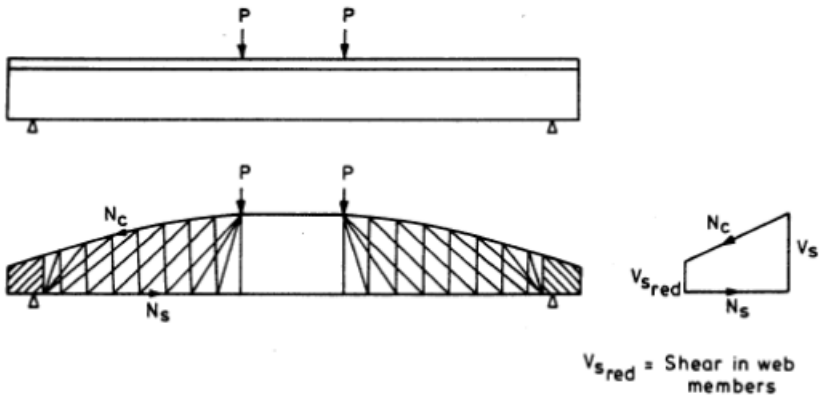

Figure 2.28 Generalized truss model with variable inclination of compression chord and struts (Swamy et al., 1993)

2.6 Shear Behavior of SFRPC

Tan et al. (1995) used steel fibers as shear reinforcement in partially prestressed beams, in which prestressing stands and mild tensile steel rebars were used to reinforce flexure. Total height of beams used in their experiment was 9.8 in. and lengths of the beams were varied depending shear span to effective depth ratio, *a/d* (6 ft for *a/d*=2.0, 7.3 ft for *a/d*=2.5, and 8 ft for *a/d*=3.0). The beams had T-section (width of beams = 3 in.). The parameters used in the study were volume fraction of steel fibers (0%, 0.5%, and 1.0%), shear span to effective depth ratio (2.0, 2.5, and 3.0), partially prestressing ratio (0%, 0.25%, 0.5%, and 1.0%), compressive strength (4569 psi ~ 6135 psi), and the stirrup reinforcement ratio (0%, 0.23%, and 0.45%). The partially prestressing ratio in their study was defined as the ratio of the ultimate moment of resistance due to the prestressed reinforcement to the moment of resistance due to all tensile steel including prestressing reinforcement. The stirrup reinforcement ratio was defined as the area of stirrups divided by the width of the beam times spacing of stirrups. A total of ten specimens were tested. The steel fibers used in the study had hooked ends and an aspect ratio of 60 (length, 1.2 in., divided by diameter, 0.02 in.) Their research concluded that adding steel fibers enhanced the ultimate shear strength of partially prestressed concrete beams with 1.0% of steel fibers by two times the shear strength predicted by the ACI 318 equation. They also observed that the load at first web cracking increased with an increase in steel fiber contents. In addition, stiffness of specimens after web cracking depended on the presence of steel fibers; the rate of decreasing stiffness after web cracking was less when a specimen contained steel fibers. They also concluded that

stirrups can be replaced by steel fibers without significant affecting the behavior and strength of partially prestressed concrete beams in shear; shear resistance provided by stirrups can be replaced by steel fibers based on following equation:

$$V_{SF} = 0.6\sigma_{tu} b_w d \qquad [2.32]$$

where, V_{SF} is the additional shear strength due to steel fibers, σ_{tu} is the post cracking tensile strength of SFRC under uniaxial tension according to the principal tensile stress-strain relation proposed by Tan et al. (Tan et al., 1993), b_w is width of beams, and d is effective depth of beams.

$$\sigma_{tu} = \frac{\eta_l \eta_0' V_f l_f \tau u}{2r'} \qquad [2.33]$$

where, η_0' is the orientation factor, η_l is the length efficiency factor, V_f is the volume fraction, l_f is the length of the fiber, τ_u is the ultimate bond strength, and r' is the ratio of the area of cross section to the perimeter of the fibers. The authors used the orientation factor as 0.405, and the length efficiency factor can be calculated as:

$$\eta_l = \begin{cases} 0.5 & for \ \ l_f \le l_c \\ 1 - l_c / 2l_f & for \ \ l_f > l_c \end{cases} \qquad [2.34]$$

where, l_c is the critical length defined in Equation 2.16.

Padmarajaiah and Ramaswamy (2001) investigated the shear behavior of steel fiber reinforced prestressed beams with fiber volume fractions of 0.5% and 1.5%, and high strength concrete. The beams used in the experiment had length of 7.2 ft., total height of 9.4 in., and width of 4.1 in. Note that the compressive strength used was 9427 psi,

which is much higher than the current ACI 318-08 limitation, 6000 psi. As can be seen in Figure 2.29, their results confirmed that the steel fiber reinforcement increased not only ultimate shear strength of a prestressed beam but also the ductility. An interesting result from the experiment work was that while the failure was induced by flexural-shear crack in PC, the failure mode of an SFRPC beams with volume fraction of fiber as 1.5% was pure flexure, indicating that steel fibers considerably enhanced the shear strength.

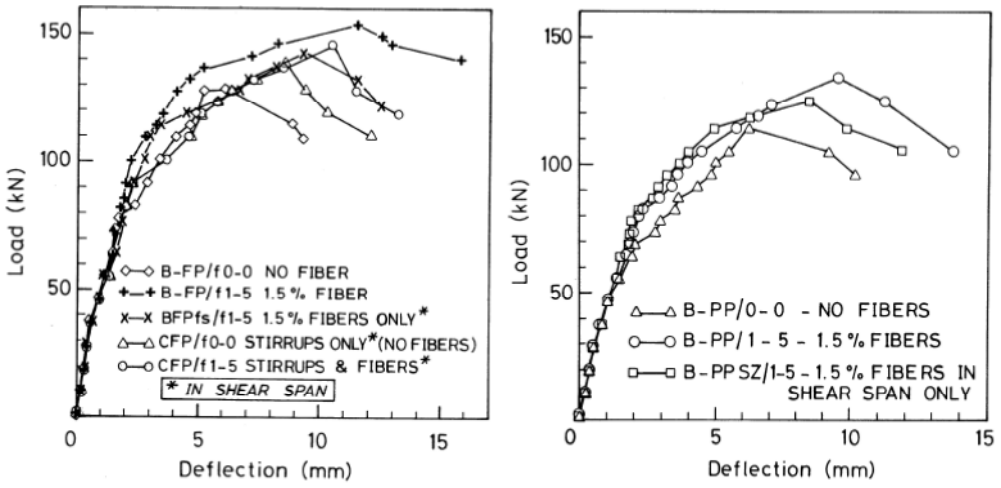

(a) (b)

Figure 2.29 Load versus deflection response for fully and partially prestressed beam specimens specimen (Padmarajaiah and Ramaswamy, 2001); (a) Fully prestressed beam specimen; (b) Partially prestressed beam

Tomas et al. (2006) also used steel fibers as shear reinforcement in high strength prestressed concrete, which normally shows more brittle failure than normal strength. The steel fibers used in their study were trough-shaped steel fibers of 1.2 in. length having an aspect ratio of 55. The volume fraction was 1.5%. Compared with plain concrete, the shear strength of SFRPC beams were increased 11, 17, and 20% for

normal (5070 psi), high strength (9420 psi), and very high strength (1232 psi) beams, respectively.

It is noted that the depths of the beams used in those prior research works were less than or equal to 10 in. only, therefore, the results may not by applied to larger size of beams due to the size effect.

2.7 Shear Test Methods for SFRC

A direct shear test method for fiber reinforced concrete (FRC) is essential to understand the basic shear transfer behavior of concrete, however, there has been no agreement upon a standard test method to evaluate the direct shear behavior of fiber reinforced concrete (FRC) even though some researchers have been attempting to develop the direct shear test method. Following section will discuss some of the attempts.

2.7.1. Z-type Push-off Test

Z-type push-off test was originally proposed by Hofbect et al. (1960). Two L-shaped blocks are connected through a ligament along which the shear loading is applied as shown in Figure 2.30. This method was used to evaluate fiber reinforced concrete by other researchers. In 1993, Valle et al. applied the Z-type push-off test method to FRC. Geometry and steel rebar reinforcement for specimen used in the experiment is shown in Figure 2.30. They used a specimen with 1.0% volume fraction

of steel fibers, but unfortunately, they did not report mechanical and geometrical properties of steel fibers. Based on their research, concrete reinforced with steel fibers showed 36% and 59% higher ultimate shear strength compared to normal and high strength concrete, respectively.

Barragán et al. (2006) also carried out shear evaluation for SFRC by using the Z-type push-off test method. The volume fractions of steel fibers were 0.26% and 0.50%, and the steel fibers used in the study had length of 2.36 inches and diameter of 0.0295 inches, i.e., aspect ratio of 80. They concluded that the energy dissipation capacity of SFRC in post cracking regime increased, and the incorporation of fibers in concrete subjected to shear leads to a better mechanical integrity upon failure.

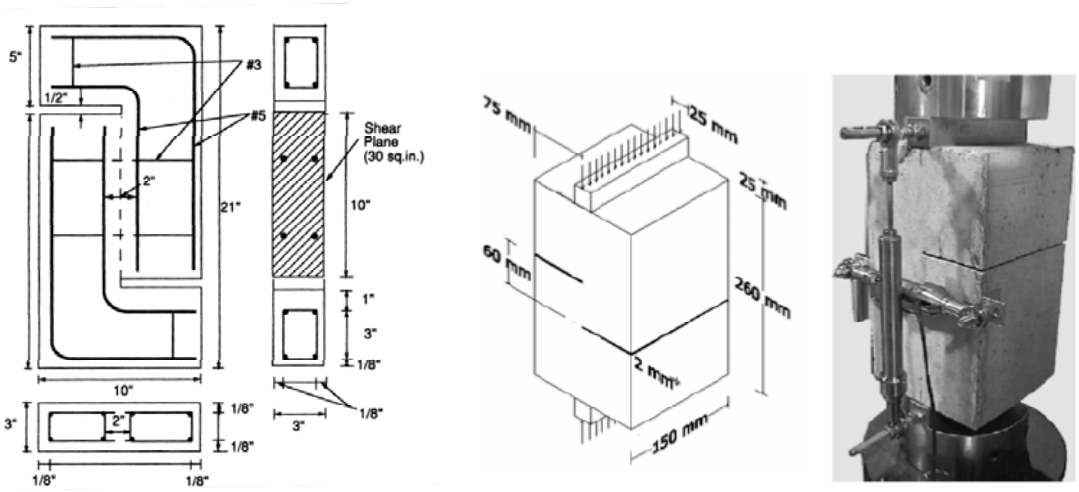

(a) (b)

Figure 2.30 Geometry and steel bar reinforcement for push-off specimen; (a) Valle et al., 1993; (b) Barragán et al., 2006

However, it has been pointed out that although the push-off specimen allows one to measure the properties of FRC in direct shear, the stress filed in the specimen beyond cracking is highly complex, and stress conditions deviated from being in pure shear due to notches (Mirsayah and Banthia, 2002). In addition, the width of shear plane between two steel rebars was 2 in. only, which is not sufficient to uniformly distribute the steel fibers.

2.7.2 JSCE-SF6 Test and Modified JSCE-SF6 Test

Japan Society of Civil Engineers (JSCE) provides a direct shear test called as JSCE-SF6 (1990). In this test, shear load is applied by two sharp knife edges and the specimen is supported by another rigid block with two sharp loading knife edges. The region between the loading and the supports are subjected to direct shear in plane A-B in Figure 2.31 (a). However, the failure plane often deviated from the narrow region under concentrated shear, which is the prescribed plane for failure. For this reason, the test generally produced invalid results (Mirsayah and Banthia, 2002).

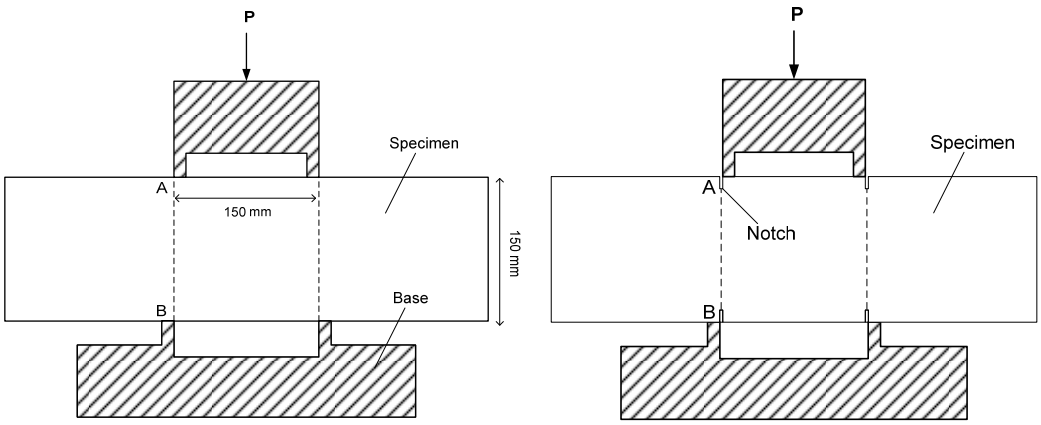

(a) (b)

Figure 2.31 Original and modified JSCE-SF6 direct shear test specimen (Mirsayah and Banthia, 2002); (a) Original JSCE-SF 6; (b) Modified JSCE-SF6

Mirsayah and Banthia (2002) proposed a modified JSCE-SF6 test method by creating notch under two sharp edges as shown in Figure 2.31 (b), and they applied this test method to SFRC. They used two different types of steel fibers; flattened ends shape (FE) had length of 2 in. and diameter of 0.04 inches, aspect ratio of 50, and crescent crimped shape (CR) had an equivalent aspect ratio of flattened ends shape one. For FE fibers, the ultimate shear strength increased 19.5%, 28.8%, 41.6%, 55.0%, and 88.0% for 0.25%, 0.50%, 0.75%, and 1.0% of volume fraction of fibers, respectively. For CR fibers, ultimate shear strength increased 31.9%, 46.7%, 51.7%, and 55% for 0.50%, 0.75%, 1.0%, and 2.0% of volume fraction of fibers, respectively. They also observed that toughness increased in SFRC compared to PC.

2.7.3 Iosipescu Test

The Iosipescu test method was developed by N. Iosipescu (1967). By adjusting loading and support position, it is possible to create a region in the specimen subjected to practically pure shear as shown in Figure 2.32. V-notched is purposely created to reduce the risk of failure in bending and fail in designated area. The Iosipescu shear test method has been widely used in testing laminated composite materials as well as in the investigation of fracture characteristics of plain concrete subjected to shear.

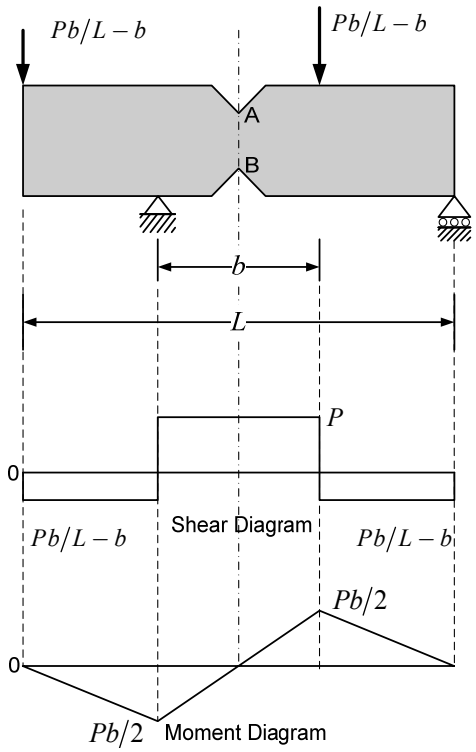

Figure 2.32 Schematic view of the Iosipescu test method

van Zijl (2007) applied the Iosipescu test method to Engineered Cementitious Composite (ECC) which contains high modulus polyethylene fibers and normally shows strain-hardening behavior under tension. He used a 90° notch angle to provide

uniformly distributed shear stress along designated area (see Figure 2.33 (a)). However, the test results showed that failure was induced at the tip of notch due to stress concentration, rather than the center of the beams, where shear stress was maximized (see Figure 2.33 (b)). It should be noted that the presence of the V-notches will alter the required random distribution of fibers, especially commonly used steel fibers with length of 1 to 2 in.

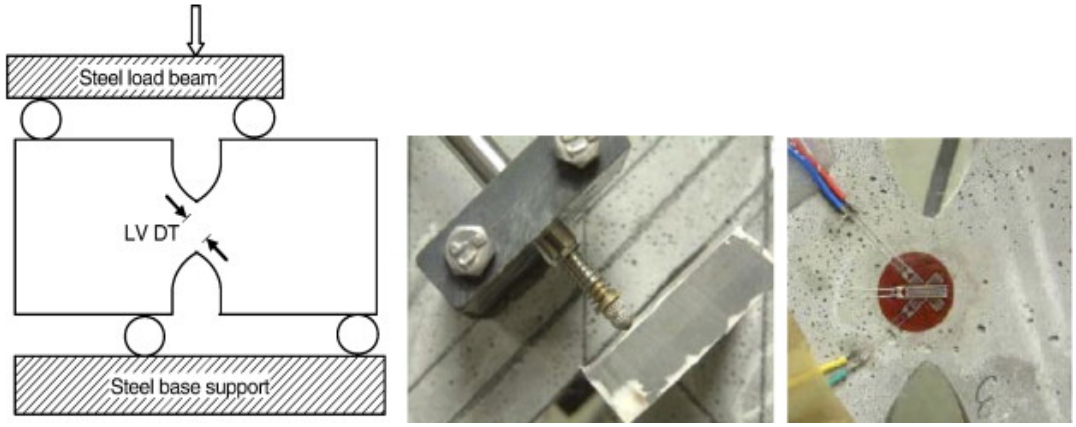

(a)

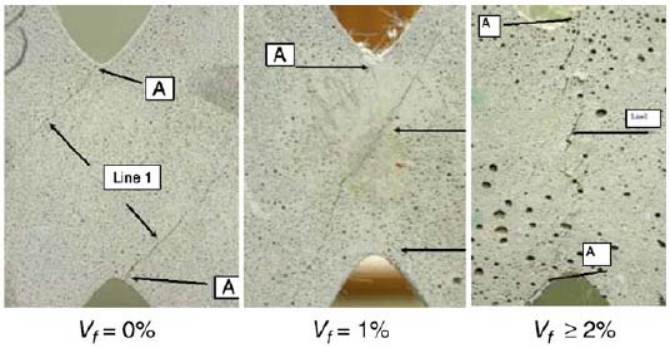

(b)

Figure 2.33 Test conducted by van Zijl; (a) Test setup; (b) Cracks in the vicinity of the notches (van Zijl, 2007)

CHAPTER 3

EXPERIMENTAL PROGRAM

3.1 General

As mentioned in Chapter 1 and Chapter 2, numerous of researches have been conducted and proved that steel fiber reinforcement enhances the shear performance of concrete beams. Based on these efforts, ACI 318 building code (2008) allowed the use steel fiber reinforcement as an alternative shear reinforcement when certain specifications, such as ACI 318-08 Section 11.4.6.1, are satisfied. However, the provision is applied to both nonprestressed and prestressed concrete flexural members even though almost all prior investigations were based on experimental tests on nonprestressed concrete flexural members. A prestressed concrete (PC) beam has an enhanced shear strength due to prestressing force, which was not explicitly considered in the current codes. For this reason, the minimum amount of steel fiber recommended by ACI 318-08 building code could be conservative for prestressed concrete beams. Unlike regular SFRC beams, limited experimental results are available in shear behavior of steel fiber reinforced prestressed concrete (SFRPC) beams. Moreover, most of tests in SFRPC beams were conducted using small scale specimens; that is, the depth of the beam was typically less than 10 in. The results may not be applicable to larger sized beams (i.e., a depth of the beam up to 24 in.) due to size effect. The experimental

programs presented in this study were planned to achieve an understanding of the shear behavior of large scale prestressed concrete beams reinforced with steel fibers. This experimental program involved the design, construction, and testing of simply supported beams subjected to a monotonically increased, concentrated load. The large scale experimental program consists of three phases. Each phase's work is treated in a separated section.

In order to evaluate the qualification of a particular SFRC mixture used for structural application, for example shear resistance, an evaluation method is essential. However, ASTM or ACI Committee 544 (Fiber Reinforced Concrete) does not recommend any standardized testing method for evaluating the shear performance of a particular SFRC material. A few test methods have been used to the evaluation of shear properties of SFRC, but most of them failed to represent a standard material shear test for SFRC. Some of the problems encountered were the difficulty of the test setup, fail to simulate a pure shear stress state, and guaranteeing uniformly distributed fibers. Current ACI 318-08 requires that ASTM C1609 *("Standard test method for flexural performance of fiber-reinforced concrete (using beam with third-point loading)"*) be used to evaluate the performance of SFRC materials in shear design, even though the test might be not a suitable method due to the fact that flexural and shear behaviors are distinctly different. This experimental program contains an attempt to develop a shear test method for SFRC and to verify it with finite element method (FEM) analysis.

3.2 Experimental Program for the Large Scale SFRPC Beams

This experimental program consisted of three phases. The first phase contained two types of specimens, one is conventional PC, used as a control specimen, and the other one with SFRC. The second phase had a total six numbers of specimens, three PC specimens used as control specimens and three SFRPC specimens with a varying volume fraction of fibers and compression reinforcement ratios. In the last phase, there were total five numbers of specimens, one PC specimen and four SFRPC specimens.

Shear span to depth ratio

A shear span to effective depth (*a/d*) ratio of 3.0 was selected for all specimens. As can be seen from Figure 3.1 (a), the beam can reach its full flexural strength when *a/d* ratio is equal to or greater than 6.5. The beam with *a/d* ratio less than 6.5 would be fail due to shear as shown in Figure 3.1 (b). However, the beam with less *a/d* ratio (< 1.0) shows higher shear strength due to the arch action, which enhances shear capacity of a beam due to direct load transfer from loading point to support. The effect of arch action would be minimized when a beam has approximately equal to or less shear span to effective depth (*a/d*) ratio of 2.5 (ASCE-ACI Committee 426, 1973). The strength of the beam with *a/d* ratio greater than 2.5 would be governed by the inclined crack eliminating the effect of the arch action. In addition, as can be seen in Figure 3.1 (b), the strength becomes almost constant even though the *a/d* is increased. Thus, in order to eliminate the enhancement of the shear strength due to the arch action as well as minimize the shear strength, *a/d* of 3.0 was selected .

Height of beam

All specimens used in the large scale experimental program were 24 in. height. This height was chosen because it is the upper bound limitation specified in ACI 318-08 building code, when steel fibers are used as alternative shear reinforcement to replace the minimum required conventional shear reinforcement (ACI 318-08, 2008). It is worth mentioning again that the height of SFRC prestressed beam beams were only approximately 10 in. in the prior investigations (see Chapter 2).

3.2.1 The First Phase Experiment

The first phase experimental program was proposed to be characterized as a pilot test. In this phase, two specimens were prepared and tested. One was SFRPC beam and the other one was conventional PC beam.

3.2.1.1 Design of Specimens – 1st phase

The two beams tested in this phase study had identical geometries; the length of beam was 204 in. (17 ft), the width of beam was 19 in., height was 24 in. (2 ft), and the designed shear span was 63 in. (5 ¼ ft). In order to have a shear span to effective depth ratio of 3.0, the concentric load was applied 63 in. from the support, as can be seen in Figure 3.2. 15 – No. 3 mild steel bars were used as stirrups with a closed shape and spacing of 7.5 in. along the longer span (117 in., 9 ¾ ft) to ensure that the shear failure would occur in the short span. No stirrups were provided in the short span. To avoid premature flexural failure, 7 – No. 8 longitudinal reinforcing bars (A_s = 5.53 in^2) were

placed, which in turn led to a total longitudinal reinforcement ratio, ρ, of 1.62% including 6 – 0.5 in. diameter of prestressing stands (A_p = 0.918 in^2). Compression reinforcements of 2 – No. 4 mild steel bars (A'_s = 0.40 in^2) were place at 3 in. below the top of the beams. Detailed dimensions of the specimens are shown in Table 3.1 and Figure 3.2. The volume fraction of steel fibers used for the SFRPC was 0.75%, which is the minimum required amount specified by ACI 318-08 building code. Six strands (0.5 in. diameter prestressing strand, ASTM A416, Grade 270 and stress-relieved) were used in the specimens and they were placed and stressed by a prestressing jack system at a local precast plant (Hanson Pipe & Precast). The applied pressure was monitored in the dial pressure gauge by professional worker at the plant. An initial prestressing of 189 ksi was applied to each strand, which in turn gave an average initial prestress of 380 psi in each beam.

3.2.1.2 Materials – 1st phase

Steel fiber

The steel fibers used in this phase of the study were Dramix RC80/60BN fibers manufactured by Bekaert Cooperation. The steel fibers have doubled-hooked shape at their ends and glued into bundles by dissolvable glue as can be seen in Figure 3.3. The manufacture advertized that the bundled steel fibers with dissolvable glue would help prevent balling, which occurs when the fibers stick together and create a ball during mixing and it become impediment of the uniformly distributed fibers when improper mix designs or long mixing time are used (ACI 544 Committee, 1998). The glue would

be dissolved by the water used in a normal mix. The mechanical properties of steel fibers used in this phase study are listed in Table 3.2. The length (L) and diameter (D) of fiber are 2.37 in. and 0.029 in. respectively, which in turn gives aspect ratio (L/D) of 82. The tensile strength of the fibers was 152 ksi (1050 MPa).

Concrete mix

A trial mix was done in the University of Texas at Arlington Civil Engineering Laboratory to ensure workability and a uniform distribution of steel fibers, as well as designed compressive strength greater than 6000 psi, which is the maximum limitation of the compressive strength specified by ACI 318-8 building code (ACI 318-08, 2008). All of the materials were provided by the local precast plant and the concrete was mixed using the local precast plant's facilities (Figure 3.4) and was transported to the prestressing bed at the plant. The mix proportions used in this study are listed in Table 3.3. Except the fibers, all the other materials were measured and dumped into the pan mixer through an automation system. Prior to mixing, exact amount of steel fibers needed to reach V_f = 0.75% were measured manually and were placed besides the mixer. In the last procedure of mixing, the mixing hatch was opened and the steel fibers were added manually as shown in Figure 3.5.

3.2.1.3 Fabrications – 1st phase

The fabrication of the specimens was done by professional workers at the local precast plant under the author's supervision, including fabricating the formworks and

the reinforcement caging as shown in Figure 3.6. Prestressing strands were held in the design locations by pre-drilled holes at the end pieces of the formwork. The prestressing strands, longitudinal reinforcement, and stirrups were placed first before the prestress was applied to the strands. The prestressing force was applied using a prestressing hydraulic jack shown in Figure 3.7. After all strands were stressed to intended stress level, the longitudinal reinforcement and stirrups were then in place, according to the design locations as indicated in Figure 3.2. Before completing the assembly of the formwork, formworks were oiled ensuring the reinforcements including strands were not stained with oil. The concrete was transferred from mixing facilities to prestressing bed using a concrete transfer a truck (the "Tuckerbilt"). The concrete was poured into the formwork and compacted by vibrators as shown in Figure 3.8. Proper viscosity of the mix for achieving a uniform fiber distribution was previously verified at the laboratory. As shown in Figure 3.9, steel fibers did not segregate and sink such that these fibers were observed at the top surface and well distributed. As can be seen in Figure 3.10, no special technique or equipment was required to provide a smooth surface or avoid fiber stick-out since a regular deconstipating job worked very well. After casting, to facilitate curing process, the specimens were covered with plastic sheets for one day. The beams were demolded and the prestressing strands were released. An attempt was made to measure the camber, but it was negligible due to relatively low prestressing force.

3.2.1.4 Instrumentations and Test – 1st phase

The steel reaction frame that was built by UT Arlington and located at Hanson Pipe & Precast plant was used (Figure 3.11). A hydraulic cylinder was mounted on horizontal beam. The hydraulic cylinder can be freely move horizontally so that the designated shear span to depth ratio can be easily achieved without moving the supports or the specimen. The specimen was placed on top of two concrete blocks which were topped with 0.5 in. thick steel plates, to provide flat surface. Supports, such as steel plates and rods, simulating roller and hinge support conditions were placed between the concrete blocks and the specimen. In this phase of the study, no internal strain gauges were mounted on the mild steel rebars. Instead, three wired potentiometers were used to measure the deflection of the beams at the loading point and the supports. Additional four Linear Variable Differential Transformers (LVDTs) were fixed to plexi-glass and were mounted diagonally on the south face of specimens to measure shear strains in the instrumented shear span. A 200 kips load cell was used for the PC specimen and a 600 kips load cell was used for the SFRPC specimen. All sensors were connected to Vishay 5000 Data Acquisition (DAQ) system shown in Figure 3. 16 and data was collected at a rate of five data points per second. In addition, all data was monitored in real time with a laptop computer connected to the DAQ system. 6×20×1 in. steel plates were used at the loading point and at the supports as the bearing plates. Non-shrink grout was patched to provide uniformly distributed load throughout the width of the beam between the specimen and the steel plate. A load cell was placed above the steel plate and the load was transferred through hydraulic cylinder and the load cell. The test setup and

sensor instrumentations are illustrated in Figure 3.12. The load was applied with 5 to 10 kip increments up to the first visible crack and then in 10 to 20 kips increments up to failure. When the applied load was paused at each load increment, the cracks were marked and test pictures were taken.

Through all phases of the study, Acoustic Emission (AE) sensors were used to monitor internal damage. The information of AE will be treated in Chapter 6.

3.2.2 The Second Phase Experiment

In the second phase of the experiment program, six specimens were prepared and tested for further investigation of the shear behavior of SFRPC beams. Three PC specimens were prepared for comparison purposes, and one of which contained the required minimum amount of conventional shear reinforcement calculated based on ACI 318-08 building code. Three specimens of SFPRC were prepared; 0.75% and 0.5% of volume fractions of steel fibers, and 0.75% of volume fraction of fibers with 0.9% of compression reinforcement ratio (ρ'). The last specimen of SFRPC was designed to investigate the effect of compression reinforcement on the shear behavior of SFRPC beam. This was done because it was observed in the first phase test that the ultimate shear failure was induced by concrete crushing in the vicinity of the loading point so the ultimate shear strength might be enhanced by adding extra compression reinforcement in the SFRPC beam.

3.2.2.1 Design of Specimens – 2nd phase

The geometries of the specimens used in the second phase had minor modifications to the first phase experimental program; the length was shortened from 17 ft to 14 ft for the ease of the placement of the beams by using the precaster's forklift while the shear span to depth ratio remained the same at 3.0, and width was reduced from 19 in. to 16 in. to reduce the amount of load needed to be applied. Prior studies on large reinforced concrete members have demonstrated that the width of beam does not affect the shear behavior of concrete including the failure mode and ultimate shear strength (in terms of stress) of the concrete beam (Sherwood, 2005), such that specimens with reduced width could be comparable to the first phase. The longitudinal reinforcement ratio was 1.64%, i.e., 6 – No. 8 mild steel bars (A_s = 4.74 in^2) plus five 0.5 – in. prestressing strands (A_p = 0.765 in^2). The specimens, 2 – PC#3 and 2 – SFRPC#3, contained 4 – No. 8 mild steel bars (A'_s = 3.16 in^2) as compression reinforcement for the previously mentioned reason. The 2 – PC#1 specimen contained the minimum shear reinforcement with 4 – No. 3 stirrups with a closed shape at 14 in. spacing in the instrumented shear span. The longer span of the specimen was reinforced with 10 – No. 3 closed shape stirrups at 7.5 in. spacing. The conventional shear reinforcement for the long span was applied to all specimens. Detailed information of the specimens is presented in Table 3.4 and Figure 3.13. The same prestressing jacking system used in the first phase study was used for applying prestressing force. An initial prestressing of 189 ksi was applied to the strands, which gave an average initial prestressing of 377 psi in the beams.

3.2.2.2 Materials – 2nd phase

Steel fiber

The steel fibers used in this phase study were the same as used in the first phase: Dramix RC80/60BN. The mechanical properties of the fibers can be found from Table 3.2.

Concrete mix

In this phase of study, the designed compressive strength was less than 6000 psi, which is the maximum strength allowed by ACI 318-08 building code when steel fibers are used as shear reinforcement (ACI 318-08, 2008). To satisfy this provision, the mix proportion used in the first phase was modified by increasing the water to cementitious material ratio from 0.37 to 0.40. The mix proportion in this phase is listed in Table 3.3. The mixing was performed at the same local precast plant as the first phase of the study. The concrete was mixed at the first and then, the steel fibers were added in the last stage of the mixing process. It should be mentioned that water content in 0.5% volume fraction of SFRC might not be correct since there were huge differences of compressive strengths between 0.5% and 0.75% volume fraction of SFRC. The water to cementitious ratio was 0.4 for both 0.5% and 0.75% volume fraction of SFRC, and 0.75% volume fraction of SFRC showed 5234 psi while 0.5% volume fraction of SFRC showed 3755 psi of compressive strength. In addition, it should be mentioned that the steel fibers do not affect the peak compressive strength (Fanella and Naaman, 1983) such that the difference of the compressive strength may not be due to the amount of fibers.

Therefore, it was doubtable that there might be excessive water during casting of 0.5% volume fraction of SFRC by a mistake for any reason.

3.2.2.3 Fabrications – 2nd phase

The fabrication of specimens including preparation of formwork and reinforcement cages was done by the local plant under the author's supervision. Some selected photos of reinforcement caging preparation and concrete casting for the second phase specimens are shown in Figures 3.14 and 3.15, respectively. All specimens were covered by plastic sheets after casting to facilitate curing process. After one day the formworks were removed and the prestressing strands were cut. The measured camber was negligible. All specimens were placed in natural environment until the tests were conducted.

3.2.2.4 Instrumentations and Test – 2nd phase

The test frame and DAQ system (Vishay 5000) used in this phase were the same as the first phase.

Unlike the first phase, strain gauges were used to monitor the strains of the longitudinal reinforcement as well as of the concrete surface and inside the compression zones. Prior to reinforcement caging, foil-type strain gauges were installed onto the bottom and top mild steel reinforcing bars to measure the strains in the bars. It was assumed that the strands and mild steel bars would experience the same strains at the same section. It is

easier to mount strain gauges on mild steel bars than on the seven-wire strands. The ribs on the reinforcing bar were grinded to create a flat area larger enough to mount the strain gauges. Each strain gauge was glued within a degreased flat area and protected by three different types of coating layers, namely polyurethance, nitrile, and rubber pad, and all were sealed by an electric liquid tape as shown in Figure 3.17. At a few selected beam sections, at least two strain gauges along the same section were installed (on different bars) to ensure that at least one data could be available even if one of the strain gauges malfunctioned. In the 2 – PC#1, which contained the minimum shear reinforcement, there were a total eight rebar strain gauges installed on the stirrups as well (four selected locations and each location has two strain gauges on each leg of the stirrup), as shown in Figure 3.18(a). The locations of the strain gauges were determined by the expected shear crack pattern based on previous tests (the shear crack patterns are presented in Chapter 5). Internal concrete strain gauges (Texas Measurements, Inc., PMFL-60-8LT) were embedded inside the concrete at the locations near the loading point and above the top surface of the compression reinforcement This type of concrete strain gauges were used in a few selected specimens, mostly SFRPC specimens. Figure 3.19 gives an example of the mounted concrete strain gages. The strain gauges were well anchored in the concrete by the enlarged ends, so the deformation especially can be measured. Figure 3.18 shows locations of strain gauges.

Another types of strain gauges, concrete surface strain gauges (Texas Measurements, Inc., PFL-30-11-3L), were also installed along the shear span as shown in Figure 3.20.

The locations where surface strain gauge would be placed were slightly grinded with sand paper and then epoxy (Texas Measurements, Inc., PS adhesive) was placed to create a film for the strain gauge. After the film was sufficiently hardened, concrete surface strain gauge was placed and mounted on the surface with the epoxy. The purpose of measuring the strains at the surface was to compare the strains in upper and lower portion of shear crack as well as the strains in adjacent loading point. To achieve this, the locations of the strain gages were determined based on an assumed shear crack path, which was determined from previous phase of the study. It should be mentioned that the strains from these strain gauges might not reflect the actual strain values in the surface. Nevertheless, these strain measurement could be valuable to observe the stress flow along the section. The locations of surface strain gauges are presented in Figure 3.21, in which the grids had 4 in. spacing vertically and horizontally. LVDTs were placed diagonally in the instrumented shear span to measure the overall shear deformation in the shear span, as shown in Figure 3.22.

To measure the deflection of the specimens at the loading point and the supports, rod types of LVDTs were used instead string pots as shown in Figure 3.23. The tests were conducted outside, therefore the data from string pots can be disturbed by the environment, such as strong wind. In general rod type of LVDTs provided more reliable data than string pots. Two LVDTs (one is for backup purpose) were used for measuring the deflection of the beams under the loading point.

3.2.3 The Third Phase Experiments

In the third phase of the experimental program, total of five specimens were prepared for further investigation of the shear behavior of SFRPC beams. One PC beam, 3 – PC#1, was fabricated as a control specimen, and four SFRPC beams were prepared: 3 – SFRC #1, 3 – SFRPC #3 contained 0.75% and 0.50% of volume fraction of steel fibers respectively. 3 – SFRPC #2 beam contained 0.75% volume fraction of fibers with 0.2% of longitudinal reinforcement ratio. 3 – SFRPC#4 contained 0.50% volume fraction of fibers with stirrups in the shear span. The detail information of the beams is listed in Table 3.6. The last specimen, 3 – SFRPC #4, was proposed to investigate the combination of steel fibers and conventional stirrups so that only small amounts of steel fibers were needed to replace conventional reinforcement in a high shear demand zone to reduce congestion.

3.2.3.1 Design of Specimens – 3rd phase

The geometry of the specimens used in the third phase was identical to that of the specimens used in the second phase. However, the amount of flexural reinforcement was reduced; all specimens, except the 3 – SFRPC#2, contained 4 – No. 8 and 5 – No. 4 mild steel bars (total area, A_s = 4.16 in^2) for longitudinal reinforcement, which in turn gave 1.47% of longitudinal reinforcement ratio including 5 – 0.5 in. strands (A_p = 0.765 in^2). The 3 – SFRPC#2 beam contained 3 – No. 3 mild steel bars (total area A_s = 0.22 in^2) for longitudinal reinforcement, which in turn gave 0.29 % of longitudinal reinforcement ratio including 5 – 0.5 in. strands (A_p = 0.765 in^2). This beam was not

overly reinforced in flexural bending such that it is worth to investigate the failure mode of the beam, i.e., the beam would fail in flexure or in shear. Longer span in beams were reinforced with conventional stirrups. (10 – No. 3 closed shaped stirrups at 7.5 in. spacing). Detailed information of the specimens is presented in Table 3.6 and Figure 3.24. The same prestressing jacking system and prestressing force were used in this phase of study; that is, five strands with an initial prestressing stress of 189, which led to a average prestress of 377 psi in concrete.

3.2.3.2 Materials – 3rd phase

Steel fiber

The steel fibers used in the third phase were different than the ones used in the first and second phases. The major reason was that the dissolvable glue on the bundled fibers used in the second phase were not completed dissolved as shown in Figure 3.25, which was found after testing. The undissolved glue led to a nonuniform distribution of fibers with uncertain quality control of fiber reinforced concrete. As a consequence, steel fiber from a different manufacturer was used in this phase. The steel fibers used in the third phase were FF3 fibers manufactured by Maccaferri Cooperation. The steel fibers have doubled-hooked shape at their ends as shown in Figure 3.26. Unlike RC80/60BN steel fibers, these fibers are discrete and not bundled by glue. The mechanical properties of steel fibers are listed in Table 3.7. Compared to Bekaert RC80/60BN fiber, FF3 has shorter length (2 in.), but an equivalent diameter, which in turn gave a slightly lower aspect ratio. The tensile strength, 159 ksi, is higher than that of RC80/60BN fiber, 152

ksi. It was observed from the mixing process that these fibers showed well distribution without balling issue. The better fiber distribution was noticed during casting and after testing from a broken piece of concrete (see Figure 3.27).

Concrete mix

In this phase study, the targeted compressive strength was 6000 psi which was similar to the second phase. There were minor modifications in mix design in the third phase compared to the second phase. Fly ash (Class – C) was used for the mix. The mixing was done at the same local precast plant. Mix proportions and compressive strength of concrete in the third phase are presented in Table 3.8.

3.2.3.3 Fabrications – 3rd phase

The fabrication of the specimens including preparation of the formwork, reinforcement cages, and concrete casting were done at the local plant under the author's supervision (see Figure 3.28). All specimens were covered by plastic sheets after casting for better curing (see Figure 3.29). After one day the formworks were removed and prestressing strands were cut. The camber was negligible. All specimens were placed in natural environment until the tests were conducted.

3.2.3.4 Instrumentations and Test – 3rd phase

Instrumentations were nearly the same as that used in the second phase. As shown in Figure 3.30, two strain gauges were installed on tensile longitudinal

reinforcements at middle of the instrumented shear span and another two strain gauges were installed on a spot of the tensile longitudinal reinforcement where was directly under the loading point. Two strain gauges were installed on compression reinforcement at a location under loading points. In the 3 – SFRPC#4 specimen additional strain gauges were installed on the stirrups that were placed in the instrumented shear span. These strain gauges were placed along an expected shear crack, which was determined by previous test results. Detailed information is presented in Figure 3.30 (b). No internal concrete strain gauges were used in this phase. Concrete surface strain gauges were attached on the instrumented shear span similar to the second phase. The locations of the surface strain gages were determined based on the crack patterns of the previous tests (the first and second phases). Detailed information regarding the locations of surface strain gauges is presented in Figure 3.31.

The instrumentations, including LVDTs measuring deflections at loading points, the supports, and the diagonally placed LVDTs measuring shear strains, were the same as those used in the second phase study.

3.3 Material Tests and Properties

3.3.1 Compressive Strength

As mentioned in previous sections, 4×8 in. cylinders were sampled when large scale beams were casted. Prior to the compressive test, the top and bottom faces of cylinders were capped with a sulfur compound, as shown in Figure 3.32, to ensure that

the cylinders were loaded uniformly and axially. The test procedure was followed by ASTM C 39 (2005), "*Standard Test Method for Compressive Strength of Cylindrical Concrete Specimens*"

Table 3.9 reports the average concrete compressive strengths for all PC and SFRPC specimens used in the three phases. As mentioned in Chapter 2, steel fibers generally do not improve the ultimate compressive strength, but instead improve the ductility. Plain concrete cylinders showed brittle failure mode; the cylinders failed explosively and were no longer able to resist load. As shown in Figure 3.33 (a), severe spalling occurred on the top portion of the cylinders, and concrete completely separated into two pieces at the end of the testing. On the contrary, as can be seen in Figure 3.33 (b), the steel fiber reinforced concrete cylinders showed ductile behavior; the top and bottom portions of cylinder were crushed and severely cracked, but none had separation, even after the load was removed.

3.3.2 SFRC Flexural Strength

Similar to the cylinder tests, Standard flexural tests were carried out. The specimen had dimensions of 6×6×20 (22 in.). The span length was 18 in. regardless of the total length of the specimen. The specimens were tested in accordance with ASTM C1609 ("*Standard Test Method for Flexural Performance of Fiber-Reinforced Concrete (Using Beam With Third-Point Loading)*") (2010). The third – point bending test setup is shown in Figure 3.34. The beams were loaded at a rate of 0.005 in. per minute as

specified by ASTM C 1609. The midspan deflection was measured by a pair of LVDTs. The test was terminated when the average deflection of midspan measured by LVDTs reached 0.12 in., equivalent to 1/150 of span length (18 in.).

The test results are summarized in Table 3.10. The first peak load, P_1, and the peak load, P_p, are defined as the load value at the point on the load – deflection curve where the slope is zero and the maximum load on the load – deflection curve respectively. The definitions of these parameters are presented in Figure 3.35. The modulus of rupture (psi) can be calculated by following formula (ASTM C 1609, 2010),

$$f = \frac{PL}{bd^2} \qquad [3.1]$$

where f, P, L, b, d are the strength (MPa or psi), the applied load (N or lbf), the span length (mm or in.), the average width of the specimen at the fracture (mm or in.), and the average depth of the specimen at the fracture (mm or in.), respectively. The test results are summarized in Table 3.10 and Figure 3.37. It should be noted that the first peak load is not the first cracking load because a load – deflection curve of SFRC specimen sometimes showed nonlinear slope after the first crack rather than losing its strength. Hauweart et al., (1999) pointed out that the first cracking strength was not easy to be observed from a load – deflection curve. The load – deflection response might be nonlinear when the scale of axis was enlarged, though it appeared to be linear as shown in Figure 3.36. The load – deflection curves for the flexural bending test are shown in Figure 3.37. It can be seen that the applied load versus deflection is normally linear up

to the first peak load and is typically followed by a rapid degradation in strength. Most of specimens with RC80/60BN steel fibers with a 0.75% volume fraction gained strength prior to steadily drop in strength after the first peak, which followed the pattern presented in Figure 3.35 (b). The other specimens showed a sudden degradation of strength after reaching the first peak strength and then showed softening behavior, which pattern is presented in Figure 3.35 (a).

ACI 318-08 provides certain criteria for using steel fibers as alternative shear reinforcement in Section 5.6.6.2 (ACI 318-08, 2008). ACI 318-08 Section 5.6.6.2 states that "… (b) The residual strength obtained from flexural testing in accordance with ASTM C1609 at a midspan deflection of 1/300 of the span length is greater than or equal to 90 percent of the measured first-peak strength obtained from a flexural test or 90 percent of the strength corresponding to f_r from Eq. (9-10), which is larger; and (c) The residual strength obtained from flexural testing in accordance with ASTM C1609 at a midspan deflection of 1/150 of the span length is greater than or equal to 75 percent of the measured first-peak strength obtained from a flexural test or 75 percent of the strength corresponding to f_r from Eq. (9-10), whichever is larger". The equation 9-10 in the ACI 318-08 is followed by,

$$f_r = 7.5\lambda\sqrt{f_c'} \qquad [3.2]$$

where f_r is modulus of rupture of concrete, psi, λ is modification factor reflecting the reduced mechanical properties of lightweight concrete, all relative to normalweight concrete of the same compressive strength, and f'_c is specified compressive strength, psi. The schematic view of these criteria is expressed in Figure 3.38. Table 3.11 gives the ACI code requirement for use of SFRC as shear reinforcement. As can be seen in the table, except 2 – 0.75% #1 and #5, most of specimens, did not pass the requirements. However, in terms of improving shear strength and ductility, all large scale specimens performed well, shown in Chapter 5.

3.4 Development of A Material Shear Test Method

The shear behavior of FRCs can be treated on two levels: structural and material. On the structural level, such as large beams, research has been conducted to investigate the use of fibers as alternative shear reinforcement since 1972. There is general agreement that fibers, especially steel fibers in structural application, enhance shear capacity in terms of ultimate strength and ductility, which sometimes transfer failure mode from shear to flexure. On the other hand, shear properties of concrete materials on the material level have been very difficult to characterize, though the information from material level is essential to understand the overall behavior of shear on a structural level. A few different configurations for shear test on the material scale have been attempted (see Chapter 2). Unfortunately, there is no general agreement in a shear test method for concrete material including SFRC. The development of a shear test on the FRC material test is necessary for quality control of FRC mixture properties.

In this section, the attempts to develop shear test method are described. Before conducting the experiment, finite element method was conducted on the proposed specimen.

3.4.1 Development of Material Shear Test Method

The basic concept of the material shear test method in this thesis was adapted from the Iosipescu test method. The dimension of the Iosipescu specimen used by van Zijl is shown in Figure 3.38. It has a height of 140 mm (5.5 in.) and a length of 320 mm (12.6 in.). It should be noted that the middle of the specimen has a reduced height of 36 mm (1.4 in.) because of notches. The height is not sufficient to ensure uniform distribution of fibers, especially for one with high aspect ratio, such as RC80/60BN and FF3 which were used in this study. In addition, existed notches in the middle of specimen would create stress concentration, causing the initial crack to develop due to something other than pure shear stress state at tip of the notches (see Figure 3.39). To overcome the disadvantages of the original Iosipescu test method, a modified Iosipescu test method was proposed in this thesis. The modified Iosipescu test method adapted loading configurations from the original Iosipescu test method to simulate pure shear stress state by adjusting the loading and support positions such that the nominal stress induced by bending moment is close to zero so only shear stress occurs in the middle section of beam as can be seen in Figure 3.40. This will lead to a “clear and uncomplicated” shear stress field in the critical section under investigation. To ensure uniform fiber distribution, the size of the specimen was increased. The size of the

specimen was determined 6×6×20 in., which coincides with the ASTM C1609 by one minor modification; insert side steel pieces to create a reduced area in the middle of specimen with transition manner, shown in Figure 3.41. Any ordinarily equipped laboratory is easily able to prepare the proposed shear beam specimen. By removing the notches required in the original Iosipescu test method, the initiation of shear cracks occurs due to a pure shear stress rather than stress concentration. To ensure that failure always occurs at the desired section (B-B in Figure 3.40), the area of the central portion is reduced through a transition pattern such that any stress concentration would be avoided.

3.4.2 Finite Element Analysis

Prior to conducting the experiment, a finite element method analysis (FEA) was conducted to obtain a general picture on the stress states in the specimens by using a commercial FEM software, ABAQUS (version of 6.9-1). The model was linear-elastic model, which excluded a model of the cracking in concrete beam. In addition, the load was applied with a ramp pattern (gradually increased from zero up to the target load). The material properties used in the analysis are listed in Table 3.12. Other shear test methods such as Z-type push-off, JSCE-SF6, and modified JSCE-SF6 test methods, on shear were analyzed to observe stress states in shear plane as well.

3.4.3 Experimental Program – Material Shear Test Method

As mentioned previously, a mold for ASTM C1609 specimen was used along with inserting a deformed steel sheet to create a reduced transition area in center portion as can be seen Figure 3.40 and 3.41. However, reinforcement is necessary to prevent premature failure and/or failure due to stresses by geometry discontinuity since this test method is a beam type of test such that some portions of beam experience flexural bending stress, which could excess its strength. The moment is only zero at the middle of beam, and the other portion of specimen would experience the significant bending stress. For the reason, different types of reinforcement layouts were provided. This experiment was try and error procedures. The reinforcement layouts tried, and its results are discussed in the Chapter 4 in detail.

The test setup for the modified Iosipescu test setup is shown in Figure 3.42. Compared to the ASTM C1609 test setup (see Figure 3.34), the test setup has a minor modification. The test setup has extra holes at the top and bottom plates so that the loading and support positions are mobile in desired locations. An equivalent test machine and method to ASTM C1609 test were used. One of major advantages is that the same setup can be used for ASTM C1609 and the modified Iosipescu test method simultaneously.

Table 3.1 Design properties of specimens used in the first phase

Specimen	Total length (L)	Total height (H)	Shear span (a)	Effective depth (d)	Longitudinal reinforcement ratio (ρ)	Average prestress in concrete
1 – PC	204 in.	24 in.	63 in.	21 in.	1.62%[1]	380 psi
1 – SFRPC						

[1]: including prestressing strands (A_s = 5.53 in^2, A_p = 0.918 in^2)

Table 3.2 Mechanical properties of steel fibers used in the first phase study [1]

Shape	Length (L)	Diameter (D)	Aspect ratio (D/L)	Tensile strength
Doubled-hooked ends	2.37 in.	0.029 in.	82	152 ksi

[1]: all values are provided by manufacture

Table 3.3 Mix proportions by weight of cement and compressive strength of concrete in the first phase study

Types of concrete	Cement (Type 1)	Fly ash (Class-C)	Sand[1]	Coarse aggregate[2]	Water	Steel fiber[3]	Compressive strength[4]
PC	1.00	0.50	1.70	1.00	0.55*	0.00	9259 psi
SFRPC	1.00	0.50	1.70	1.00	0.55	0.12	9100 psi

[1]: ASTM Natural River sand (Fineness modulus = 2.57)
[2]: Crushed limestone with maximum size of ¾ in.
[3]: Mechanical properties are provided in Table 3.2.
[4]: The strengths were measured at testing day of large – scale beams
*w/cm = 0.37

Table 3.4 Summary of the second phase specimens

Specimen Number	Longitudinal Reinforcement ratio	Compression Reinforcement	Volume fraction of fibers	Average prestress in concrete
2 – PC#1	1.64 % (A_s [1]= 4.74in^2, A_p [2]= 0.765 in^2)	2 - #4 (0.12%, 0.40 in^2)	-	377 psi
2 – PC#2	1.64 % (A_s = 4.74in^2, A_p = 0.765 in^2)	2 - #4 (0.12%, 0.40 in^2)	-	
2 – PC#3	1.64 % (A_s = 4.74in^2, A_p = 0.765 in^2)	4 - #8 (0.94%, 3.16 in^2)	-	
2 – SFRPC#1	1.64 % (A_s = 4.74in^2, A_p = 0.765 in^2)	2 - #4 (0.12%, 0.40 in^2)	0.75%	
2 – SFRPC#2	1.64 % (A_s = 4.74in^2, A_p = 0.765 in^2)	2 - #4 (0.12%, 0.40 in^2)	0.50%	
2 – SFRPC#3	1.64 % (A_s = 4.74in^2, A_p = 0.765 in^2)	4 - #8 (0.94%, 3.16 in^2)	0.75%	

[1]: area of mild steel rebars
[2]: area of prestressing strands

Table 3.5 Mix proportions and compressive strength of concrete in the second phase

Types of concrete	Cement (Type 1)	Sand[1]	Coarse aggregate[2]	Water	Steel fiber[3]	Compressive strength[4]
PC	1.00	1.13	0.67	0.40	-	4769 psi
SFRPC V_f = 0.50%	1.00	1.13	0.67	0.40	0.05	3755 psi
SFRPC V_f = 0.75%	1.00	1.13	0.67	0.40	0.08	5234 psi

[1]: ASTM Natural River sand (Fineness modulus = 2.57)
[2]: Crushed limestone with maximum size of ¾ in.
[3]: Mechanical properties are provided in Table 3.2.
[4]: The strengths were measured at testing day of large – scale beams.

Table 3.6 Summary of the third phase specimens

Specimen Number	Longitudinal Reinforcement ratio	Compression Reinforcement	Volume fraction of fibers	Average restress in concrete
3 – PC#1	1.47% (A_s [1]= 4.16 in^2, A_p [2]= 0.765 in^2)	2 - #4 (0.12%, 0.40 in^2)	-	377 psi
3 – SFRPC#1	1.47% (A_s [1]= 4.16 in^2, A_p [2]= 0.765 in^2)	2 - #4 (0.12%, 0.40 in^2)	0.75%	
3 – SFRPC#2	0.29% (A_s [1]= 0.22 in^2, A_p [2]= 0.765 in^2)	2 - #4 (0.12%, 0.40 in^2)	0.75%	
3 – SFRPC#3	1.47% (A_s [1]= 4.16 in^2, A_p [2]= 0.765 in^2)	2 - #4 (0.12%, 0.40 in^2)	0.50%	
3 – SFRPC#3	1.47% (A_s [1]= 4.16 in^2, A_p [2]= 0.765 in^2)	2 - #4 (0.12%, 0.40 in^2)	0.50%	

[1]: area of mild steel rebars
[2]: area of prestressing strands

Table 3.7 Mechanical properties of steel fibers used in the third phase study [1]

Shape	Length (L)	Diameter (D)	Aspect ratio (D/L)	Tensile strength
Doubled-hooked ends	2.00 in.	0.03 in.	67	159 ksi

[1]: all values are provided by manufacture

Table 3.8 Mix proportions by weight of cement and compressive strength of concrete in the third phase

Types of concrete	**Cement (Type 1)**	**Fly ash (Class-C)**	**Sand[1]**	**Coarse aggregate[2]**	**Water**	**Steel fiber[3]**	**Compressive strength[4]**
PC	1.00	0.50	1.70	1.00	0.60*	-	5772 psi
SFRPC V_f = 0.50%	1.00	0.50	1.70	1.00	0.60	0.08	5276 psi
SFRPC V_f = 0.75%	1.00	0.50	1.70	1.00	0.60	0.12	4884 psi

[1]: ASTM Natural River sand (Fineness modulus = 2.57)
[2]: Crushed limestone with maximum size of ¾ in.
[3]: Mechanical properties are provided in Table 3.7.
[4]: The strength was measured at testing day of large – scale beams.
*w/cm = 0.4

Table 3.9 Average compressive strengths in all phases of studies

Phases	**PC**	**SFRPC, V_f = 0.50%**	**SFRPC, V_f = 0.75%**
1st phase	9259	-	9100
2nd phase	4769	3755	5234
3rd phase	5772	5276	4884

Table 3.10 Test results of ASTM C 1609

Specimen	The first peak load, P_1 (lb)	The peak load, P_p (lb)	The peak strength (psi)
1-0.75% #1	10695	12190	1016
1-0.75% #2	10890	11159	930
1-0.75% #3	11938	12288	1024
2-0.50%#1	7130	7130	594
2-0.50%#2	7691	7691	641
2-0.50%#3	7118	7118	593
2-0.50%#4	6220	6220	518
2-0.50%#5	6141	6214	518
2-0.50%#6	7411	7905	715
2-0.75%#1	7441	8198	683
2-0.75%#2	8216	8216	685
2-0.75%#3	6983	6983	592
2-0.75%#4	7862	7862	655
2-0.75%#5	7777	9474	789
2-0.75%#6	7765	7765	647
3-0.50%#1	6977	7179	598
3-0.50%#2	5200	5305	442
3-0.50%#3	5283	5424	452
3-0.50%#4	4383	4490	374
3-0.50%#5	6275	6422	535
3-0.50%#6	5717	5851	488
3-0.75%#1	5414	5414	451
3-0.75%#2	6660	6660	555
3-0.75%#3	5378	5378	448
3-0.75%#4	5988	5988	499
3-0.75%#5	5797	5797	483

Table 3.11 Check ACI code requirement for use of SFRC as shear reinforcement

Specimen	Modulus of rupture (f_r, psi)	90% of the first peak strength, f_1 (psi)	The residual strength at 0.06 in. deflection (L/300) (psi)	75% of The first peak strength, f_1 (psi)	The residual strength at 0.12 in. deflection (L/150) (psi)	Satisfy ACI requirement?
1-0.75% #1	716	802	503	668	305	No
1-0.75% #2	716	817	575	681	362	No
1-0.75% #3	716	895	333	746	196	No
2-0.50%#1	460	535	370	446	269	No
2-0.50%#2	460	577	372	481	240	No
2-0.50%#3	460	534	282	445	233	No
2-0.50%#4	460	424	432	353	253	No
2-0.50%#5	460	461	507	384	377	No
2-0.50%#6	460	556	499	463	330	No
2-0.75%#1	543	558	645	465	545	Yes
2-0.75%#2	543	616	407	514	309	No
2-0.75%#3	543	524	409	441	321	No
2-0.75%#4	543	590	568	491	464	No
2-0.75%#5	543	583	728	486	558	Yes
2-0.75%#6	543	582	526	485	346	No
3-0.50%#1	545	523	355	436	256	No
3-0.50%#2	545	390	221	325	153	No
3-0.50%#3	545	396	360	330	283	No
3-0.50%#4	545	329	305	274	186	No
3-0.50%#5	545	471	271	392	214	No
3-0.50%#6	545	429	227	357	166	No
3-0.75%#1	524	406	258	338	198	No
3-0.75%#2	524	500	304	416	242	No
3-0.75%#3	524	403	296	336	239	No
3-0.75%#4	524	449	254	374	190	No
3-0.75%#5	524	435	463	362	367	No

Table 3.12 Material properties for concrete used in FEM analysis for material shear test

Material	Compressive strength (f'_c)	Young's modulus[1]	Poisson's ratio
Concrete	5000 psi	4030509 psi	0.3

[1]: Young's modulus = $57000\sqrt{f'_c}$ *(psi)*

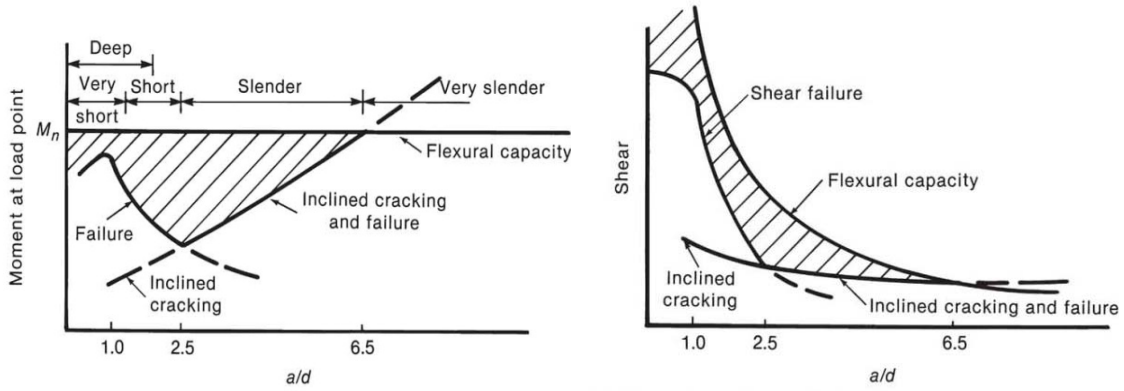

(a) (b)

Figure 3.1 Variation in moment and shear capacity with a/d for rectangular beams in concrete without web shear reinforcement; (a) Moment capcity; (b) Shear capcity (Wight and MacGregor, 2009)

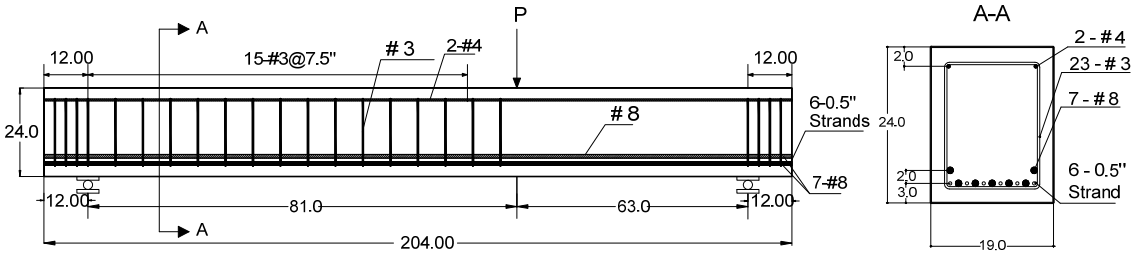

Figure 3.2 Dimension (in.) of specimens used in the first phase (PC & SFRPC)

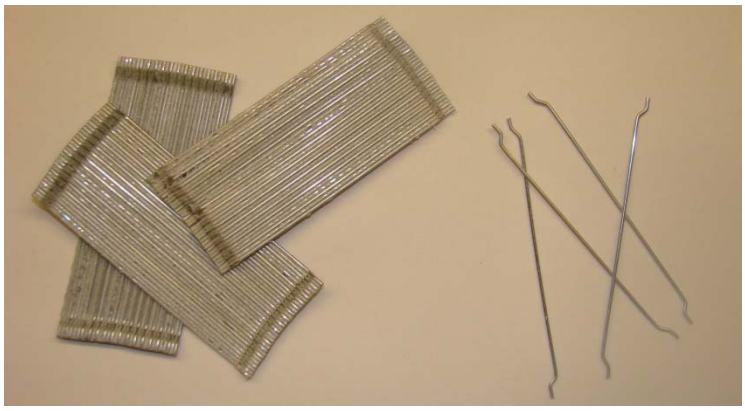

Figure 3.3 Dramix RC-60/80-BN steel fibers manufactured by Bekaert Corp.

Figure 3.4 Concrete mixing facilities in Hanson Pipe & Precast

Figure 3.5 Typical photos of concrete mixing

Figure 3.6 Typical photos of reinforcement caging

Figure 3.7 Prestressing bed and jacking in Hanson Pipe & Precast Plant

Figure 3.8 Typical photos of casting concrete

Figure 3.9 Uniformly distributed steel fibers

Figure 3.10 Finishing surface

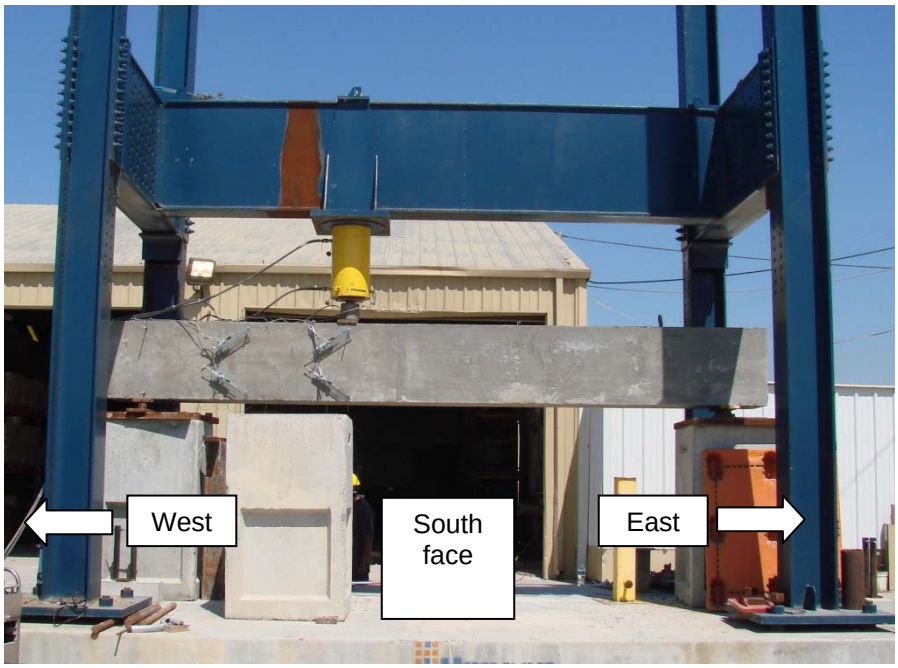

Figure 3.11 Test frame

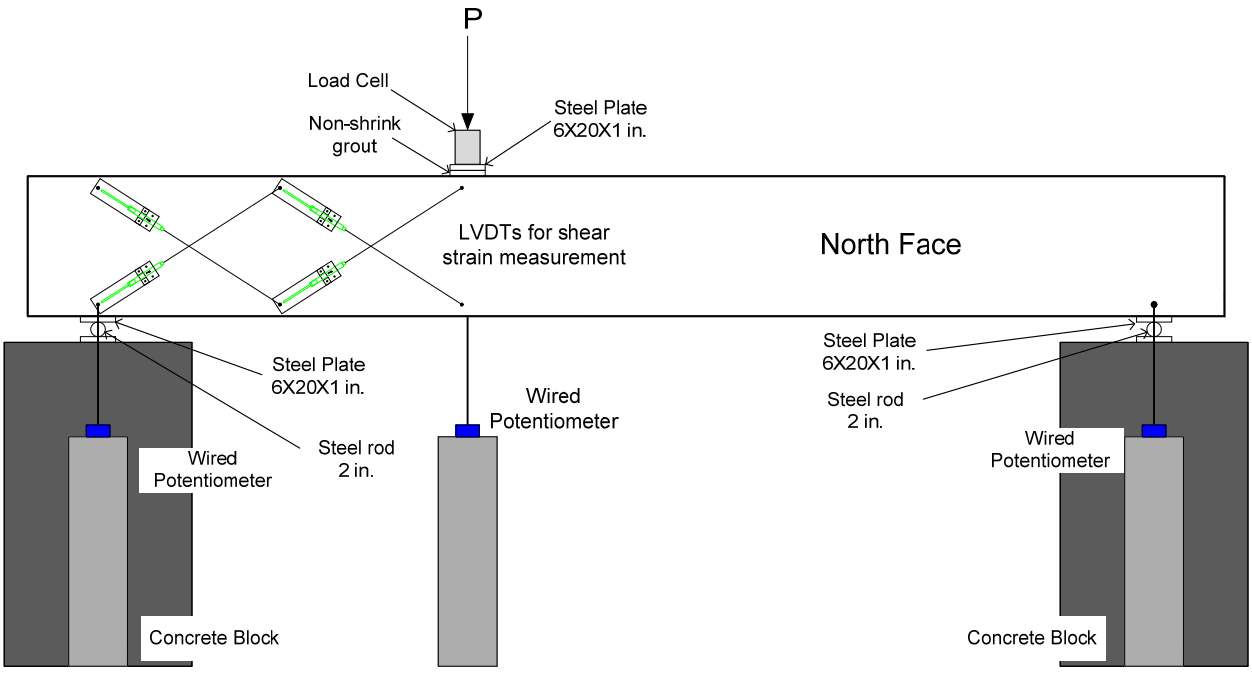

Figure 3.12 Sensor instrumentation

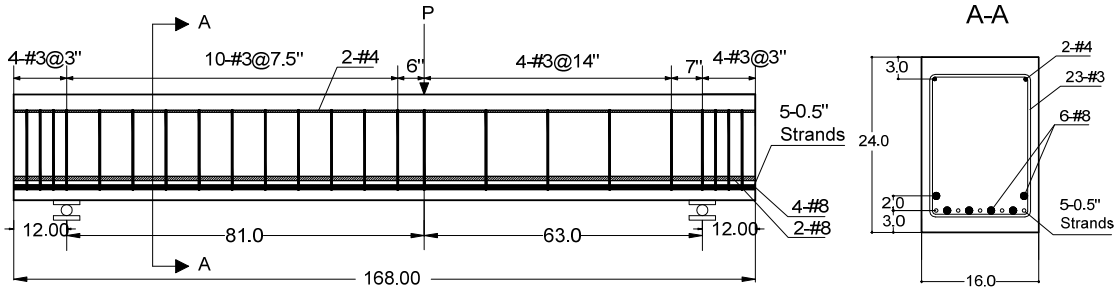

(a)

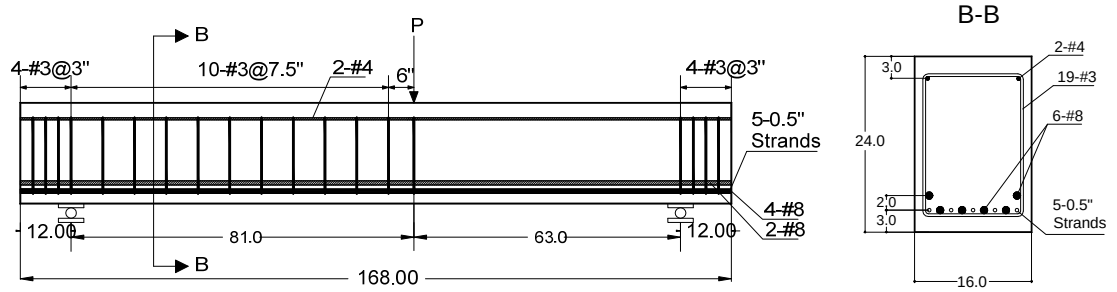

(b)

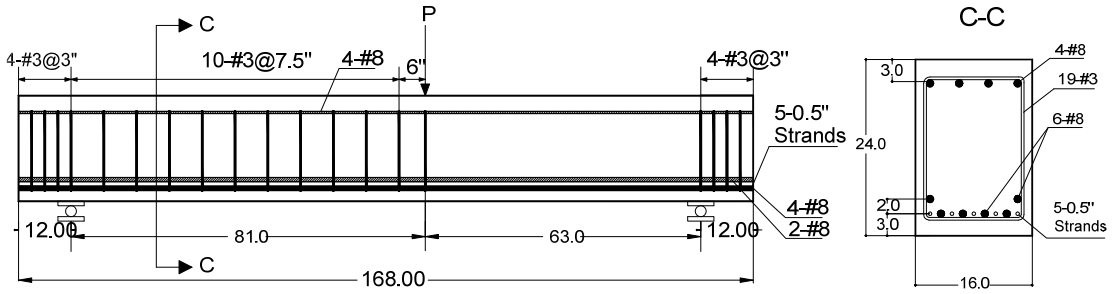

(c)

Figure 3.13 Dimensions (in.) of specimens used in the second phase; (a) 2 – PC#1; (b) 2 – PC#2, 2 – SFRPC#1, and 2 – SFRPC#2; (c) 2 – PC#3 and 2 – SFRPC#3

Figure 3.14 Typical photos of reinforcement caging – the second phase study

Figure 3.15 Typical photos of casting – the second phase study

Figure 3.16 Vishay 5000 DAQ system

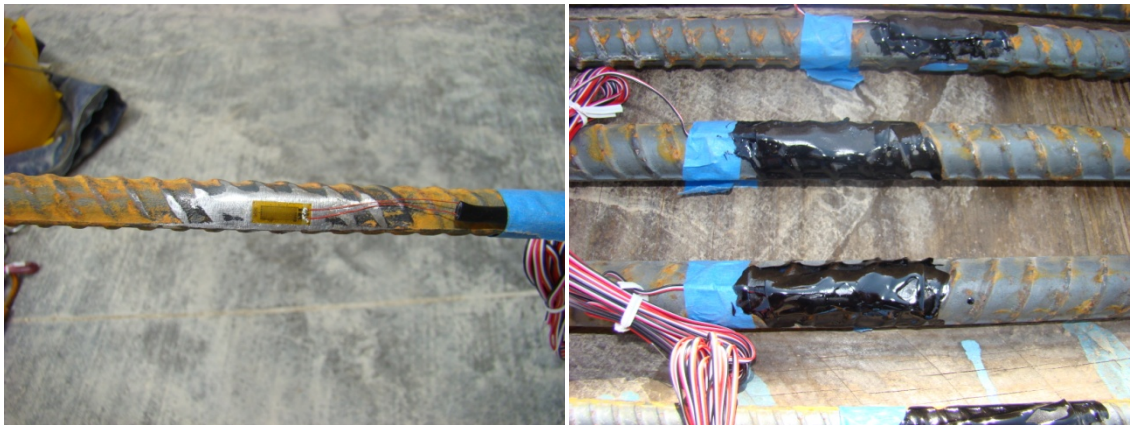

(a) (b)

Figure 3.17 Example of strain gage installment: (a) glued in a degreased flat area; (b) after coated

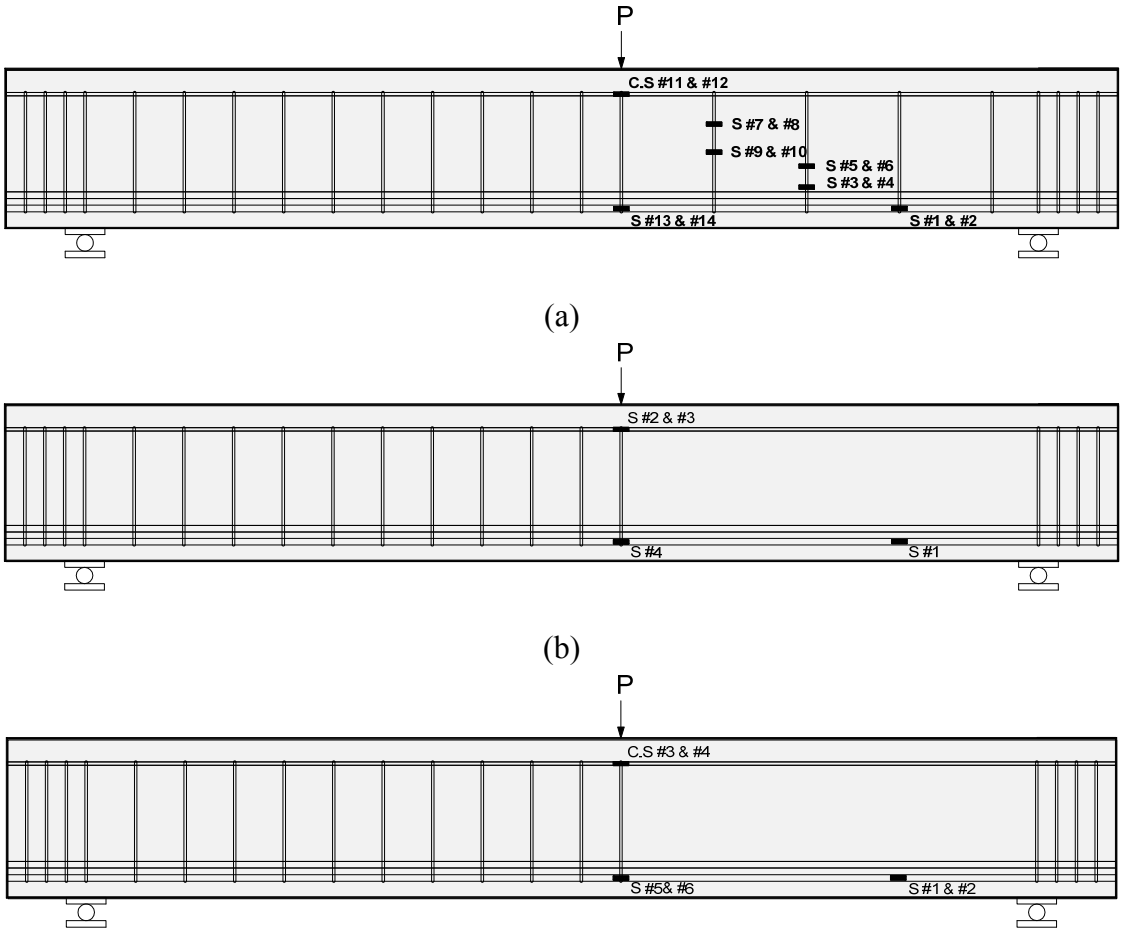

Figure 3.18 Locations of strain gages in the second phase study; (a) 2 – PC#1; (b) 2 – PC#2 & #3; (c) 2 – SFRPC #1, #2, & #3

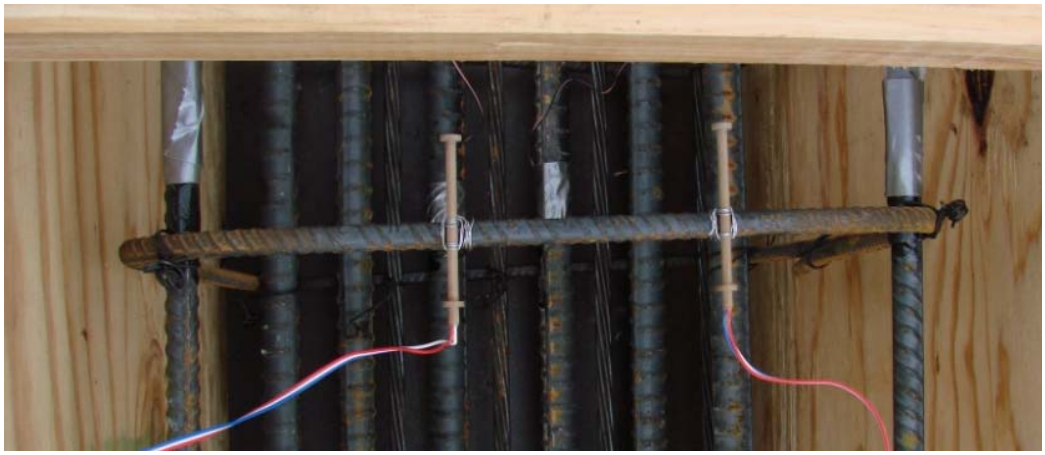

Figure 3.19 Example of concrete embedded strain gages

Figure 3.20 Example of concrete surface strain gage

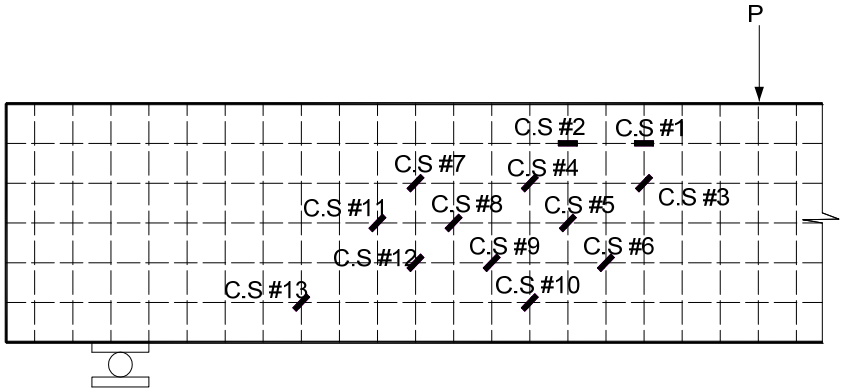

(a)

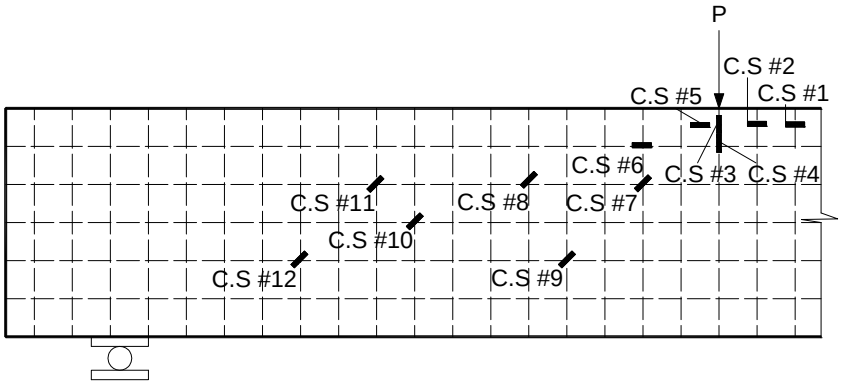

(b)

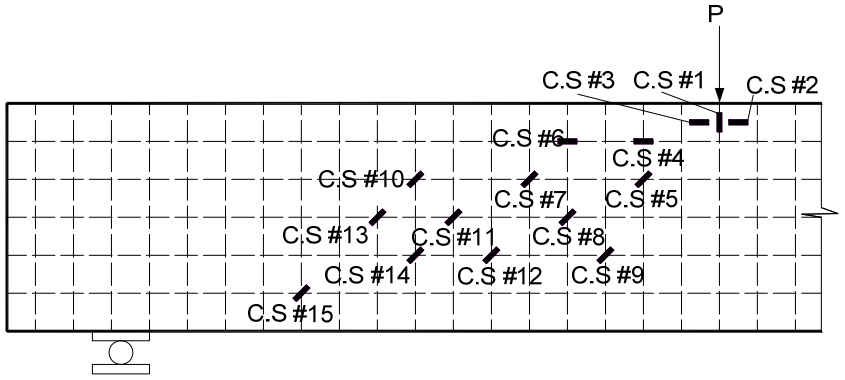

(c)

Figure 3.21 Locations of concrete surface strain gages in the second phase experiment; (a) 2 – PC#2 & #3; (b) 2 – SFRPC#1; (c) 2 – SFRPC#2 & SFRPC#3

Figure 3.22 Typical instrumentation of diagonally placed LVDTs

(a) (b)

Figure 3.23 LVDTs for measuring deflection: (a) String pot; (b) Rod type of LVDTs

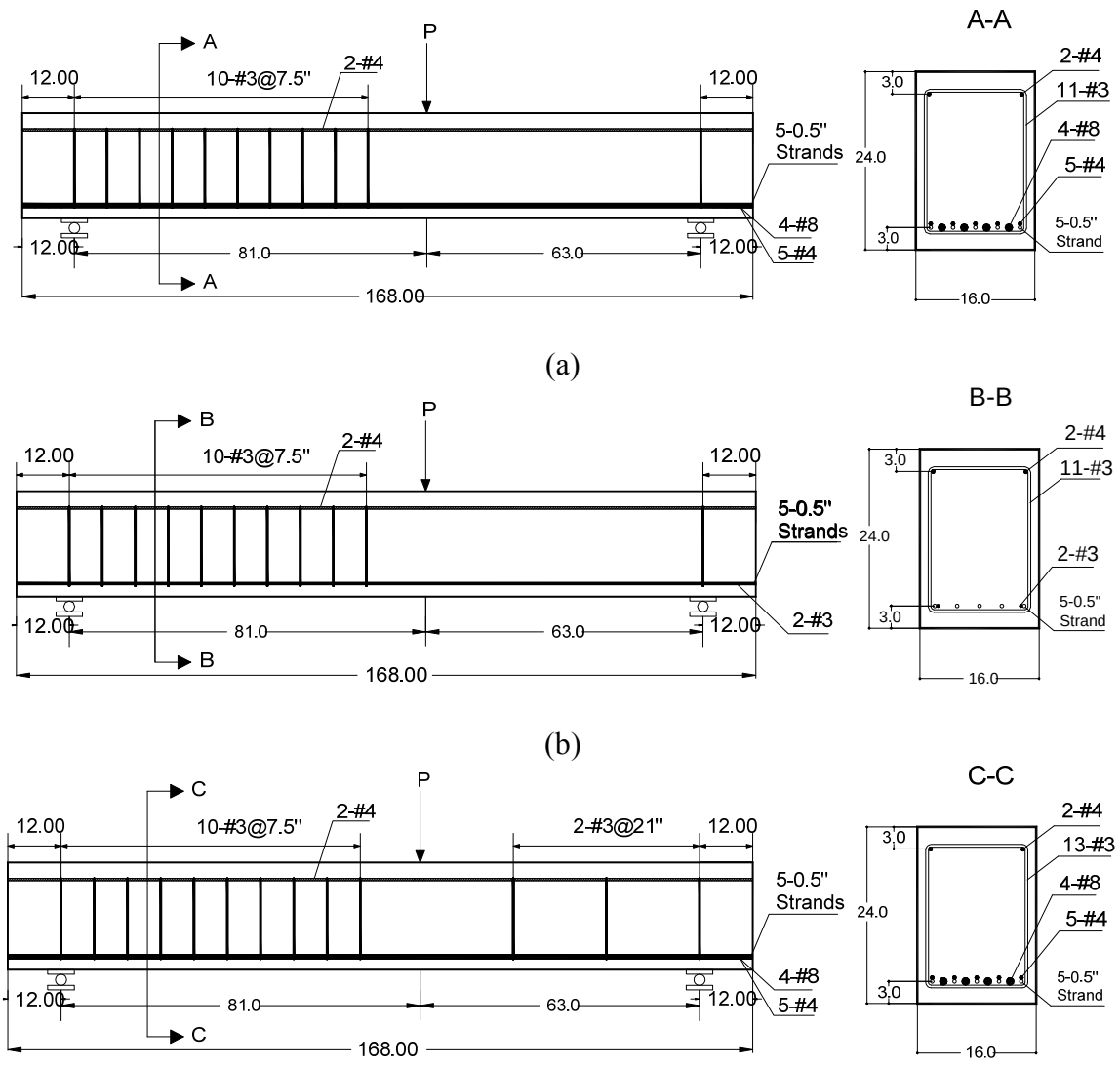

Figure 3.24 Dimensions (in.) of specimens used in the third phase; (a) dimension of 3 – PC, SFRPC#1, and SFRPC#3; (b) dimensions of 3 – SFRPC#2; (c) dimensions of 3 – SFRPC#4

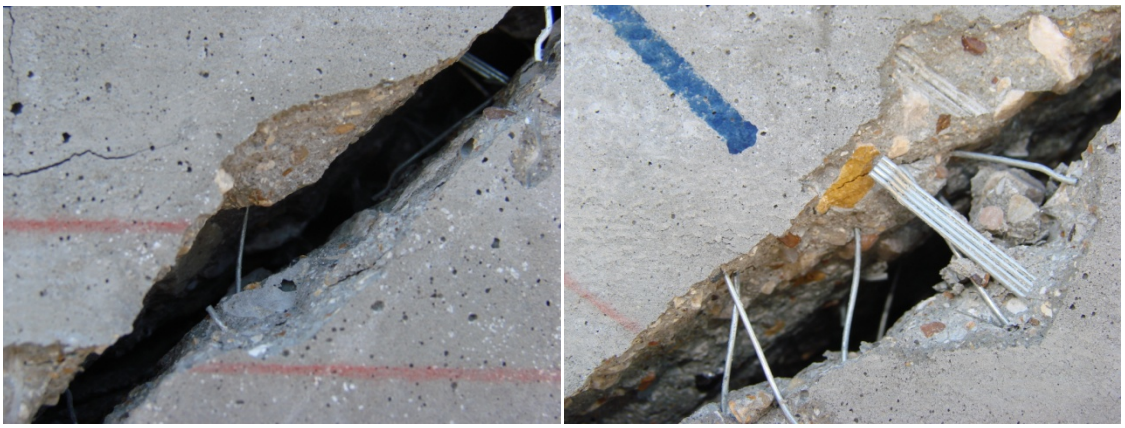

Figure 3.25 Poor fiber distributions due to undissolved glue

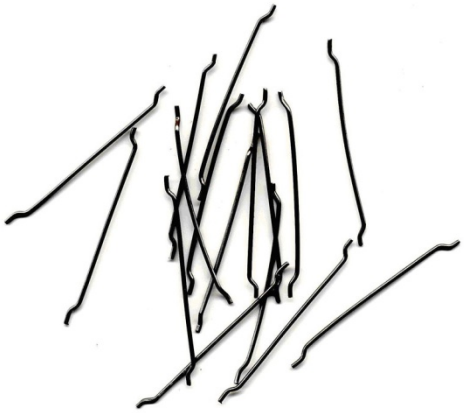

Figure 3.26 FF3 steel fibers manufactured by Maccaferri Inc.

Figure 3.27 Uniformly distributed steel fiber in the third phase specimens

Figure 3.28 Typical photos of reinforcement caging and formworks in the third phase study

Figure 3.29 Typical photos of casting in the third phase study

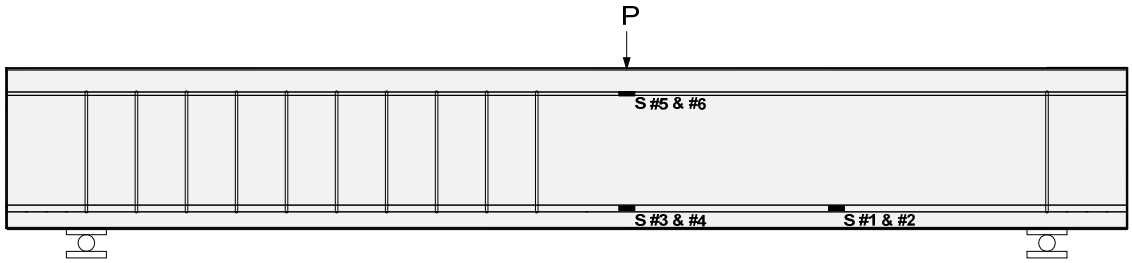

(a)

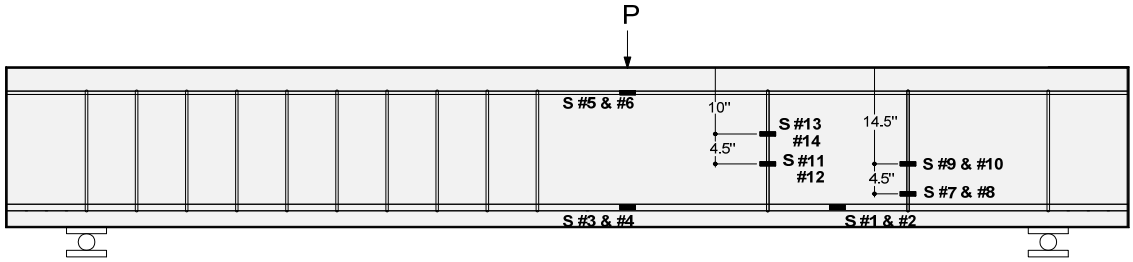

(b)

Figure 3.30 Locations of strain gauges in the third phase study; (a) 3 – PC, SFRPC #1, #2, and #3; (b) 3 – SFRPC #4

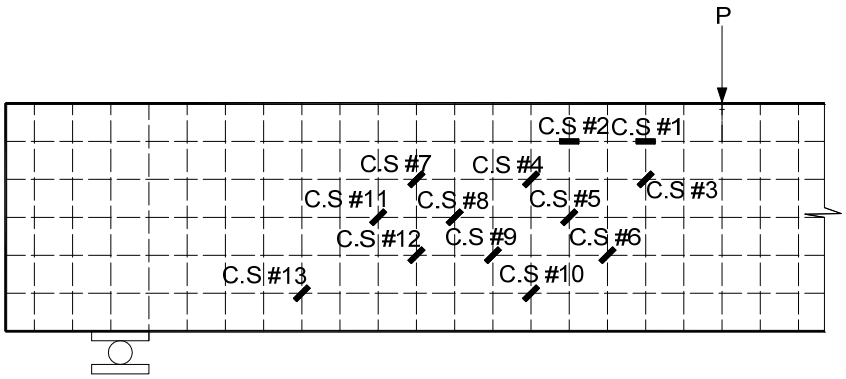

Figure 3.31 Locations of concrete surface strain gages in the third phase study

(a) (b)

Figure 3.32 Capping material and setup; (a) Capping material; (b) Capping setup

(a) (b)

Figure 3.33 Typical photos of compressive test in the second phase study: (a) Typical plain concrete cylinder after testing; (b) Typical steel fiber reinforced concrete cylinder after testing

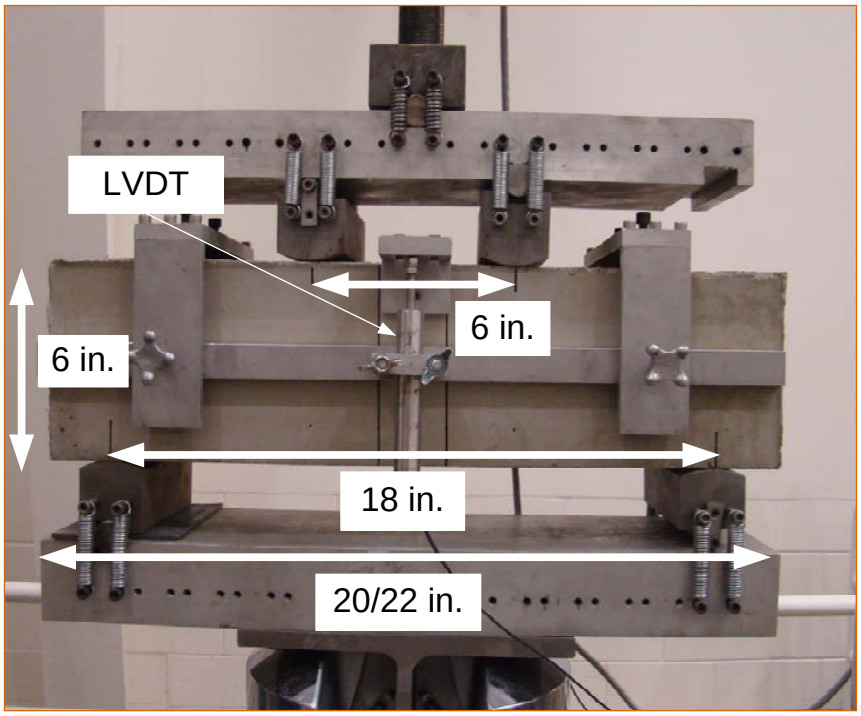

Figure 3.34 Test setup for ASTM C 1609

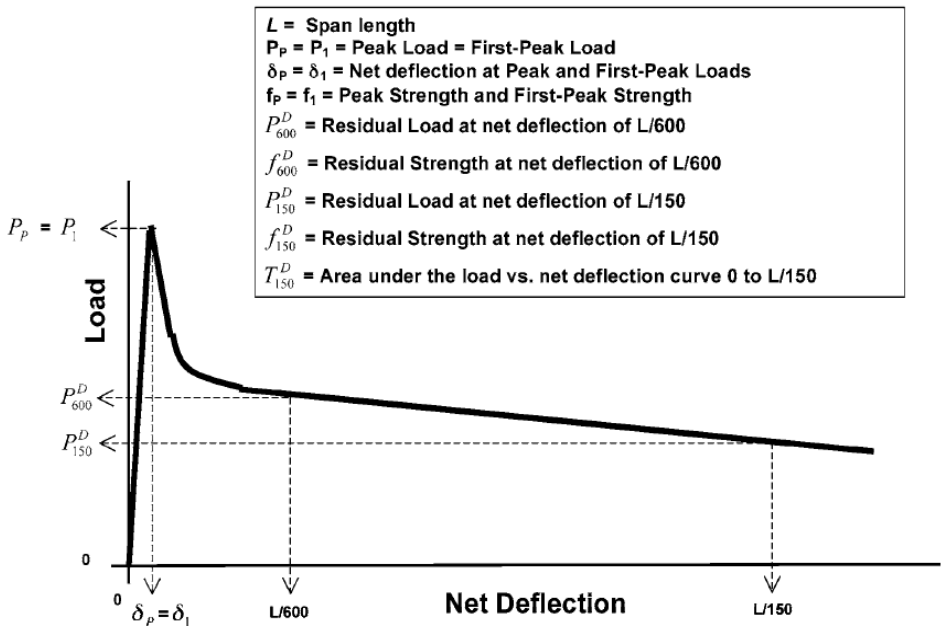

(a)

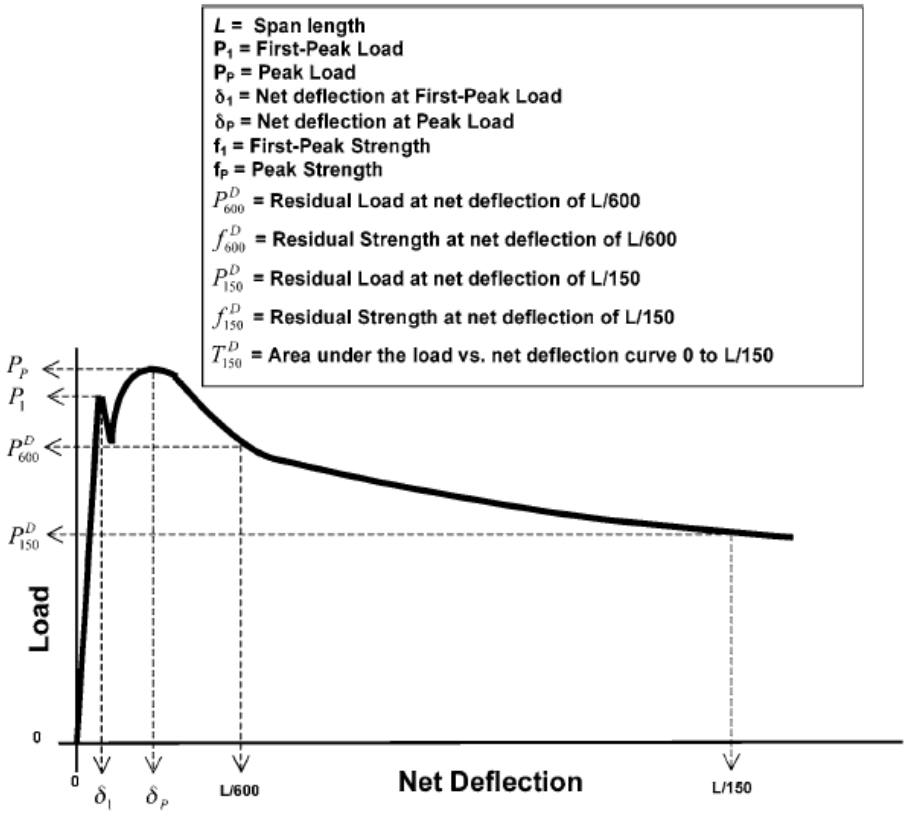

(b)

Figure 3.35 Example of calculation of parameters in ASTM C 1609; (a) The first peak load equals to peak load; (b) The first peak load is greater than peak load (ASTM C 1609 – 10)

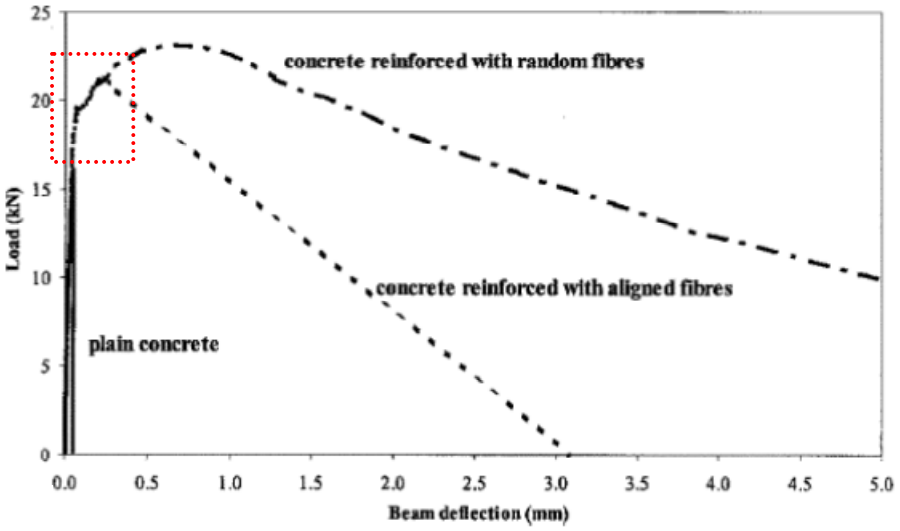

(a)

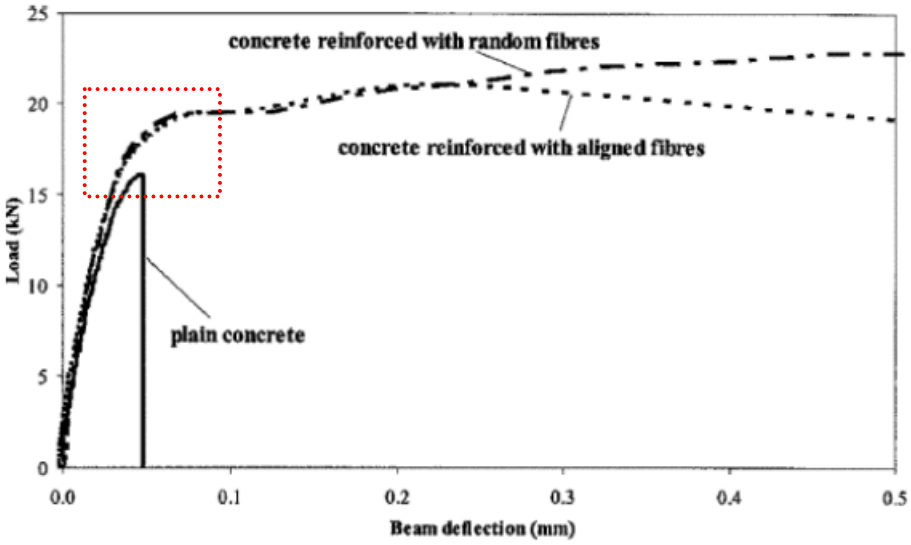

(b)

Figure 3.36 Load – deflection curve (Hauweart et al., 1999); (a) On scale of 50 mm; (b) On scale of 0.5 mm

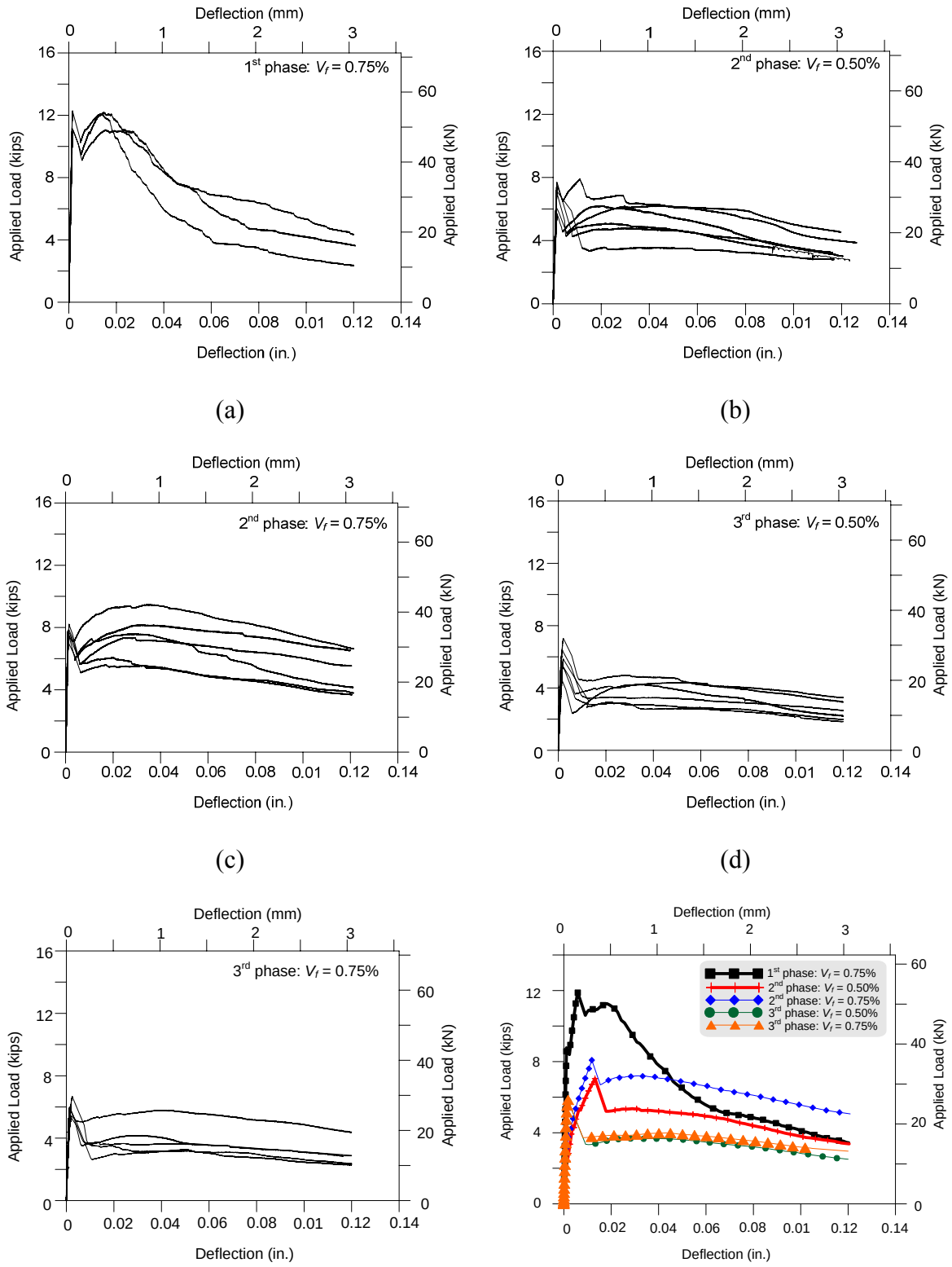

Figure 3.37 Flexural bending test result; (a) 1 – 0.75%; (b) 2 – 0.50%; (c) 2 – 0.75%; (d) 3 – 0.50%; (e) 3 – 0.75%; (f) Average curve for all specimens

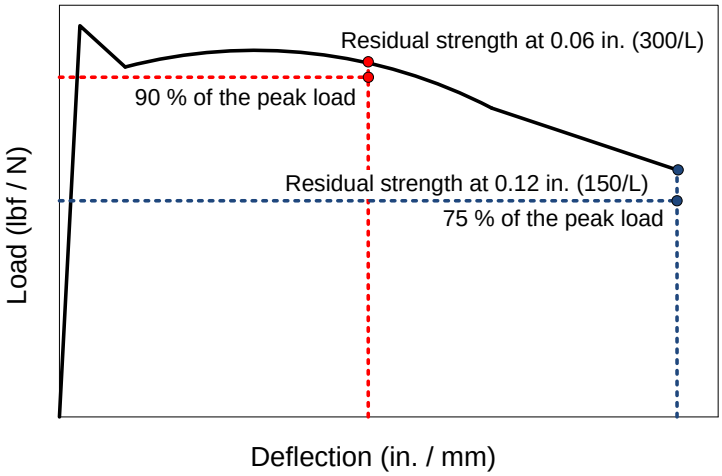

Figure 3.38 The load versus deflection curve for ASTM C 1609 satisfying ACI 318-08 criteria

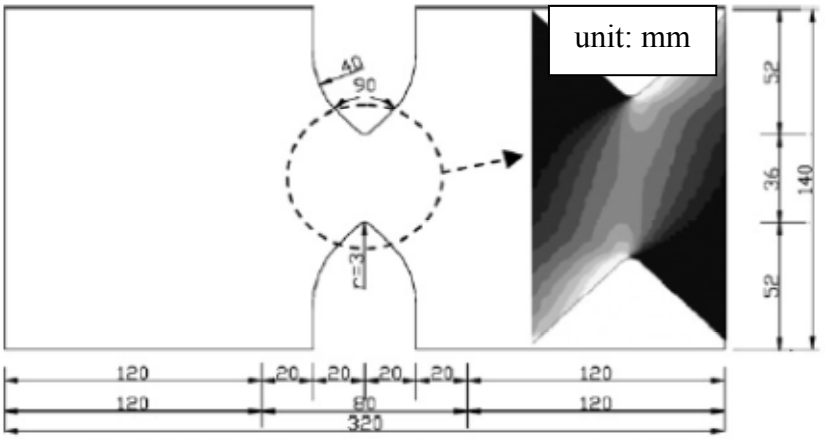

Figure 3.39 Dimensions of original Iosipescu specimen (van Zijl, 2007)

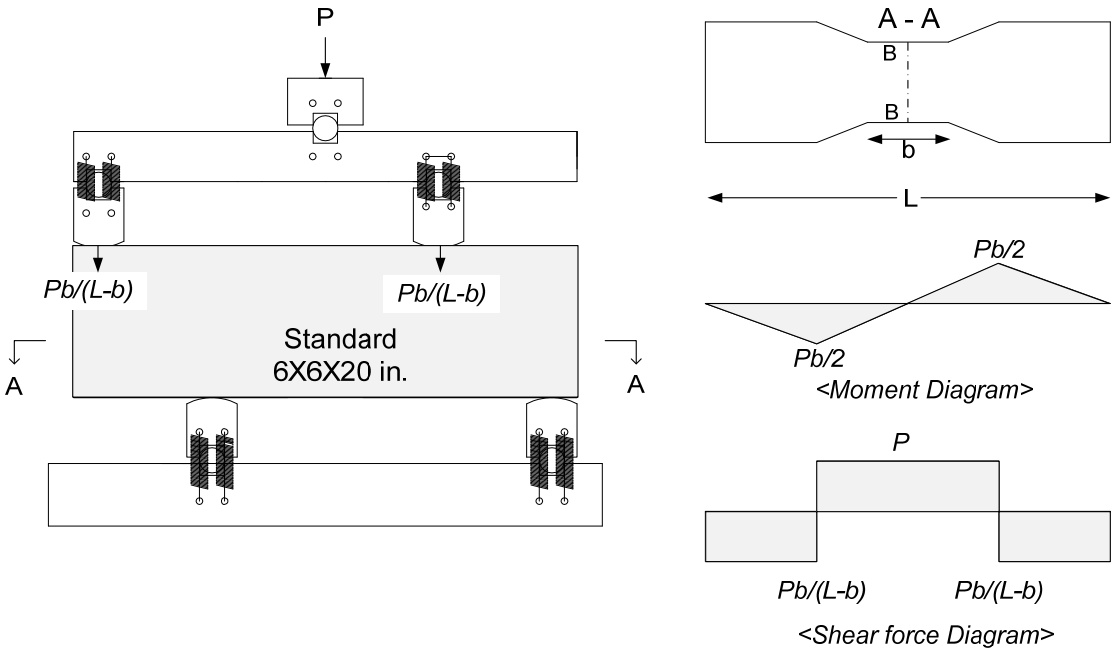

Figure 3.40 Schematic view of the Iosipescu test method

Figure 3.41 Photos of the modified Iosipescu specimen mold

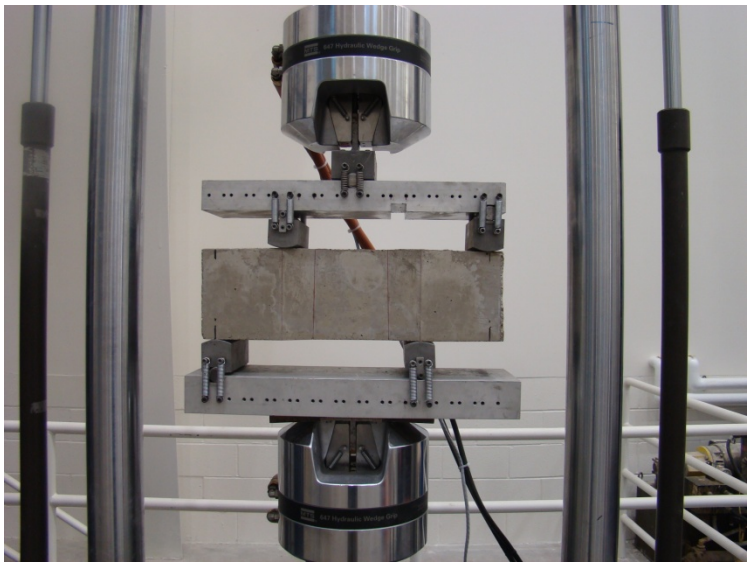

Figure 3.42 Test setup for the modified Iosipescu test method

CHAPTER 4

DEVELOPMENT OF MATERIAL SHEAR TEST

4.1 General

A shear test method on the material scale for the evaluation of FRC shear performance can be more suitable when the FRC materials are used for the purpose of enhanced the shear resistance of plain concrete, as per the provisions in the current ACI 318 code. The material scale test is valuable because it leads to a better comparison of experimental results obtained in different laboratories. To this end, the shear test method referred to as the panel/shell test has been employed for reinforced concrete (e.g. Stevens et al., 1991 and Bentz, 2000). It is well recognized that the panel/shell test method is very close to simulating a pure shear stress state. However, the panel/shell test is not suitable for routine laboratory test methods due to the complexity of the setup and its size, as shown in Figure 4.1. Moreover, very limited numbers of laboratories in North America could conduct this type of test. To develop a shear test method on the material scale, much effort has been devoted, especially for FRC materials (see Chapter 2). Nevertheless, at this time, neither ASTM nor ACI Committee 544 (ACI Committee, 2002) recommends any standardized test method to measure material properties of FRC in shear.

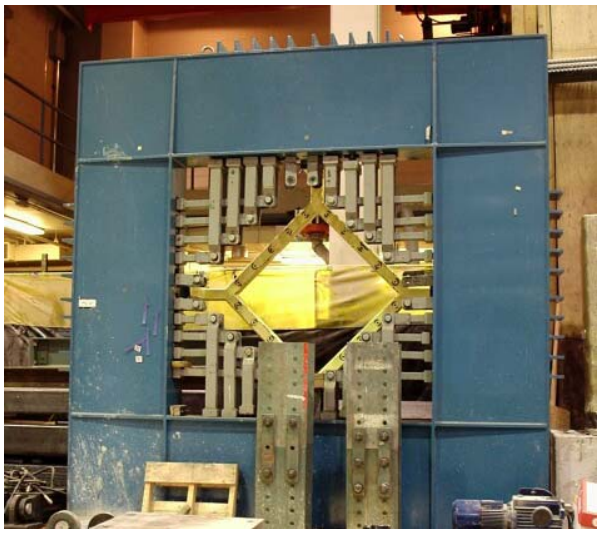

(a)

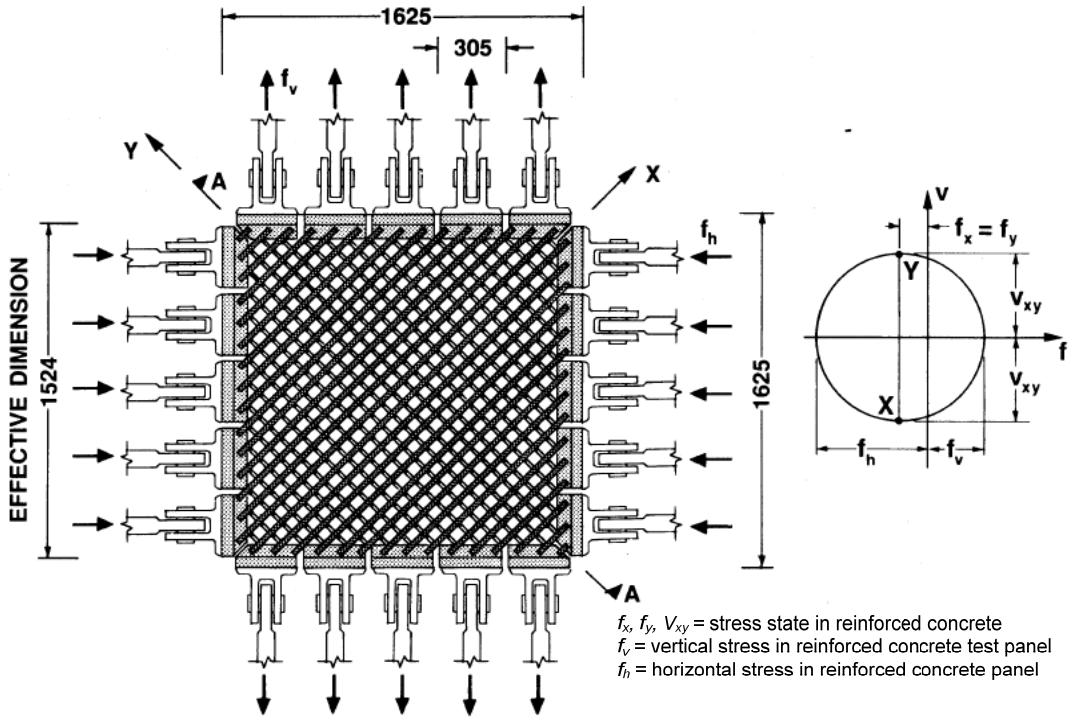

(b)

Figure 4.1 Shear panel and shell element testers in University of Toronto; (a) Shear panel tester (http://www.civil.engineering.utoronto.ca); (b) Shear panel – specimen dimensions (mm) and application of stresses (Stevens et al., 1991)

In this Chapter, a shear test method for the material scale is proposed by adopting the best practice from previous attempts. This chapter contains finite element analysis (FEA) results observing the stress distribution in the targeted shear plane, not only in the proposed specimen in this study but also in the previously proposed specimens by different researchers. In addition, primary experimental results are presented.

4.2 Finite Element Analysis – Material Scale Shear Test Method

4.2.1 General

Prior to the experiment, a linear elastic finite element analysis (FEA) analysis was conducted. The analysis was performed to analyze previously proposed shear test methods, including the Z-type push-off test (Valle and Büyüköztürk, 1993), JSCE-SF6 test (Mirsayah and Banthia, 2002), modified JSCE-SF6 test (Mirsayah and Banthia, 2002), Iosipescu test (van Zijl, 2007), and the modified Iosipescu test method proposed in this study. It should be noted that these previously proposed shear test methods have been applied to the FRC members. The primary purpose of the analysis was to observe stress distribution in the targeted shear plane such that linear elastic analysis was applied for each test method; a nonlinear concrete model was excluded since overall behavior of the specimens were not investigated. The specimens were modeled with three-dimensional solid elements using commercially used finite element software, ABAQUS (version of 6.7, Abaqus/CAE User's manual, 2007). The material properties of each element are given in Table 3.9 in the Chapter 3.

4.2.2 Z – type Push-off Test

The dimensions of the Z-type push-off specimen are shown in Figure 4.2. The three-dimensional solid element and mesh are shown in Figure 4.3. As shown in Figure 4.3, the load was applied on the top and bottom faces of the specimen along the Y-direction (vertical direction). The boundary conditions restricted the displacement in the X - and Z - directions, and rotations in all directions. .

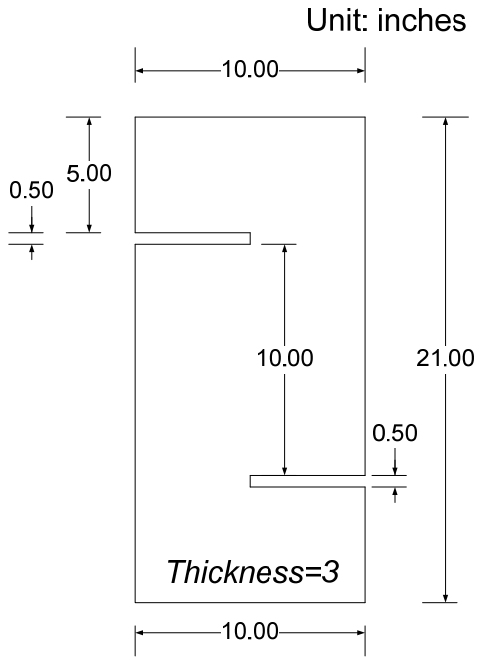

Figure 4.2 Dimensions of the Z-type push off model (Valle and Büyüköztürk, 1993)

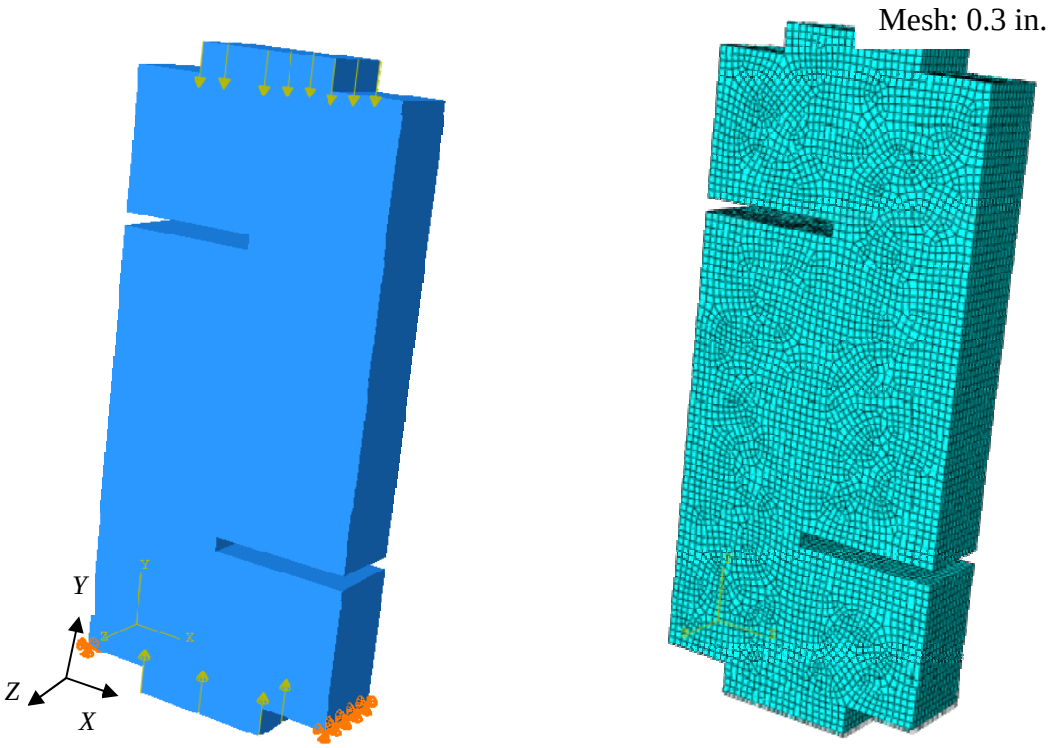

(a) (b)

Figure 4.3 Model for the Z-type push-off specimen; (a) Load and boundary conditions; (b) Mesh used in the model

The stress distribution along the targeted shear plane (A-B) is shown in Figure 4.4 and 4.5. The shear stress, represented by S12 in Figure 4.4, showed a parabolic shape of distribution, but it was practically uniform at the middle of the shear plane (4 in. to 6 in. of the heights). However, relatively high compressive stress (S22, Y-direction) existed at the shear plane, especially at tips of notches (0 in. and 10 in. of the heights). This may be in part due to the fact that the loading fashion was compression such that it could create relatively high compressive stress in the shear plane, i.e., the compressive stress was higher than shear stress, and it became significant at these notches. As a consequence, there is a strong interaction between normal stresses and shear stresses

along the entire shear plane. Note that in typical prestressed or reinforced concrete beams the maximum shear occurs at a location with relative minor normal stresses.

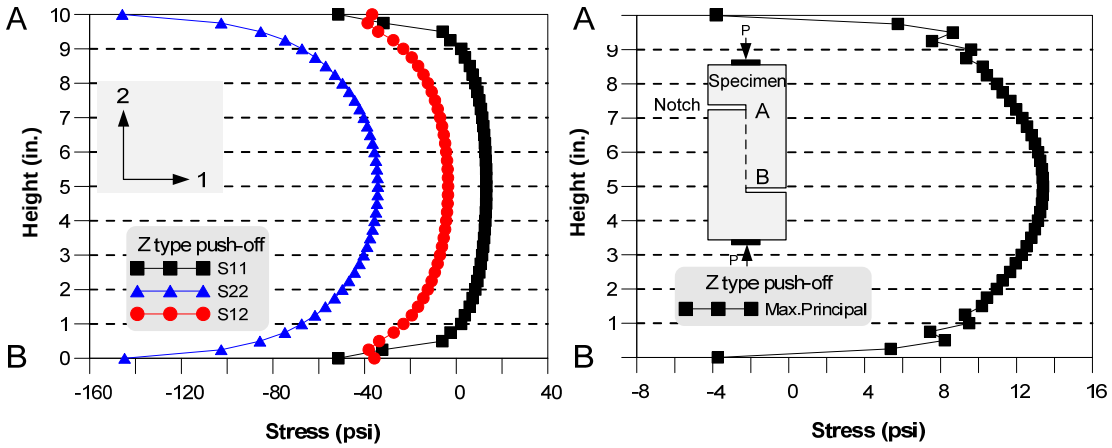

Figure 4.4 Stress distributions in the Z – type push off test

The stresses contours shown in Figure 4.5 (c) and (d) indicated that the maximum principle stresses were at these notches.

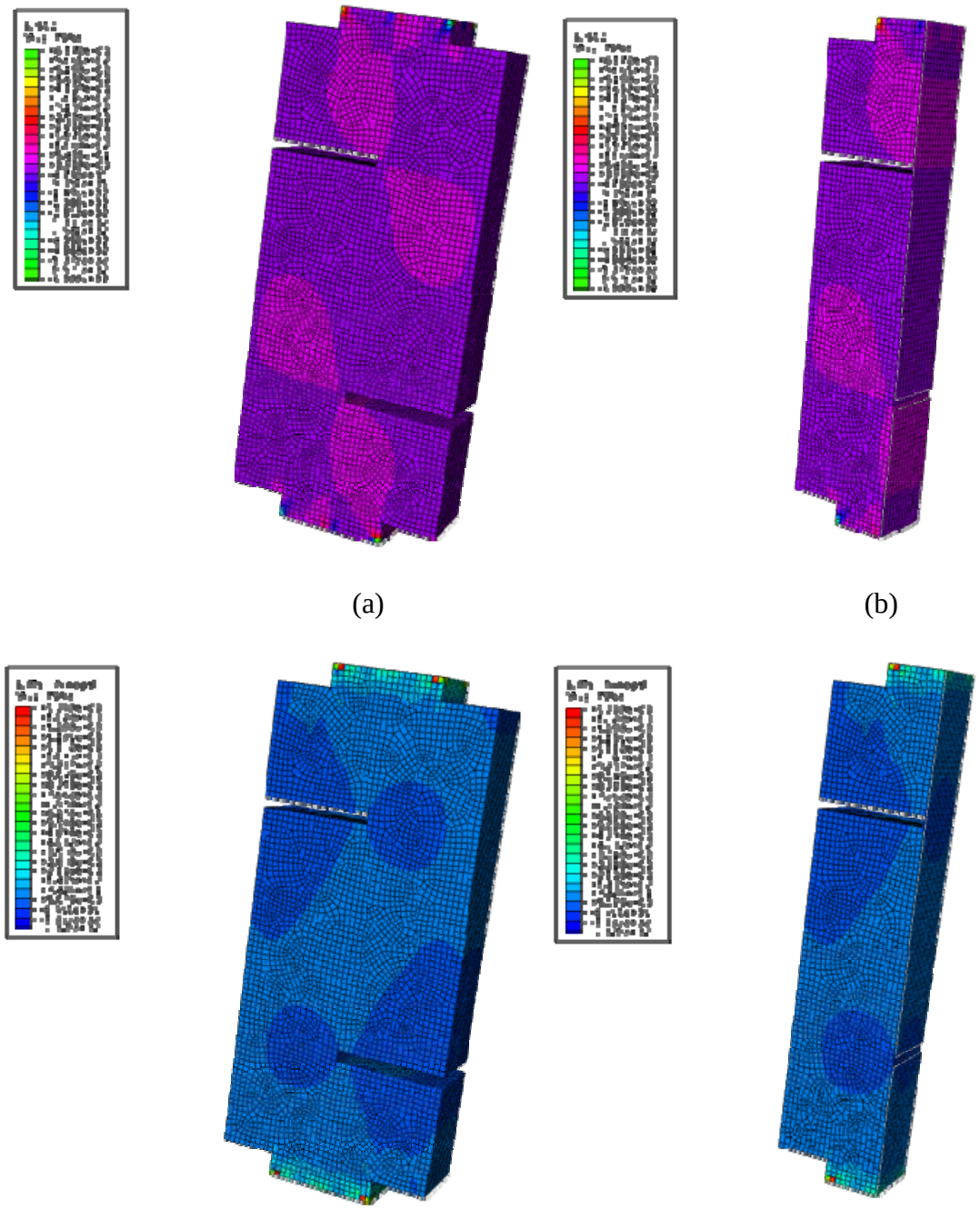

(a) (b)

(c) (d)

Figure 4.5 Stress contours in the Z-type push-off specimen; (a) Shear stress distribution; (b) Shear stress distribution at the targeted shear plane; (c) Principal stress distribution; (d) Principal stress distribution at the targeted shear plane

One of drawbacks of the presence of notches is that the fibers tend to be collinear rather than randomly distributed especially for steel fibers with length approximately 2 in. used in this research. In addition, researchers reported that the stress field in a specimen of the Z-type push-off test becomes highly complex after cracking occurs, and the stress conditions are no longer purely shear (Mirsayah and Banthia, 2002).

4.2.3 JSCE – SF 6 Test

The three-dimensional finite element model for the specimen specified in JSCE-SF6 (1990) was created by using ABAQUS. The dimensions of the model, load and boundary conditions, and mesh are shown in Figures 4.6 and 4.7. As shown in Figure 4.6, the edge of the bottom block was 0.01 in. away the edge of the top block. The loads were applied through the top prisms that simulate the steel loading edges of the steel block used in the test. Displacements were restricted in X – and Z – directions, as well as rotations in all directions at the bottom prisms.

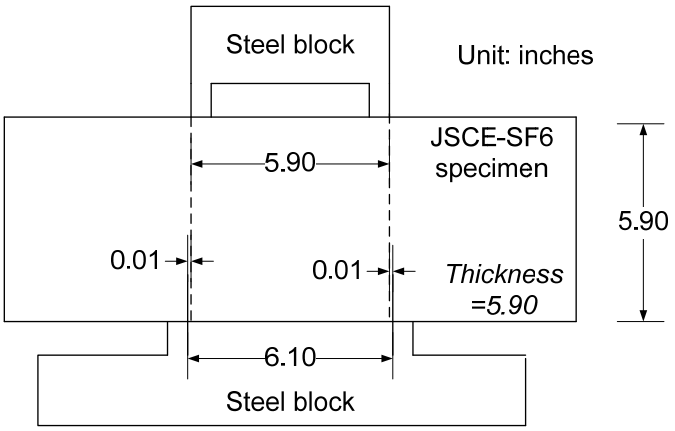

Figure 4.6 Dimensions of the JSCE-SF 6 model (Mirsayah and Banthia, 2002)

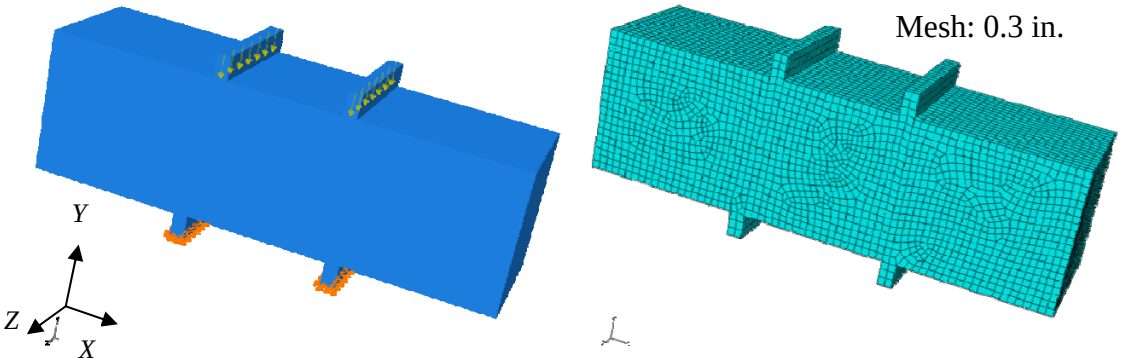

(a) (b)

Figure 4.7 Model for the JSCE-SF6 specimen; (a) Load and boundary conditions; (b) Mesh used in the model

As can be seen in Figure 4.8, the shear stress distribution (S12) was adequately uniform along the targeted shear plane (A-B). However, a relatively high normal stress (S22, Y – direction) prevailed during the pure shear stress state. In addition, stress concentration existed at the point where the sharp edge and the specimen contacted (H = 6 in. in Figure 4.8). The maximum tensile principle stress also occurred at the top steel block edge, which indicates that the initial crack would occur at this location. Therefore, the failure might occur at the location where the specimen may have an appreciable normal stresses and/or stress concentration. It also can be seen in Figure 4.9 that the high shear and principle stresses, represented by bright wine and blue colors respectively, occurred under the loading edge. In addition, prior experimental results indicated that the failure occurred at a deviated point from the targeted shear plane in many instances meaning this test method generally produced invalid results (Mirsayah and Banthia, 2002).

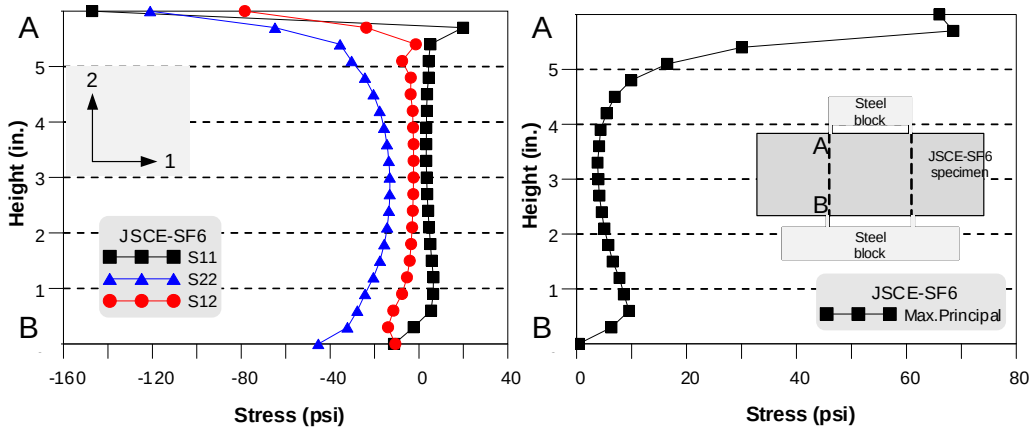

Figure 4.8 Stress distributions in the JSCE-SF6 test

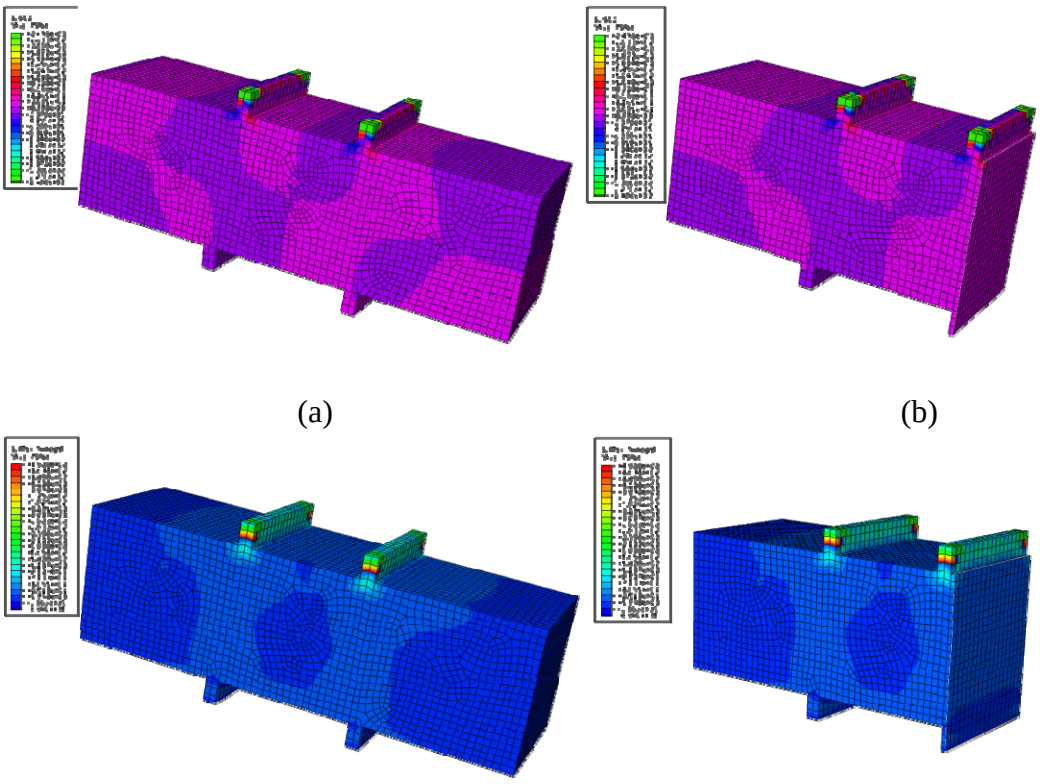

(a) (b)

(c) (d)

Figure 4.9 Stress contours in the JSCE-SF6 specimen; (a) Shear stress distribution; (b) Shear stress distribution at the targeted shear plane; (c) Principal stress distribution; (d) Principal stress distribution at the targeted shear plane

4.2.4 Modified JSCE – SF 6 Test

Mirsayah and Banthia (2002) suggested a modified JSCE-SF6 test method to overcome the drawback of JSCE-SF6 (i.e., the failure crack deviated from the desired shear plane) by introducing notches. This test method was also analyzed. The dimensions of the modified JSCE-SF6 model are presented in Figure 4.10. As shown in Figure 4.11, the loading and boundary conditions were similar to JSCE-SF6, but the notches of 0.001 in. in width (see Figure 4.10 and 4.11) were included in the model as Mirsayah and Banthia used in their specimens (2002).

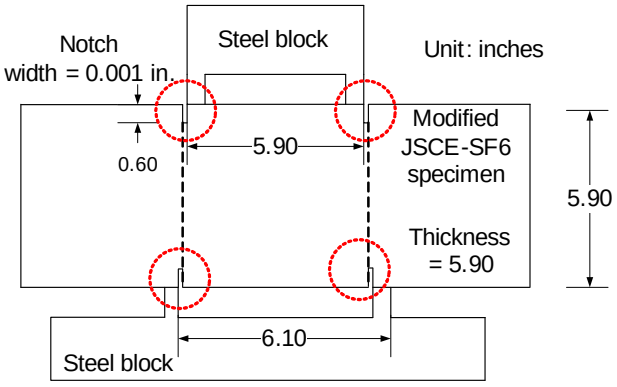

Figure 4.10 Dimensions of the modified JSCE-SF6 model

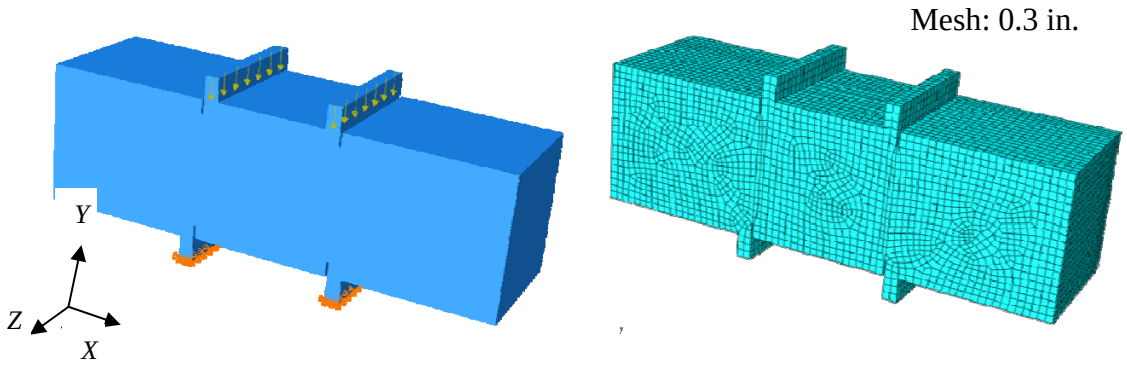

(a) (b)

Figure 4.11 Model for the modified JSCE-SF6 specimen; (a) Load and boundary conditions; (b) Mesh used in the model

It should be noted that there was no data point at 0 in. and 6 in. of heights due to the notches. As can be seen in Figure 4.12 and 4.13, the analysis results indicated that the stress distributions were similar with JSCE-SF6 in normal stresses (S11 and S22), however, the shear stress was less uniform compared to the JSCE-SF6 test. In addition, high stresses (S11, S12, and S12) exhibited at the top notch. That could create complicated stress states and failure mode opposed to pure shear failure. It should be mentioned that the notches were created after casting. This procedure possibly makes a difficulty of fabricating consistent notches as well as specimens, i.e., consistent size of notches might not able to be created along specimens.

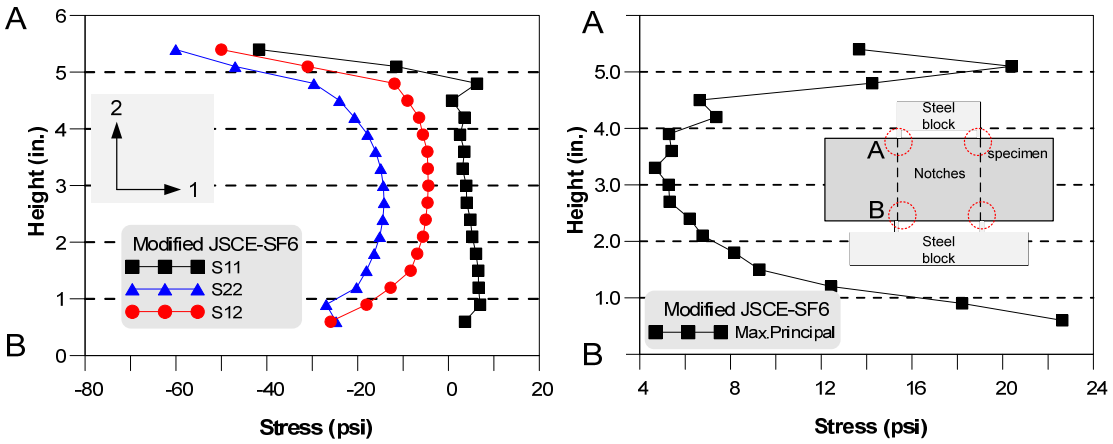

Figure 4.12 Stress distributions in the modified JSCE-SF6 test

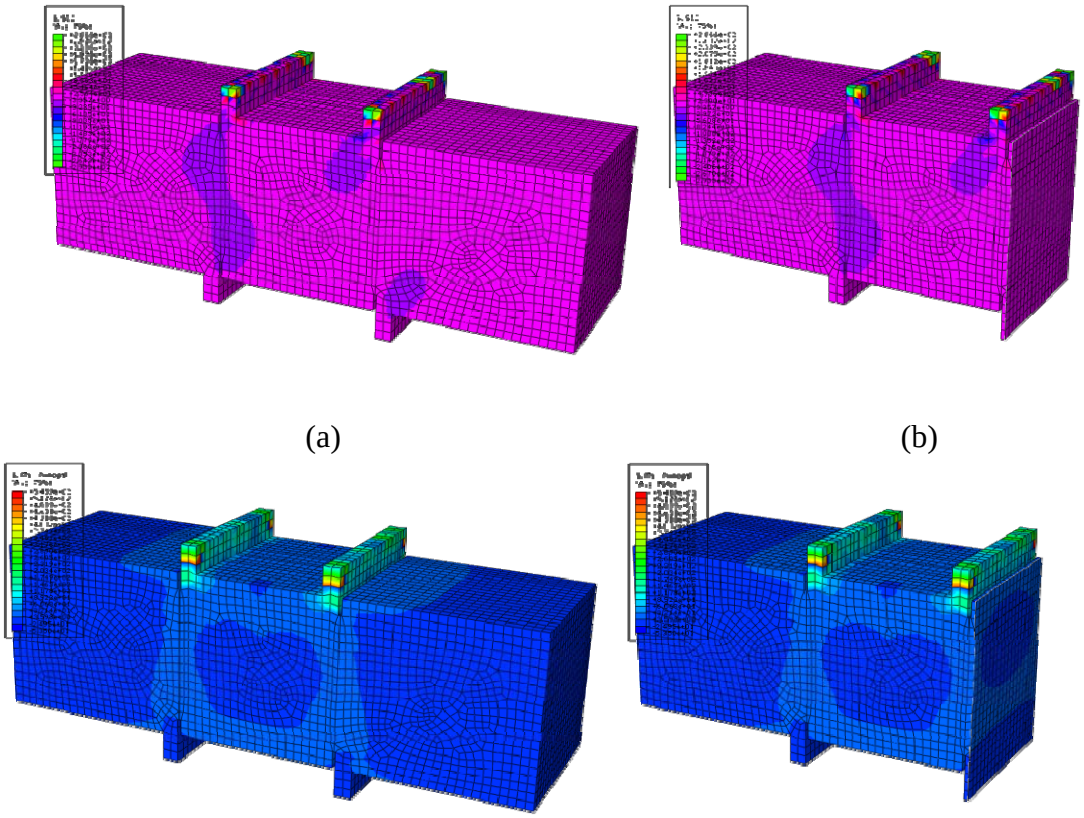

(a) (b)

(c) (d)

Figure 4.13 Stress contours in the modified JSCE-SF6 specimen; (a) Shear stress distribution; (b) Shear stress distribution at the targeted shear plane; (c) Principal stress distribution; (d) Principal stress distribution at the targeted shear plane

4.2.5 Iosipescu Test

The Iosipescu test was developed by N. Iosipescu (1967) originally, and it had been widely used in testing laminated composite materials as well as the in the investigation of fraction characteristics of plain concrete subjected to shear. The test method is a beam type, but by adjusting positions of loadings and supports, practically pure shear zone could be created at the middle and center of the specimen as shown in Figure 4.14.

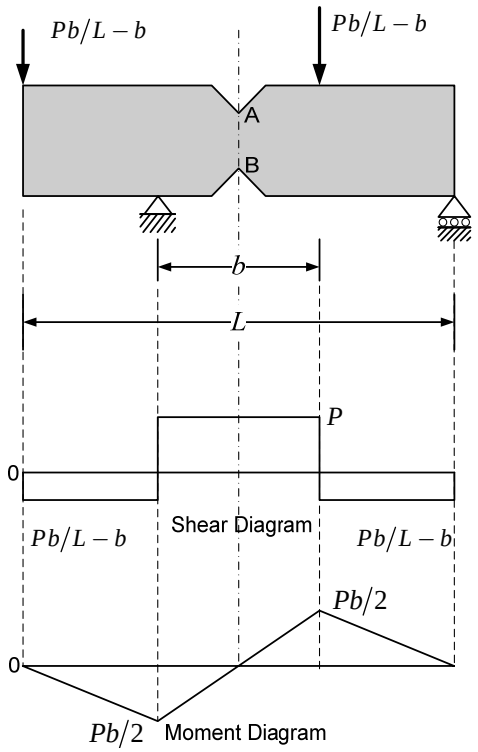

Figure 4.14 The shear and moment diagrams in the Iosipescu test

The dimensions of the model used were adopted from the specimen tested by van Zijl (2007) and are presented in Figure 4.15. It should be noted that he used polymeric fibers whose modulus is generally low.

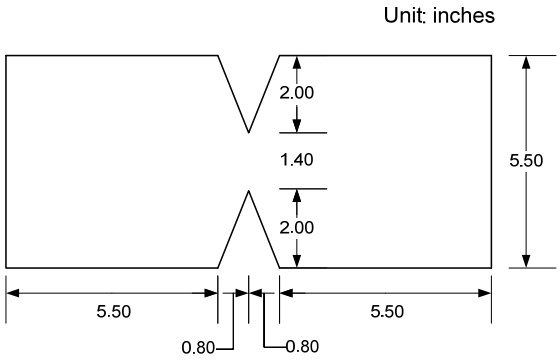

Figure 4.15 Dimensions of the Iosipescu model

The FEA model and mesh are presented in Figure 4.16. The boundary conditions were hinge at right and bottom face and roller at left and bottom face. The load was applied at the top face as shown in Figure 4. 16.

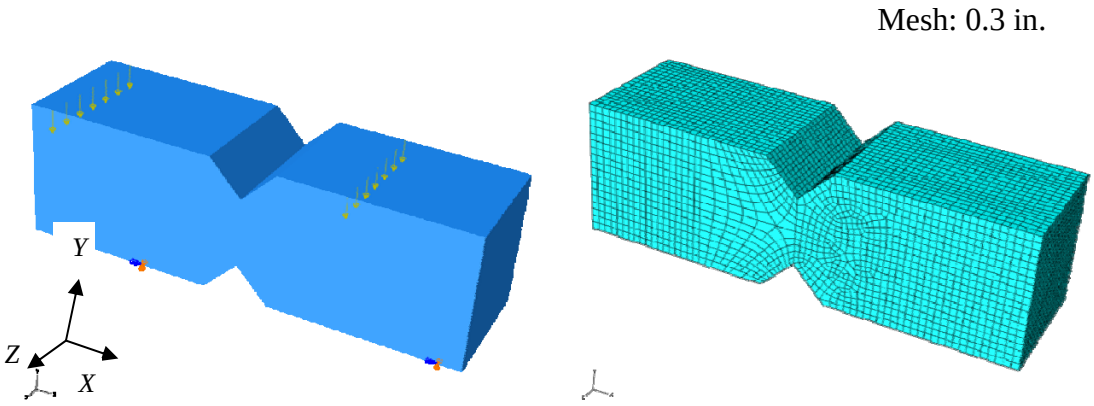

(a) (b)

Figure 4.16 Model in the Iosipescu specimen; (a) Load and boundary conditions; (b) Mesh used in the model

The FEA results for Iosipescu test are presented in Figures 4.17 and 4.18. Note that scale of Y-axis was the height of the specimen, but there was no data point at top and bottom point due to the notches. These results show uniform shear stress distribution as well as principle stress along the desired depth, as shown in Figure 4.17. Compared to the other test methods mentioned previously, the model was less affected by normal stresses due to the relatively smaller normal stresses (S11 and S22) as compared to the shear stresses (S12). However, the experimental conducted by van Zijl showed that the first crack, indicated at location “A” as noted in Figure 4.19 (b), always initiated from the tip of the V-notch rather than the middle of the shear plane where the maximum shear stress would have occurred. This showed that the initiation of the crack was not

primarily induced by shear stress, but by stress concentration due to notches. Moreover, FRC specimens with polymeric fibers, which modulus is generally low, showed that cracks always initiated at the notches. (van Zijl, 2007). In addition, V-notches will alter the fiber distribution as mentioned.

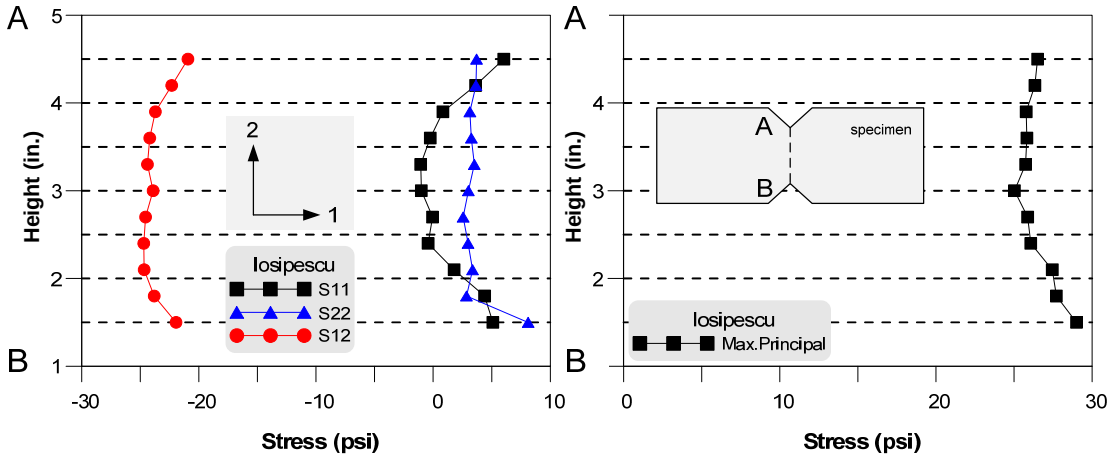

Figure 4.17 Stress distributions in the Iosipescu specimen

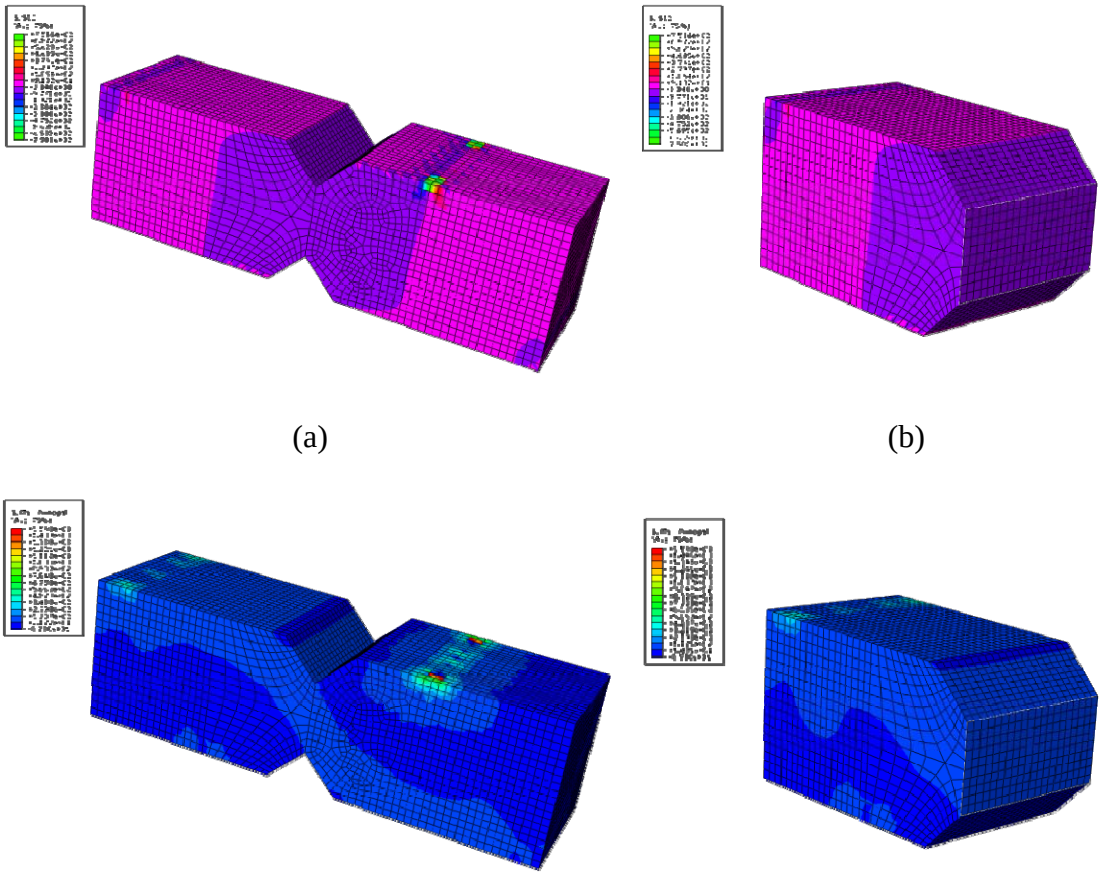

(a) (b)

(c) (d)

Figure 4.18 Stress contours in the Iosipescu specimen; (a) Shear stress distribution; (b) Shear stress distribution at the targeted shear plane; (c) Principal stress distribution; (d) Principal stress distribution at the targeted shear plane

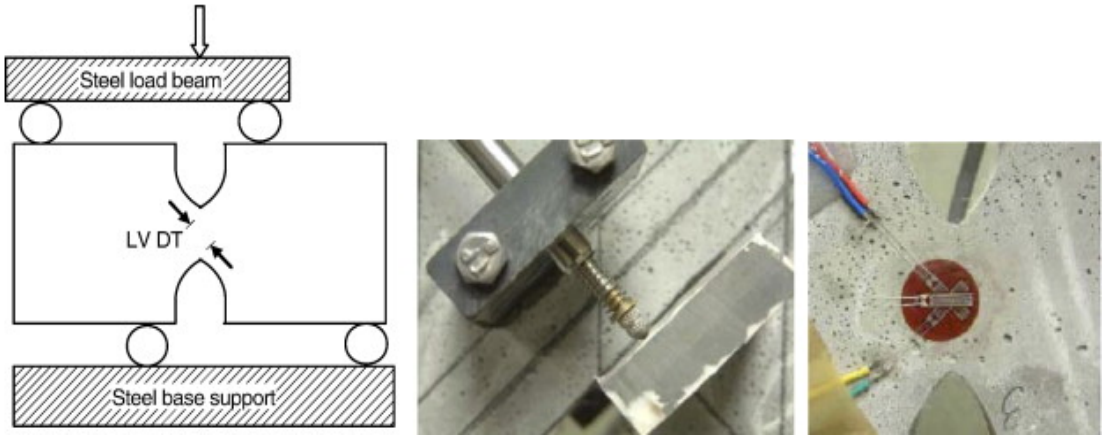

(a)

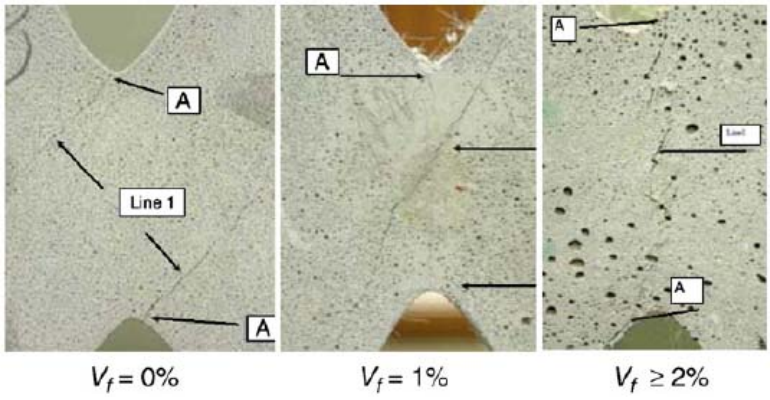

(b)

Figure 4.19 Test conducted by van Zijl; (a) Test setup; (b) Cracks in the vicinity of the notches (van Zijl, 2007)

4.2.6 Modified Iosipescu Test

As discussed above, the FEA results for Iosipescu specimen indicated that a nearly pure shear stress plane could be created by adjusting loading and boundary positions. However, the problem is the stress concentration induced by notches. In addition, the height of the shear plane is only 1.4 in., which is even less than the length of many commonly used steel fibers and the ones (approximately 2 in.) used in this

study. Therefore, the uniform fibers distribution could not be accomplished. The modified Iosipescu method was proposed in an effort to adopt the merit of the original Iosipescu test, i.e., creating a nearly pure shear stress plane, and to eliminate the fiber distribution and stress concentration problems by enlarging the specimen sizes and removing the notches. The dimensions of the model used are presented in Figure 4.20.

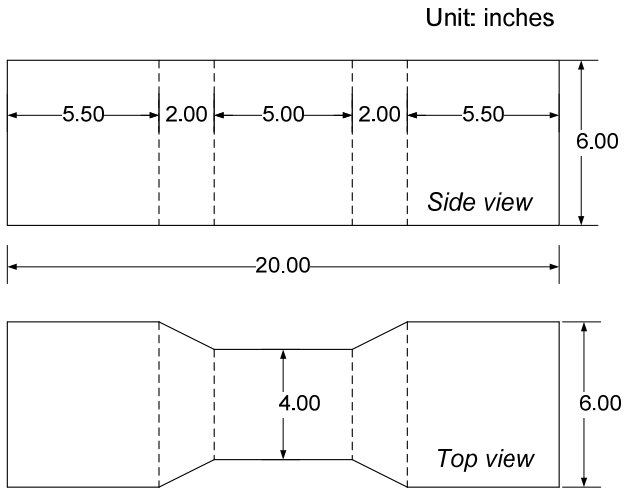

Figure 4.20 Dimensions and geometry of the modified Iosipescu model

The load and boundary conditions and mesh used in the FEA model are shown in Figure 4.21. The left and right side of the boundary conditions were simulated as hinge and roller respectively.

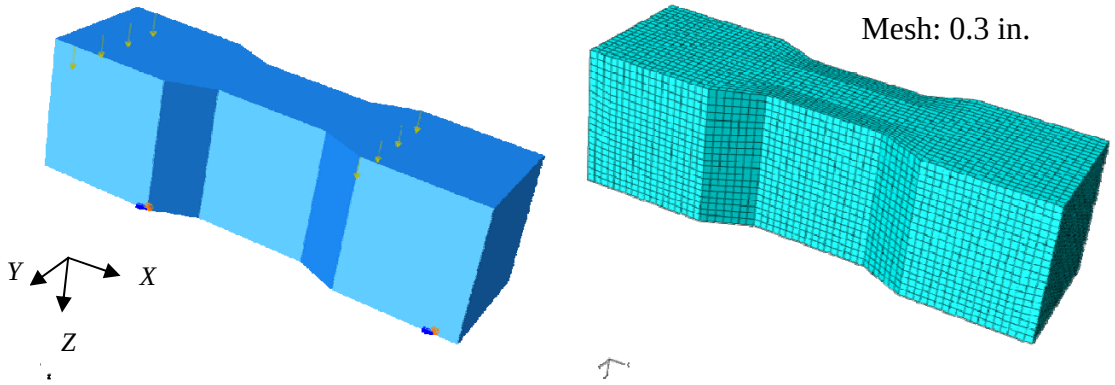

(a) (b)

Figure 4.21 Model for the modified Iosipescu specimen; (a) Load and boundary conditions; (b) Mesh used in the model

As can be seen in Figure 4.22, the results showed that the shear stress was maximized in the vicinity of middle of the specimen, along with minimized effects of normal stresses. In Figure 4.23 (c), the principle stress distribution had an angle of 45° at middle of the specimen, which can lead to the 45° shear crack. In addition, instead of using notches, the varying sectional areas between the end and the middle section was done to reduce stress concentration, as well as to force the failure occur at the intended shear plane.

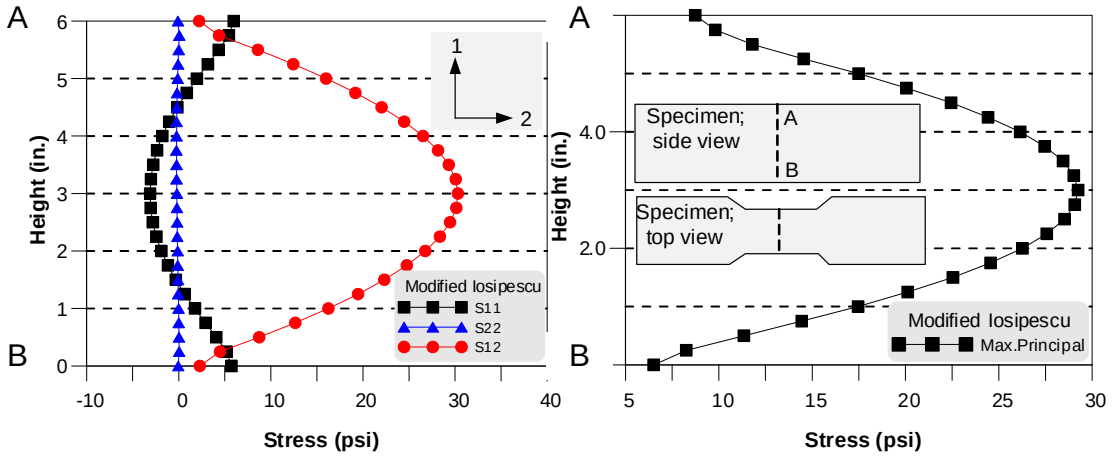

Figure 4.22 Stress distributions in modified Iosipescu test

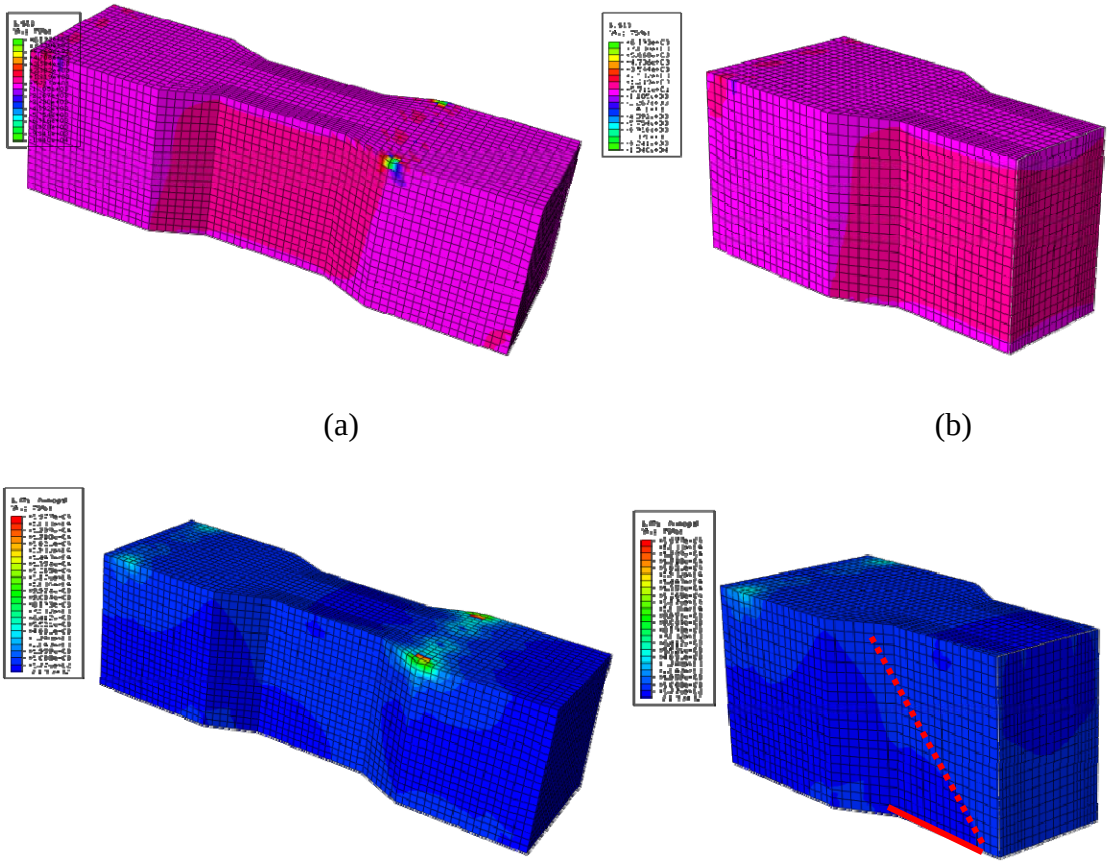

(a) (b)

(c) (d)

Figure 4.23 Stress contours of the modified Iosipescu specimen; (a) Shear stress distribution; (b) Shear stress distribution at the targeted shear plane; (c) Principal stress distribution; (d) Principal stress distribution at the targeted shear plane

4.3 Experimental Results

The FEA results showed that the modified Iosipesuc test method was able to simulate the pure shear stress state at the middle of the specimen such that shear behavior of SFRC on a material scale could be observed. However, it was necessary to provide certain reinforcement to prevent premature flexural failure in the specimen since the test is a beam type such that the specimen might fail due to the flexure before

the shear cracks occur. Several reinforcement layouts were evaluated to prevent premature flexural failure while introducing no interference to the shear plane.

The first attempt was done by using a galvanized wire mesh to reinforce the locations having the maximum bending stresses, as well as the regions with geometry discontinuity, as shown in Figure 4.24.

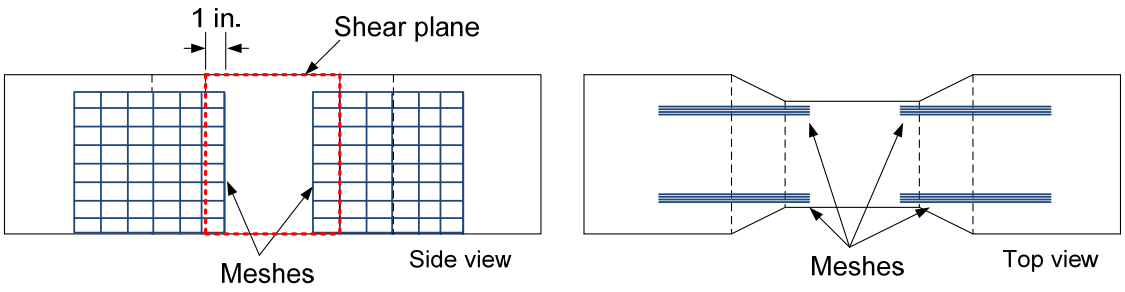

Figure 4.24 Layout of meshes

Four layers of meshes were used and they were extended 1 in. into the shear plane. However, the test result using a plain concrete specimen showed that the all meshes fractured and were not strong enough to prevent flexure failure, as shown in Figure 4.25 (b).

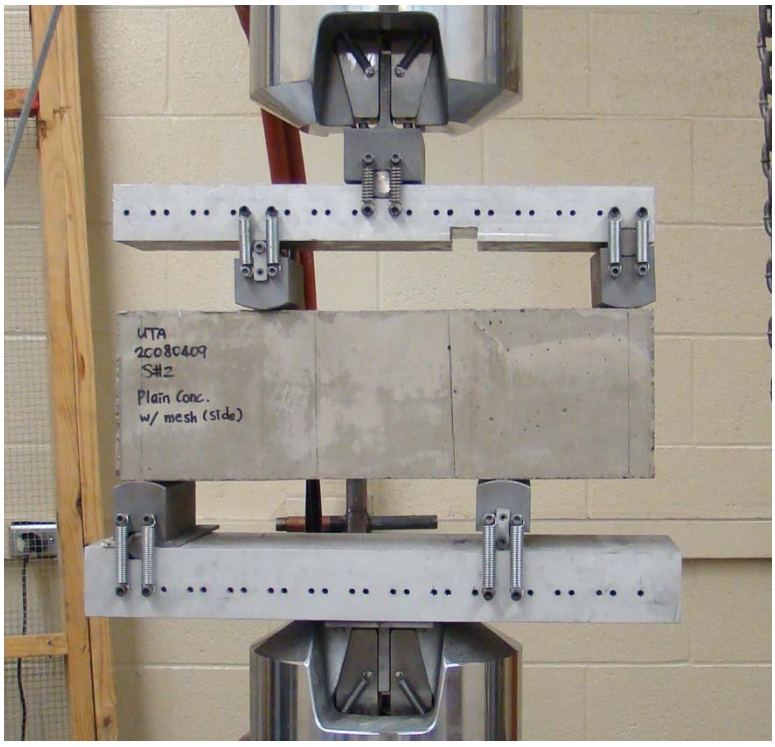

(a)

(b)

Figure 4.25 Test the specimen with meshes; (a) Test setup; (b) At failure

The failure occurred at the location where the area of the cross section was reduced as well as the bending stresses are maximized.

In the second trial, mild steel rebars were used to provide greater strength. C-shaped rebars (Figure 4.26) were used so that the locations with largest bending stresses (i.e., the top and bottom of the beam) were reinforced.

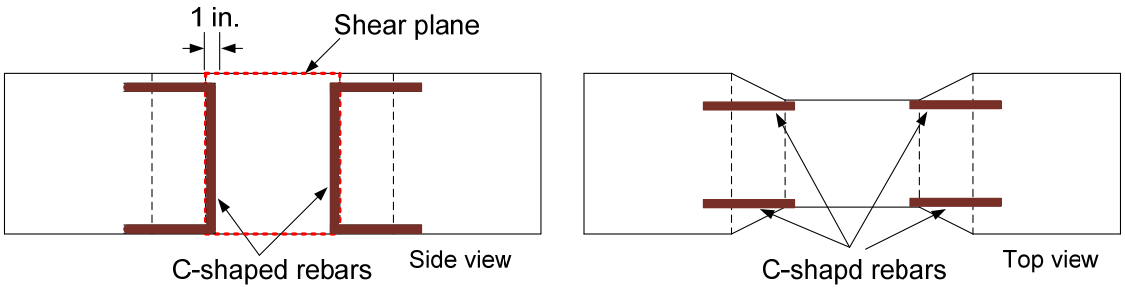

(a)

(b)

Figure 4.26 Layout of C- shaped No. 3 rebars; (a) Schematic view of reinforcement; (b) Reinforcement layout

The rebars used for the reinforcement were No. 3 (Grade 60). These C-shaped rebars were placed 1.5 in. into the shear plane to minimize the interference with the shear plane.

(a) (b)

Figure 4.27 Test results of the specimen with C- shaped rebar reinforcement; (a) Initial crack; (b) At failure

The initial crack occurred above the location where the area was reduced, and the direction of the crack was vertical meaning that the crack was due to flexural stress. As seen in Figure 4.27 (b), the crack propagated along the C-shaped rebars, and it led to fail. Therefore, the third attempt was to use the same size of rebars (No. 3 rebar) which went through the shear plane at the top and bottom of the beam, as can be seen in Figure 4.28. In addition, layers of mesh were used at the transition zone and were extended to the end to provide longer embedded length.

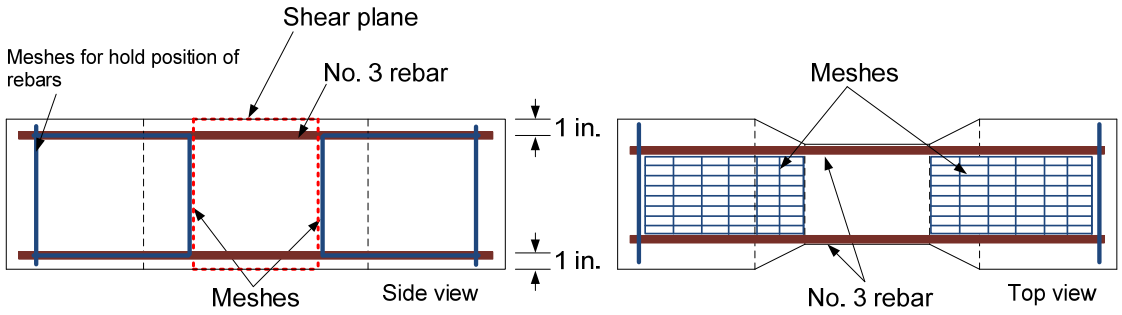

(a)

(b)

Figure 4.28 Layout of longitudinal reinforcement and meshes; (a) Schematic view of reinforcement; (b) Reinforcement layout

As can be seen in Figures 4.29, the initial crack had 45° angle with the specimen axis, indicating a shear type crack, and the vertical crack occurred right above shear crack. However, the location of crack was on the transition section where the cross-sectional area was reduced to 4x4 in. This reinforcement layout was able to prevent premature flexural failure, but further improvement was needed to be made since the shear crack occurred at the location of the transition section rather than the intended middle section.

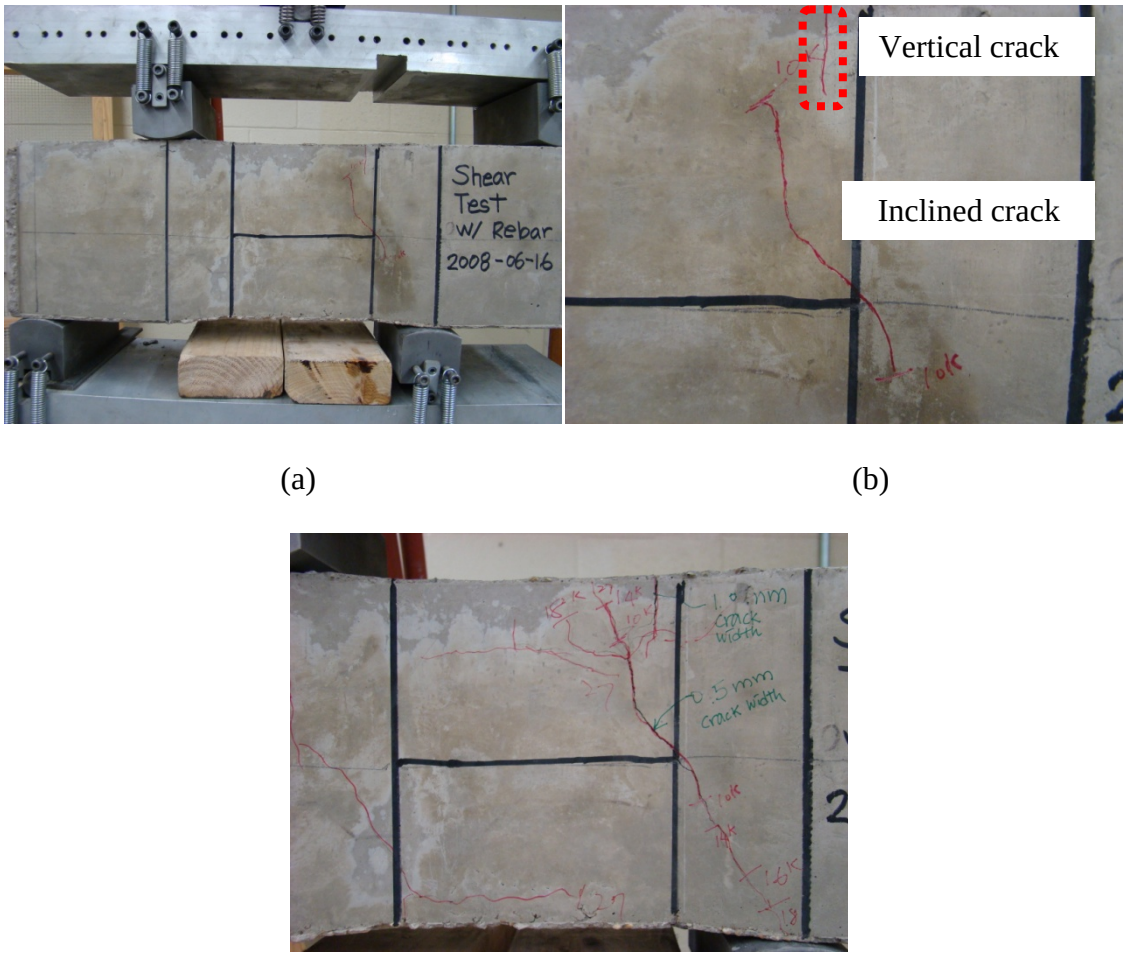

Figure 4.29 Test photos; (a) Initial crack; (b) Inclined and vertical cracks; (c) Prior to the failure

In the fourth attempt, in order to prevent the shear failure from occurring at the transition sections, three pieces of steel wire meshes were placed at each side of the beam at the transition regions (Figure 4.30). The same rebar layout as in the third trial was used. At this trial, these rebars were not at the fixed position, i.e., rebars were just embedded approximately 1 in. into concrete by assuming that the concrete was viscous enough such that rebars were at the position where these were originally embedded. The

mix design used in this trial were same as one used in the second large-scale beams having 0.75% volume fraction of steel fibers. The steel fibers used were also same.

Figure 4.30 Layout of longitudinal reinforcements and meshes at sides

As shown in Figure 4.31, initiation of the crack was due to shear stress, leading to a crack at an angle approximately 45° angle. The location of the crack was not at the center and middle of the specimen where the theoretical maximum shear stress existed. While the applied load increased, the cracks propagated beyond the targeted shear plane.

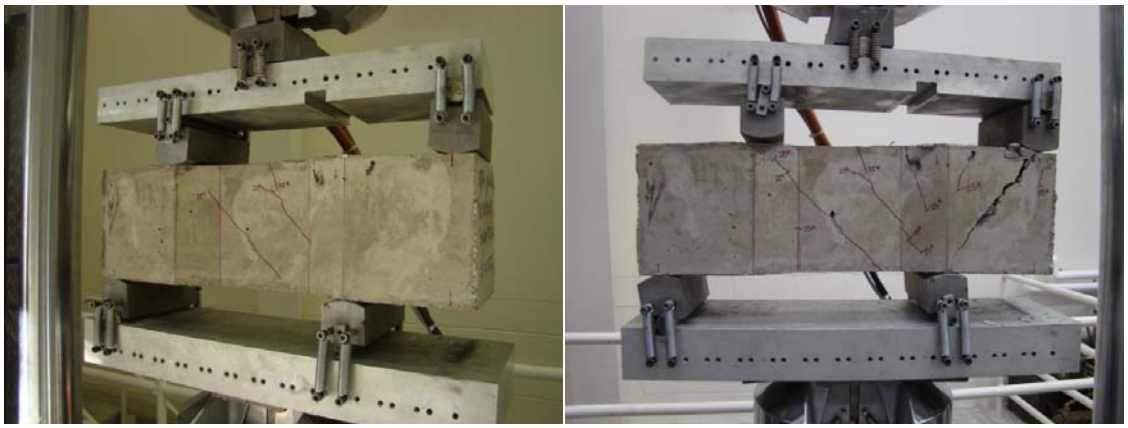

(a) (b)

Figure 4.31 Test photos; (a) Initial crack-1; (b) At failure

As can be seen in Figure 4.31, the specimen was failed due to the shear crack that initiated under right side of the loading. The meshes were not sufficient to prevent it. Therefore, in the next trail, closed loop stirrups were provided.

In the fifth attempt, instead of using wire meshes, No.3 closed loop stirrups, were used as shown in Figure 4.32. Three of the stirrups were placed at each transition region to enhance the shear capacity of these regions. The longitudinal tensile rebars were not at the fixed position similar to the fourth attempt. Also the SFRC was used, which mix design and volume fraction of steel fibers were same as the fourth attempt.

Figure 4.32 Layout of longitudinal reinforcement and closed loop stirrups

As can be seen in Figure 4.33, the initial crack occurred near the center and middle of the specimen, with approximately 45° angle with respect to the beam axis. When the load was further increased, multiple cracks occurred at the targeted shear plane. Figure 4.33 (c) shows the failure stage of the north face of specimen. The shear crack occurred at the center and middle of the specimen with 45° angle, accompanied with multiple

cracks. These shear cracks extended beyond the middle region with reduced area, and the ultimate failure was due to shear as can be seen in Figure 4.33.

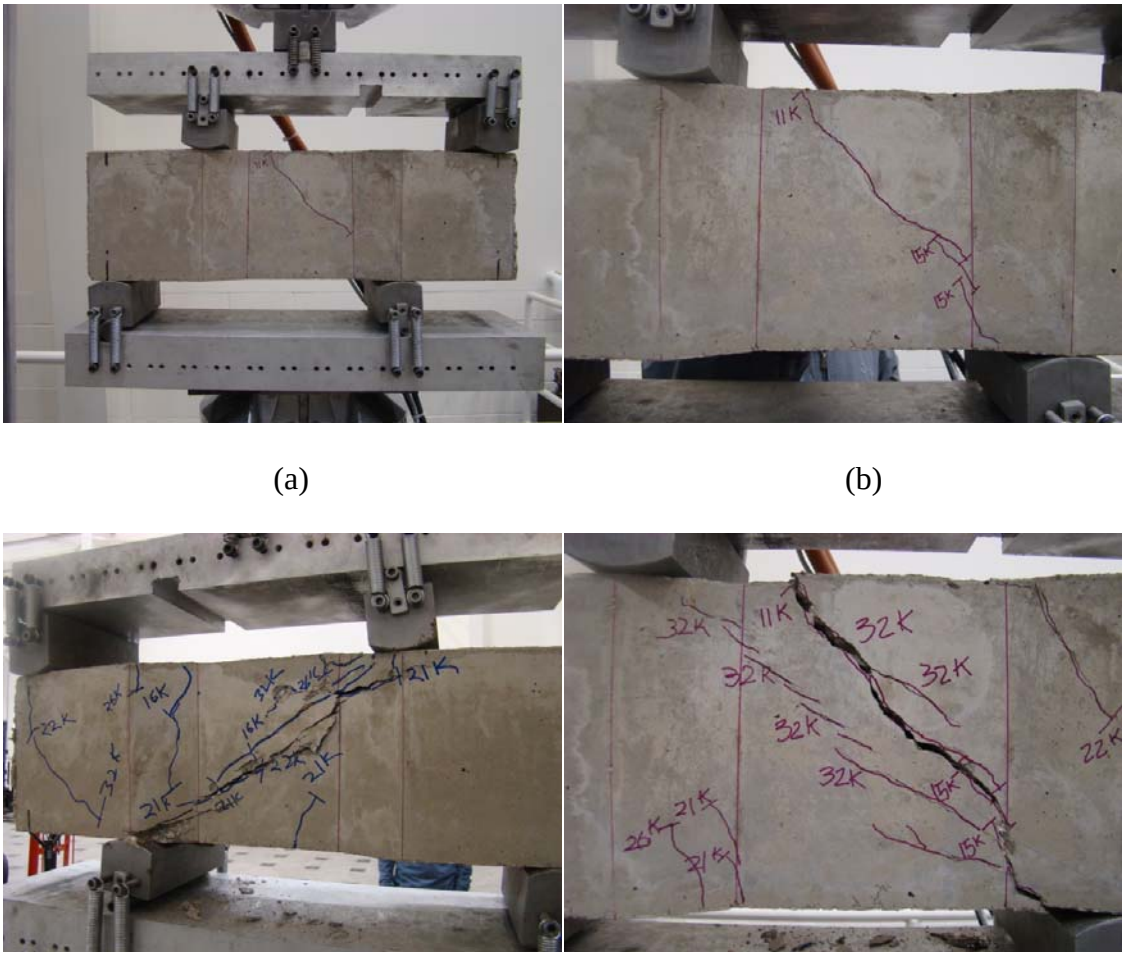

(a) (b)

(c) (d)

Figure 4.33 Test photos; (a) Overall view of the beam at the first crack; (b) Cracks at early stage; (c) Failure in north face; (d) Failure in south face

It was observed that the shear cracks propagated beyond the top and bottom longitudinal reinforcement, thus the ultimate shear strength was increased by dowel effect induced by the longitudinal rebars. It also should be mentioned that the rebars were found at approximately middle of the section after the test as shown in Figure

4.34, even though these were embedded 1 in. into concrete originally. Therefore, to prevent displacement of rebars, the longitudinal tensile rebars were tied with stirrups with either aluminum wire (in the sixth trial) or tap welding (in the seventh trial) as illustrated in Figure 4.35

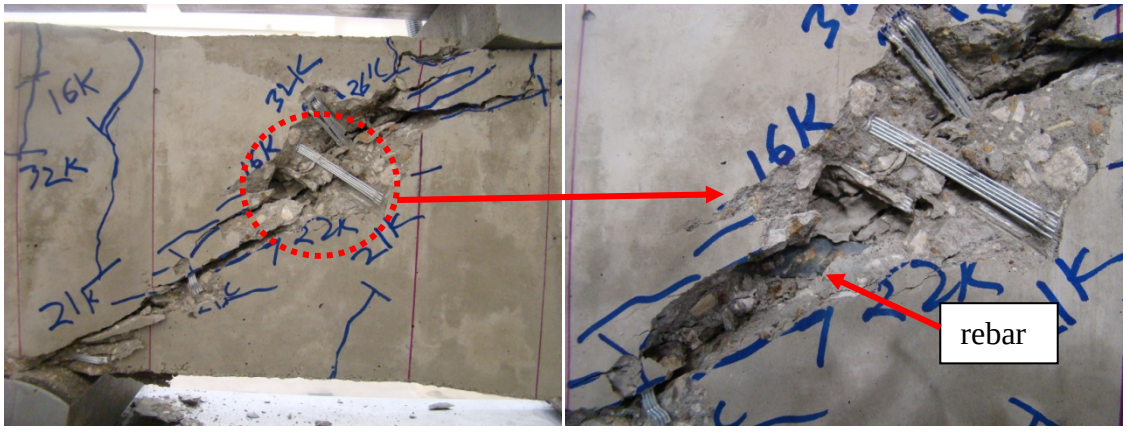

Figure 4.34 Locations of rebars

In addition, to avoid this interference, in the sixth and seventh attempts, the longitudinal reinforcement was terminated before the anticipated path of shear crack, as can be seen in Figure 4.35. Slight modifications were done for the reinforcement used in the seventh attempt to further reduce the length of the longitudinal bars to minimized interference to the crack path while maintain sufficient anchorage length. In addition, the first stirrups at both transition regions were extended to eliminate possible shear cracks in these regions as observed in some of the specimens in the sixth attempt (see Figure 4.35 (a)).

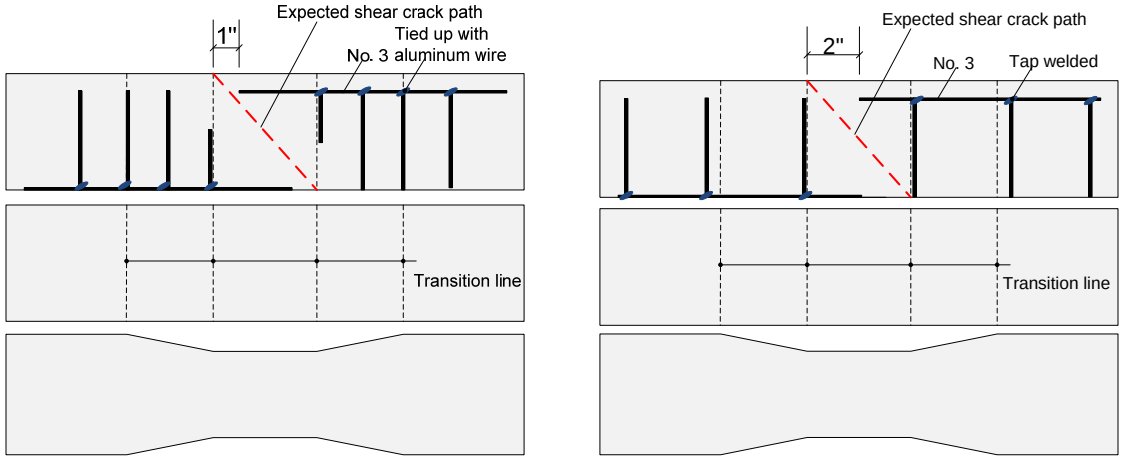

(a) (b)

Figure 4.35 Schematic of layout of reinforcement for modified Iosipescu specimens; (a) the sixth attempt (cast with the SFRPC beams in the second phase); (b) the seventh attempt (cast with SFRPC beams in the third phase)

It was believed that the reinforcement layouts could prevent the premature flexural crack such that it might be possible to investigate overall shear behavior of SFRC materials. For the reason, specimens were prepared and casted with the large-scale beams in the second and third phases as shown in Figure 4.36 and 4.37.

(a)

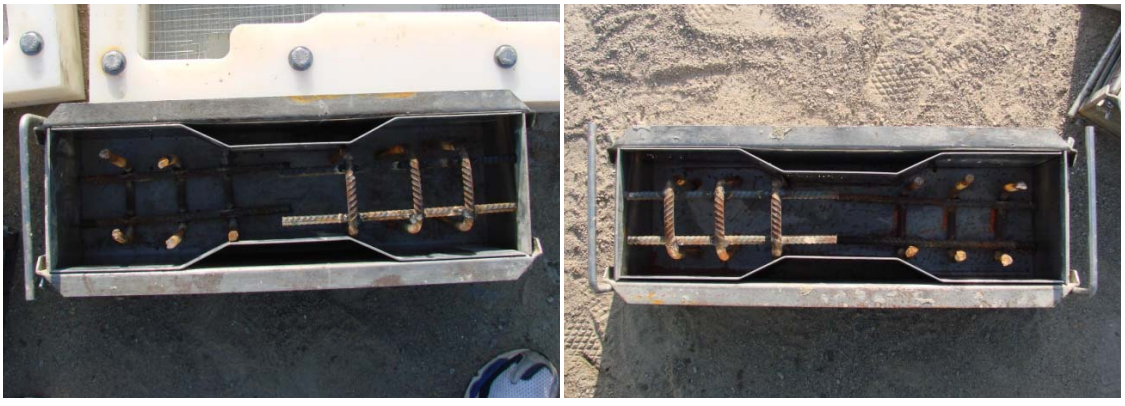

(b)

Figure 4.36 Photos of reinforcement for the modified Iosipescu; (a) The second phase; (b) The third phase

Figure 4.37 Typical photos of casting of the modified Iosipescu specimens

A total three specimens from the second phase study and six specimens from the third phase study were tested. Most of specimens failed as undesirable manner. For example, the shear crack occurred at the transition region in Specimen # 3 (V_f = 0.75%) of the sixth attempt (Figure 4.38 (a)), and the flexural cracks occurred in the transition region in Specimen #3 (V_f = 0.75%) in the seventh attempt (Figure 4.38 (b)). The possible reason for the flexural crack was that No. 3 bars was not sufficient to resist flexural bending stress. In addition, the first shear crack strength was enhanced due to the inclusion of steel fibers such that higher load was necessary to create the shear crack. In the previous attempt, the 2 – No. 3 might be enough to resist flexural bending until the shear crack occurred, but in this case, it was not. Therefore, more precise calculation is necessary to reinforce flexural bending stress. In addition, the calculation should consider the enhancement of shear strength due to the inclusion of steel fibers. It is recommended that over-reinforcement in flexure can be used to ensure not to have flexure crack prior to the shear crack such that it is possible to obtain reliable testing date.

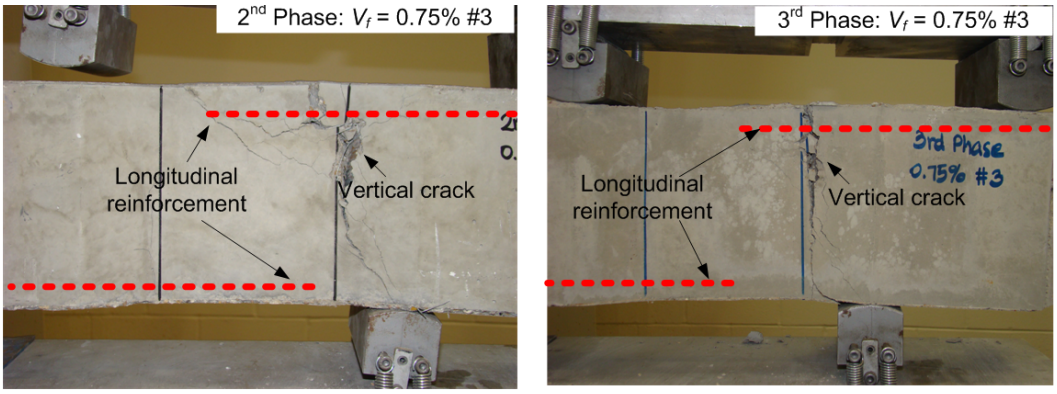

(a) (b)

Figure 4.38 Failure due to flexural bending stress; (a) Specimen with 0.75% volume fraction of steel fibers in the second phase; (b) Specimen with 0.75% volume fraction of steel fibers in the third phase

For some of specimens, such as Specimen #1 (V_f = 0.75%) in the seven attempt, the shear crack initiated at the transition zone and propagated the targeted shear zone as shown in Figure 4.39. Since the crack was initiated at the transition zone and propagated upward with approximately 45° angle, the crack was reached at the middle of the shear zone at the top as seen in Figure 4.39 (b). It should be mentioned that longitudinal tensile rebar at the top was stopped at the middle of the shear plane.

(a) (b)

Figure 4.39 Shear crack in Specimen #1 (V_f = 0.75%) in the seventh attempt; (a) South face; (b) North face

A few specimens did exhibit the expected behavior; for example, Specimen #3(V_f = 0.5%) from the third phase (or the seventh attempt), showed that the shear crack was initiated at the center and middle of the beam and then propagated with nearly 45° toward the top and bottom faces of the beam until failure, as shown in Figure 4.40.

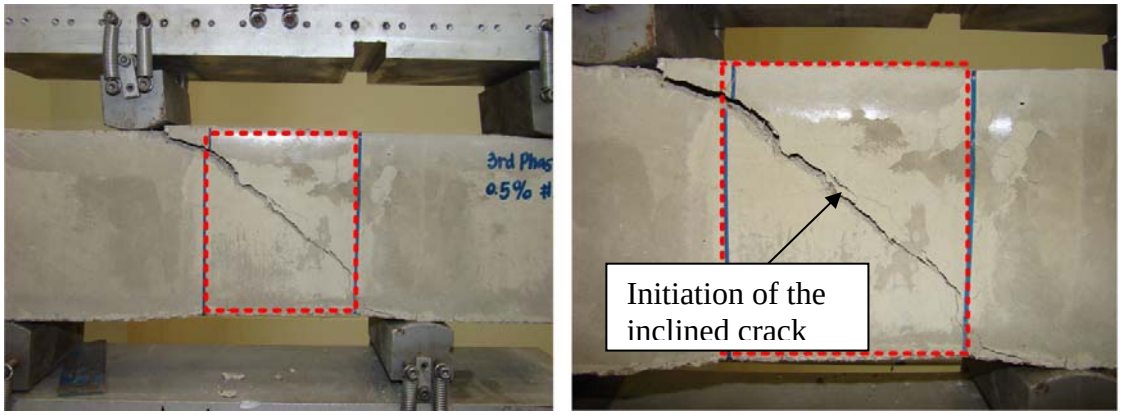

Figure 4.40 Shear crack at the shear plane

The development of a shear material test method was first investigated by FEA and through various treatments in the reinforcing details used in the specimens. It was seen that a nearly pure shear could be achieved by the proposed test method. The major difficulties are due to the bending stresses which are not avoidable since the test method is beam type test. Even though many trials were attempted, it was not able to obtain reliable testing data. Therefore, further attempts will be carried out to fine-tune the reinforcement layouts to prevent undesirable failure modes. Nevertheless, this test method should be valuable for the evaluation of shear properties of the SFRC materials since it showed the possibility that the pure shear crack can be initiated, and it was verified by FEA and experiment.

CHAPTER 5

EXPERIMENTAL RESULTS – LARGE SCALE SFRPC BEAMS

5.1 The First Phase Experiments

In this phase of the study, two large scale specimens were prepared and tested. One was a conventional prestressed concrete beam without web shear reinforcement in the instrumented shear span (short span), and the other one was a SFRPC beam having 0.75% volume fraction of steel fibers. The design parameters used in this study are listed in Table 5.1, and key experimental results for the first phase study are summarized in Table 5.2, including the first observed flexural and shear cracking loads, the ultimate load, the corresponding shear force in the shear span, and the normalized shear strength (psi), $V_u/\sqrt{f'_c}$.

5.1.1 Beam 1 - PC#1

5.1.1.1 Load versus Deflection Response, Crack Pattern, Failure Mode

The load versus deflection response for the 1 – PC is shown in Figure 5.1. The first visible crack was a flexural crack occurring at 85 kips of applied load, which initiated from the bottom of the specimen and then propagated near vertically toward the loading point (see Figure 5.2). The first visible shear crack occurred at 110 kips, which is corresponding to a shear force of 71.5 kips. This crack was a web shear crack.

As shown in Figure 5.1, the stiffness of the beam was degraded after the flexural and shear cracks developed. The failure occurred at 146 kips, which is corresponding to a shear force of 95 kips. The deflection at ultimate stage was 0.513 in. The shear force is corresponding to a normalized shear strength ($V_c/\sqrt{f'_c}b{\cdot}d$) of $2.5\sqrt{f'_c}$. Figure 5.2 illustrates the crack patterns at various loading stages. At 110 kips, a web shear crack developed across the beam at approximately a 45° angle. At that moment, the shear crack had already reached the loading point, creating a reduced compression depth, less than 2 in. Prior to failure, multiple cracks also along the longitudinal reinforcement propagated and toward the support. At the failure stage, the shear crack passed the loading point leaving an approximate compressive depth of 1 in., leading to crushing in the reduced compression zone and significant subsequent sliding of the cracking plane, as shown in Figure 5.3.

5.1.2 Beam 1 - SFRPC#1

5.1.2.1 Load versus Deflection Response, Crack Pattern, Failure Mode

The load versus deflection curve for the 1 – SFRPC specimen is presented in Figure 5.4. A wrong calibration was used for the load cell during the test, which was justified in a post analysis step. Because of this reason, the load was continuously applied to 170 kips (the true value) without inspecting any crack. The load was stopped when the first visible web shear crack occurred. As a consequence, the applied load corresponding to the first visible flexural crack was missed, partly because the width of the crack was not visible. The first observed shear crack was formed by web shear at

170 kips, which is corresponding to a shear force of 110.5 kips. The normalized shear strength at the first shear crack was $3.0\sqrt{f'_c}$. When load was further increased, multiple cracks developed in the shear span, and some of the web shear cracks were connected with the flexural cracks. It is clearly seen in Figures 5.5 and 5.6 that there were more cracks in the 1 – SFRPC than in the 1 – PC. This is an evidence of stress redistribution in SFRC, meaning that greater portion of the concrete contributed to the resistance of forces. When the load was further increased, the shear crack propagated at a flatter angle, less than 45° angle, and eventually the angle of crack was almost parallel to the axis of the beam when the crack reached near the loading point. The compression zone had approximately 4 in. deep when the concrete researched its ultimate strain. It should be mentioned that concrete in the vicinity of the loading point was under very high bi-axial compressions (the loading was 320 kips), which significantly reduced the diagonal principle tensile stress, thus preventing the crack from propagating into the compression zone. The high bi-axial compression was a direct result of the bridging effect of steel fibers, which slowed down the propagation of the critical diagonal crack and a greater load was required in order for the crack to propagate upward to reduce the area of compression zone. Prior to failure, the concrete under loading point was crushed, as shown in Figure 5.6 (c). Finally, major spitting of the concrete along a compression strut and instability of the crushed compression zone led to failure and sliding between the two crack surfaces. According to the observation of the 45^o red lines, as shown in Figures 5.6 (b) and (c), the sliding between the two cracked surfaces resulted from the crushing of concrete. It should be mentioned that many additional cracks occurred upon

crushing of the compression zone. This observed failure mode was an evidence of the direct load transfer via strut as the load resistance mechanism.

5.2 The Second Phase Experiments

As mentioned in Chapter 3, three conventionally reinforced prestressed concrete (PC) beams and three steel fiber reinforced prestressed (SFRPC) beams were prepared for the experiments of the second phase. One PC beam, 2 – PC#1, contained the minimum shear reinforcement, calculated based on ACI 318-08 building code, in the short shear span. Two additional PC beams without shear reinforcement in the short shear span were tested: 2 – PC#2 had a 0.12 % of compression reinforcement ratio (ρ'=0.12%, 2 – No.4), and the third beam, 2 – PC#3, had a 0.94 % of compression reinforcement ratio (ρ' = 0.94%, 4 – NO. 8). For the SFRPC beams, 2 – SFRPC#1 had a 0.75% volume fraction of steel fibers (V_f = 0.75%); 2 – SFRPC#2 had a 0.5% volume fraction of steel fibers (V_f = 0.50%); 2 – SFRPC#3 beam had a 0.75% volume fraction of steel fibers and a 0.94% of compression reinforcement ratio (ρ' = 0.94%, 4 – NO.8). The intention of using high ratio of compression reinforcement in specimens 2 – PC#3 and 2 – SFRPC#3 was to investigate the effect of the compression reinforcement in enhance the shear resistance. This was done because it was observed in 1 – SFPRC beam that crushing of the concrete compression zone was the major cause of the failure. Key experimental results for the second phase study are summarized in Table 5.3, including the first observed flexural cracking load, the first observed shear cracking

load, the ultimate load, the corresponding shear force in the shear span, and the normalized shear strength (psi), $V_u / (\sqrt{f'_c} \cdot b \cdot d)$

5.2.1 Beam 2 – PC#1

2 – PC#1 beam was prepared and tested for comparison purpose with SFRPC beams. The beam had the minimum shear reinforcement designed as per the ACI 318-08 building code.

5.2.1.1 Load versus Deflection Response, Crack Pattern, Failure Mode

The load versus deflection response is shown in Figure 5.7. The first visible flexural crack occurred at 85 kips, and the first visible shear crack occurred at 105 kips in the formation of flexural – shear crack. At 120 kips a web shear crack occurred, as shown in Figure 5.8. While the load was increased, the stiffness of the beam was decreased gradually. The load was suddenly dropped to approximately 200 kips immediately after the load reached 225 kips, due to a sudden shear failure with crushing of concrete adjacent to the loading point, which indicated the shear compression failure, as shown in Figure 5.9.

The crack patterns with the various load stages are shown in Figure 5.8. The first visible crack was due to flexural stress at bottom of the beam, as expected. Only single flexural crack existed up to 95 kips and the crack propagated toward the loading point. At 105 kips, multiple flexural cracks and flexural – shear crack occurred. At 120 kips, the web

shear crack was observed. While the load increased, multiple shear cracks developed in the short shear span. Prior to the failure, gradual crushing of concrete in the compression zone was observed (see Figure 5.9 (c)), when the major shear crack extended up and reduced the depth of the compression zone. Complete fracture of the concrete led to failure of the beam.

5.2.1.2 Strains in Concrete and Mild Steel Bars

In 2 – PC#1 beam, two strain gauges were embedded inside the concrete under loading point, which were intended to measure strains in the concrete. Eight rebar strain gauges were installed on the stirrups, which were distributed within the short shear span. Four rebar strain gauges were mounted on longitudinal mild steel bars. The load versus strains relations from the concrete embedded strain gauges (C#1 and C#2) and strain gauges on the compression reinforcement (S#11 and S#12) are shown in Figure 5.10. Beyond 85 kips, the point at which the first visible flexural crack occurred, the slope of curves gradually decreased. The concrete strain increase rate kept increasing, which could be attributed to the gradually reduced compression area. At the ultimate load, 220 kips, the measured concrete strains were approximately 1050 and 1200×10^{-6} for C#1 and C#2, respectively. S#11 showed a hardening behavior at this moment where the concrete crushing in the compression zone was observed. As illustrated in Figure 5.11, the projected strains were 3537 and 4042 $\times 10^{-6}$ at the top of the section. The top of the concrete underwent its ultimate strain for plain concrete, which is generally assumed as 3000×10^{-6}. Beyond the ultimate load, strain data was fluctuated.

Figure 5.12 shows the strains in the longitudinal tensile reinforcements. Two strain gauges (S#1 & S#2) for mild steel rebars were installed at the middle of the short shear span and the other two (S#14 & S#15) were installed at loading point. Unfortunately, one of the strain gauges (S#15) at the loading point was damaged during the casting of the beam. The strain from S#14 increased rapidly beyond a load of approximately 85 kips, which corresponded to the first visible flexural crack. The maximum measured strain was 3500 $x10^{-6}$ (at 175 kips), which was greater than the yield strain for mild steel rebar. Unlikely S#14, the strains from S#1 and S#2 showed that the slope was linear up to 120 kips and then beyond 120 kips, in which point the web shear crack occurred, the slope was slightly degraded. At 150 kips, the strains dramatically increased from 500 to 2000$x10^{-6}$ because multiple splitting cracks developed along the longitudinal reinforcements. Strain gauges S#1 and S#2 showed nearly the same strain of 3750 $x10^{-6}$ at the ultimate load. Any rupture of the longitudinal reinforcements including prestressing strands was not observed. Figure 5.13 shows the strains in the stirrups. The locations of the strain gauges are noted in Chapter 3. In both stirrups #1 and #2 (Figure 5.13) No strain increment was observed up to the applied load of 125 kips. However, the strains suddenly increased after the first web shear crack occurred at approximately 125 kips. This indicted that the concrete significantly lost its load-carrying capacity after cracking occurred. At ultimate, all of strains from the strain gauges in the stirrups were over 6000$x10^{-6}$ and some of them, S#3, S#5, and S#6, were beyond 15000$x10^{-6}$. This indicated an important role of those stirrups in carrying the shear force.

5.2.2 Beam 2 – PC#2

5.2.2.1 Load versus Deflection Response, Crack Pattern, Failure Mode

The load versus deflection response and the crack patterns for the 2 – PC#2 beam are shown in Figure 5.14 and 5.15 respectively. Note that this specimen was different from the PC#1, i.e., any shear reinforcement was not provided in the short span. The first visible crack, a flexural crack, occurred when the load reached 60 kips. When the load increased, the flexural crack propagated near vertically toward loading point. The first shear crack, noticed as a flexural – shear crack, occurred at a load of 100 kips. At 115 kips, a loud sound was heard, but it was not able to identify the origin of the sound by observation, and load was dropped to 103 kips as can be seen in Figure 5.14. Due to safety concerns, the cracks were not marked until the beam was completely failed. The beam was inspected from a safe distance away. However, the beam was able to keep picking up load. The fracture sound was observed again at 125 kips. This time there was no significant change in the load versus deflection curve caused by the sound, neither new cracks or crack propagation was observed. A sudden failure was occurred at 200 kips, which corresponds to a shear force of 112.5 kips. Crushing of concrete in the compression zone was observed and then significant sliding and the splitting along compressive strut led to the failure of the beam, shown in Figure 5.16 (b).

5.2.2.2 Strains Measured in Reinforcing Bars

Two strain gauges were installed in the longitudinal tensile mild steel bars; one under the loading point and one at middle of the short shear span. The strains measured

by those strain gauges are presented in Figure 5.17. As shown in the figure, the steel section near the loading point started to take load earlier than the one close to the middle of the short shear span. Both gauges reached and exceed the yield strain, approximately $2000x10^{-6}$ at the ultimate stage. There was a rapid increase in strains in S#1 when the load reached 100 kips, at the time a shear crack occurred. After 100 kips, two strain gauges (S#1 and S#4) showed a similar increment pattern. The strain from the compression reinforcement showed skeptical data from 120 to 200 kips loading stages as shown in Figure 5.18. The compression strain increased up to 105 kips, and then suddenly decreased when the flexural-shear occurred (Figure 5.15). This seems to indicate a shifting in the load transfer mechanism. While load was increased, the strains were continuously decreased. Prior to failure, a sudden increase in compressive strains was noticed, when the new diagonal splitting crack appeared.

5.2.2.3 Concrete Surface Strains

Concrete surface strains in the short shear span are shown in Figure 5.19 and 5.20. C.S. #3 was on the path of the major flexural-shear crack, while both C.S #1 and #2 were on the path of the new splitting crack that occurred when failure of the beam occurred. The highest strain was obtained from C.S #1. It is interesting to note that beyond approximately a load of 100 kips, strains in C.S #3 decreased to zero; on the other hand, stain values in C.S #2 and #3 increased rapidly. This again confirms that the major force transferring mechanism for this beam was through a direct strut between the load point to the support. Data for other strain gauges (Figures 5.19 and 5.20) along

the initial flexural-shear crack and new splitting crack also indicated the same conclusion. It should be mentioned that the strain value from the concrete surface strain gauges might not reflect the actual strain values, however, it could provide the force flow along the section. Based on the observation of these strains, the force was transferred through a strut, which was formed from the loading point to the support.

5.2.3 Beam 2 - PC#3

5.2.3.1 Load versus Deflection Response, Crack Pattern, Failure Mode

The load versus deflection response and the crack patterns for 2 – PC#3 beam are shown in Figure 5.21 and 5.22 respectively. The 2 – PC#3 was identical with 2 – PC#2 beam except the compression reinforcement ratio, i.e., the ratio was changed from 0.12% (2 – No. 4) to 0.94% (4 – No. 8). The first visible flexural crack occurred at 60 kips. As can be seen in Figure 5.21, the stiffness of the beam decreased after the first crack occurred. Unlike to 2 – PC#2, the first shear crack formed as web shear, which was connected with one of existed flexural crack, and around 125 kips, the load was dropped slightly without observation of any significant damage (see Figure 5.21 and 5.22). From 140 kips to directly before failure, two web shears were initiated at the middle of the shear span. At the failure stage, a new splitting crack along the compression strut was developed right after concrete crushing occurred beside the load bearing plate like the 2 – PC#2 beam as shown in Figure 5.23. The phenomenon provided instability of beam and led to failure. Splitting cracks were observed along a position where the longitudinal reinforcements were placed, and the complete

debonding between the concrete and reinforcement was observed at the failure, shown in Figure 5.23 (d). It should be mentioned that 2 – PC#2 and #3 beams showed similar behavior in terms of the load versus deflection responses, crack patterns, and failure mode. Therefore, it can be said that the compression reinforcement would be ineffective in the shear behavior of PC beams.

5.2.3.2 Strains Measured in Reinforcing Bars

Unfortunately, the strain in the longitudinal reinforcements was not available to measure due to careless treatment during the installation of the strain gage in the fabrication. However, it can be assumed that the strains in 2 – PC#3 were similar to 2 – PC#2 since overall behavior of specimens was similar. Only strains in the compression reinforcement were available, shown in Figure 5.24. The strain pattern from S#3 was similar to S#3 in 2 – PC#2; increased in compression up to 100 kips, where the first shear crack occurred, and then showed fluctuation. As mentioned in 2 – PC#2 beam, this could indication of a shifting in the load transfer mechanism. Strain gage S#2 showed very minute strain changes up to fail; the strain reached less than 100×10^{-6}. However, the strain gauge also showed some fluctuation at 100 kips similar to S#3.

5.2.3.3 Concrete Surface Strains

Concrete surface strains in the short shear span are showed in Figure 5.25. Similar to 2 – PC#2, the strain in the gauges close to compression strut were typically higher than of portions of the beam. Additionally, the strains in the lower portion of the

beam was less than the upper portion. It should be mentioned that the slopes of most of the strain gauges were changed around the applied load 100 kips, which were closed to the first visible shear crack, especially the strain gauges located closed to the compressive strut (C.S #1, #2, and #4) were increased at that load. This might imply that the load transfer mechanism was changed right after the initiation of the shear crack, i.e., the load was transferred through a direct strut between the loading point to the support. It is also worth to note that the strains measured by C.S#2, which was located just above compression strut splitting at failure, showed the highest strains of all the other strains.

5.2.4 Beam 2 - SFRPC#1

5.2.4.1 Load versus Deflection Response, Crack Pattern, Failure Mode

2 – SFPRC#1 beam had the identical geometries and reinforcement with 2 – PC#2 beam except that 2 – SFRPC#1 contained 0.75% volume fraction of steel fibers. The load versus deflection response is shown in Figure 5.27. The first visible flexural crack was occurred at 100 kips load, and the first visible shear crack was occurred at 140 kips, which is corresponding to shear force of 79 kips. The first shear crack was a web shear crack. As seen in Figure 5.27, the stiffness of beam decreased slightly when the first flexural crack was occurred, and decreased when the first shear crack was occurred. As load increased, the stiffness of beam gradually decreased. At failure, the ultimate load was 211 kips which correspond to a shear force of 119 kips, which in turn gave normalized shear strength of $4.94\sqrt{f'_c}$.

The crack patterns at various load stages are shown in Figure 5.28. At 100 kips, the first visible flexural crack was occurred under loading point in the bottom of beam. At 120 kips, multiple flexural cracks were occurred, but no shear crack was exhibited. While the load increased, two major shear cracks were initiated at 140 kips; one formed as a web shear and the other formed as flexural – shear. These cracks were merged adjacent to the middle height of the beam. It was unclear that which shear crack, either web or flexural shear cracks was occurred at the first since the loading increment was 10 kips. At 160 kips, the shear crack propagated toward the loading point at a flatter angle, and then the angle was perfectly horizontal with the beam axis when it was directly beneath the loading point creating a depth of the compression zone of 4 in. The crack propagation was stopped under the loading point prior to failure. Multiple cracks developed along the location where longitudinal reinforcements were placed after the shear cracks were initiated. At failure, concrete crushing was observed underneath the loading point, and finally crushing of compression zone led to fail as shown in Figure 5.27.

It should be noted that the quality of fiber distribution of the material used in the beam was not well controlled, shown in Figure 5.29 (d), which was caused by non-dissolved glued-bundle. The glue-buddle steel fibers supposedly were dissolved properly with the water in the mixture and mechanical force from the mixing procedure. Uniform fiber distribution was not properly achieved due to non-dissolved steel fiber. This is one of major reason why the steel fibers were changed in the third phase.

5.2.4.2 Strains Measured in Reinforcing Bars

In 2 – SFRPC#1 beam there were two strain gauges embedded in the compression zone, two rebar strain gauges in compression reinforcement under loading point, two rebar strain gauges in longitudinal reinforcement, and twelve concrete surface strain gauges were installed. The detail information on the sensor instrumentation is provided in Chapter 3. The strains from the strain gauges embedded in the concrete are shown in Figure 5.30. The compressive strain values increased while the load increased up to 130 kips prior to the development of the first web shear (see Figure 5.30 and 5.31). After 130 kips the strain decreased until the beam failed. It should be noted that the strain patterns from the embedded concrete strain gages were similar to the strain patterns from compression reinforcement, shown in Figure 5.31. In addition, the strains profiles were similar with the profiles in 2 – PC#2 and #3, which indicates that the load transfer mechanism could be similar each other. Figure 5.32 shows the strains in the longitudinal tensile mild steel bars. The strain under loading point, S#5, showed that the slope of curve was decreased around 100 kips, which is corresponding to the first flexural crack loading. The strain increased up to 2000×10^{-6} at failure stages. The strains from S#1, located in the middle of the instrumented shear span showed a sudden increment at around 140 kips, which corresponds to the load at first web shear crack. At the failure stage, the strain was reached 2600×10^{-6}.

5.2.4.3 Concrete Surface Strains

The concrete surface strains are shown in Figure 5.33 and 5.34. C.S.#1, C.S.#2, and C.S.#4 were installed adjacent to the loading point. While the load was increased, all strain gauges were in compression. However, at 100 kips, C.S.#4 turned from compression to tension; in addition, C.S.#1 and C.S.#2 showed a sudden increase in compressive strains. At the ultimate stage, C.S.#1 and C.S.#2 reached strains of -1500×10^{-6} and -800×10^{-6} respectively and C.S#4 had almost zero strain. The strains from C.S#3 and C.S.#5, which were located in right underneath of the loading point, showed tensile strains. It is possible that the concrete surface tried to pop-out making parabolic shape out of the plane. It is hard to estimate the realistic concrete strain levels using only the information from those two strain gauges. The strains from C.S.#6 and C.S#7 is shown in Figure 5.34 (a). C.S#6 was located above the shear crack and C.S#5 was located below the shear crack. Until the load reached 125 kips, the strains measured by two strain gauges were compressive strains of -250×10^{-6}. After the load stage, C.S.#6 suddenly had a tension and then at 140 kips, when the shear crack occurred, the strains from C.S.#6 was compressive. This also could be the indication of that the load transfer mechanism was changed, which was observed in the previous beams. The strains from C.S#6 changed suddenly before and after the shear crack occurred. At the same load stage, the strains from C.S.#7 decreased in compression. As similar to the previous beams, the strains under the shear crack showed almost no change after the occurrence of the shear crack. At the ultimate stage, C.S.#6 and C.S#7 reached strains of -1750×10^{-6}, and -200×10^{-6} respectively. It is clearly seen that the portion above the

shear crack experienced a higher compression than the portion below the shear crack, and the increment rate increased after the shear crack occurred. That could imply that the section under the shear crack had very little contribution in the stress resistance. This was observed in C.S#8 to C.S #12 as well. It should be noticed that the strains from C.S.#6, C.S.#8, C.S.#11, and C.S.#12, which laid along or above the compressive strut line, showed relatively higher strains such that the load transferred mechanism was possibly through a direct strut as similar to the PC beams.

5.2.5 Beam 2 - SFRPC#2

5.2.5.1 Load versus Deflection Response, Crack Pattern, Failure Mode

2 – SFRPC#2 beam had the identical geometries with 2 – PC#2 and SFRPC #1 (V_f = 0.75%) beams, however, 2 – SFRPC#2 contained 0.50% volume fraction of steel fibers. The graph displaying the load versus deflection response for 2 – SFRPC#2 beam is presented in Figure 5.35. At 70 kips, where the first crack was observed to be a flexural crack, the stiffness of the beam was degraded slightly. At 120 kips, where the first shear crack initiated in the form of the web shear, and the stiffness of the beam was dropped. The beam was failed at 199 kips, which corresponds to a shear force and normalized shear strength of 112 kips and $5.44\sqrt{f'_c}$, respectively. The deflection of the beam at the ultimate stage was 0.736 in. The crack patterns recorded during the test at the various loading steps are presented in Figure 5.36. At 70 kips, the first visible flexural crack occurred under the loading point. While the load was increased by 110 kips, multiple flexural cracks developed, and existing the cracks propagated toward the

loading point to half of depth of beam. At 120 kips, two web shear cracks suddenly developed. At 140 kips, these cracks propagated toward the loading point at a flatter angle than the initial angle. It is interesting to note that the web shear cracks propagated toward the loading point yet, and the propagation under the loading point stopped at a certain loading (after 150 kips), similar to previous SFRPC beams. At 190 kips, concrete crushing was observed under the loading point, and the crushing of the concrete adjacent to the loading point created instability and significant sliding leading to failure. It should be noticed that there were multiple shear cracks in addition to multiple flexural cracks, in turn, means that larger area of the beam contributed to resist stresses. As can be seen in Figure 5.37 (c), steel fibers were pulled-out such that the end-hooked shape became straight, this mechanism could contribute to energy dissipation. In addition, the bridge effect could contribute to delay the propagation of the crack. Similar to the 1 – SFRPC and 2 – SFPRC#1, the sliding between two cracked surfaced was observed after the crushing of concrete as shown in Figure 5.37 (d).

5.2.5.2 Strains Measured in Reinforcing Bars

Strains measured in the tensile mild steel bars are showed in Figure 5.38. The strain gauge number S#1 was located in middle of the short shear span and the strain gauges number S#5 and S#6 were installed under the loading point. Similar to the previous beams, the strains from S#1 showed no significant change when multiple flexural cracks developed as oppose to S#5 and S#6, however the strains showed significant increment around 120 kips, where approximately the web shear occurred.

Strains from S#5 and S#6 at the ultimate stage were less than yield strain indicating that there were no ruptures from the longitudinal reinforcement. Two strain gauges, S#3 and S#4, were installed in the compression reinforcement. Figure 5.39 shows strain changes in the compression reinforcement at various loading stage. The strain from S#3 was dropped at 175 kips, but it was fluctuated around 120 kips. This strain profile was similar to the previous beams. At the ultimate, the strains from S#3 and S#4 were -100×10^{-6}, and -1500×10^{-6} respectively. Two concrete strain gauges were embedded in the concrete right above the compression reinforcement. The strains are shown in Figure 5.40. For some reasons, the strain increased in tension up to 125 kips, and then the strain reversed to compression until the ultimate stage. Nevertheless, it should be noted that the strain fluctuation in compression zone was observed after the shear crack occurred. At this point of view, the strain profiles had agreement with the previous beams. The strains were -700×10^{-6} and -200×10^{-6} for C#1 and C#2 respectively.

5.2.5.3 Concrete Surface Strains

Concrete surface strain gauges were installed in the short shear span A total of thirteen strain gauges were attached to the concrete surface, the information of the locations of these are provided in Chapter 3. Figure 5.41 and 5.42 show the strains recorded from concrete surface strain gauges. C.S#1 was placed vertically under the loading point and C.S.#2 was placed horizontally. The strain from C.S.#1 was tensile throughout the test. On the other hand, C.S.#2 was in compression. C.S.#2 showed that the rate of strain increased after 75 kips, reaching -1400×10^{-6} prior to fail. It seems that

the strains were affected by the flexural bending stress. The strains from C.S.#3, C.S#4, and C.S.#5 are shown in Figure 5.41 (b). All strain gauges showed compression when the load increased. It can be seen that the strain above the shear crack was higher than the strain of the one below the crack, i.e., strains in C.S.#3, located close to the loading point, showed relatively higher strains than the C.S.#4 and C.S.#5. At the ultimate stage, the strains from C.S.#3, C.S.#4, and C.S.#5 reached -1900×10^{-6}, -1000×10^{-6}, and -700×10^{-6}, respectively. Another set of concrete surface strain gages including C.S#6, C.S.#7, and C.S.#8 are shown in Figure 5.42 (a). Similar to the previous set of strain gauges, the strain showed compression and the strains above the shear crack was relatively higher than the strain below the crack. It is interesting to note that the strains from C.S.#6 showed a sudden incremental jump at 120 kips, at the point in which the first shear crack occurred. It can be said that the load was transferring through a direct strut such that the compressive strut took stress right after the first web shear crack was developed. At the ultimate stage C.S#6, C.S#7, and C.S#8 reached strain values of -950×10^{-6}, -200×10^{-6}, and -80×10^{-6}, respectively. The next set of concrete surface strain gauges including C.S.#9, C.S.#10, and C.S.#11 are presented in Figure 5.42 (b). All of the strain gauges were in compression up to 120 kips, but C.S.#11 suddenly switched to tension at 120 kips, C.S. #11 was located below the shear crack. However, C.S.#9 and C.S.#10 were in compression until the ultimate stage and reached strain values of -300×10^{-6} and -650×10^{-6}, respectively. It should be noted that the strains from C.S#9 and C.S.#10 increased after 120 kips similar to C.S.#6. The strain from C.S.#10 was higher than C.S.#9. At the ultimate stage, the strains from C.S#9, C.S.#10, and C.S.#11

reached -300 x10^{-6}, -650 x10^{-6}, and 100 x10^{-6} respectively. The last set of concrete surface strain gages included C.S#12 and C.S.#13 and are shown in Figure 5.43. Two strain gauges showed a similar pattern indicating sudden jumps in the strain around 120 kips. At the ultimate stage, the strains from C.S.#12 and C.S.#13 reached -250 x10^{-6} and -400 x10^{-6}. By observation of concrete surface strains, 2 – SFRPC#2 beam also showed again that load was transferring through a direct strut, which lie from loading point to the support, i.e., located above the shear cracks. It should be mentioned that strain profiles in 2 – SFRPC#2 showed similar to 2 – SFRPC#1 even though it contained less amount of steel fibers.

5.2.6 Beam 2 - SFRPC#3

5.2.6.1 Load versus Deflection Response, Crack Pattern, Failure Mode

2 – SFRPC#3 beam had the identical geometries with 2 – PC#3, but contained steel fibers (V_f = 0.75%). The graph displaying the load versus deflection response is presented in Figure 5.44. The first visible crack occurred at 80 kips in the form of a flexural crack under the loading point. The first visible shear crack occurred at 150 kips, which corresponds to a shear force of 84 kips. The shear crack was in the form of web shear crack. The stiffness of the beam decreased when the first flexural and shear cracks occurred, respectively. The ultimate load was 230 kips, which corresponds to a shear force and normalized shear strength of 129 kips and $5.26\sqrt{f'_c}$, respectively. The deflection at the ultimate stage was 0.534 in. The crack patterns at the various loading stages until failure are shown in Figure 5.45. After the first visible flexural crack at 80

kips, multiple flexural cracks occurred until the load reached 140 kips. At a load of 150 kips, which means the normalized shear strength was $3.47\sqrt{f'_c}$, the first shear crack occurred in the form of a web shear crack. At 170 kips, the first web shear crack propagated toward the loading point and the bottom portion of the crack connected with the flexural crack. While the load increased, the existing cracks propagated and multiple cracks developed. At the final stage, concrete crushing occurred adjacent to the loading point and the crushed part connected to the critical shear crack, which was also observed previous SFRPC beams. After crushing, significant sliding and instability of the beam led to failure as shown in Figure 5.46. All SFPRC beams in the second phase study had an equivalent failure mode

5.2.6.2 Strains Measured in Reinforcing Bars

The strains in the tensile mild steel bars are shown in Figure 5.47. The strain gauges, S#1 and S#2 were installed in the middle of the short shear span and S#5 and S#6 were installed under the loading point. S#1 and S#2 showed a similar pattern with the previous SFRPC beams; initially a linear increase in strain and then the strain suddenly increased at 145 kips. Based on the previous strain profiles in the location, there was a possibility that the shear crack occurred around 145 kips; the loading increment was 10 kips and the shear crack might initiate at the middle of the increment. At 170 kips, the strain from S#2 showed sudden increase. At the ultimate stage S#1 and S#2 reached strains of 1500×10^{-6} and 1250×10^{-6} respectively, which are less than the yield strain of the rebar, 2000×10^{-6}. The strains for S#5 and S#6 showed a similar

pattern until the load reached 80 kips. After the loading stage in which the first visible flexural crack occurred, the rate of strain increased. At the ultimate stage, S#5 and S#6 reached 2125×10^{-6} and 1625×10^{-6}. All of the strains for the tensile mild steel rebars were less than or right above the yield strain of the rebar (2000×10^{-6}). Two strain gauges, S#3 and S#4, were installed on the compressive reinforcements, but S#3 malfunctioned during the test leaving only the strain from S#4, as shown in Figure 5.48. The strain increased until the load reached 150 kips in compression, but the strain was reversed, and at the failure stage, the strain showed sudden increase in compression when the first shear crack occurred, which was also observed in the previous beams. That could confirm that the load transfer mechanism was changed at this moment. At the ultimate stage, the strain reached -650×10^{-6}. Two concrete embedded strain gages, C#1 and C#2, were installed right above the compressive reinforcement. The strains are shown in Figure 5.49. These strains are practically identical and increased linearly prior to the failure C#1 and C#2 reached strains of -900×10^{-6} and -1100×10^{-6} at the ultimate.

5.2.6.3 Concrete Surface Strains

Concrete surface strain gauges were installed in the short shear span. Figure 5.50 and 5.51 show graphs of the load versus concrete surface strains. C.S#1 was placed vertically under the loading point enabling the measurement of strain in the vertical direction. C.S#2 and C.S#3 were placed horizontally. The strain measured by C.S#1 showed a typical stair shape in strain diagram with the different loading increments. The compressive strain increased prior to a load of 180 kips and then reversed up to failure.

It should be noted that there might be an indication of concrete crushing even though it was not observed visually, the surface of concrete under loading point was spalled and broken off, in turn, the direction of strain reversed. The strains measured by C.S#2 and C.S#3 were compressive and C.S.#2 showed a higher strain than C.S.#3. In the case of C.S.#3 there was a similar strain increment pattern to C.S.#1; the strain from C.S.#3 was also reversed until load of 180 kips, this is due to the fact that the concrete crushing occurred in the vicinity of C.S.#1 and C.S.#3. At 180 kips C.S#1 and C.S#3 reached strain of $-1000\text{x}10^{-6}$ and $-700\text{x}10^{-6}$ respectively. For C.S.#2 the strain was $-1400\text{x}10^{-6}$ at the failure stage. The strains measured by the second set of the concrete surface strain gauges, which consisted of C.S#4, C.S#5, and C.S#6, are presented in Figure 5.50 (b). It can be seen that the strains from all strain gauges in the second set showing compression almost equivalent prior to a load of 170 kips. However, the strain from C.S#4 showed a sudden change to tensile strain. The strains from C.S#5 and C.S#6 attained were $-750\text{x}10^{-6}$ and $-500\text{x}10^{-6}$ at the failure stage. The strains measured by C.S#7, C.S#8, and C.S#9, which were grouped in the third set, are shown in Figure 5.51 (a). The strain from C.S#7 showed a sudden jump in tension after 190 kips. The inclined shear crack propagated underneath where C.S#7 was installed. Similar to C.S#4, it was possible that the opening of the crack affected the value of the strain from C.S#7, meaning the strain from C.S#7 might only be valid until 190 kips of the applied load. However, it should be noted that the C.S#7 strain gage showed the highest compressive strain in the third set at 190 kips the strain being $-250\text{x}10^{-6}$, and rest of the values of strain were close to zero. This could be evidence that the load transferred a direct strut,

which might be lying above the shear crack since other section below the shear crack was not able to contribute load resistance. At the ultimate stage, the strain from C.S#8 was close to zero and the strain from C.S#9 was -250×10^{-6}. The strain gauges C.S#10, C.S.#11 and C.S.#12 were grouped as the fourth set, as shown in Figure 5.51 (b). All strains in the fourth set were registered in compression while the load was applied. The straining rate in C.S#10 was higher than that of C.S#11 and C.S#12. The compressive strain measured by C.S.#10 increased until the applied load reached 200 kips and then, it was fluctuated. The strains from C.S#11 increased until 200 kips and then data fluctuated beyond the load, similar to C.S#10. The strain from C.S#12 increased in compression up to 125 kips, and then consistently decreased until the ultimate stage. In this concrete surface strain gauge set, the strain pattern, such as showing higher strain above the shear crack, was appeared as well. The last set of concrete surface strain gages are shown in Figure 5.52. Up to 170 kips, all strain gauges in the fifth set showed a linear trend in compression similar to the previous sets. C.S#13 and C.S#14 showed sudden jumps in strain, in contrast, the strain measured by C.S#15 were in tension. The strain measured by the concrete surface strain gauges showed a higher compressive strain in the upper portion of the web shear cracks.

5.3 The Third Phase Experiments

For further investigations of the shear behavior of SFRPC beams, the third phase of the experimental program was proposed. In the third phase study, five specimens, which had identical geometrical properties to the beams in the second phase, were

prepared and tested. 3 – PC#1 beam was prepared for comparison purposed with the SFPRC beams, and two SFRPC beams, 3 – SFRPC#1 and #2, were prepared with a 0.75% volume fraction of fibers; one had a 1.47% longitudinal reinforcement ratio, which was over-reinforced in flexure, and the other one had a 0.29% longitudinal reinforcement ratio. 3 – SFRPC#3 and #4 was prepared with a 0.5% volume fraction of fibers, 3 – SFRPC#4 beam was prepared with a 0.5% volume fraction of fibers and stirrups with 21 in. spacing used as shear reinforcement. The use of steel fibers and conventional stirrups as shear reinforcements simultaneously is worth investigation since steel fibers can partially replace conventional shear reinforcement in zones of high shear demand to reduce congestion. The design parameters of the specimens are listed in Table 5.1. The steel fibers used in this study were different than the one used in the second phase due to the previously mentioned fact; bundled fibers did not properly dissolved in concrete mix and even prevented uniformly distributed of the fibers. The steel fibers used in this study were discrete, had a hooked-end shape, an aspect ratio of 67 (l/d = 67, l= 2.0 in., d = 0.03 in.), and a tensile strength of 159.5 ksi. Further information on the beams and the steel fibers used in this study is referred in Chapter 3.

5.3.1 Beam 3 – PC#1

5.3.1.1 Load versus Deflection Response, Crack Pattern, Failure Mode

3 – PC#1 contained neither steel fibers nor stirrups in the short shear span. Figure 5.53 shows the load versus deflection response for 3 – PC#1 beam. The first visible flexural crack appeared at a load of 80 kips. The stiffness of the beam was

decreased slightly, and then as the load increased the first visible shear crack occurred at 100 kips load which corresponds to a normalized shear strength of $2.2\sqrt{f'_c}$ with the formation of the web shear crack. The ultimate load for 3 – PC#1 beam was 186 kips corresponding to a shear force and normalized shear strength of 105 kips and $4.1\sqrt{f'_c}$, respectively. After reaching the ultimate, the beam showed a slight hardening, and then failed in a brittle manner. The deflection of the ultimate and failure stage were 0.572 in. and 0.627 in. respectively. The crack pattern for 3 – PC#1 beam is presented in Figure 5.54. At 90 kips two flexural cracks appeared in the side surface below loading point. At 100 kips a web shear crack initiated at the middle of the beam as well as multiple flexural cracks that initiated at the bottom of the specimen. It is interesting to note that only one shear crack existed prior to the failure, unlike SFRPC beams in the previous phases, which normally contained multiple shear cracks. Prior to failure, concrete crushing to the adjacent loading point was observed. It exhibited a brittle failure and a huge part of concrete surface popped-out as shown in Figure 5.55. As can be seen in Figure 5.55 (c), the compression reinforcement buckled out of plane.

5.3.1.2 Strains Measured in Reinforcing Bars

The strains in the tensile mild steel bars are shown in Figure 5.56. Similar to the second phase, two strain gauges, S#1 and S#2, were installed under the loading point and two, S#3 and S#4, were installed in the middle of the short shear span. S#1 and S#2 showed identical strain patterns prior to the initiation of the first shear crack. S#3 and S#4 also showed identical strain patterns before the web shear crack occurred. It is clear

that the strains from S#1 and S#2 showed sudden increment jumps, S#1 had a dramatic jump at 100 kips where the web shear crack occurred. S#1, S#2, S#3, and S#4 reached strains of $2169x10^{-6}$, $2251x10^{-6}$, $2008x10^{-6}$, and $1950x10^{-6}$, respectively at failure. By observing the strains in the mild steel bars, it can be seen that they were just beyond the yield. The strains in the compression reinforcement are shown in Figure 5.57. S#5 showed a fluctuation at 100 kips, where the web shear crack occurred, but the general pattern for the strains in the compression reinforcement were similar to each other. S#5 and S#6 reached $-1800x10^{-6}$ and $-1400x10^{-6}$ respectively.

5.3.1.3 Concrete Surface Strains

Thirteen concrete surface strain gauges were installed. The concrete surface strain gauges were grouped in five sets; C.S#1, C.S#2, and C.S#3 were the first set; C.S#4, C.S#5, and C.S#6 were second set; C.S#7, C.S#8, C.S#9, and C.S#10 were the fourth set; and C.S#11, C.S#12, C.S#13 were the fifth set. Figure 5.58 and 5.59 show the strains measured by the concrete surface strain gauges. Figure 5.58 (a) shows the strains from the first set. C.S#1 and C.S#2 shows an identical strain increment rate up to 100 kips, in which the first web shear crack occurred. At 100 kips, all measured strains fluctuated. This could indicate a shifting in the load transfer mechanism as observed in the previous beams. C.S#3 reached $-170x10^{-6}$ and then the strain decreased by $-50x10^{-6}$. After the initiation of the shear crack, it is interesting that C.S#3, which was positioned below the major shear crack, showed a decrease in strain while C.S#1 and C.S#2, installed upon the shear crack, showed an increase in strain. This could be explained by

the fact that a section below the shear crack may not be able to transfer stress evenly when the stress was released, while a section above shear crack experienced a stress increase such that C.S#1 and C.S#2 were in the direct strut. At the ultimate stage, C.S#1 and C.S#2 had a strain of -670×10^{-6} and -520×10^{-6} respectively. The second set of concrete surface strain gauges are shown in Figure 5.58 (b). Similar to the first set, C.S#6, which located below the shear crack, changed from compression to tension after the initiation of the shear crack. C.S#4 and C.S#5 showed compression, however, the strains from C.S#5, installed in the vicinity of shear crack, showed almost no increase. C.S#4, installed farthest from the shear crack, showed the highest compressive strain, similar to that of C.S#1. Figure 5.59 (a) shows the strains from the third set of concrete surface strain gauges. All of the strains were practically linear up to 100 kips, and then changed their rate of increase. In the case of C.S#10, the strain gauge was in tension after 100 kips while C.S#7, C.S#8, and C.S#10 were in compression. The fourth set of concrete surface strain gauges are presented in Figure 5.59 (b). The strain increasing rates were similar for C.S#11 and C.S#12, however, after the development of the first shear crack, the increasing rate for C.S#11 was higher than C.S#12. C.S#13, presented in Figure 5.60, was in tension after 120 kips, where the cracks initiated adjacent to the longitudinal reinforcement. It could be said that the de-bonding crack occurred under the location of the strain gages allowing the crack opening to affect the strain reading from C.S#13. It should be mentioned that the strain recorded from the strain gauges located below the shear crack were tension, or small values of compression, while the strain recorded from the strain gages installed above shear crack were compression and

increased until the ultimate stage, which was observed PC and SFRPC beams in the second phase study as well. By observing the strain from the concrete surface strain gauges installed at various locations, the compressive strut was placed above the shear crack.

5.3.2 Beam 3 – SFRPC#1

The 3 – SFRPC #1 beam was prepared and compared with its counterpart in the second and the third phases. The beam contained a 0.75% volume fraction of steel fibers.

5.3.2.1 Load versus Deflection Response, Crack pattern, Failure Mode

3 – SFRPC#1 beam had the identical geometries with 3 – PC#1, but it contained 0.75% volume fraction of steel fibers. The graph displayed in Figure 5.61 shows the load versus deflection response for 3 – SFRPC#1 beam. The graph is linear up to 100 kips, where the first visible flexural crack was developed. The first web shear was visible at 140 kips which is a 40% increase in applied load compared to the 3 – PC#1 beam. An applied load 140 kips corresponds to 79 kips of shear force and $3.35\sqrt{f'_c}$ of normalized shear strength. Prior to failure, the beam showed hardening behavior, and right after hardening the load dropped to 111 kips with a corresponding deflection of 0.903 in. At the peak stage, the applied load was 241 kips with a deflection of 0.673 in. It is clear that the ultimate shear strength and its ductility are considerably enhanced compared to the PC beam. It should also be noted that the 3 – SFRPC #1 beam had a

higher ultimate shear strength than 2 – SFRPC#1 (failed at 211 kips of the applied load), where the fibers were not well distributed due to failure of the glue to dissolve. It is reasonable to say that the quality control of the FRC mix is a primary factor that affects the performance of FRC beams. Figure 5.62 shows the crack patterns at the various loading stages. The first visible crack occurred at 100 kips under the loading point due to flexural bending moment. When the load reached 140 kips, the first shear crack occurred in the middle of the short shear span, and then another web shear crack developed at 160 kips. This may mean that the stress redistribution due to the fiber bridging effect existed enabling the stress redistribution; this mechanism was not available in the PC beam, i.e., a single shear crack exhibited. While the load increased, multiple cracks, both shear and flexural, developed and the existing cracks propagated toward the loading point. Beyond a certain loading stage, for example 180 kips, the rate of propagation decreased and the propagations stopped under the loading point. At 200 kips, concrete crushing was observed and at failure there was crushing of the compression zone and splitting along the compressive struts causing instability and ultimately led to failure. The failure mode was similar to the previous SFRPC beams. However, unlikely the 3 – PC#1, no part of the concrete popped out, which was due to the steel fibers holding the concrete together (see Figure 5.63).

5.3.2.2 Strains Measured in Reinforcing Bars

The graphs in Figure 5.54 and Figure 5.65 show the strains in the tensile steel bars and compressive reinforcements respectively. Two strain gauges, S#1 and S#2, were installed in the middle of the short shear span and another two strain gauges, S#3 and S#4, were installed under the loading point. Unfortunately, one of strain gauges installed in the middle of the short shear span was malfunctioned during the fabrication. The strain registered from S#2 suddenly increased at 140 kips where the first web shear crack occurred similar to the previous beams. The increasing rate of strain in S#4 changed after 100 kips, in contrast, the strains from S#3 increased at 80 kips meaning there might be micro-cracks inside of the concrete even though the crack was not visible from outside the beam. In addition, the crack was possibly held by the steel fiber because there was no special change in the strain from S#4, thus the strain in tensile steel bars due to micro-crack could be minimized. The strains from S#2, S#3, and S#4 reached 2025×10^{-6}, 2250×10^{-6}, and 2160×10^{-6}, respectively. Similar to the previous phases, these rebars experienced yield strains, but no rupture. Compared to PC#1, the strains were slightly higher due to a higher applied load. For strains in compression reinforcement as shown in Figure 5.65, the strain from S#5 fluctuated at the beginning of test and then became stable. Beyond 25 kips, the strains from both strain gauges became similar. Around 220 kips, the rates of strain increased when concrete crushing was observed. The strains from S#5 and S#6 reached -1700×10^{-6} and -2000×10^{-6}. It should be mentioned that the stress states was biaxial rather than uniaxial; horizontal compression due to flexural bending and vertical compression due to the applied load.

5.3.2.3 Concrete Surface Strains

Similar to the 3 – PC#1, in 3 – SFRPC#1, twelve concrete surface strain gauges were used. The first set, including C.S#1 and C.S#2, is shown in Figure 5.66 (a). Both of the gauges the compressive strain increased continuously, however the rate of the strain increment for C.S#1 was slightly higher than that of C.S#2. Prior to failure, the strains reached -2125×10^{-6} and -1083×10^{-6} for C.S#1 and C.S#2, respectively. The second of concrete surface strain gauges is displayed in Figure 5.66 (b). C.S#4 showed the compressive strain and the rate of the strain increment increased after 140 kips. The strain from C.S#5 increased in compression up to 100 kips and then barely changed; the change was less than -100×10^{-6} prior to failure. It should be noted that the shear crack was located right above C.S#5. The strain from C.S#6, which showed compressive strain, turned to tension from 100 kips. Similar to the previous test results, the measured strains from the strain gauges installed below a shear crack turned into tension after the shear crack developed, and strains from strain gauges installed above the shear crack showed relatively higher compressive strain. Figure 5.67 (a) shows the strains from C.S#8 to C.S#10. It should be noted that the primary shear crack occurred below C.S#7, C.S#8, and C.S#9 but above C.S#10. The strain from C.S#7 increased continuously up to failure. C.S#8 showed a lower rate of strain increase than C.S#7 before the first flexural crack occurred. The strain from C.S#9 was compressive up to 180 kips and then the strain turned tensile. A crack propagated under C.S#9, which could have possibly affected the strain data. The last set of concrete surface strain gauges is shown in Figure 5.67 (b). The strains were almost linear up to 180 kips.

However, the strain from C.S#13 turned tensile rapidly. The concrete surface strain gauges showed a general pattern with previous test results; higher strains were recorded above and close to a major shear crack and the strains measured below the major shear were either small compressive values or tensile. That possibly indicates that all SFRPC beams had similar load transfer mechanism; the load was transferred from the loading point to the support directly through the strut.

5.3.3 Beam 3 – SFRPC#2

5.3.3.1 Load versus Deflection Response, Crack pattern, Failure Mode

3 – SFRPC#2 had the identical geometries and amount of steel fibers (V_f = 0.75%) with 3 – SFRPC#1, however, it had 0.29% of longitudinal reinforcement ratio including prestressing strands. Figure 5.68 shows the load versus deflection response for 3 – SFRPC#2 beam. The graph shows the typical flexural behavior of a beam rather than the shear behavior; linearly elastic up to the first flexural crack and strain hardening behavior prior to failure. The first visible flexural crack occurred at 90 kips, and the first shear crack occurred at 120 kips in the form of a flexural – shear crack. After reaching 165 kips, strain – hardening behavior was exhibited. While the deflection increased, the load dropped slightly and the test was controlled by deflection after this point. Prior to failure, the applied load was right below 160 kip and the deflection reached 2.23 in. Figure 5.69 shows the crack pattern at the various loading stages. The first flexural crack occurred under the loading point and multiple flexural cracks developed while the applied load increased. At 120 kips, a couple of flexural cracks

changed propagation angle to where they were close to 45°, which means that the flexural cracks became flexural – shear cracks. While the load increased, multiple cracks generated and propagated vertically toward the loading point. However, after 150 kips, there was no significant change in the crack pattern. A huge deflected in the beam was recognized visually during the test. Prior to failure, concrete crushing under loading point was observed due to a high compressive stress. At the failure stage, the sound of rupturing longitudinal reinforcements was heard, but it was not possible to recognize whether the sound was from the mild steel rebars or prestressing strands. At that moment, the test was stopped due to safety issues. As can be seen in Figure 5.70, the beam showed a clear flexural failure mode.

5.3.3.2 Strains Measured in Reinforcing Bars

The graph in Figure 5.71 shows the strain in the tensile mild steel rebars. There were two strain gauges, S#1 and S#2 in the middle of the short shear span, but unfortunately, one of strain gauges was broken meaning the data from this strain gauge, S#2, was not available. The strains from S#3 and S#4 showed identical strain patterns prior to failure. The strains were linear up to 100 kips and then its slope was changed. In the case of S#3, the strains reached 5000×10^{-6}, then fluctuated, and suddenly jumped to 16000×10^{-6}. ASTM A615 (*Standard Specification for Deformed and Plain Carbon-Steel Bars for Concrete Reinforcement*, 2009) specifies the mechanical properties of steel rebar, the minimum elongation of No. 8 rebar used in this study for tensile mild steel bars should be larger than 8 in. with a gage length of 8 in. that corresponds to

$10000x10^{-6}$ (1%). S#3 indicated the strain as $16000x10^{-6}$ (1.6%), was much larger than the rupturing strain. The strain fluctuation in S#3 could be explained by the fact that the rebar might be ruptured at the ultimate stage, in turn the strain was lost. By observing the strain profiles in the mild steel rebars, the failure of the beams was due to flexure unlike the other beams in this experiment. Two strain gauges, S#5 and S#6, were installed on the compressive reinforcements. The strains measured by the two strain gauges showed an identical profile prior to 125 kips, the strains indicated compression in the rebars. The strains reached approximately $-500x10^{-6}$ and then slowly changed to tension. By the time the peak load was reached, the strains measured by S#5 reached $-13000x10^{-6}$ and then dropped to tension.

5.3.3.3 Concrete Surface Strains

For comparison purposes, thirteen concrete surface strain gauges were installed in the same manner as the other beams in this experiment. The locations and grouping of the strain gauges were identical to 3 – SFRPC #1. The strain profiles for the first set, C.S#1, C.S#2, and C.S#3, are shown in Figure 5.73 (a). The strains from C.S#1 and C.S#2 had a larger strain increase rate than that of C.S#3. The strains measured in C.S#1 and C.S#2 indicated that the surface strain of the concrete increased almost linearly prior to failure and then showed a hardening profile. By the time the peak load was reached C.S#1 and C.S#2 indicated strains of $-950x10^{-6}$ and $-1220x10^{-6}$, respectively. The hardening behavior of surface strains in the compression zone could be explained as a ductile behavior of concrete due to the inclusion of steel fibers. The

strain measured by C.S#3, located below a major shear crack, registered in compression up to 125 kips, and then the surface strain indicated tension. The strain profile from C.S#3 is similar to 3 – SFRPC#1 where surface strains below a major shear crack were tensile after the shear crack developed. However, it is partially true because other strain gauges located below the major shear crack indicated compression meaning the beam action was not completely broken down. C.S#4, C.S#5, and C.S#6 are in the second set of concrete surface strain gauges and are shown in Figure 5.73 (b). Prior to 105 kips, all were in compression. The strain measured by C.S#4 increased continuously up to the failure point even although it fluctuated prior to failure. In the case of C.S#5, the strain decreased slightly after 105 kips and then increased prior to failure, reaching a strain of $-114x10^{-6}$. C.S#6 showed a rapid strain increase at 105 kips even though this sudden jump was not reflected by any visible physical damage. After the considerable jump, there was no significant strain change until the applied load reached the peak value. As the peak load was obtained, the strain measured by C.S#6 increased continuously without an increase in the load, attaining a maximum strain of $-285x10^{-6}$. This could be associated with the overall beam behavior. In the previous beams, concrete surface strains, which were located below a primary shear crack, were in tension, but in 3 – SFRPC#2 beam the surface strains below a major shear crack remained in compression. This could be definite evidence such that the failure mechanism in 3 – SFRPC#2 was different from other SFRPC beams. The third set of concrete surface strain gages are shown in Figure 5.74 (a). All strain gauges in the third set were in compression initially except C.S#10. C.S#7 and C.S#8 had identical strain profiles until the applied load

reached 100 kips, when multiple flexural cracks developed. At this loading stage, the strain measured by C.S#7 suddenly increased, in contrast the strain measured by C.S#8 had a considerable increase at 120 kips where the first shear crack was visible. After this loading stage, there was no significant strain difference between C.S#7 and C.S#8, which reached strains of -194×10^{-6} and -185×10^{-6}, respectively. The strain measured by C.S#9 increased linearly up to 130 kips. However, prior to the peak load, there was no significant change in strain. The fluctuation of strains was exhibited and then softening behavior was shown in the displacement control stage. It is interesting to observe the strain profile for C.S#10 since it indicated a considerably high strain increase in tension between 130 and 140 kips of applied load. It located at the bottom of the beam such that it might be affected by the flexural bending stress. The fourth set of surface strain gages are shown in Figure 5.74 (b). The rate of increase of the strain C.S#11 was the highest among the strain gages in this set. The strains measured by C.S#13 did not change significantly prior to the peak load but increased in the displacement control stage. It should be noted that prior to failure, the strain from C.S#11 and C.S#12 fluctuated, while the strain from C.S#13 rose without increasing the applied load. It can be said that surface strains measured by C.S#11 and C.S#12 were governed by the shear behavior of the beam, however, the surface strains measured by C.S#13 were affected by the flexural behavior of the beam. Since the strains profiles in 3 – SFRPC#3 were different than other beams, it could be an additional evidence that 3 – SFRPC#3 failed at flexure. This flexural failure mode could be explained by the fact that the enhancement of shear strength induced by steel fibers such that it failed before reaching its shear capacity.

5.3.4 Beam 3 – SFRPC#3

5.3.4.1 Load versus Deflection Response, Crack Pattern, Failure Mode

3 – SFRPC#3 beam had the identical geometries and the longitudinal reinforcement ratio with 3 – PC#1 (V_f = 0%) and 3 – SFRPC#1 (V_f = 0.75%). However, it contained 0.50% volume fraction of steel fibers (V_f = 0.50%). It should be mentioned that the 0.50% volume fraction, which is corresponding to 67 lb per cubic yard of concrete, is less than the minimum amount of steel fibers (V_f = 0.75%, 100 lb per cubic yard of concrete) required by ACI 318-08. Figure 5.75 shows the load versus deflection response for 3 – SFRPC#3 beam. The first flexural crack was visible at 100 kips, and the first shear crack occurred at 120 kips in the form of a web shear crack. The shear force creating the first shear crack is 17% lower than 3 – SFRPC#1 (V_f = 0.75%), while that is 20% higher than 3 – PC#1 beam. Compared with 3 – SFRPC#1, the stiffness of the beam after the initiation of the web shear crack declined and its degree was rapid. In addition, the slope became non-linear when multiple cracks developed. Prior to complete failure, the beam showed slight strain hardening behavior. The peak load and deflection were 221 kips and 0.567 in., respectively. At the failure stage, the load dropped to 66% of the peak and the corresponding deflection was 0.75 in. The crack patterns are shown in Figure 5.76. Two flexural cracks were visible at 100 kips; one crack did not initiated from the bottom fiber of concrete, however, it can be said that the crack occurred due to flexure by observing the angle of the crack, which was perpendicular to the longitudinal axis. While the load increased, multiple flexural cracks generated and one of the existing flexural cracks propagated toward the loading point.

At a load of 120 kips, a web shear crack developed around one of third of the shear span from the loading point. At 130 kips, a new flexural crack generated from the bottom fiber of the concrete and connected to the existing web shear crack. As the load increased, multiple web shear and flexural cracks generated. The web shear cracks propagated toward the loading point, but the propagation of the existing flexural cracks stopped. It can be seen in Figure 5.76 that there were multiple shear cracks. It was observed in the beam with a 0.75% volume fraction of steel fibers as well, but not in the PC beams. As can be seen in Figure 5.77, prior to failure, concrete crushing was observed under loading point followed by concrete crushing and splitting of a compression strut along the shear crack leading to fail. As shown in the second phase, 3 – SFRPC#2 beam (V_f = 0.50%) showed similar behavior with SFRPC beams, which were contained 0.75% volume fraction of steel fibers.

5.3.4.2 Strains Measured in Reinforcing Bars

Two strain gauges were installed in the middle of the short shear span and under loading point. However, one of strain gauges, S#3, malfunctioned and only the strain from S#4 were available under the loading point. The strains registered in each strain gauge in the tensile mild steel rebars are shown in Figure 5.78. The strains measured by S#1 and S#2 were practically identical up to 140 kips. After 140 kips, the strain from S#1 and S#2 increased considerably, S#1 registered a slightly higher strain than S#2. At the peak, S#1 and S#2 reached 1957×10^{-6} and 1636×10^{-6}, respectively The rate of strain increase for S#4 changed right after 80 kips, however, there was no visible damage. It

might be speculated that a certain degree of damage occurred inside the concrete section, however, steel fibers played a role to constrain the damage meaning the damage was not able to progress to the surface. The slope of the strain from S#4 maintained practically constant from 80 kips to its peak. By the time the peak load was reached, S#4 showed a strain of 2276×10^{-6}.

5.3.4.3 Concrete Surface Strains

Similar to the previous beams, thirteen concrete surface strain gauges were installed in the designed locations. The strain profiles for the first set consisting of C.S#1, C.S#2, and C.S#3 are shown in Figure 5.79 (a). The strain from C.S#1 increased linearly until the ultimate load was reached, except a minor fluctuation at 170 kips. The strain dramatically increased without increasing the load such that the concrete in the compression zone experienced strain hardening, this was also observed in C.S#2 even though its portion was relatively small when compared to C.S#1. The strain from C.S#3 showed a similar strain profile to that of C.S#1 and C.S#2 up to 170 kips. At 170 kips, the curvature of the strain graph increased, and then jumped at 180 kips. The strains measured by C.S#4, C.S#5, and C.S#6 are shown in Figure 5.79 (b). The strains from C.S#4 and C.S#5 increased linearly up to 180 kip while the strain from C.S#6 barely increased. By the time the applied load reached 180 kips, the strain from C.S#4 showed a sudden increase, while the strain from C.S#5 showed that the gauge lost compressive strain. At the ultimate stage, C.S#4 had the highest compressive strain among the surface strain gages in the second set. These strain patterns are similar with 3 –

SFRPC#1. In the third set, C.S#7 and C.S #8 had an identical strain profile up to 180 kips. After 180 kips, the strain profile for C.S#7 barely changed until failure. C.S#9 showed compressive strains though the increase in strain was minor, but it lost strain and finally turned into tensile strain at 175 kips. In the case of C.S#10, the strain and was tensile from the beginning of the test and dramatically increased at 130 kips. The tensile strain continued to increase at failure. It is interesting to note that the strain measured by C.S#8 was the highest compressive strain and this was shown in 3 – SFRPC#1 as well; it is comparable since the coordinate of each strain gauge was identical. In case of the C.S#10, similar to the C.S#10 in 3 – SFRPC#1, it also might be affected by the flexural bending stress due to its location. The fourth set is shown in Figure 5.80 (b). While the applied load increased, C.S#11 and C.S #12 had compressive strains and C.S#13 had practically no strain increase. At 180 kips, all strains in the fourth set fluctuated; the strains measured by C.S#11 increased suddenly in compression up to failure, the strains measured by C.S#12 turned to tension, and C.S#13 showed sudden increase in compressive strain prior to failure. It should be noted that the overall strain profiles for the concrete surface strain gages in 3 – SFRPC#3 had similar profiles to 3 – SFRPC#1, which indicates that the load transfer mechanism was similar each other.

5.3.5 Beam 3 – SFRPC#4

5.3.5.1 Load versus Deflection Response, Crack Pattern, Failure Mode

3 – SFRPC#4 had the identical geometries and amount of steel fibers with 3 – SFRPC#3 beam. However, it contained 21 in. spacing of stirrups in the short shear span. The graph in Figure 5.81 displays the load versus deflection response curve for 3 – SFRPC#4 beam. Up to the first flexural crack, the slope was linear and then the stiffness of the beam decreased after the web shear crack occurred. While the strain increased, the applied load reached 233 kips and then dropped to 43% of its peak. The ultimate load of 233 kips is 3.4% lower than the ultimate load of the 3 – SFRPC#1 beam but 5.4% higher than the 3 – SFRPC#3 beam. The first shear crack formed as a web shear crack at 130 kips, which corresponds to 73 kips of shear force. The shear force is 8.3% larger than 3 – SFRPC#3, but 7.7% lower than the 3 – SFRPC#1. When the ultimate load was reached, the corresponding deflection was 0.605 in. that is 11.3% and 15.7% smaller than 3 – SFRPC#1 and SFRPC#3, respectively. As the beam reached the failure stage, the deflection was 1.011 in.; this is 10.8% and 34.3% larger than 3 – SFRPC#1 and SFRPC#3, respectively meaning the beam showed an enhanced ductility behavior. Consequently, 3 – SFRPC#4 beam did not exhibit better performance in terms of ultimate strength compared to 3 – SFRPC#1, but it did showed better performance in terms of ductility. Compared to 3 – PC#1 beam, the 3 – SFRPC#4 showed 25.3% and 61.2% increase in the ultimate strength and deflection, respectively. The crack pattern for 3 – SFRPC#4 beam shown in Figure 5.82 exhibited a similar pattern to that of the other SFRPC beams; multiple flexural and web shear cracks. The relatively large area

of the compression region (larger than 4 in.) was crushed and simultaneously splitting along the compressive strut leading to failure as shown in Figure 5.83. In addition, the sliding between the two cracked surfaces was shown after the crushing of concrete as shown in Figure 5.83 (d).

5.3.5.2 Strains Measured in Reinforcing Bars

The strains in the tensile mild steel rebars are shown in Figure 5.84. There were four rebar strain gauges installed originally, however, one of strain gauges, S#2, located in the middle of the short shear span was malfunctioned. S#1, located in the middle of the shear span, had a similar strain profile to the previous beams in this phase, i.e., strain linearly increased up to 130 kips where the first web shear crack occurred and then dramatically increased. The rate of strain increase of S#3 and S#4 was similar. The strains from S#3 and S#4 showed a linear increase up to the first flexural crack. After that, the strains increased gradually until the beam failed. S#1, S#3, and S#4 had strains of 1660×10^{-6}, 2416×10^{-6}, and 2171×10^{-6}, respectively. By observing the strain values, the tensile mild steel rebars yielded, but these were beyond the value for rupture. Two strain gauges, S#5 and S#6, were installed on the compression reinforcements under the loading point, and their strain profiles are presented in Figure 5.85. The compressive strains increased linearly while the load was applied. Prior to failure, strain reached -1810×10^{-6} and -1485×10^{-6} for S#5 and S#6, respectively.

Eight strain gauges were installed on the stirrups. Unfortunately, the data for four strain gauges was not available since four strain gauges malfunctioned due to careless treatment. However, each location had strain gauges in pair such that at least one strain gauge value was available in each location. The strain profiles for the strain gauges on the stirrups are shown in Figure 5.86. No strain increase was exhibited in S#8 and S#10 until the applied load reached 160 kips where the second web shear crack initiated and passed the stirrups. After 160 kips, S#8 and S#10 showed a dramatic strain increase. However, strains in S#12 and S#14 increased at right above 120 kips. By observing these strain profiles, stirrups played in a role to resist load after the shear crack passed the stirrups. While the load increased, strains from all of the strain gauges increased as well. At failure, S#8, S#10, S#12, and S#14 reached strains of $2107x10^{-6}$, $4661x10^{-6}$, $2514x10^{-6}$, $1112x10^{-6}$, respectively. It should be noted that the strain of the stirrups in 3 – SFRPC#4 beam were considerably less than the one in the 2 – PC#1, though the spacing of the stirrups in the SFRPC beam was larger than PC beam (21 in. as opposed to 14 in.); most of the strain gauges in the PC beam were above $10000x10^{-6}$. This can be evidence that the steel fibers and stirrups assisted in the resistance of shear stress, and the steel fibers prominently contributed to the shear resistance.

5.3.5.3 Concrete Surface Strains

Thirteen concrete surface strain gauges were installed. The strain profiles of the first set are shown in Figure 5.87 (a). The strains from all the strain gauges were increased while the applied load increased. The increasing rates for C.S#1 and C.S#2

were faster than that of C.S#3. It is interesting to note that the strain from C.S#2 showed strain hardening prior to failure, which means that the concrete in the compression zone showed strain hardening behavior as well by adding steel fibers, and the direction of compressive stress was horizontal rather than vertical. The other strain gauges showed similar strain profiles to that of the other SFRPC beams. It should be noted that the profiles of concrete surface strains in all SFPRC beams showed very similar pattern; strain fluctuation was exhibited after the first shear crack occurred, and strain gauges located above the shear crack showed higher value than strain gauges located below the shear crack. It could indicate that the load transfer mechanism would be changed after the initiation of the shear crack, and the load was transferred from the loading point to the support. Also the strut might located above the shear crack in the uncracked section.

Table 5.1 Design parameters

Specimen	Longitudinal reinforcement ratio	Shear span to effective depth ratio	Compressive strength (psi)	Steel fibers		
				Volume fraction	Aspect ratio	Tensile strength (ksi)
1 – PC	1.62 %	3.0	9259	-	-	-
1 – SFRPC			9100	0.75 %	82	152
2 – PC#1	1.64 %		4769	-	-	-
2 – PC#2				-	-	-
2 – PC#3				-	-	-
2 – SFRPC#1			5234	0.75 %	82	152
2 – SFRPC#2			3755	0.50 %		
2 – SFRPC#3			5234	0.75 %		
3 – PC#1	1.47 %		5772	-	-	-
3 – SFRPC#1			4884	0.75 %	67	159
3 – SFRPC#2	0.29 %					
3 – SFRPC#3	1.47 %		5276	0.50 %		
3 – SFRPC#4						

Table 5.2 Summary of key testing results in the first phase

Specimens	Load at first flexural cracking* (kips)	Load at the first Shear cracking (kips)	Ultimate load (kips)	Shear force[1] (kips)	Normalized shear strength[2] $\sqrt{f'_c}$ (psi)
1 –PC	85	110 (web shear)	146	94.9	2.47
1 – SFRPC	-[3]	170 (web shear)	327	213	5.58

[1]: Shear force = Ultimate applied load ×0.65
[2]: Normalized shear strength = $V_u/(\sqrt{f'_c}\cdot b\cdot d)$
[3]: Not recorded
*Observed; the actual first cracking could be too small to be noticed.

Table 5.3 Summary of key testing results in the second phase

Specimens	Flexural cracking load (kips)	Shear cracking load (kips)	Ultimate applied load (kips)	Shear force[1] (kips)	Normalized shear strength[2]
2 -PC#1	85	105 (flexural-shear)	225	127	5.5
2 -PC#2	60	100 (flexural-shear)	200	113	4.9
2 -PC#3	60	110 (web shear)	216	122	5.2
2 -SFRPC#1	100	140 (web shear + flexural-shear)	211	119	4.9
2 -SFRPC#2	70	120 (web shear)	199	112	5.4
2 -SFRPC#3	80	150 (web shear)	230	129	5.3

[1]: Shear force = Ultimate applied load ×0.5625
[2]: Normalized shear strength = $V_u/(\sqrt{f'_c}\cdot b\cdot d)$

Table 5.4 Summary of key result of experiment in the third phase

Specimens	Flexural cracking load (kips)	Shear cracking load (kips)	Ultimate applied load (kips)	Shear force[1] (kips)	Normalized shear strength[2]
3 -PC#1	80	100 (web shear)	186	105	4.1
3 -SFRPC#1	100	140 (web shear)	241	136	5.6
3 -SFRPC#2	95	120 (flexural shear)	165	93	3.8
3 -SFRPC#3	100	120 (web shear)	221	124	5.3
3 -SFRPC#4	90	130 (web shear)	233	131	5.4

[1]: Shear force = Ultimate applied load ×0.5625
[2]: Normalized shear strength = $V_u/(\sqrt{f'_c}\cdot b\cdot d)$

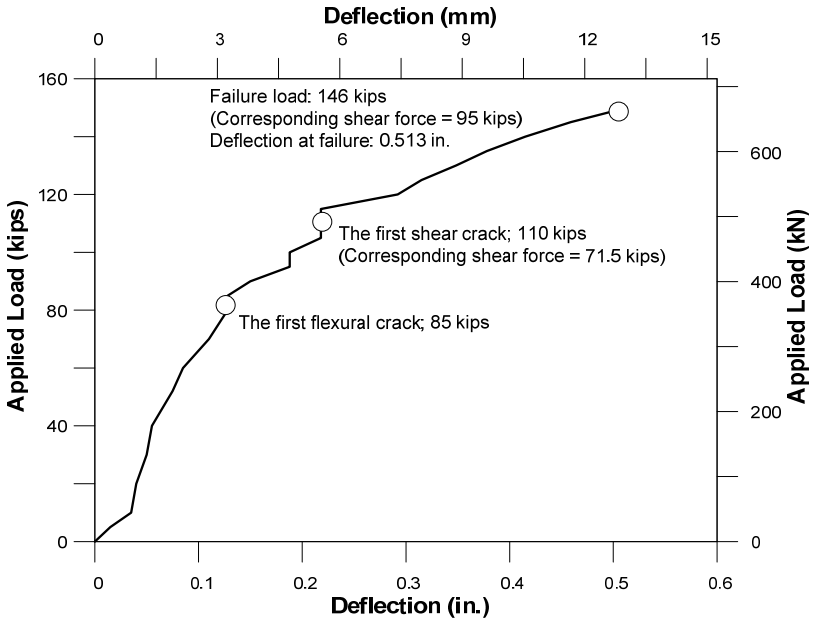

Figure 5.1 Load versus deflection response for 1 – PC

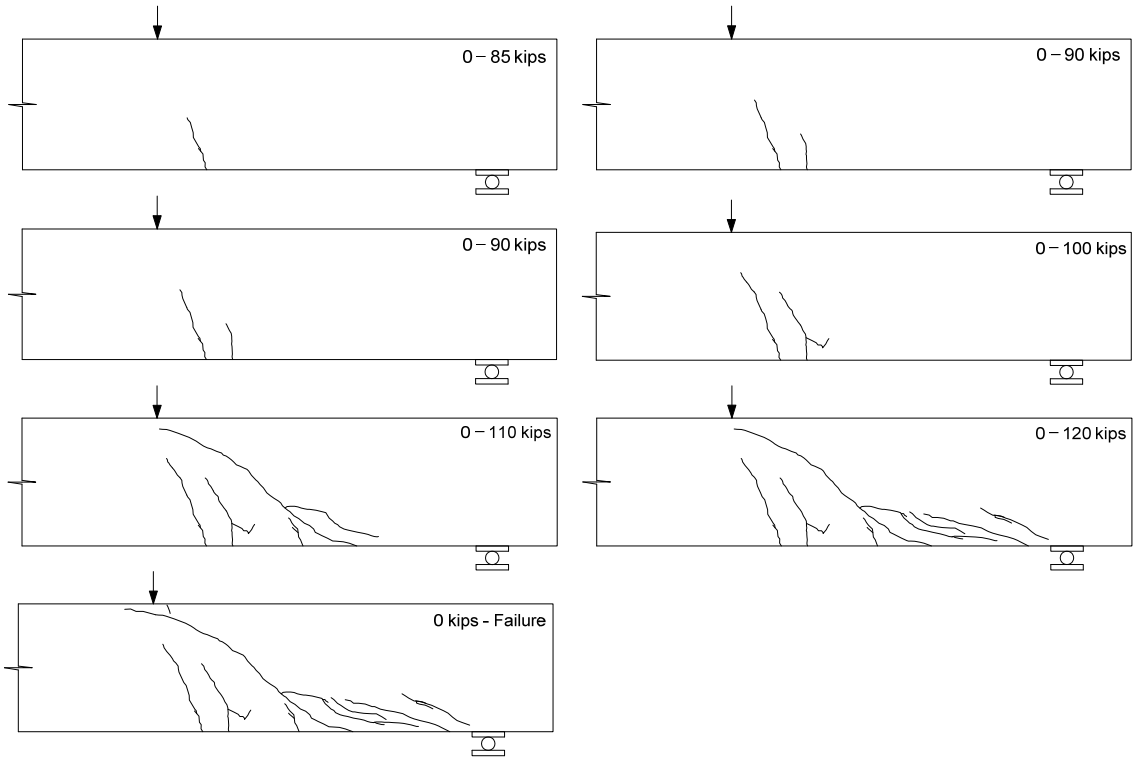

Figure 5.2 Crack pattern for 1 – PC

(a)

(b)

(c)

Figure 5.3 Typical photos during test for 1 – PC; (a) Prior to failure; (b) At failure; (c) Crushing in compression zone

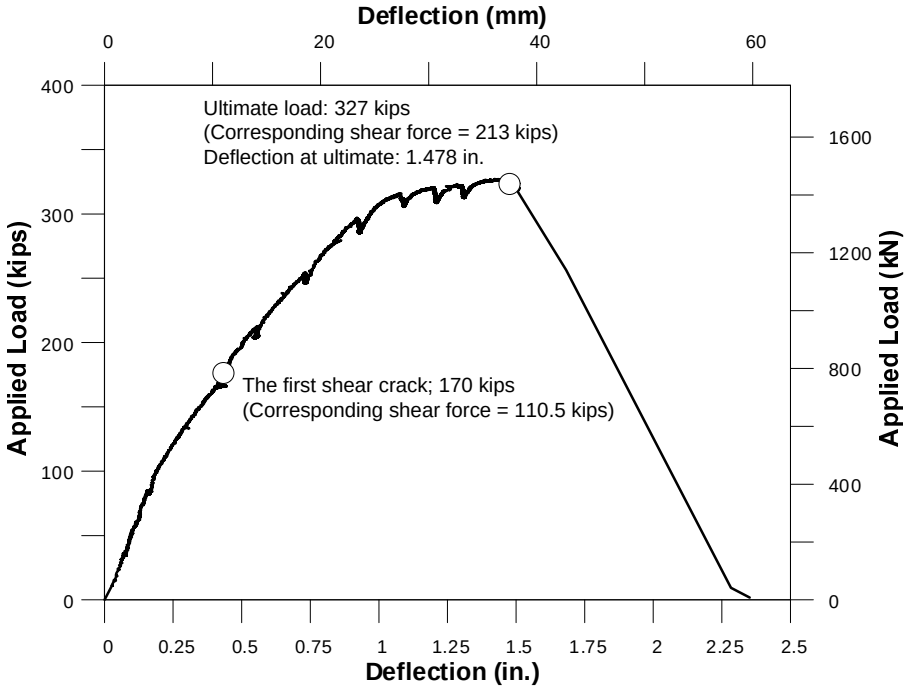

Figure 5.4 Load versus deflection response for 1 – SFRPC

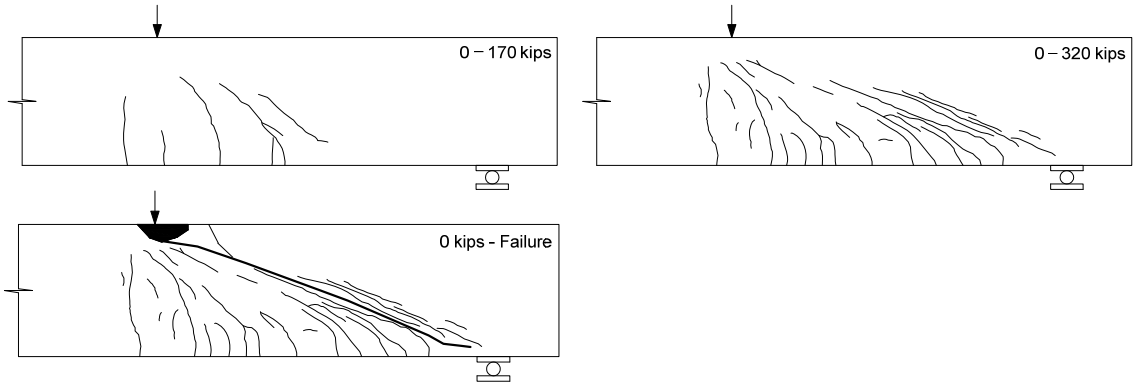

Figure 5.5 Crack pattern for 1 – SFRPC

(a)

(b)

(c)

Figure 5.6 Typical photos during test for 1 – SFRPC; (a) Prior to failure; (b) At failure; (c) Crushing in compression zone (Note that, according to the observation of the 45° read lines, the sliding between the two cracked surfaces was the consequence of the crushing of concrete)

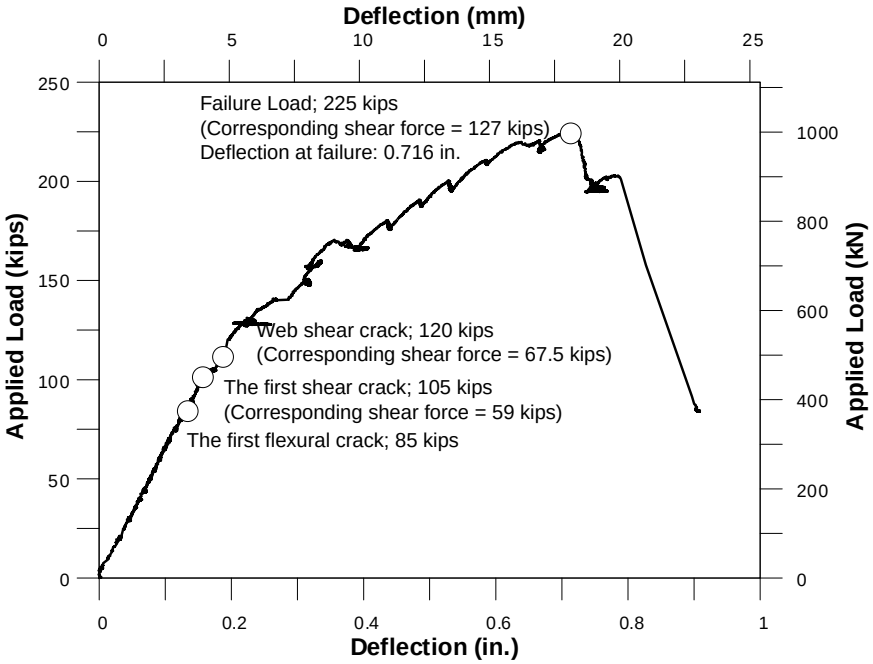

Figure 5.7 Load versus deflection response for 2 – PC#1

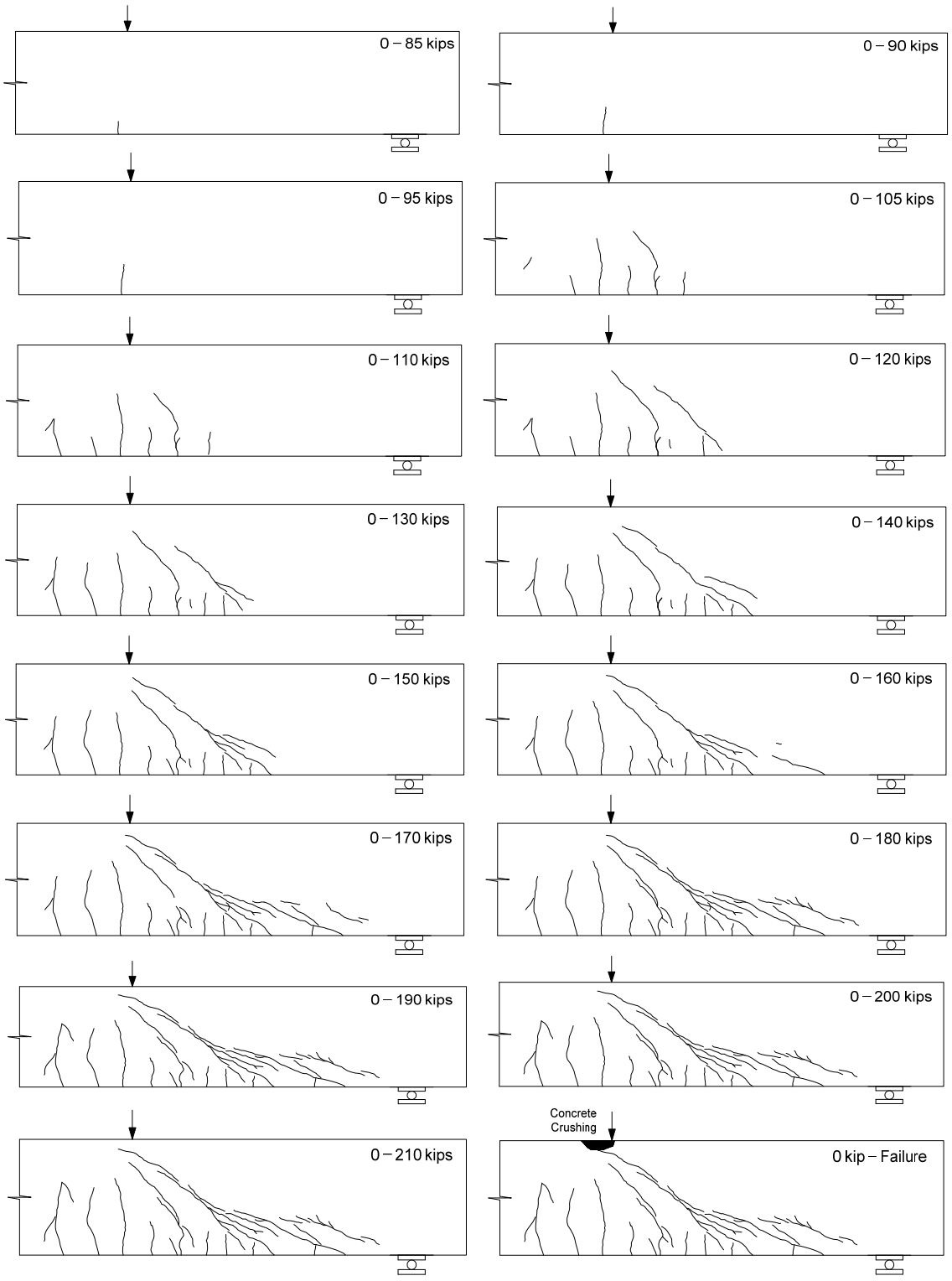

Figure 5.8 Crack pattern for 2 – PC#1

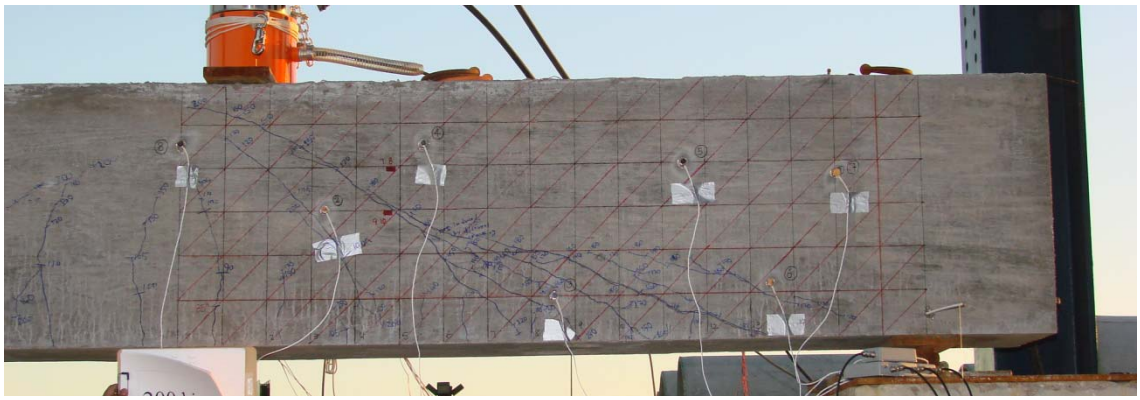

(a)

(b)

(c) (d)

Figure 5.9 Typical photos during test for 2 –PC#1; (a) Prior to failure; (b) At failure; (c) Crushing in compression zone prior to failure; (d) Crushing in compression zone after failure

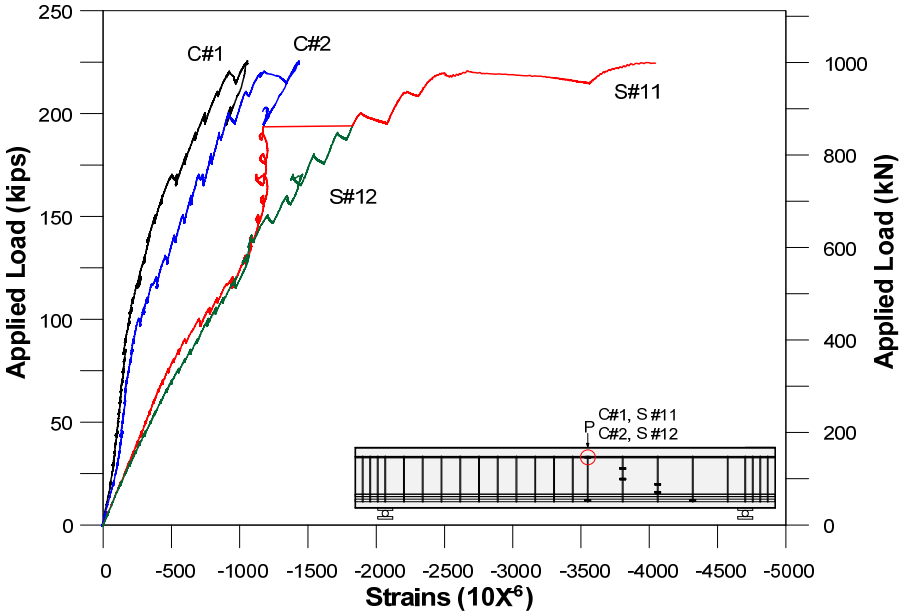

Figure 5.10 Concrete strains in compressive zone – 2 – PC#1

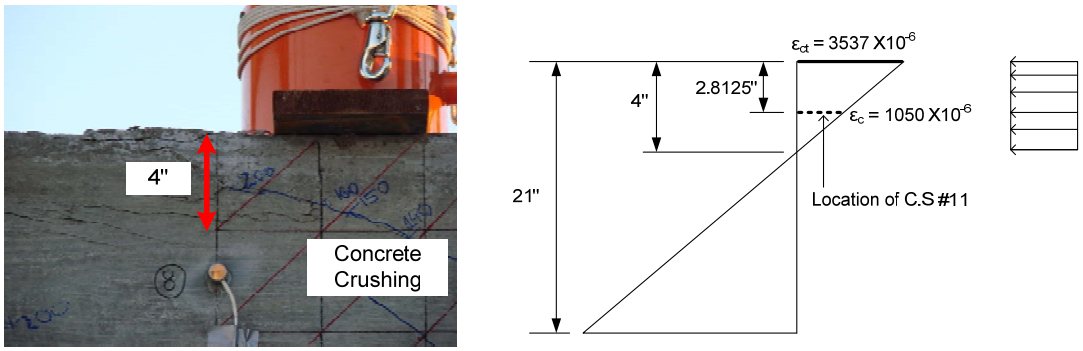

Figure 5.11 Strains in top fiber of concrete – 2 – PC#1

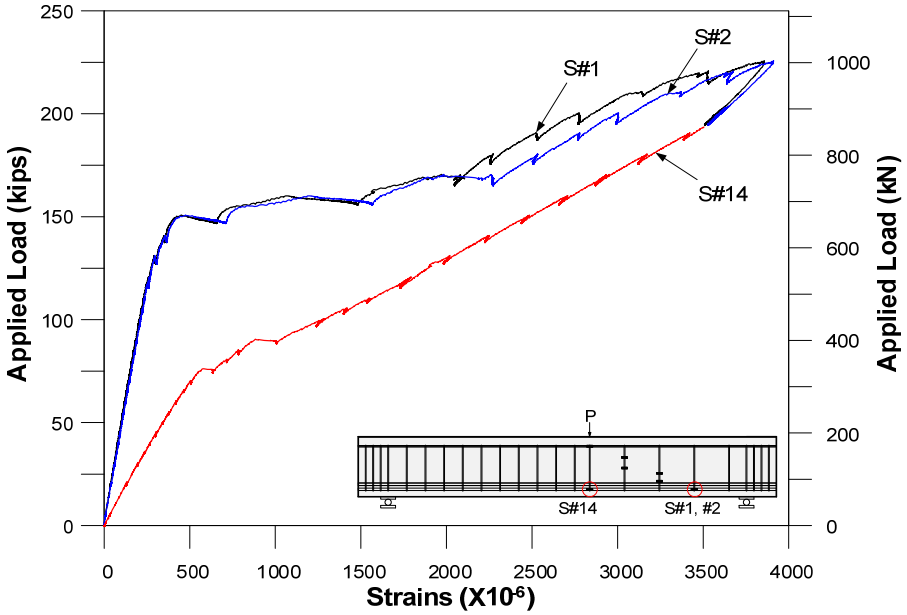

Figure 5.12 Strains in longitudinal reinforcements – 2 – PC#1

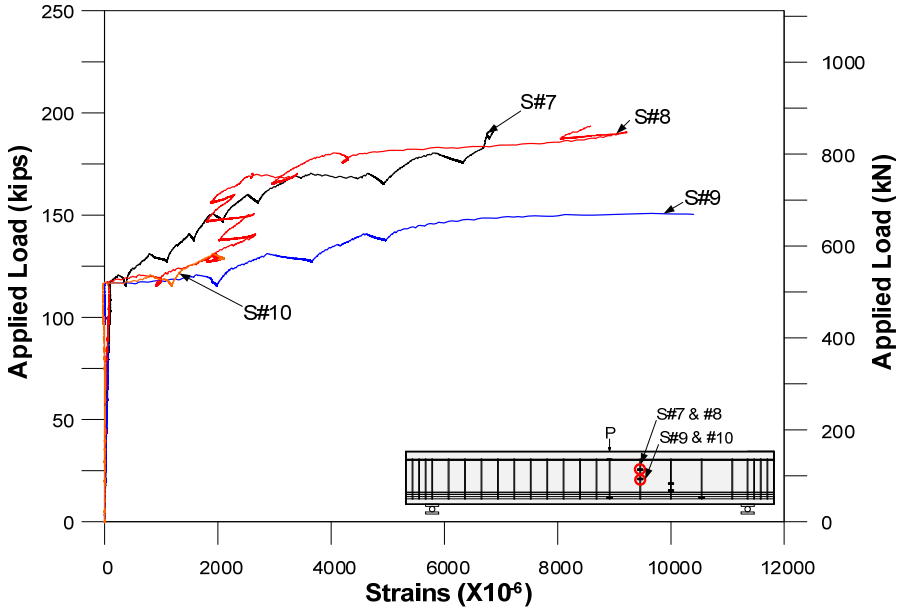

(a)

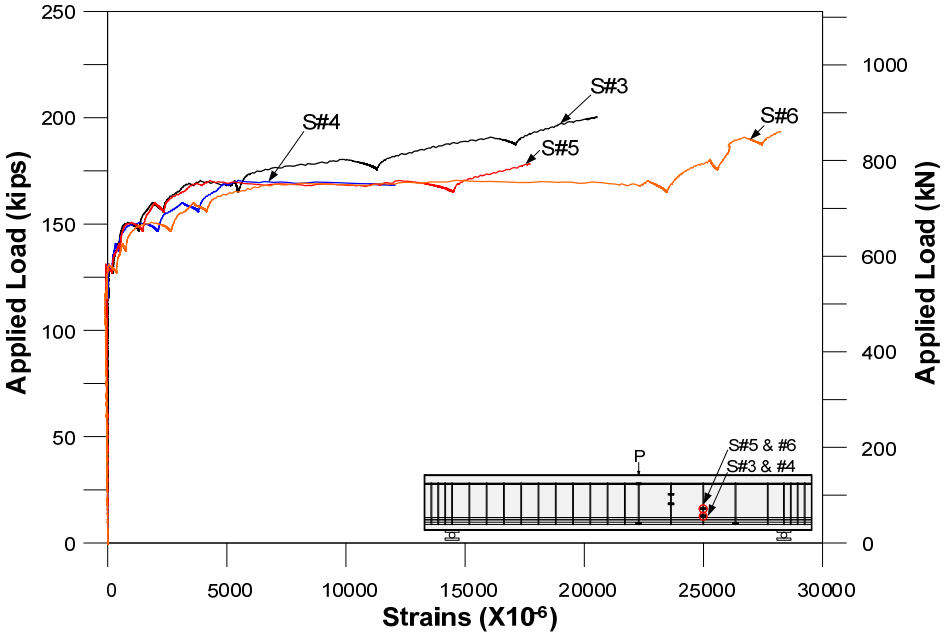

(b)

Figure 5.13 Strains in stirrups – 2 – PC#1; (a) Stirrups #1; (b) Stirrups#2

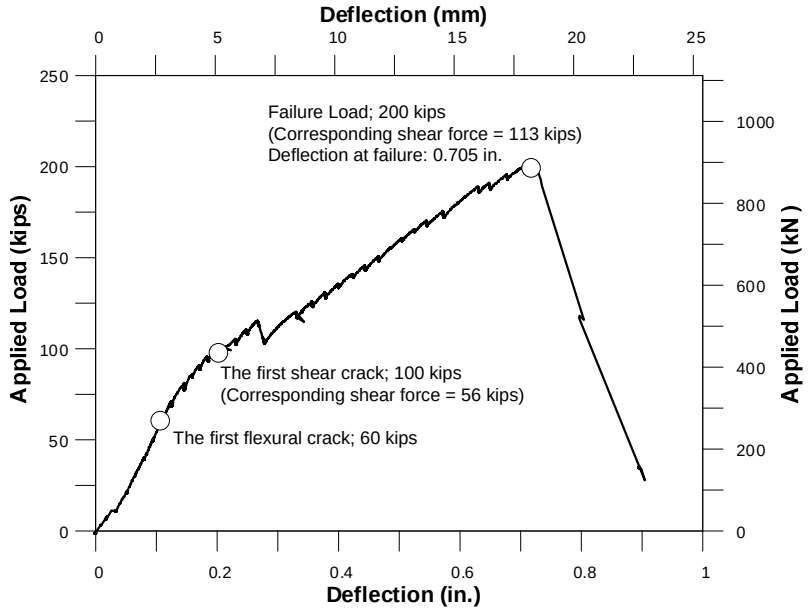

Figure 5.14 Load versus deflection response for 2 – PC#2

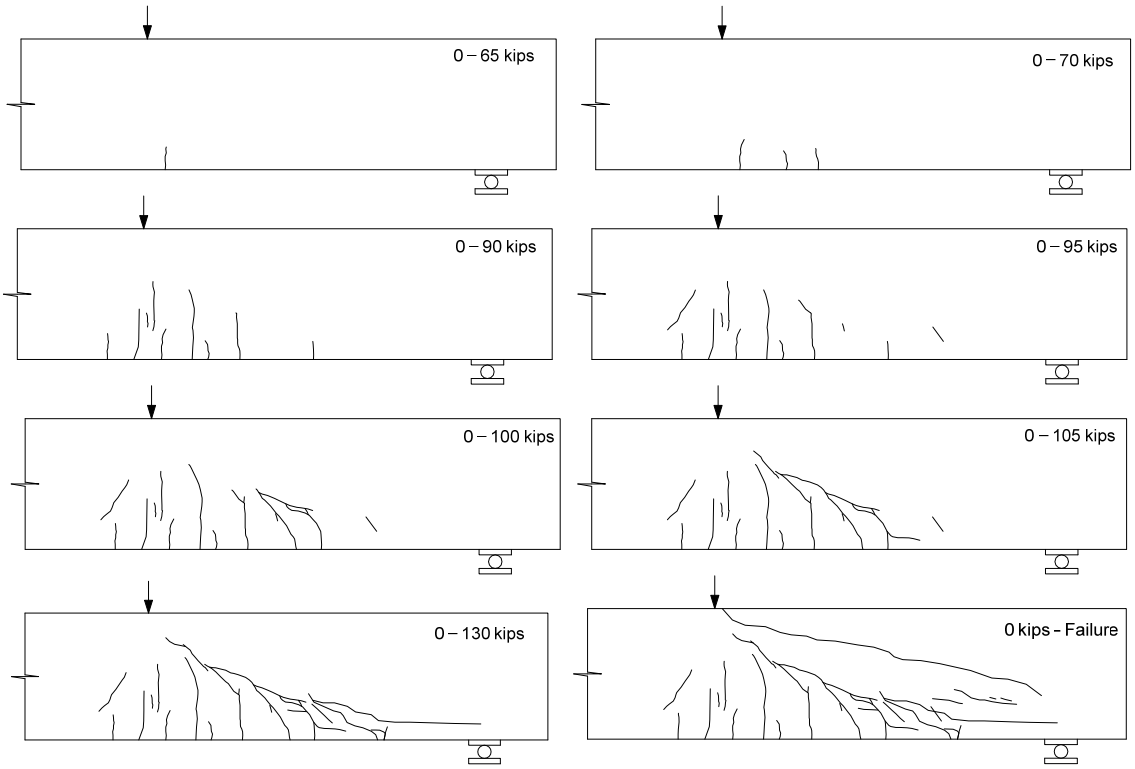

Figure 5.15 Crack pattern for 2 – PC# 2

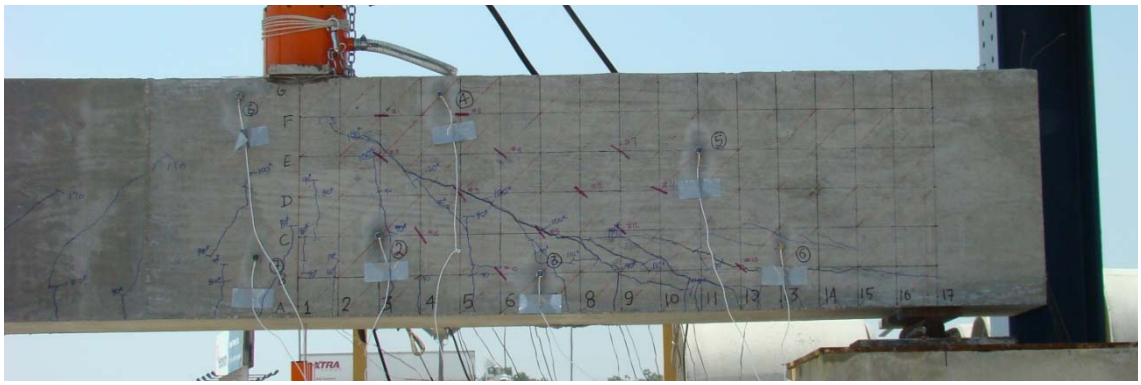

(a)

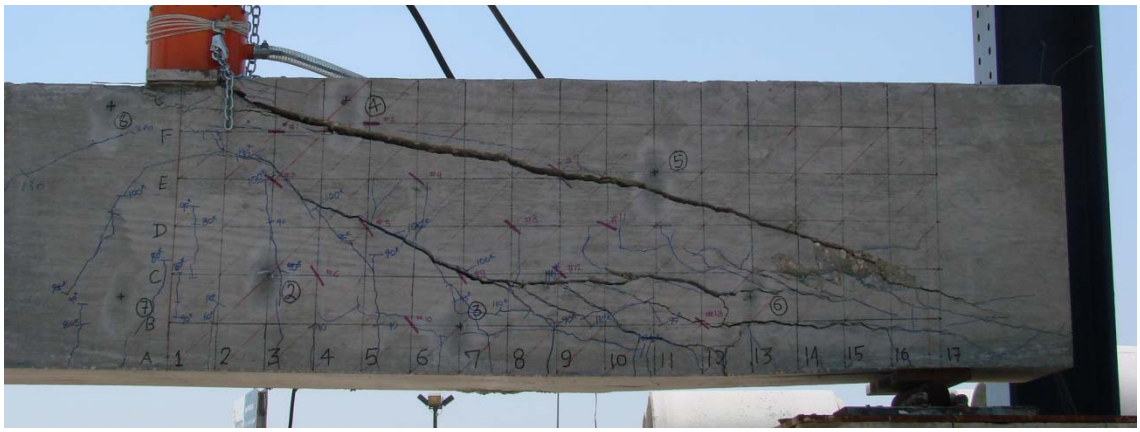

(b)

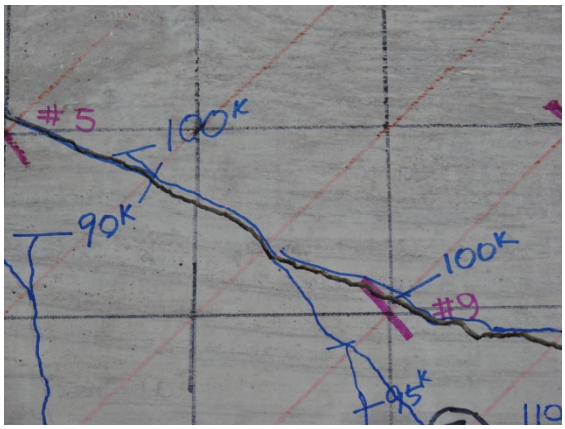

(c) (d)

Figure 5.16 Typical photos during test for 2 –PC#2; (a) Prior to failure; (b) At failure; (c) No sliding prior to failure; (d) Crushing in compression zone

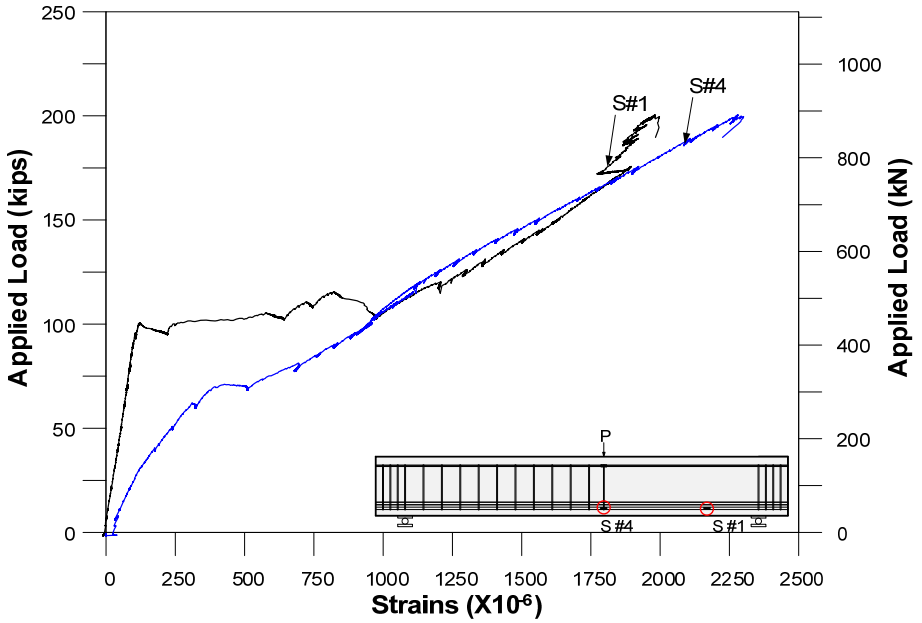

Figure 5.17 Strains in longitudinal reinforcements – 2 – PC#2

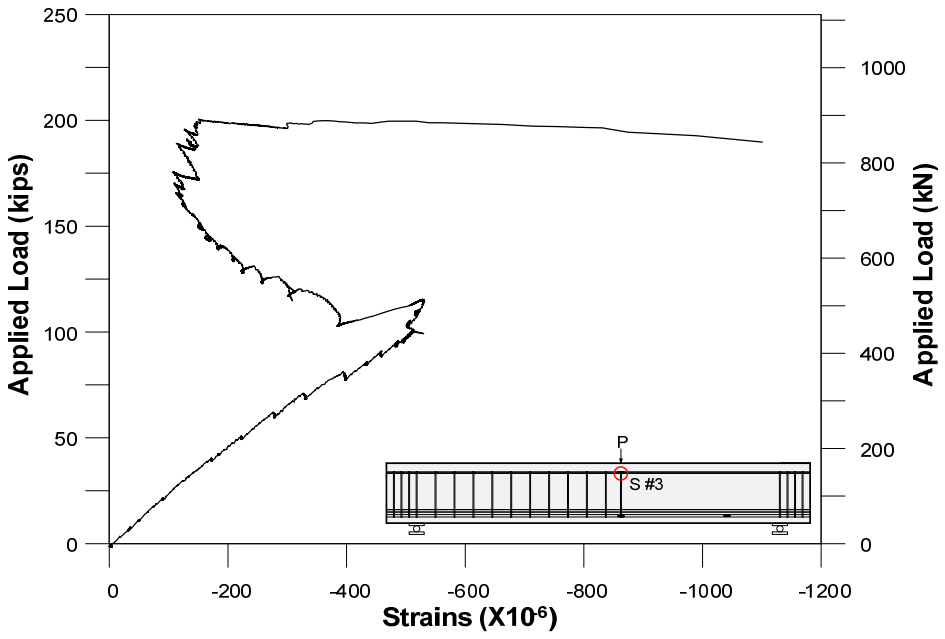

Figure 5.18 Strains in compression reinforcement – 2 – PC#2

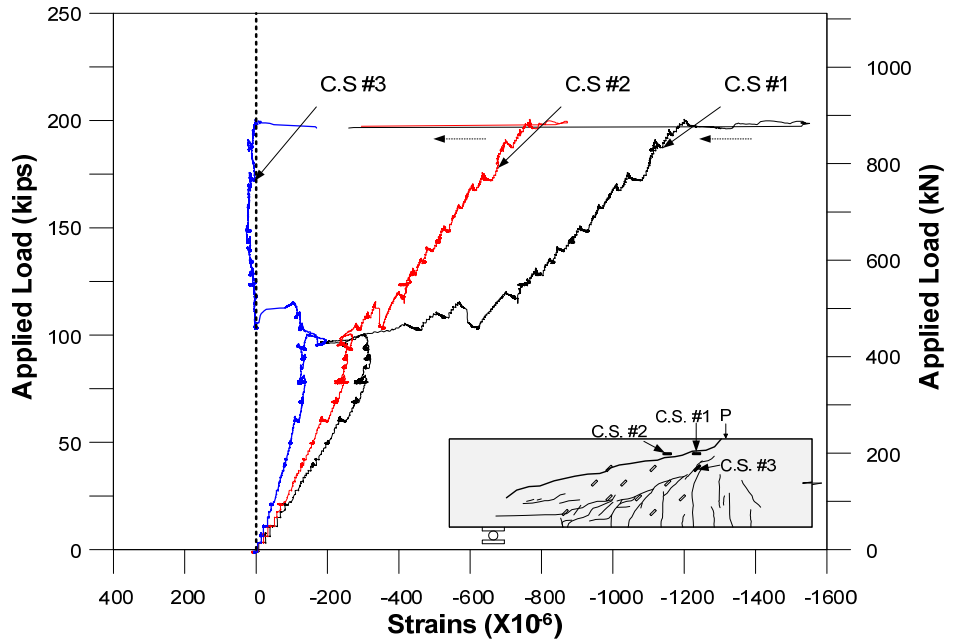

(a)

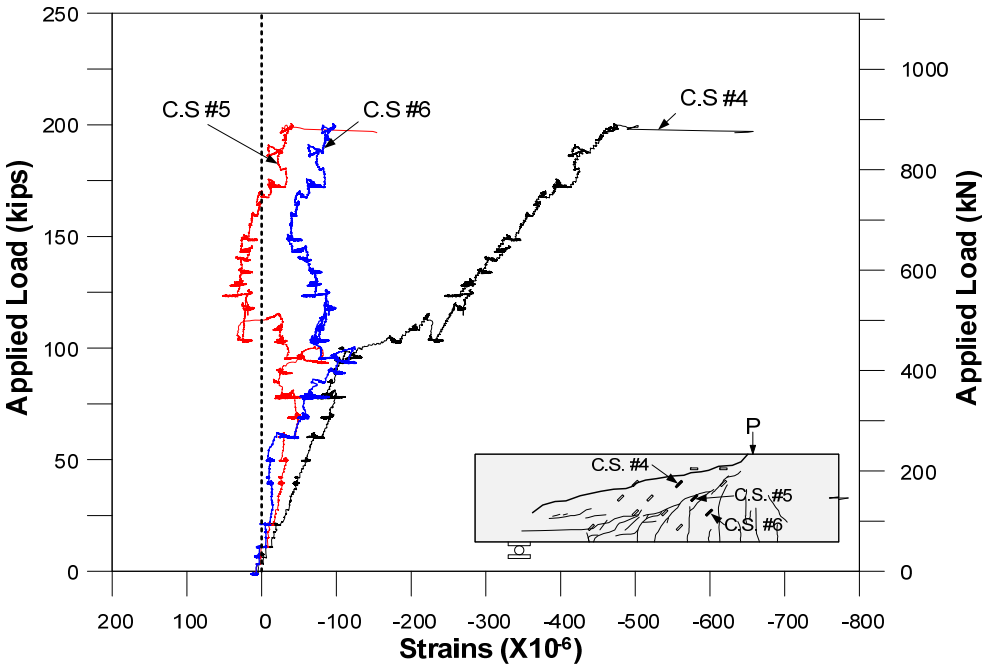

(b)

Figure 5.19 Concrete surface strains – 2 – PC#2; (a) Concrete surface strains set #1; (b) Concrete surface strains set #2

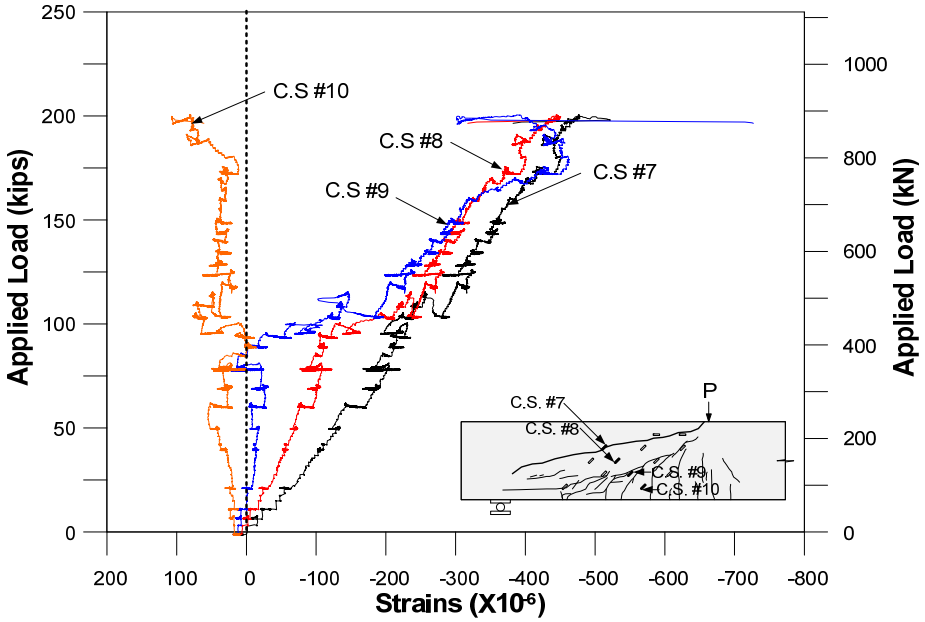

(a)

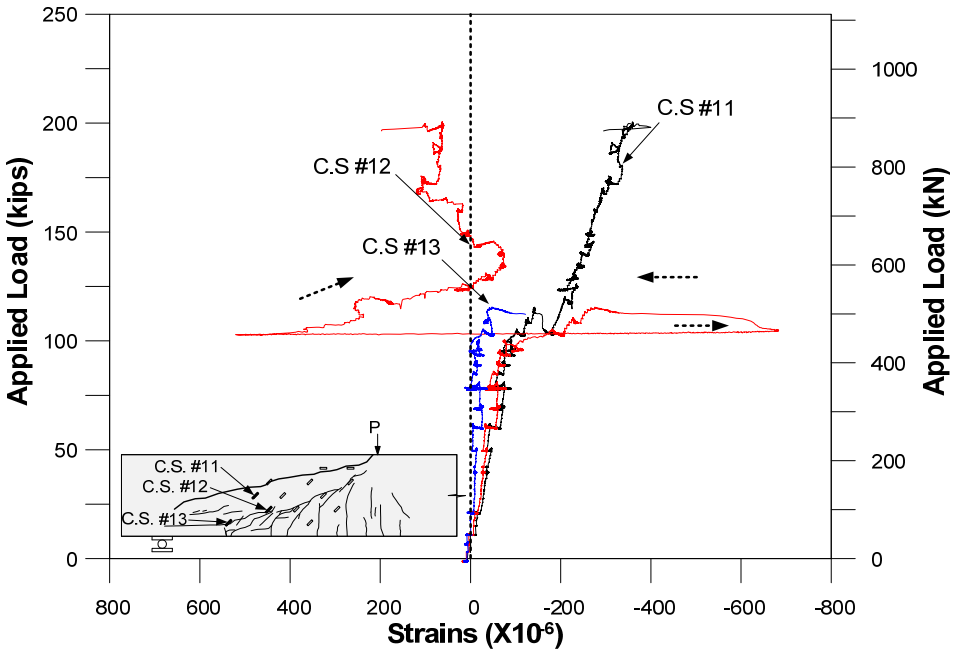

(b)

Figure 5.20 Concrete surface strains – 2 – PC#2; (a) Concrete surface strains set #3; (b) Concrete surface strains set #4

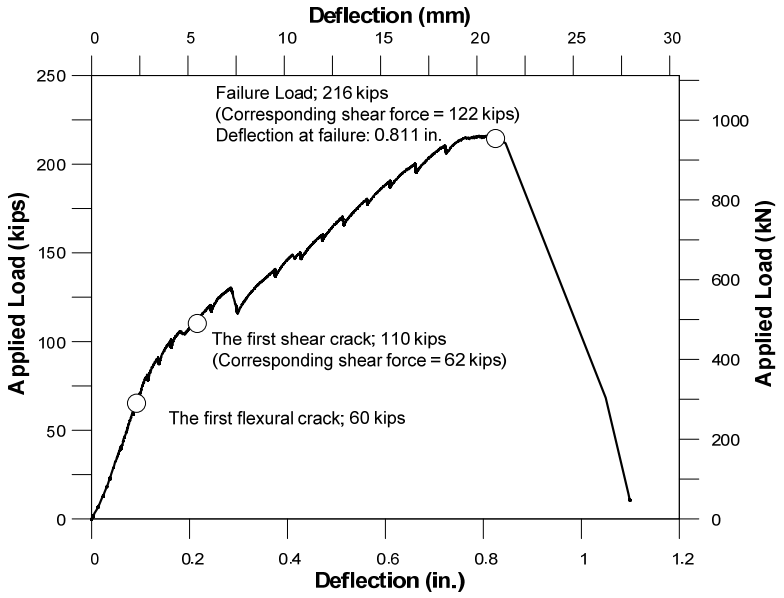

Figure 5.21 Load versus deflection response for 2 – PC#3

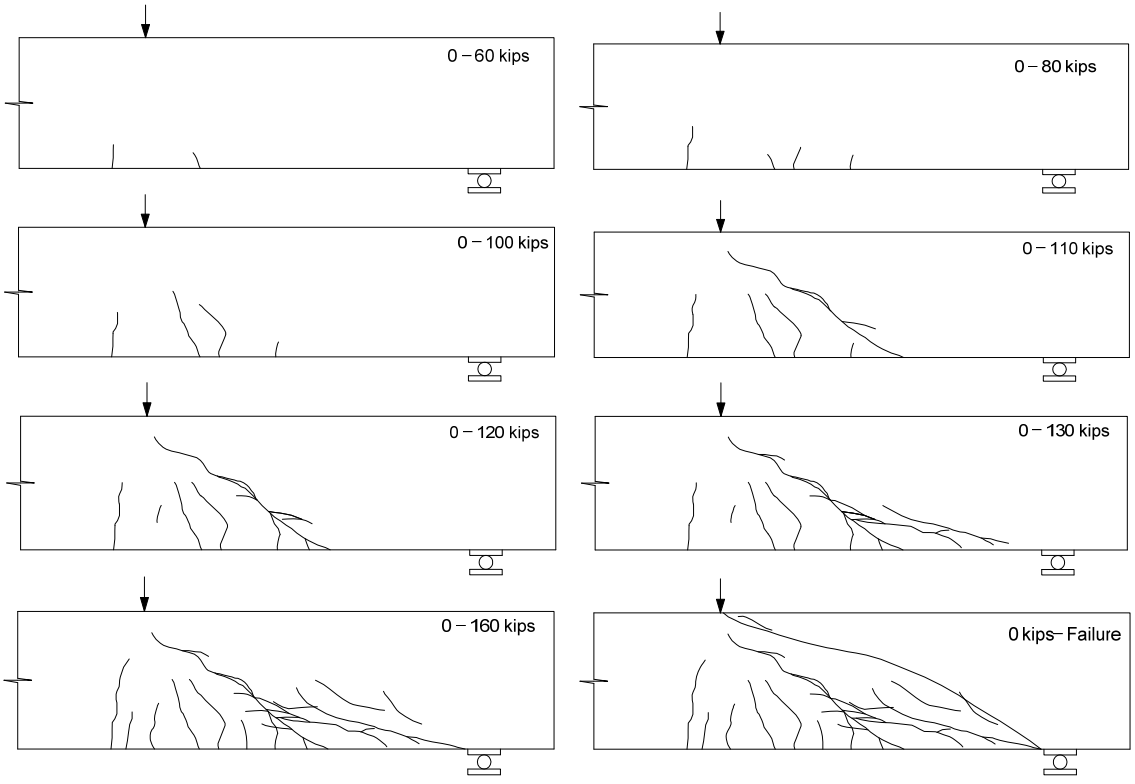

Figure 5.22 Crack pattern for 2 –PC#3

(a)

(b)

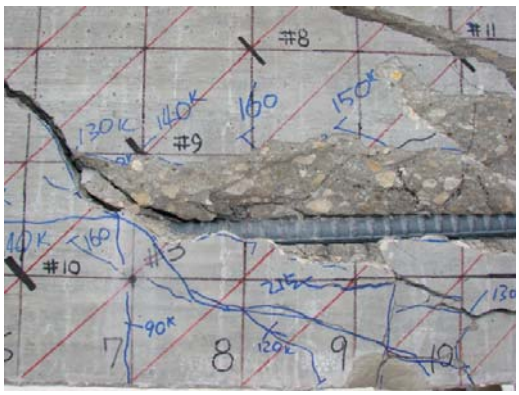

(c) (d)

Figure 5.23 Typical photos during test for 2 –PC#3; (a) Prior to failure; (b) At failure; (c) Compression zone at failure; (d) Debonding of longitudinal reinforcement at failure

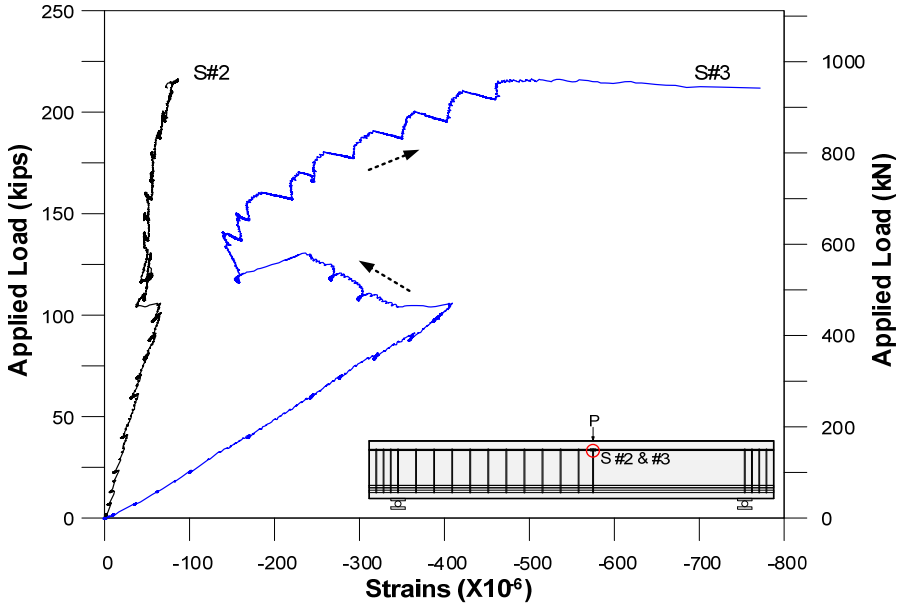

Figure 5.24 Strains in compression reinforcements – 2 - PC#3

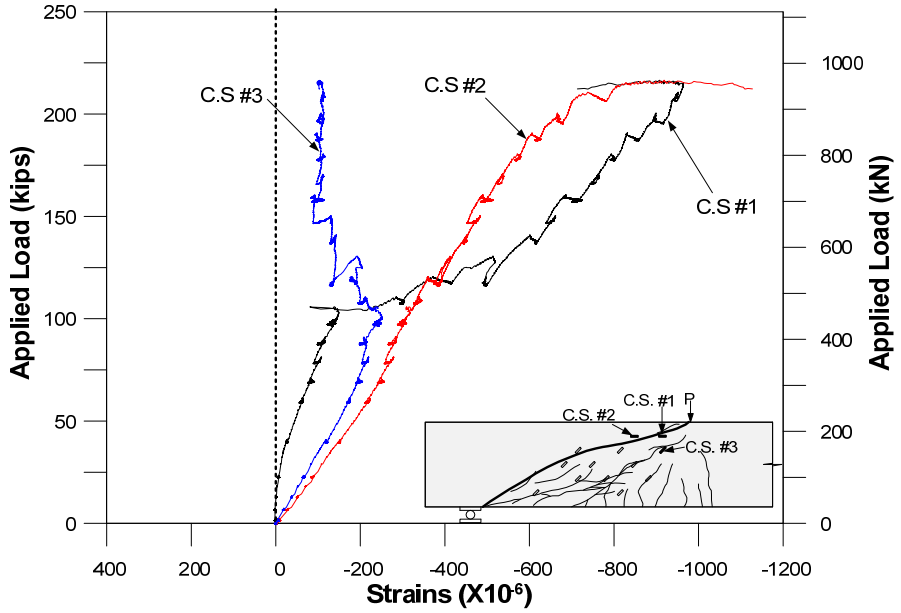

(a)

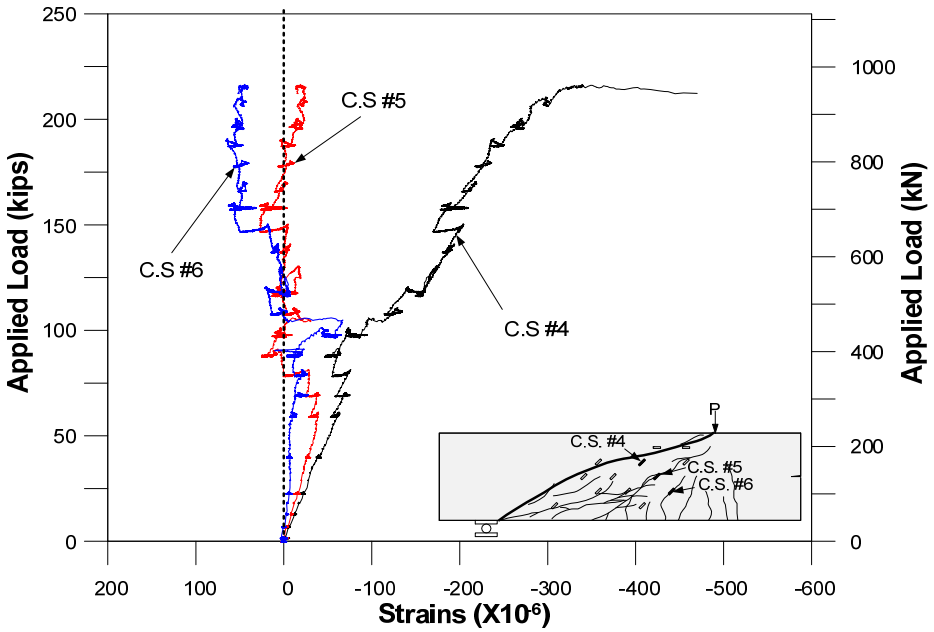

(b)

Figure 5.25 Concrete surface strains – 2 – PC#3; (a) Concrete surface strains set #1; (b) Concrete surface strains set #2

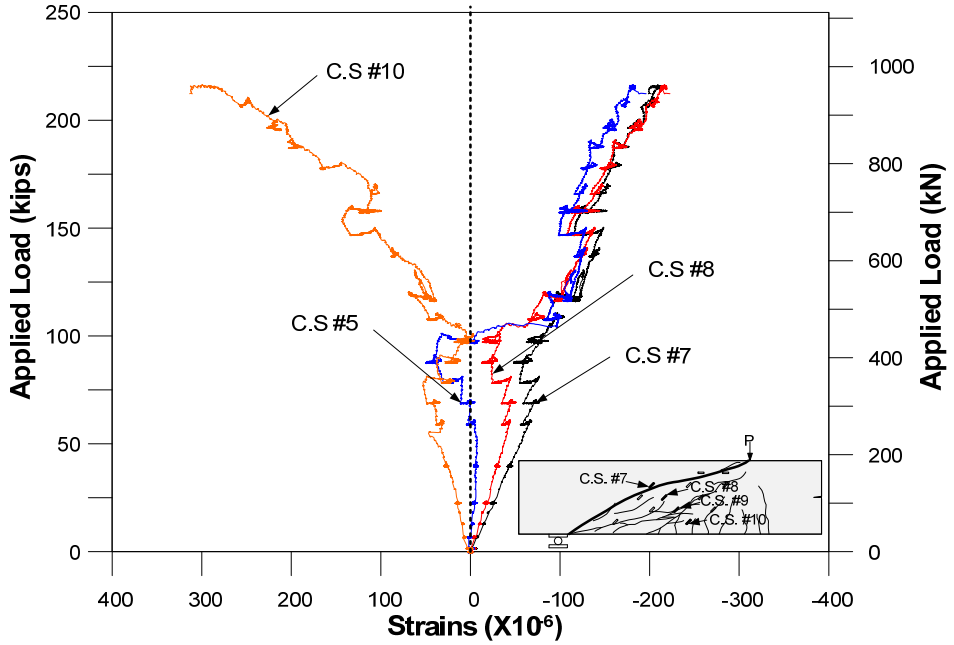

(a)

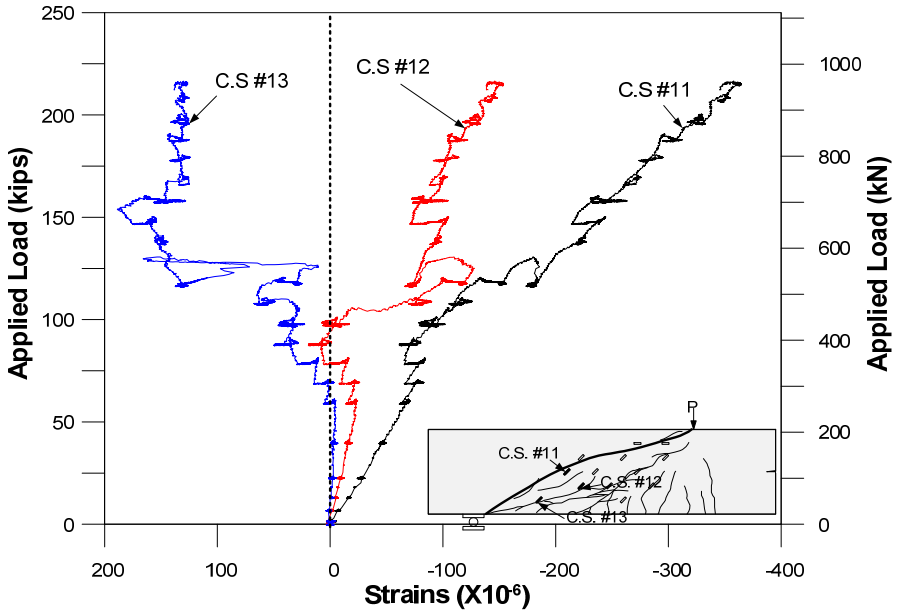

(b)

Figure 5.26 Concrete surface strains – 2 – PC#3; (a) Concrete surface strains set #3; (b) Concrete surface strains set #4

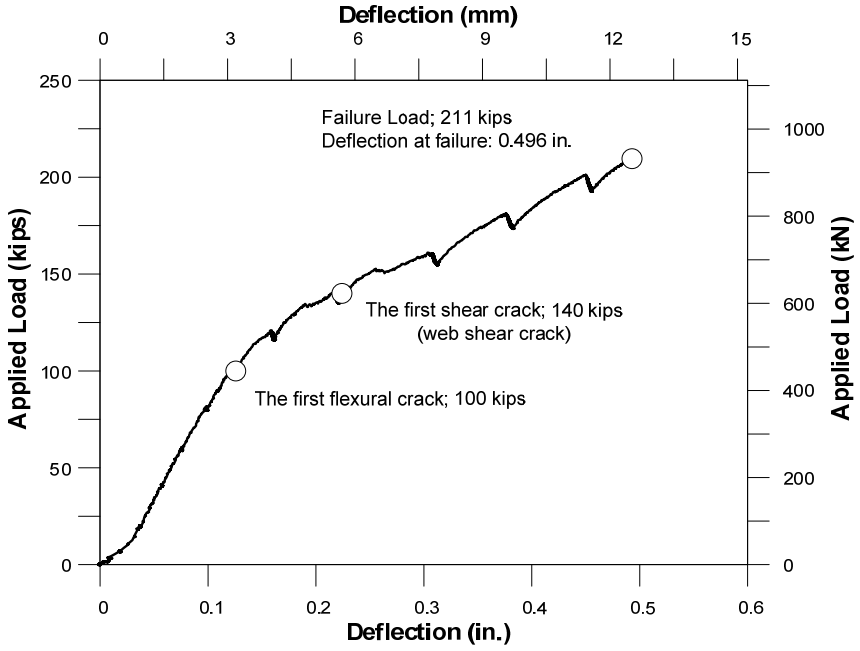

Figure 5.27 Load versus deflection response for 2 – SFRPC#1

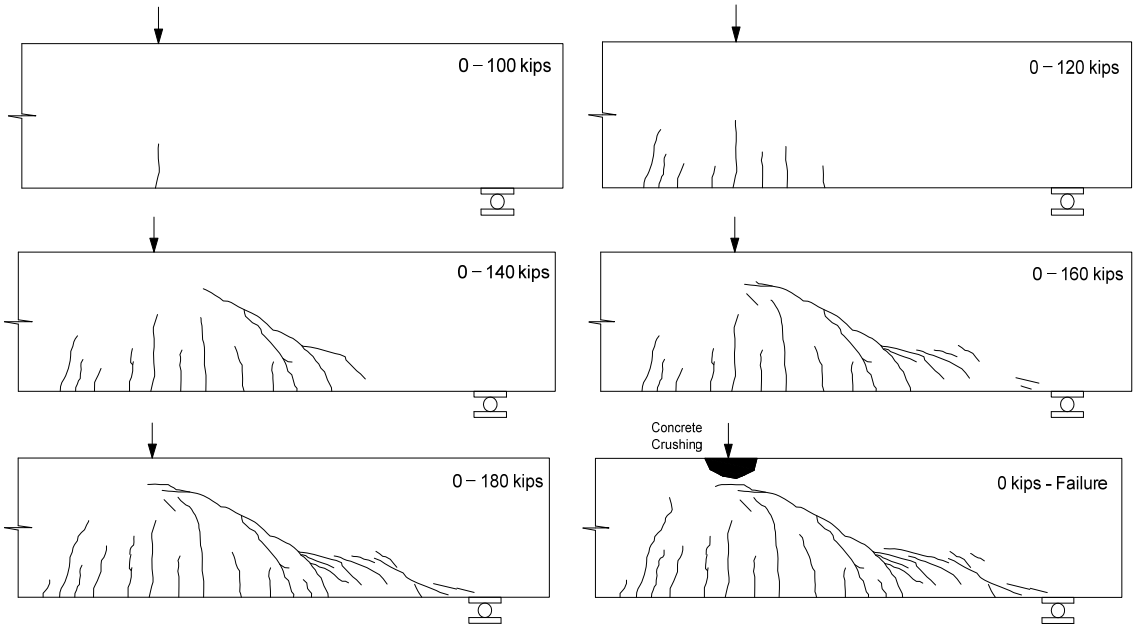

Figure 5.28 Crack pattern for 2 – SFRPC#1

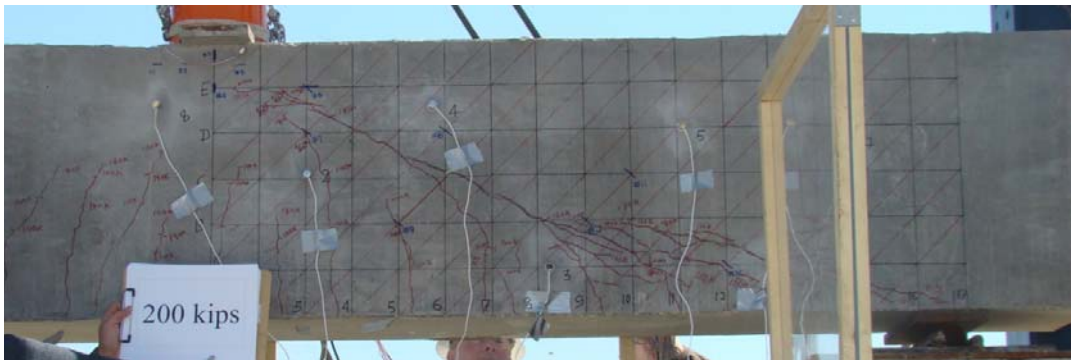

(a)

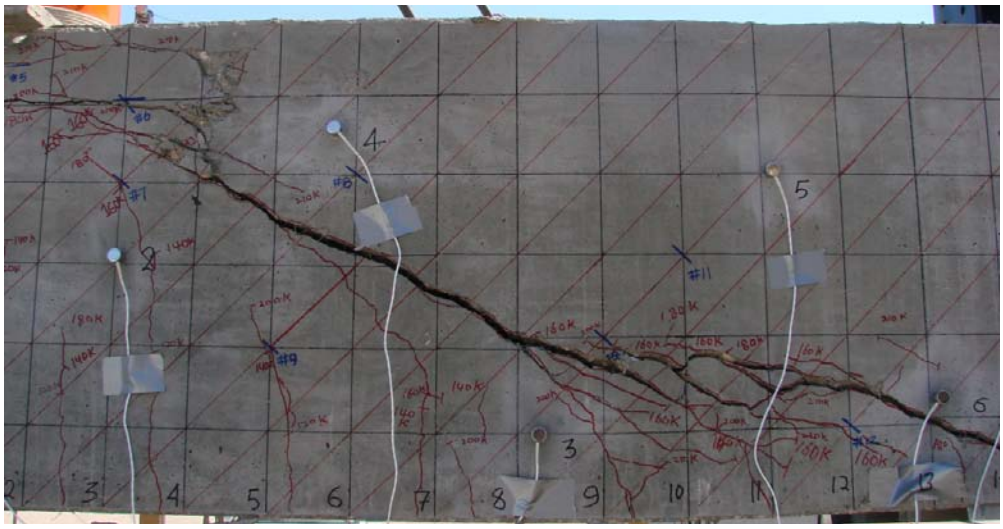

(b)

(c) (d)

Figure 5.29 Typical photos during test for 2 –SFRPC#1; (a) Prior to failure; (b) At failure; (c) Compression zone at failure; (d) Not dissolved fibers

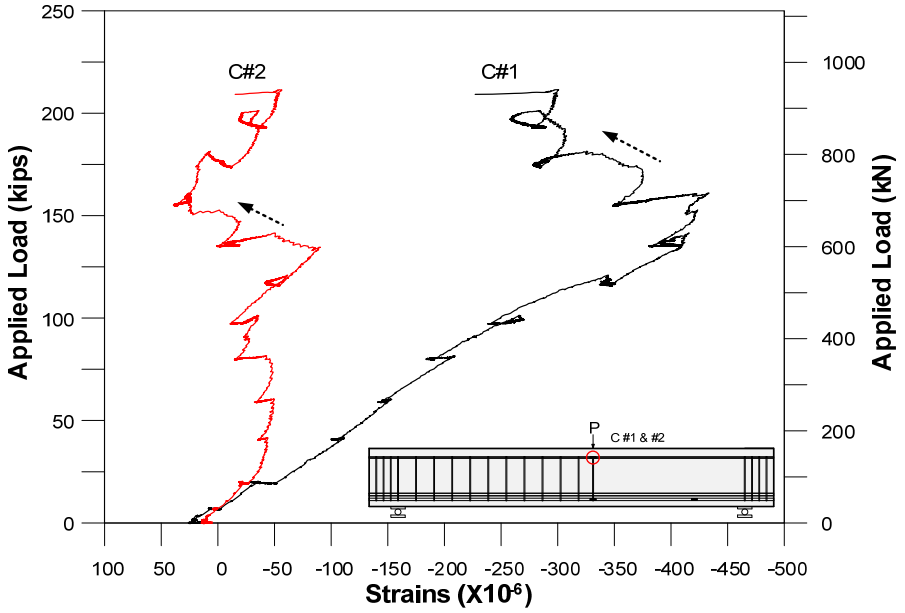

Figure 5.30 Concrete strains in compression zone – 2 - SFRPC#1

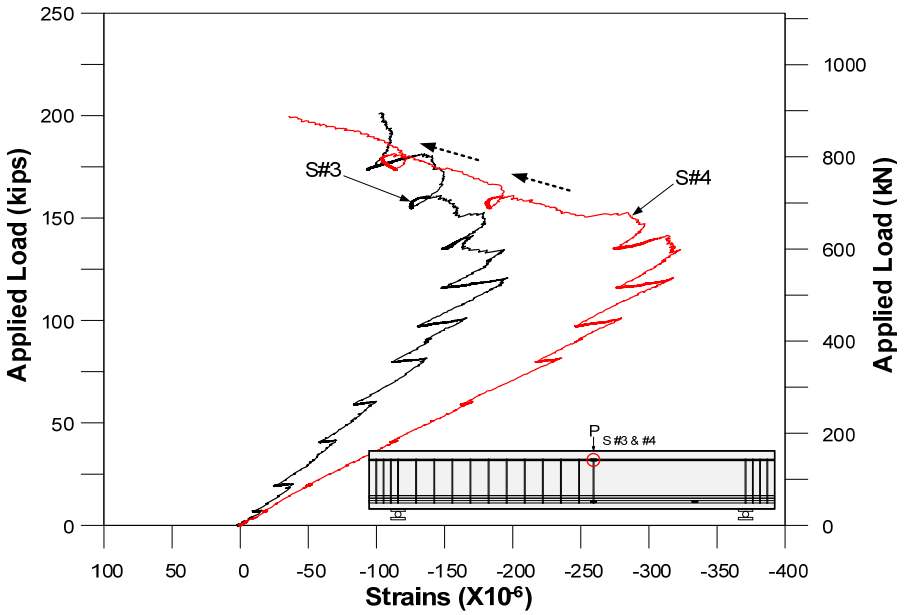

Figure 5.31 Strains in compression reinforcements – 2 - SFRPC#1

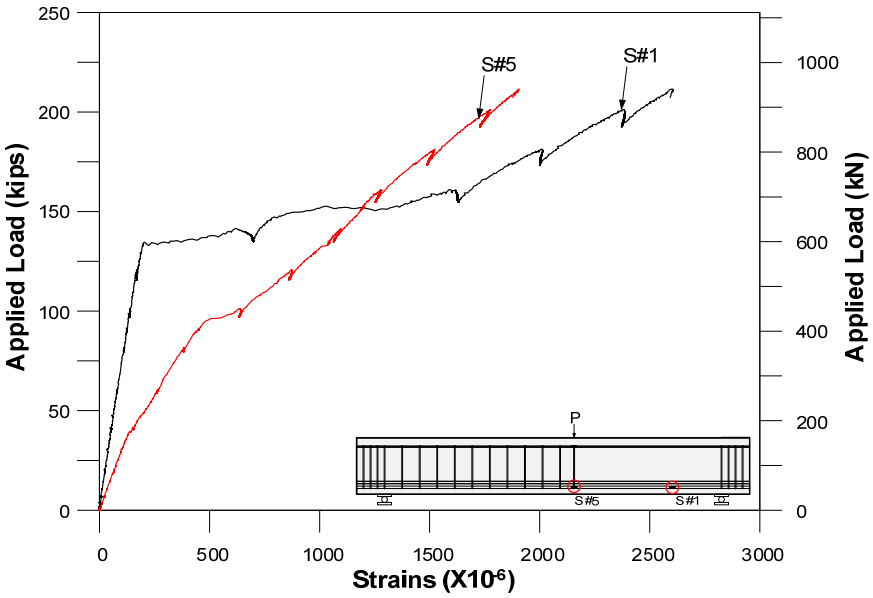

Figure 5.32 Strains in longitudinal reinforcements – 2 - SFRPC#1

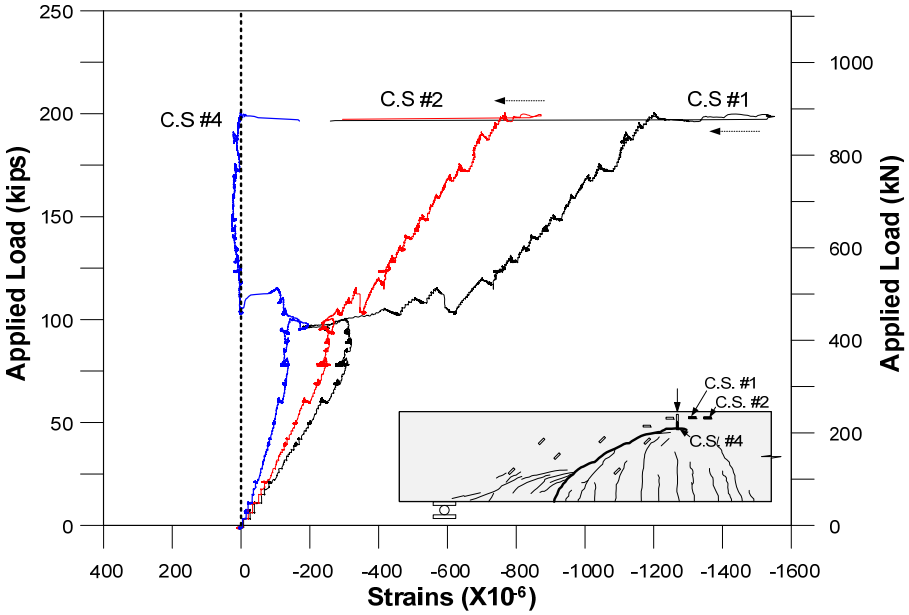

(a)

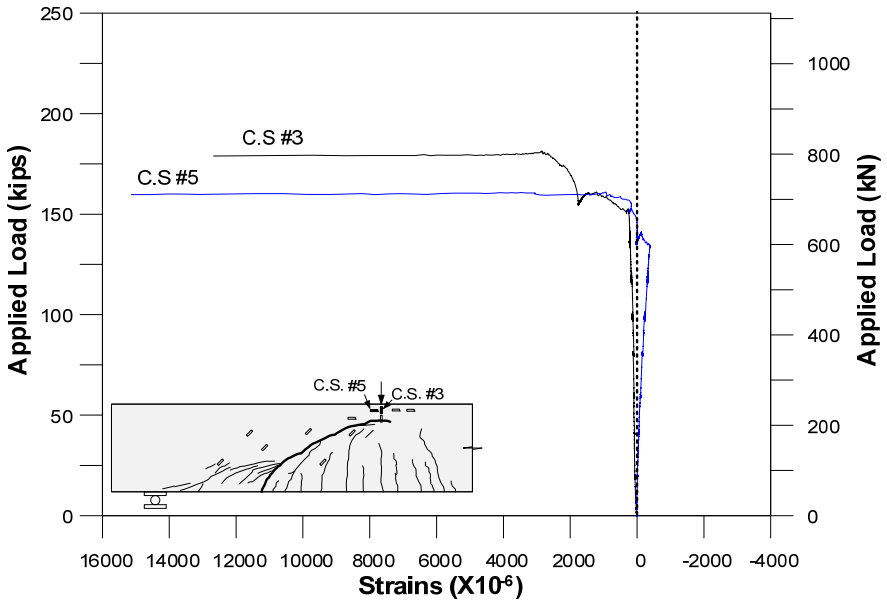

(b)

Figure 5.33 Concrete surface strains – 2 – SFRPC#1; (a) Concrete surface strains set #1; (b) Concrete surface strains set #2

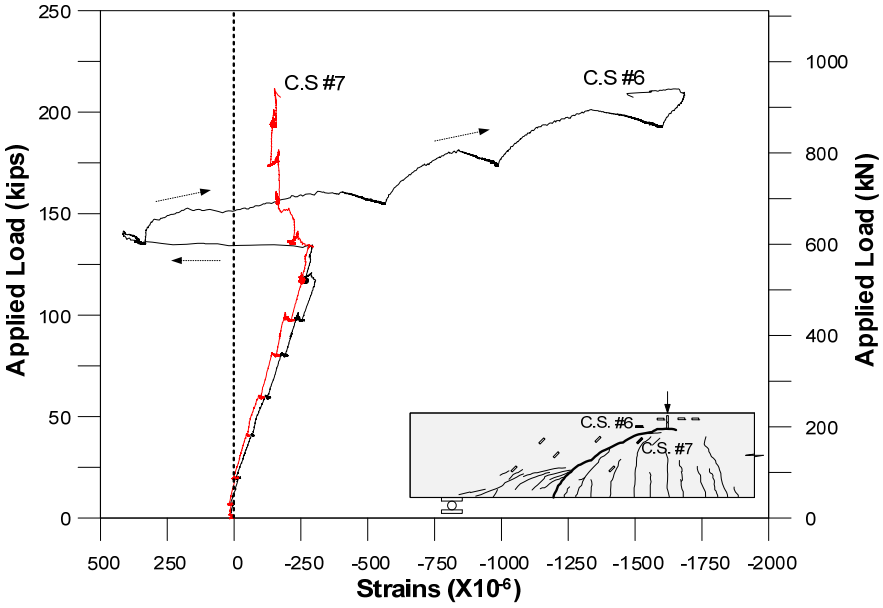

(a)

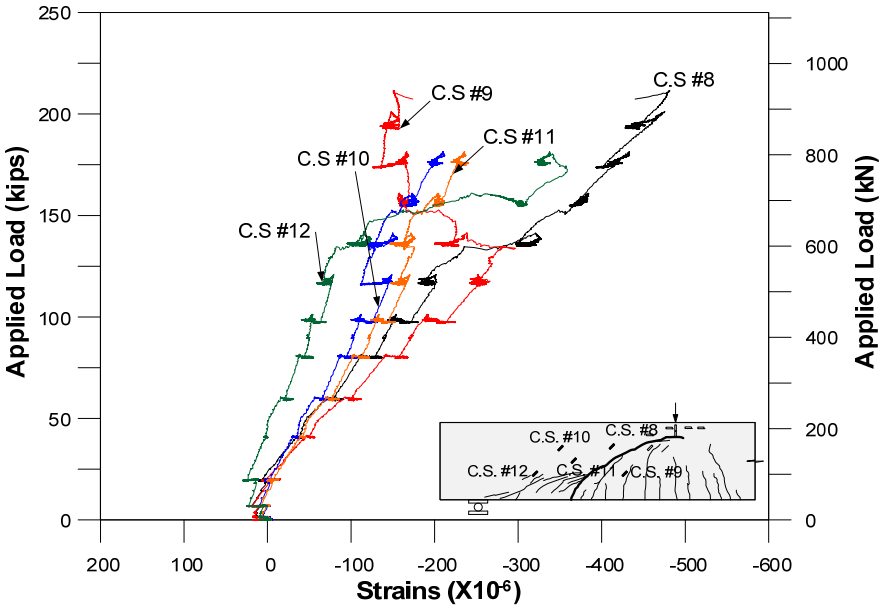

(b)

Figure 5.34 Concrete surface strains – 2 – SFRPC#1; (a) Concrete surface strains set #3; (b) Concrete surface strains set #4

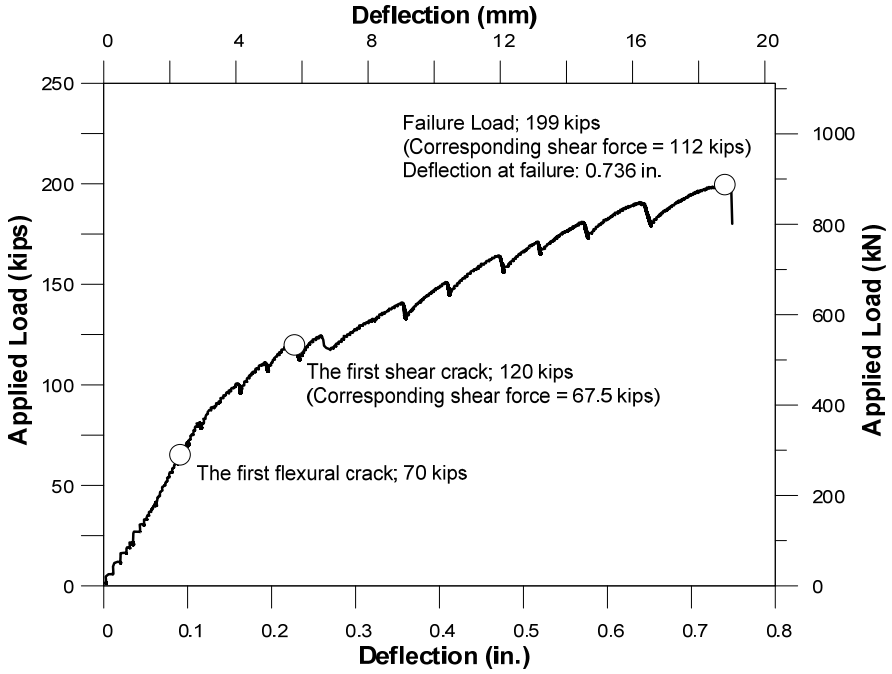

Figure 5.35 Load versus deflection response for 2 – SFRPC#2

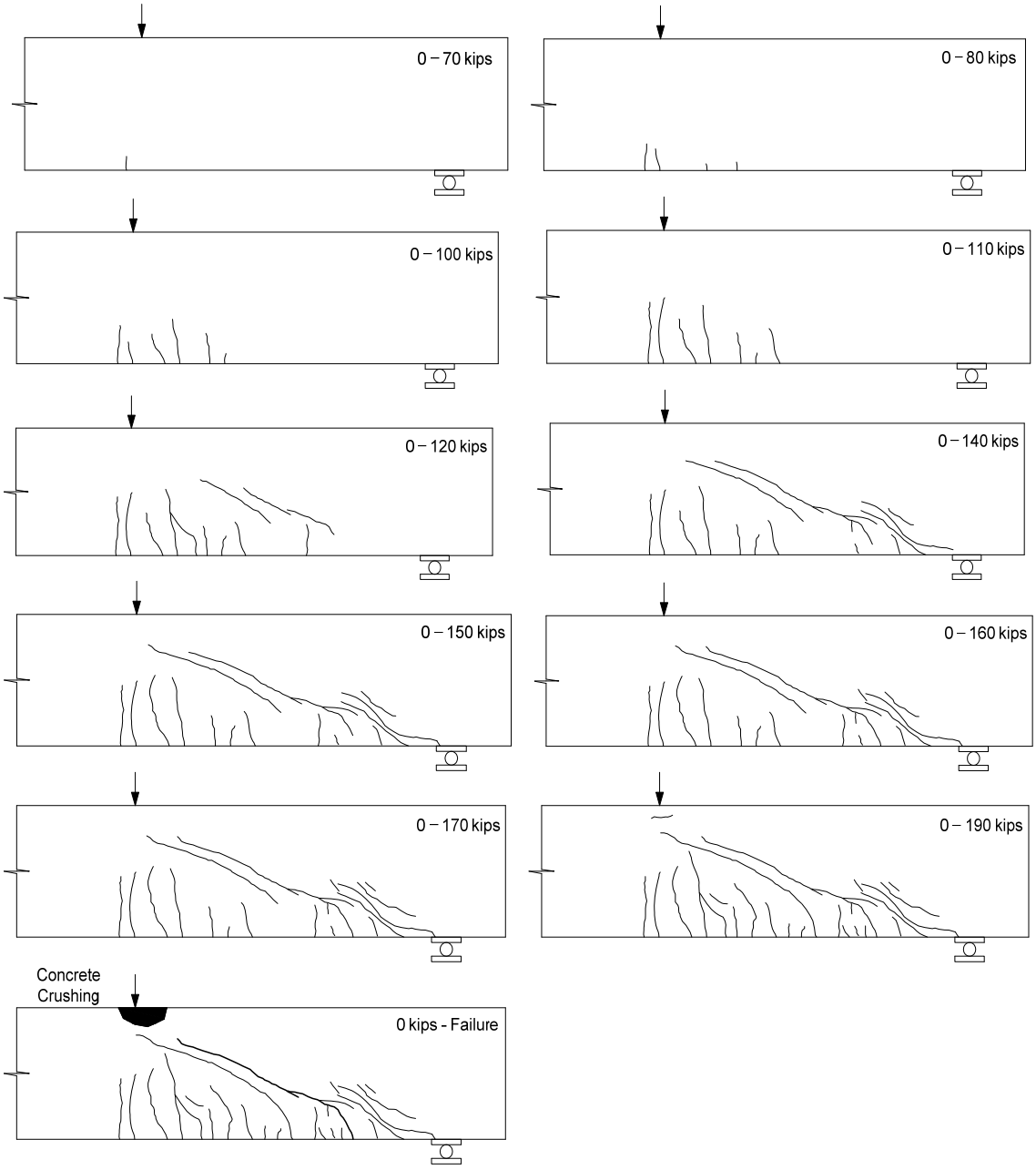

Figure 5.36 Crack pattern for 2 – SFRPC#2

(a)

(b)

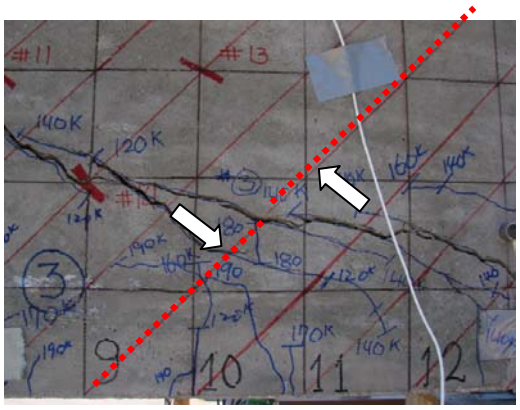

(c) (d)

Figure 5.37 Typical photos during test for 2 – SFRPC#2; (a) Prior to failure; (b) At failure; (c) Fiber pull-out; (d) Sliding after crushing of compression zone

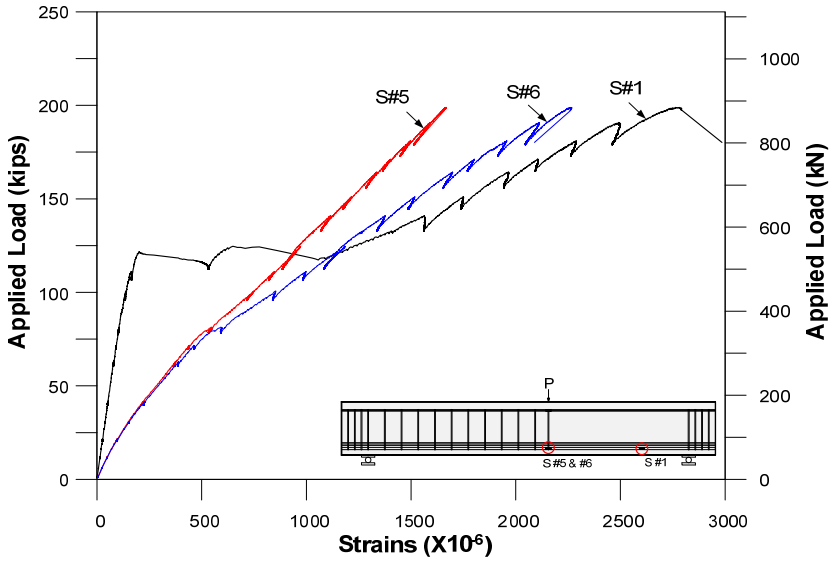

Figure 5.38 Strains in longitudinal reinforcements – 2 – SFRPC#2

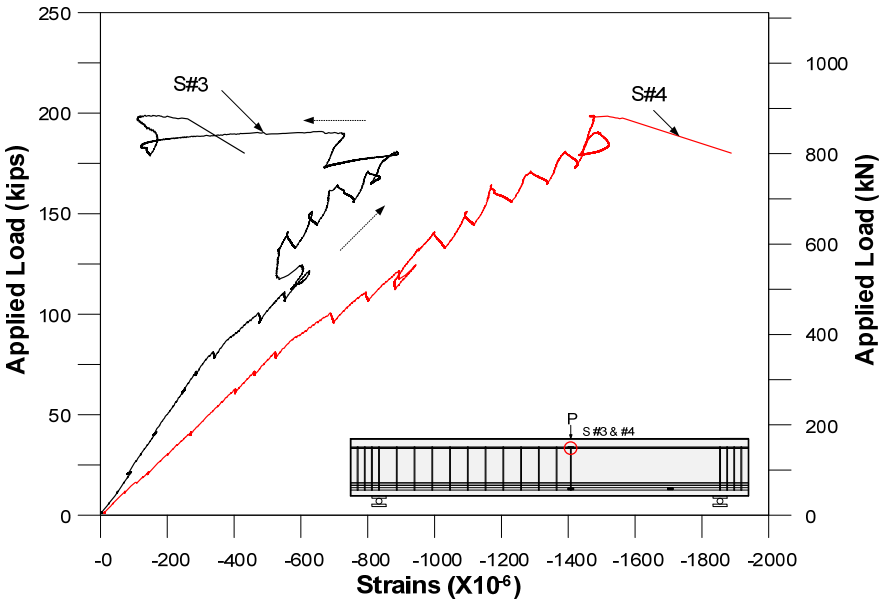

Figure 5.39 Strains in compression reinforcements – 2 – SFRPC#2

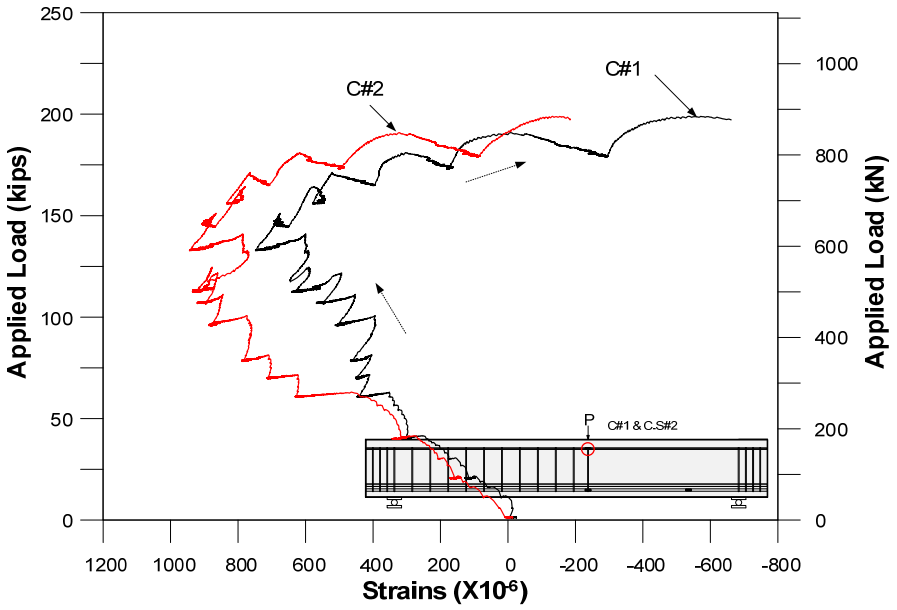

Figure 5.40 Strains in compression zone – 2 – SFRPC#2

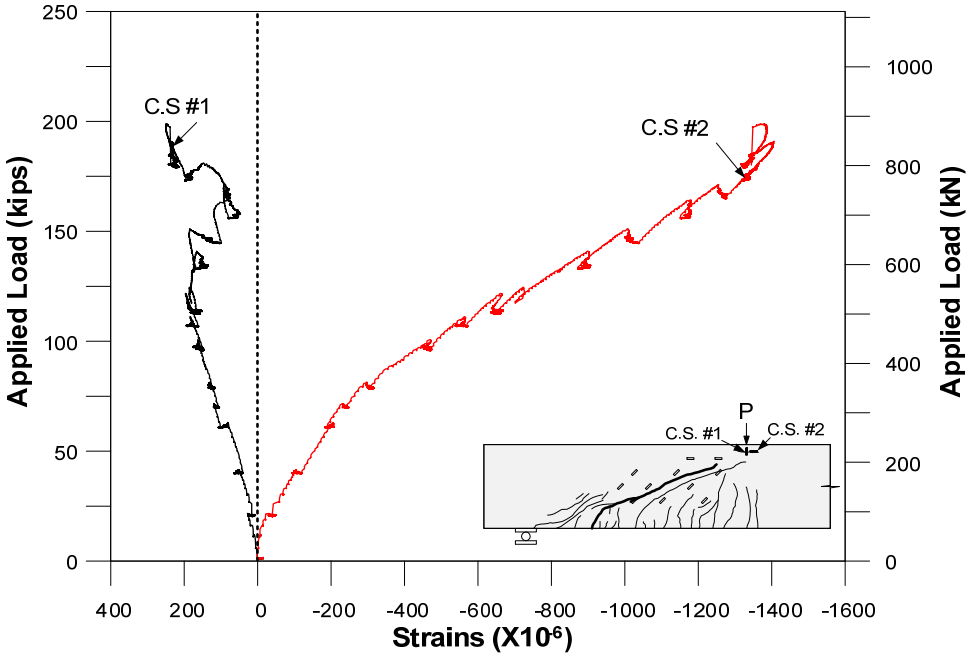

(a)

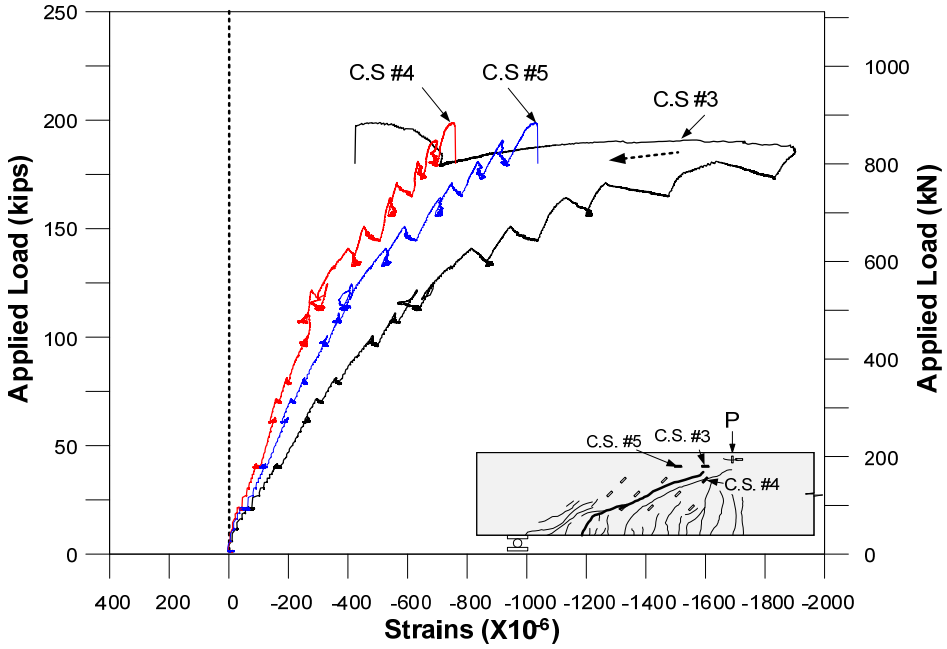

(b)

Figure 5.41 Concrete surface strains – 2 – SFRPC#2; (a) Concrete surface strains set #1; (b) Concrete surface strains set #2

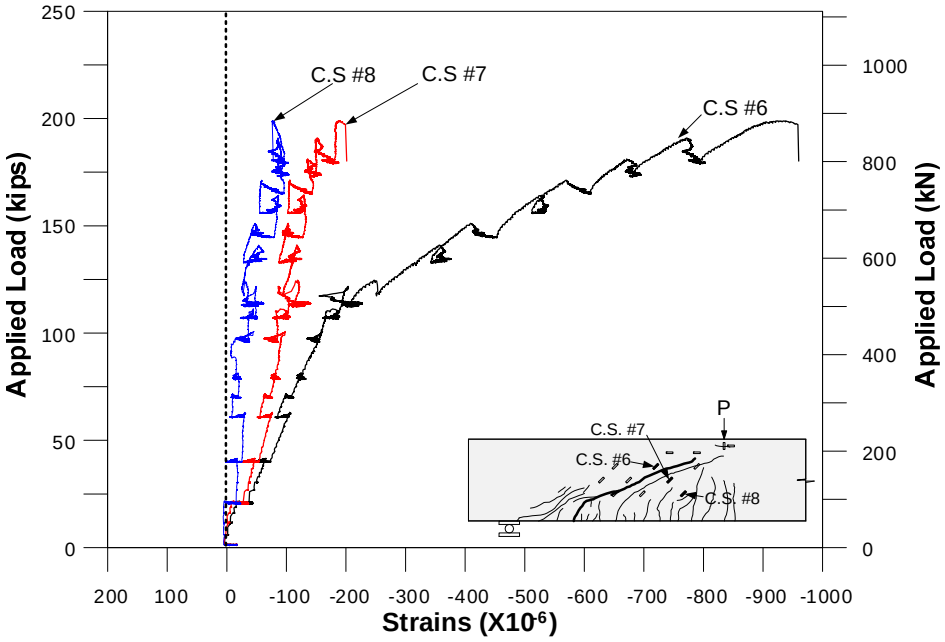

(a)

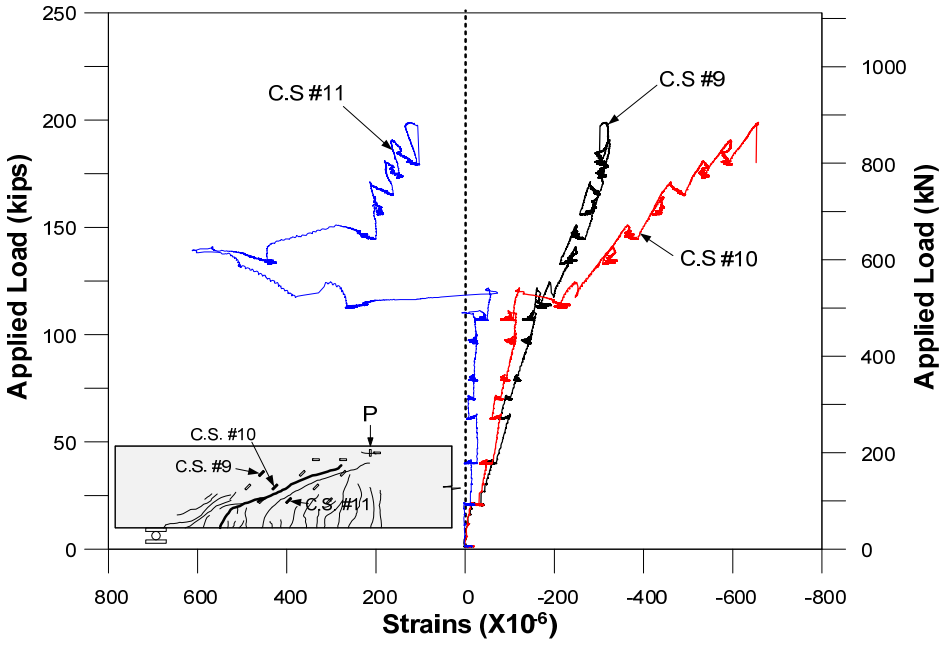

(b)

Figure 5.42 Concrete surface strains – 2 – SFRPC#2; (a) Concrete surface strains set #3; (b) Concrete surface strains set #4

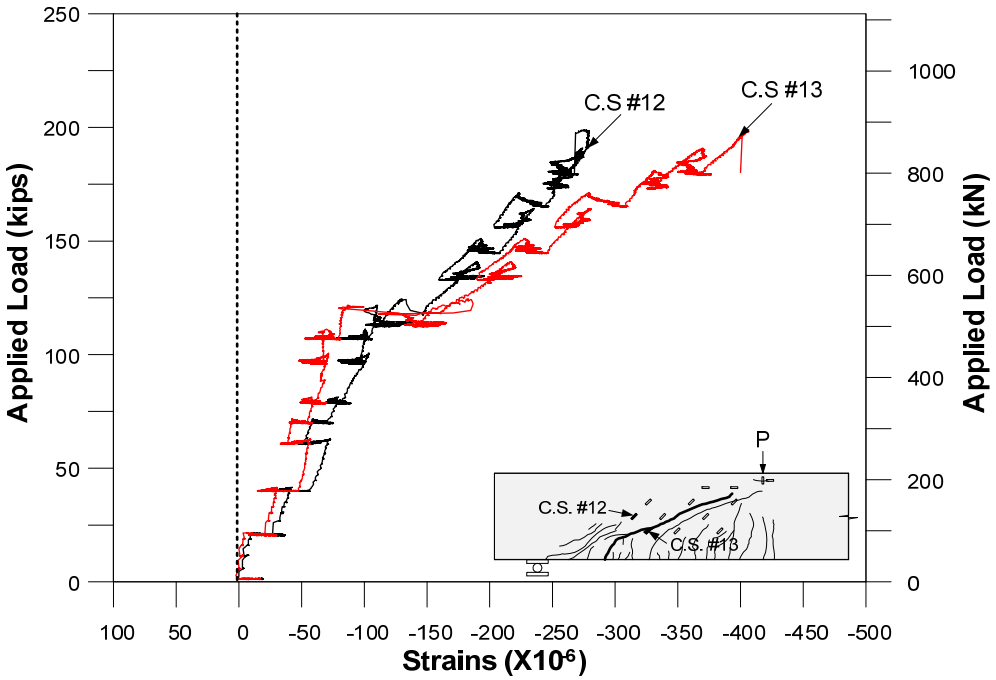

Figure 5.43 Concrete surface strains set #5 – 2 – SFRPC#2

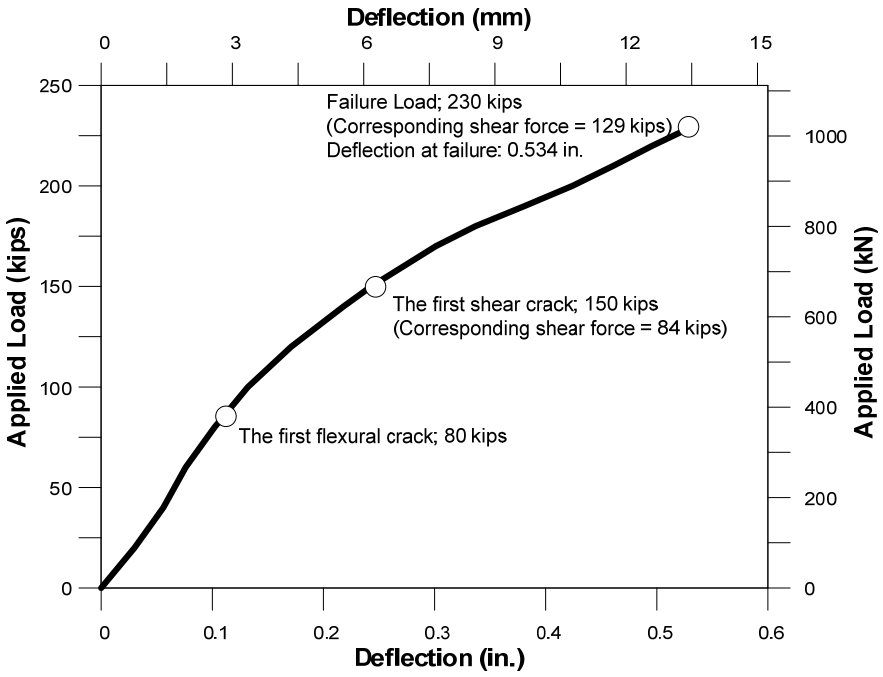

Figure 5.44 Load versus deflection response for 2 – SFRPC#3

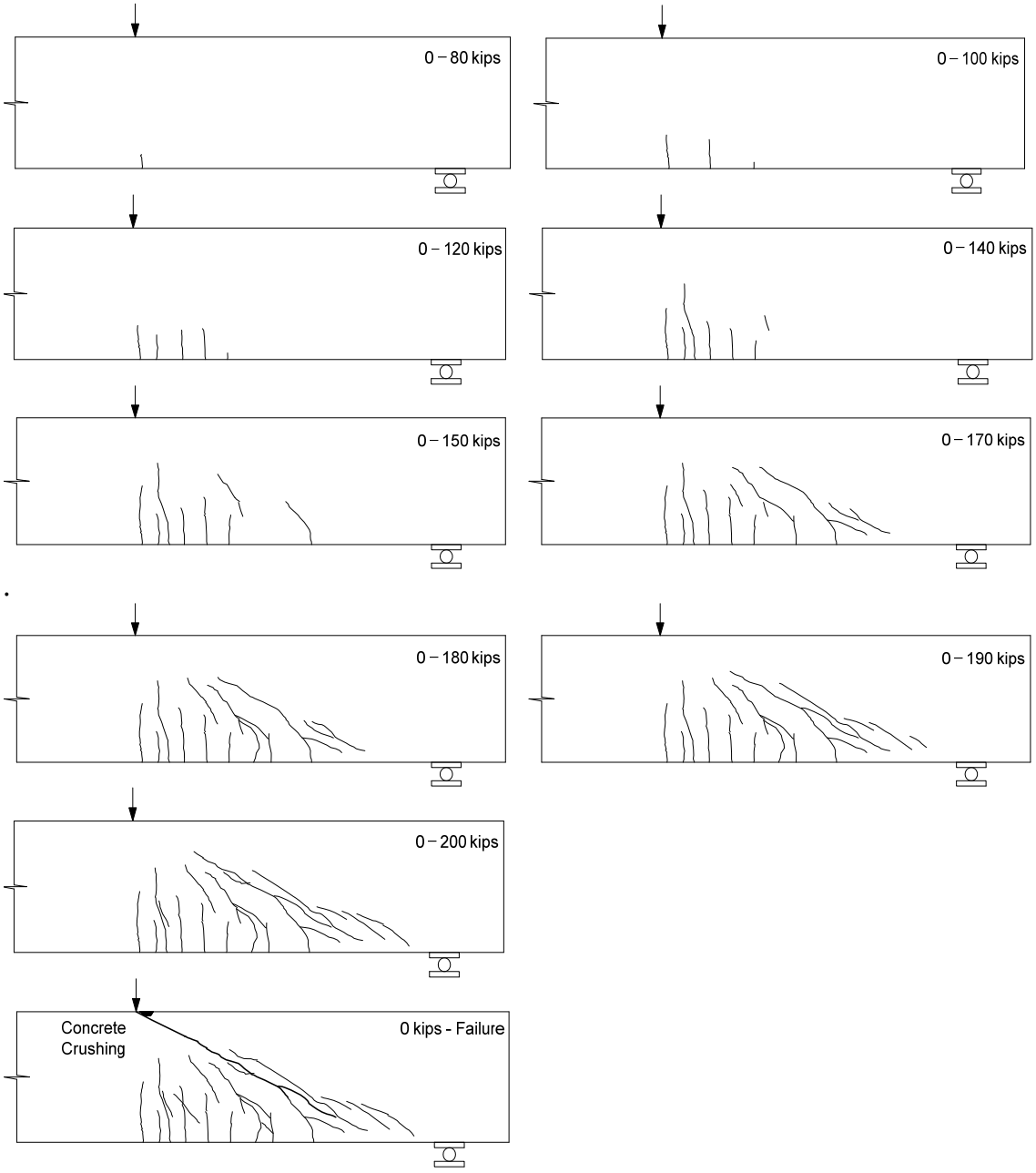

Figure 5.45 Crack pattern for 2 – SFRPC#3

(a)

(b)

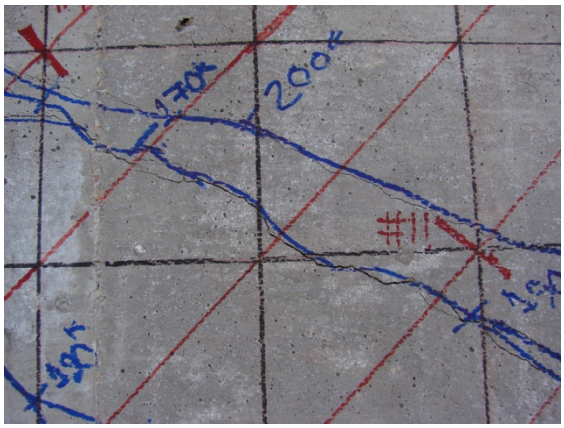

(c) (d)

Figure 5.46 Typical photos during test for 2 – SFRPC#3; (a) Prior to failure; (b) At failure; (c) Concrete crushing in compression zone; (d) No sliding prior to failure

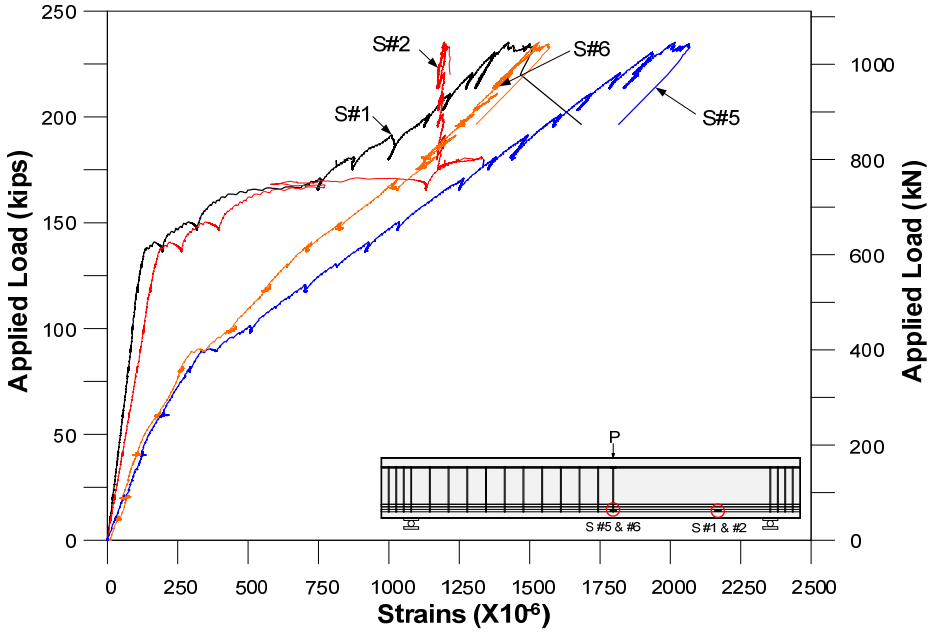

Figure 5.47 Strains in longitudinal reinforcements – 2 – SFRCP#3

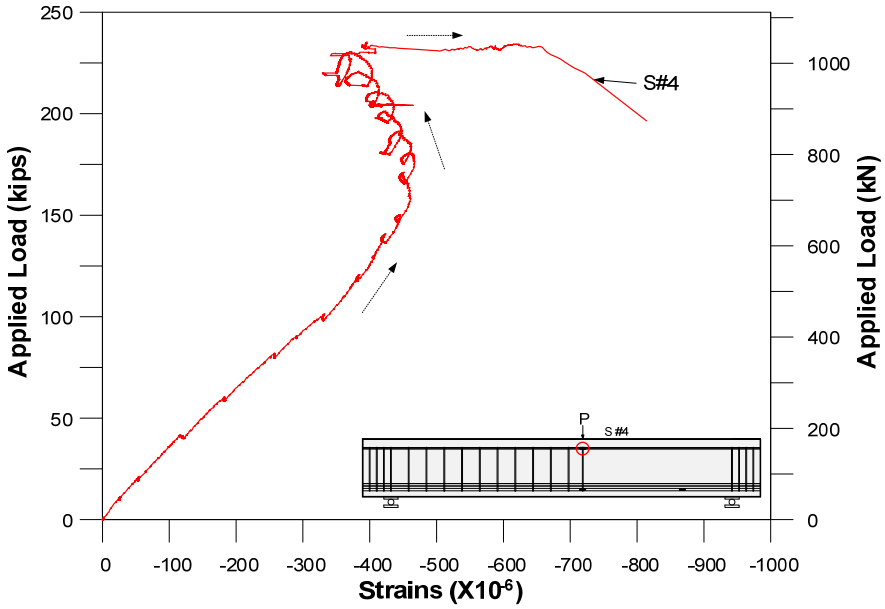

Figure 5.48 Strains in compression reinforcements – 2 – SFRPC#3

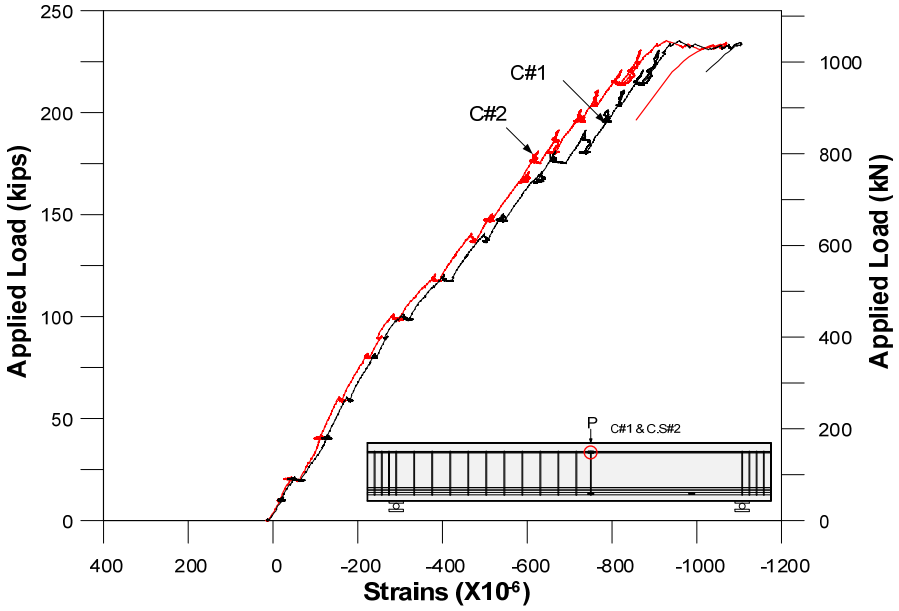

Figure 5.49 Concrete strains in compressive zone – 2 – SFRPC#3

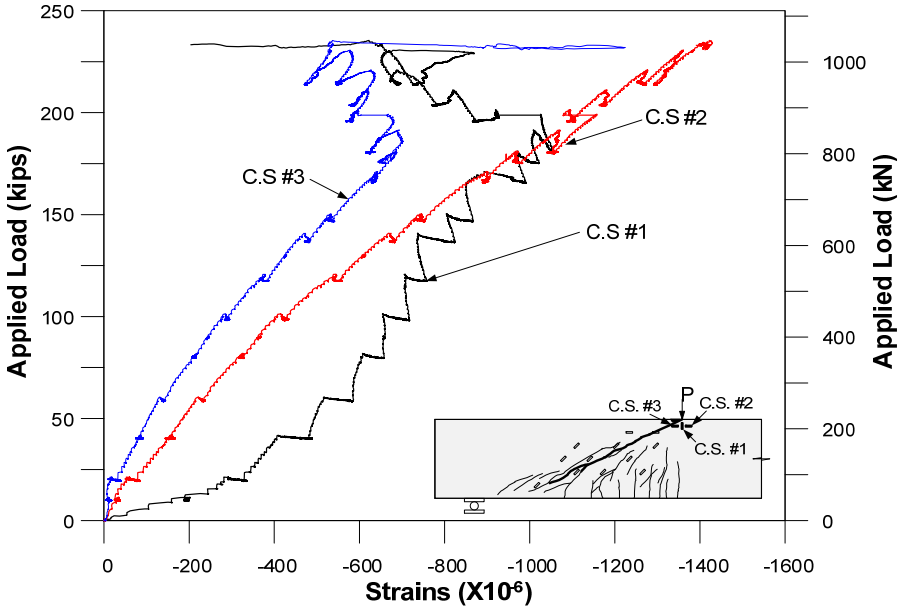

(a)

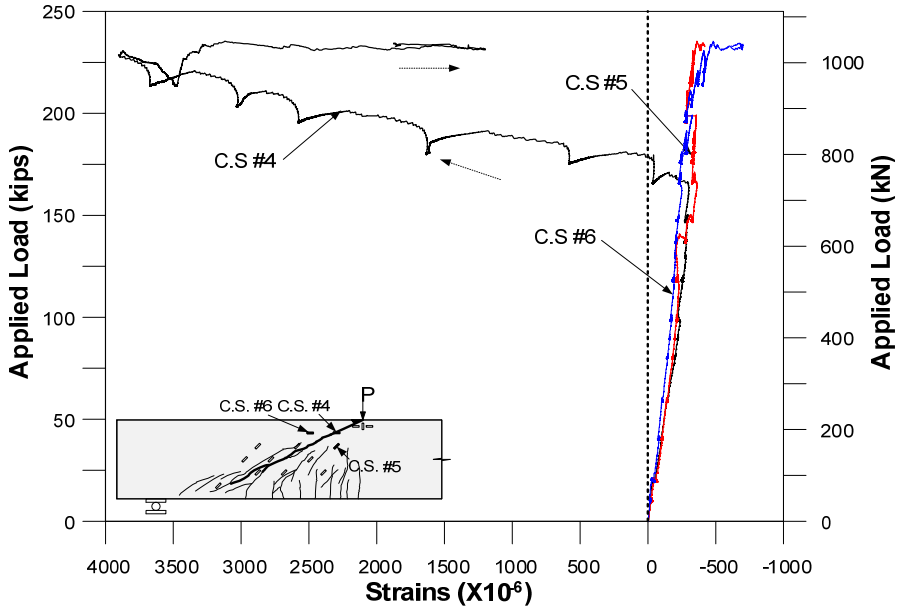

(b)

Figure 5.50 Concrete surface strains – 2 – SFRPC#3; (a) Concrete surface strains set #1; (b) Concrete surface strains set #2

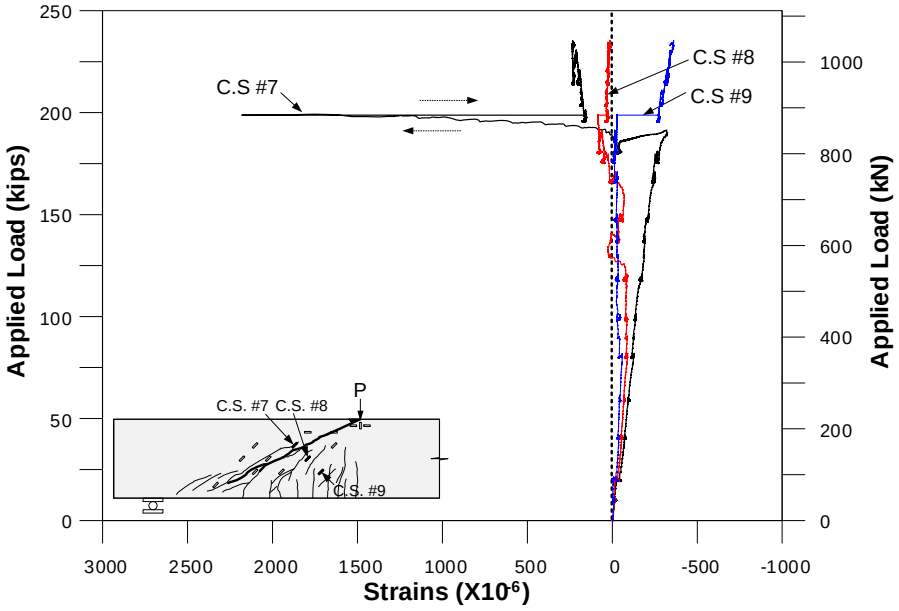

(a)

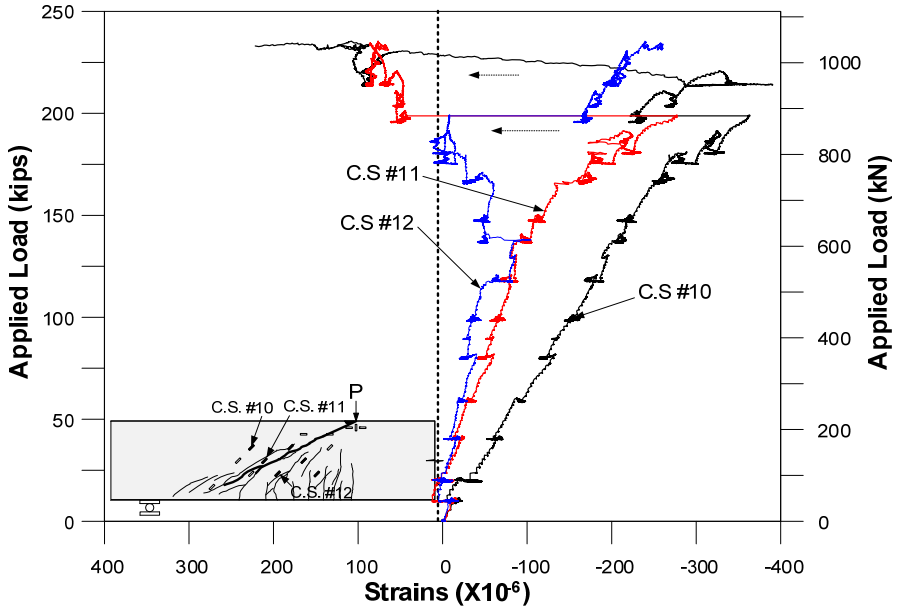

(b)

Figure 5.51 Concrete surface strains – 2 – SFRPC#3; (a) Concrete surface strains set #3; (b) Concrete surface strains set #4

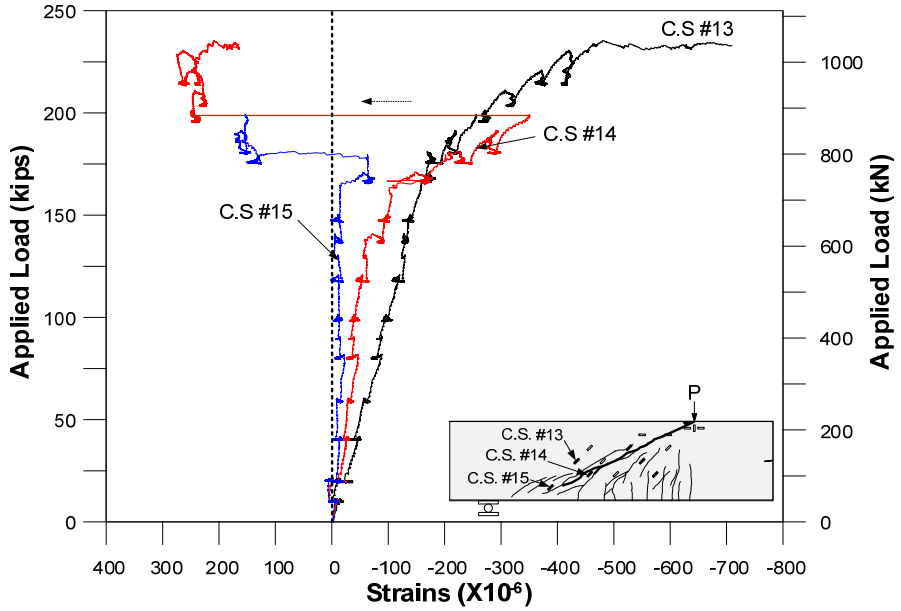

Figure 5.52 Concrete surface strains set #5 – 2 – SFRPC#3

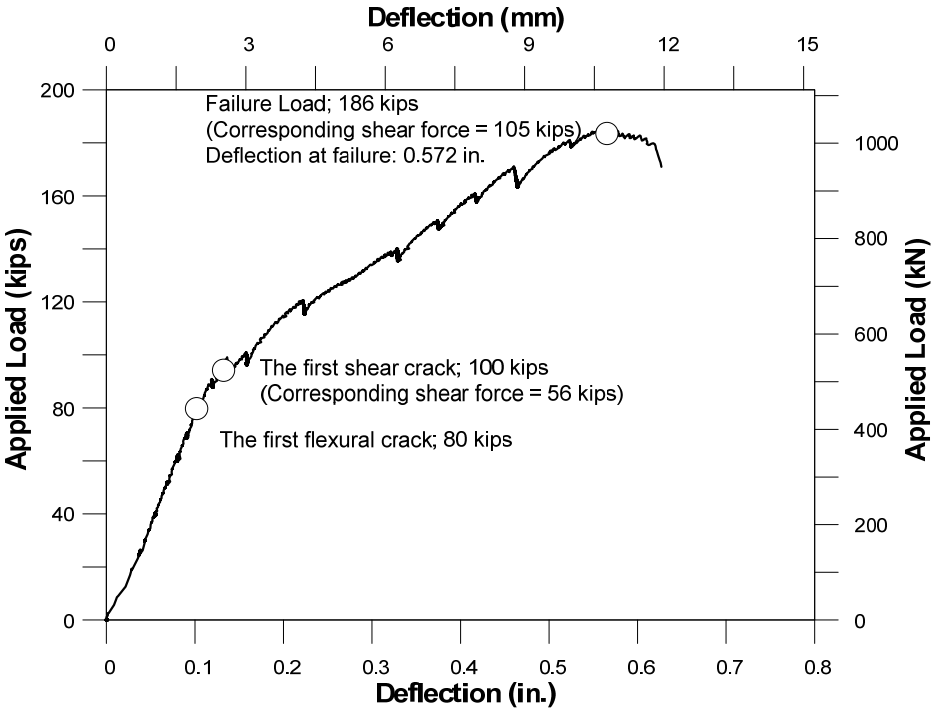

Figure 5.53 Load versus deflection response for 3 – PC#1

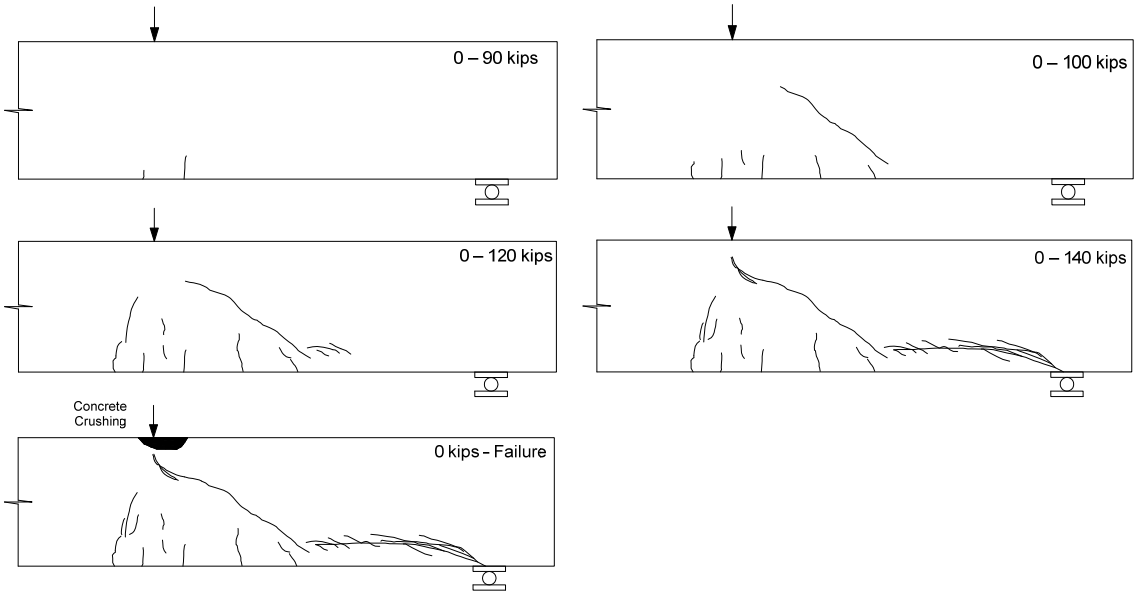

Figure 5.54 Crack pattern for the 3 – PC#1

(a)

(b)

(c) (d)

Figure 5.55 Typical photos during test for 3 – PC#1; (a) Prior to failure; (b) At failure; (c) Concrete crushing in compression zone; (d) Debonding of longitudinal reinforcement

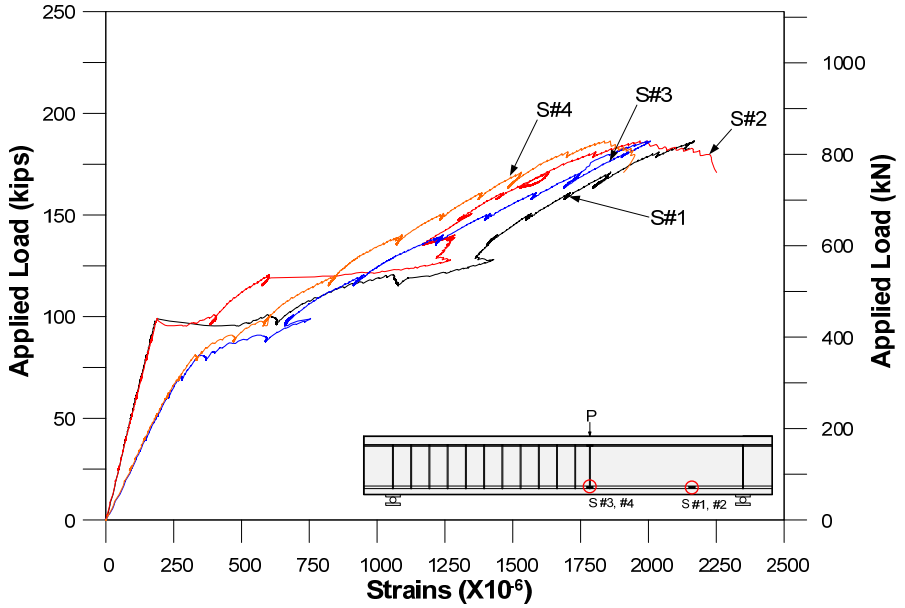

Figure 5.56 Strains in longitudinal reinforcements – 3 – PC#1

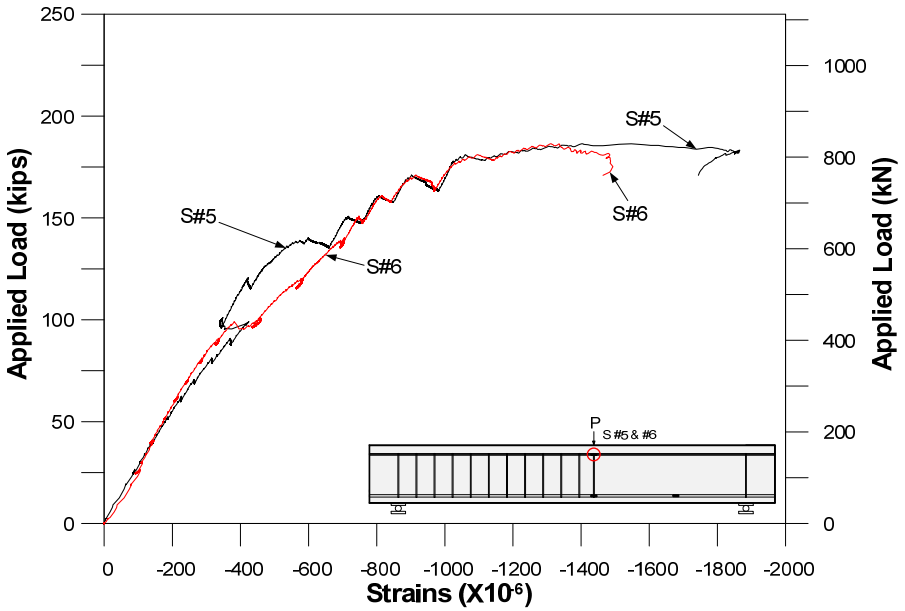

Figure 5.57 Strains in compression reinforcement – 3 – PC#1

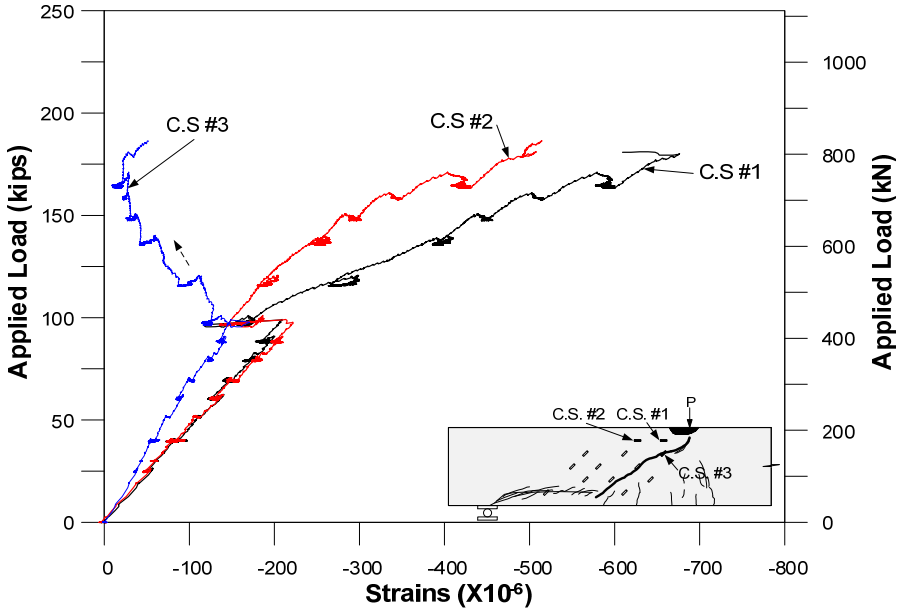

(a)

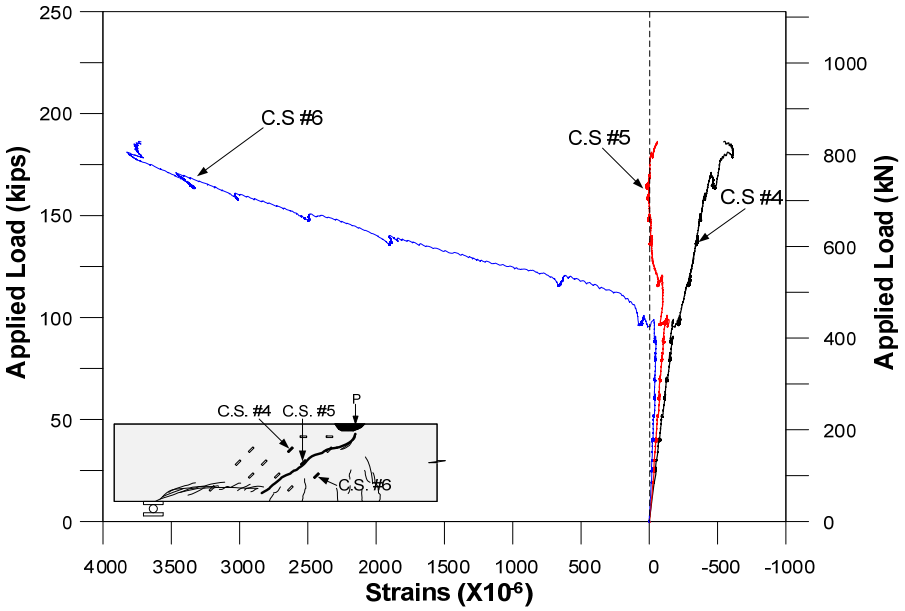

(b)

Figure 5.58 Concrete surface strains – 3 – PC#1; (a) Concrete surface strains set #1; (b) Concrete surface strains set #2

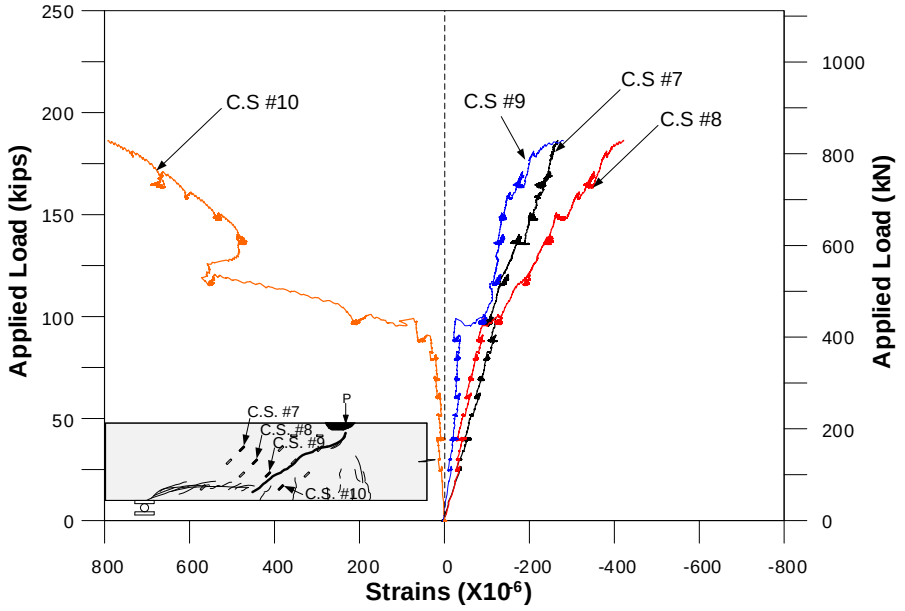

(a)

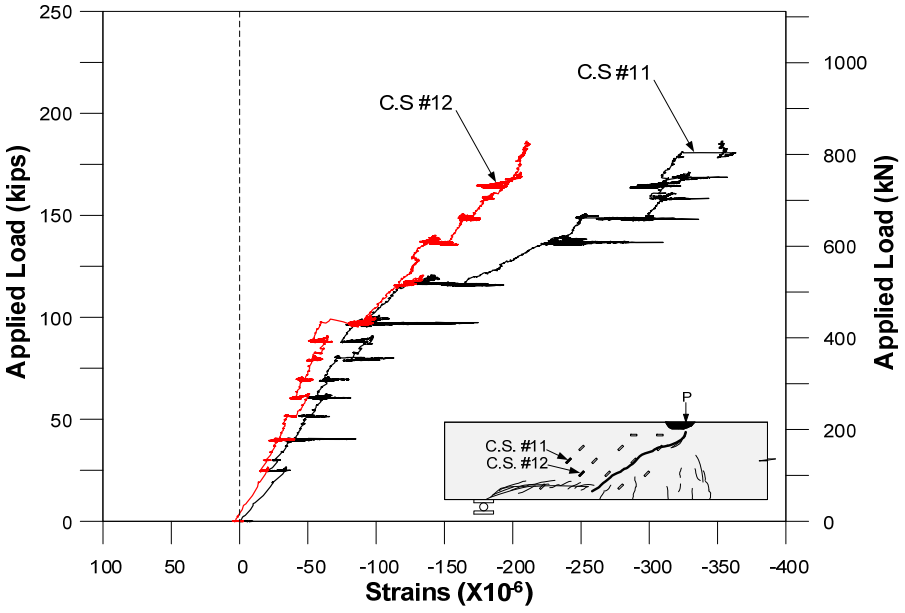

(b)

Figure 5.59 Concrete surface strains – 3 – PC#1; (a) Concrete surface strains set #3; (b) Concrete surface strains set #4

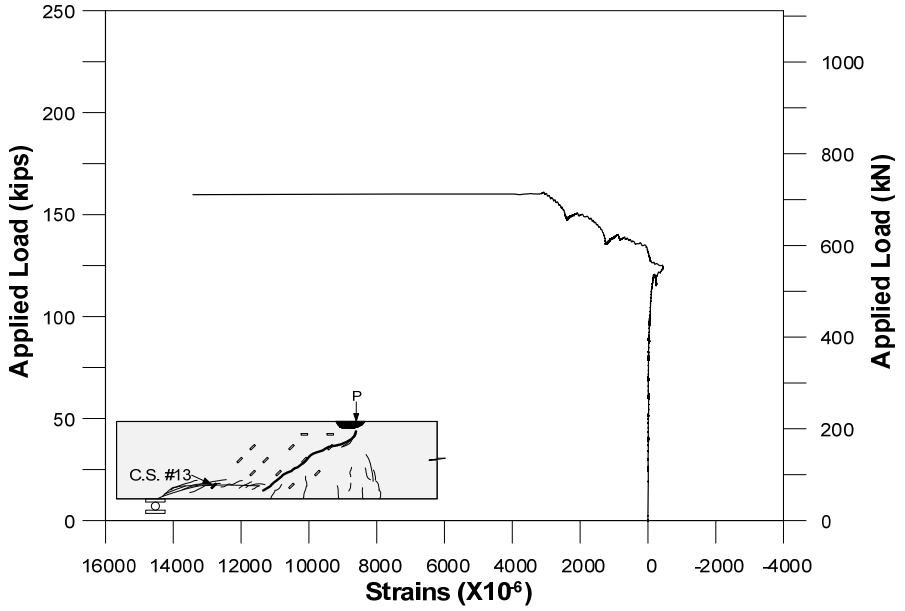

Figure 5.60 Concrete surface strains set #5 – 3 – PC#1

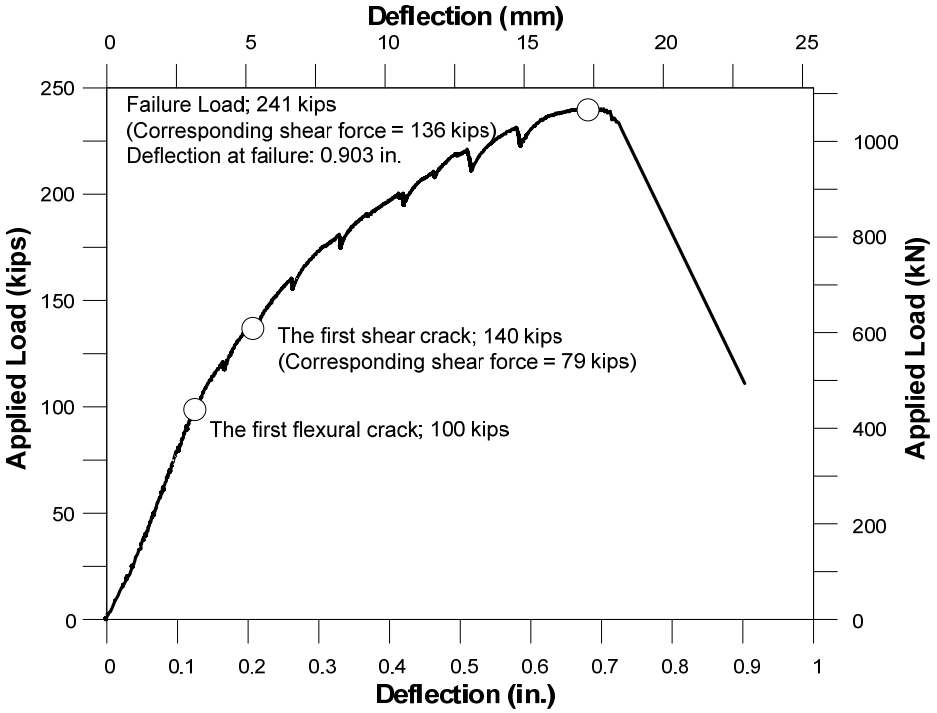

Figure 5.61 Load versus deflection response for 3 – SFRPC#1

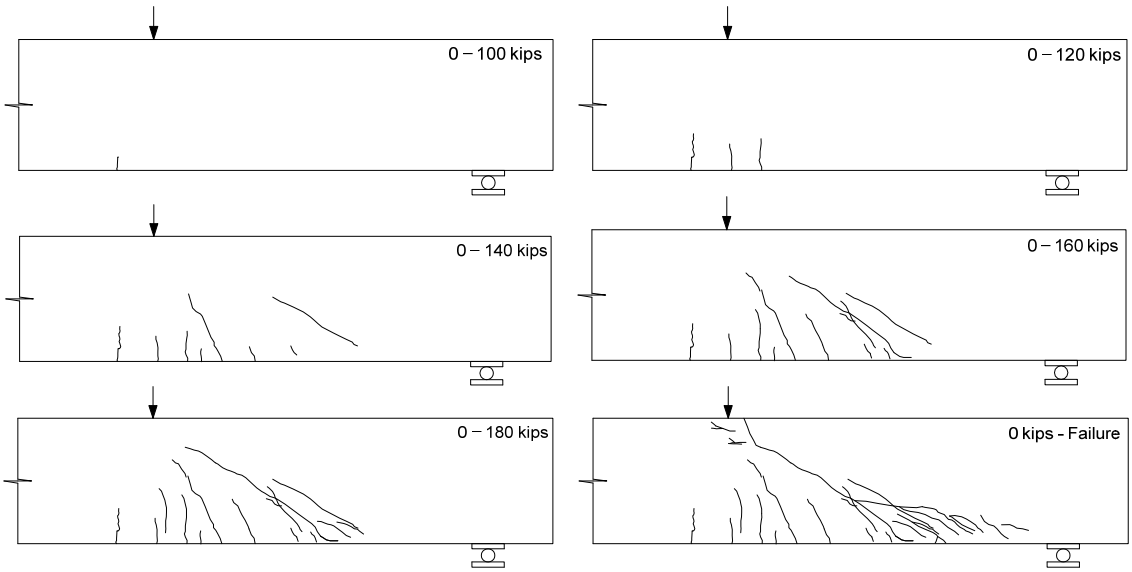

Figure 5.62 Crack pattern for 3 – SFRPC#1

(a)

(b)

(c)

(d)

Figure 5.63 Typical photos during test for 3 – SFRPC#1; (a) Prior to failure; (b) At failure; (c) Concrete crushing in compression zone; (d) Fiber pull-out

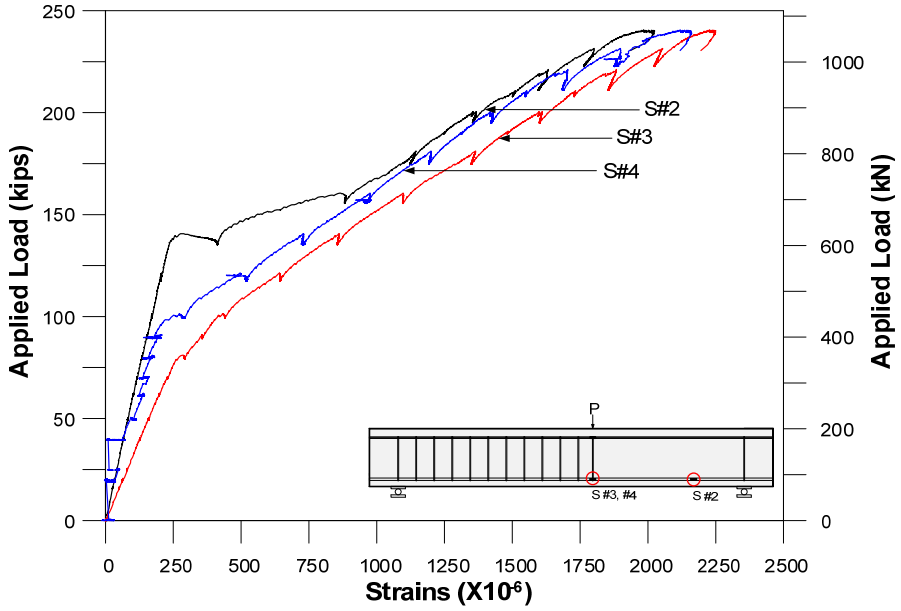

Figure 5.64 Strains in longitudinal reinforcements – 3 – SFRPC#1

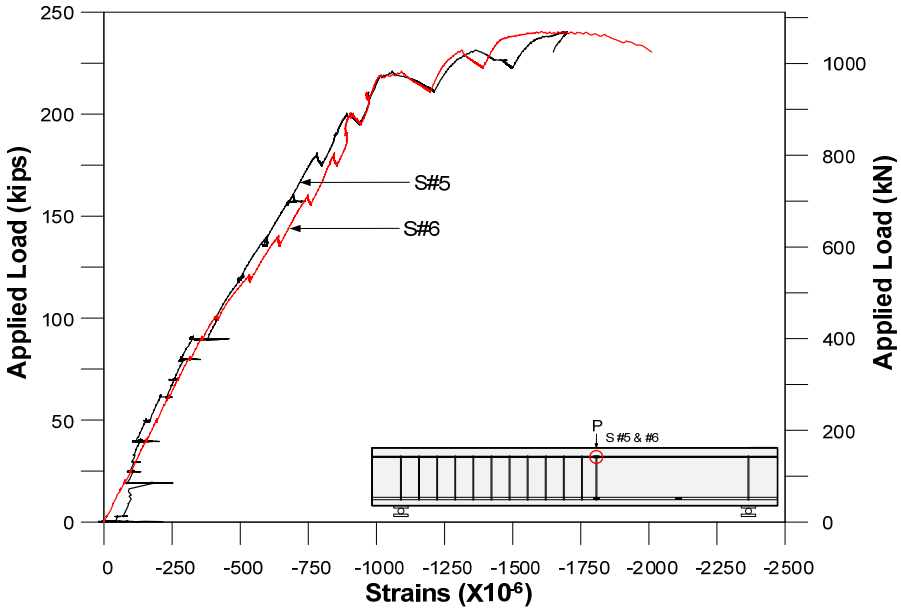

Figure 5.65 Strains in compression reinforcement – 3 – SFRPC#1

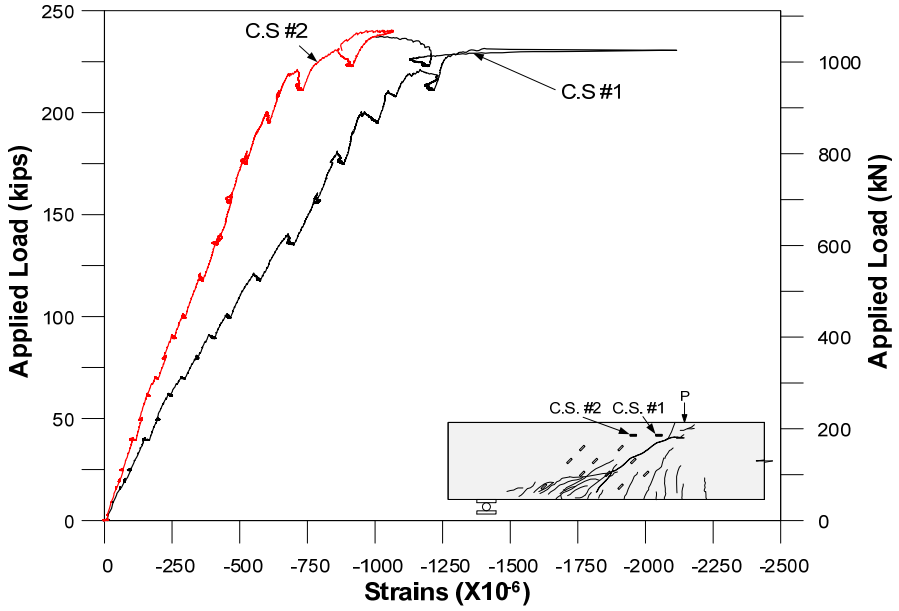

(a)

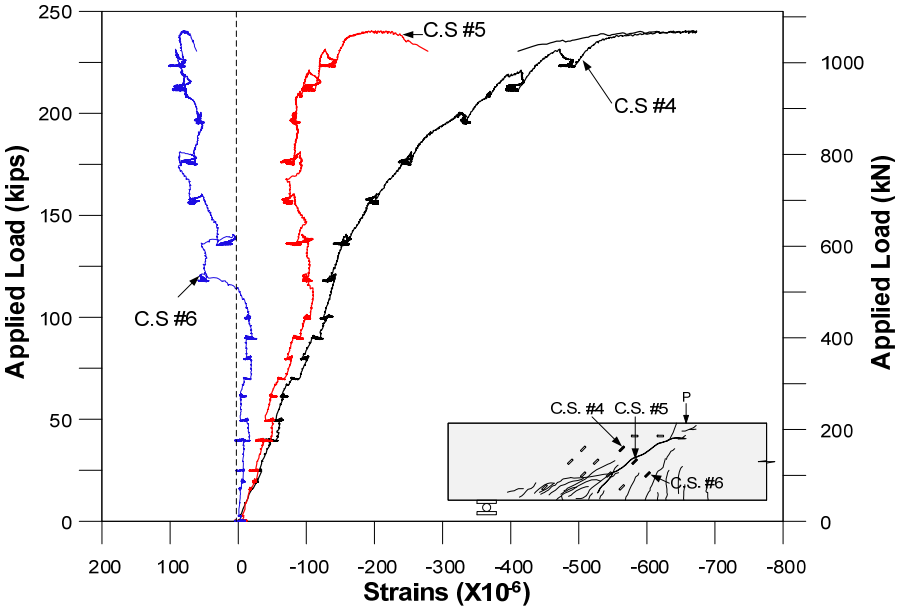

(b)

Figure 5.66 Concrete surface strains – 3 – SFRPC#1; (a) Concrete surface strains set #1; (b) Concrete surface strains set #2

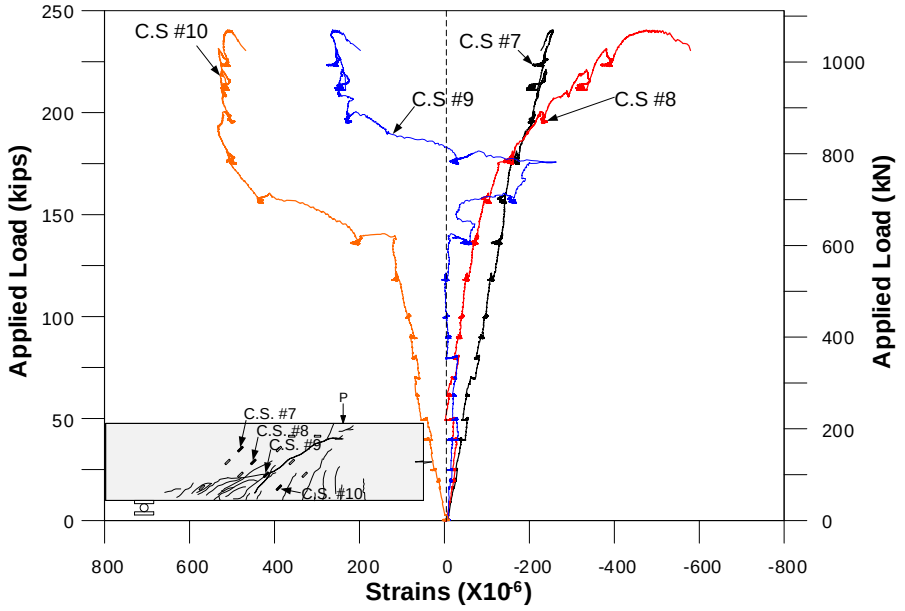

(a)

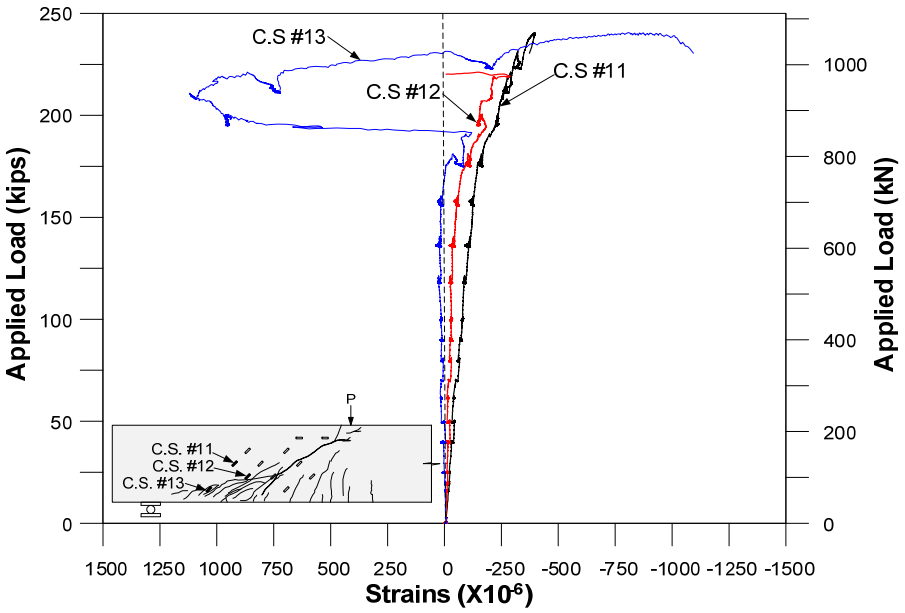

(b)

Figure 5.67 Concrete surface strains – 3 – SFRPC#1; (a) Concrete surface strains set #3; (b) Concrete surface strains set #4

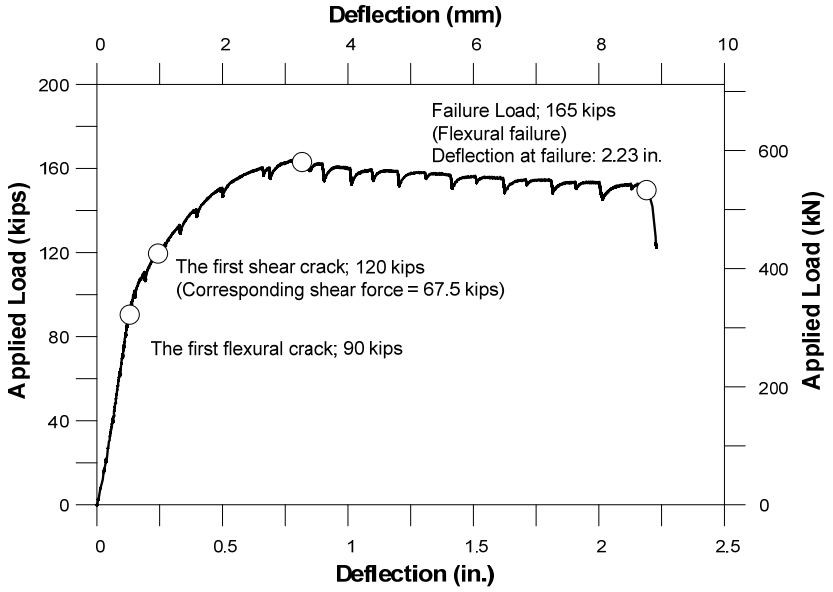

Figure 5.68 Load versus deflection response for 3 – SFRPC#2

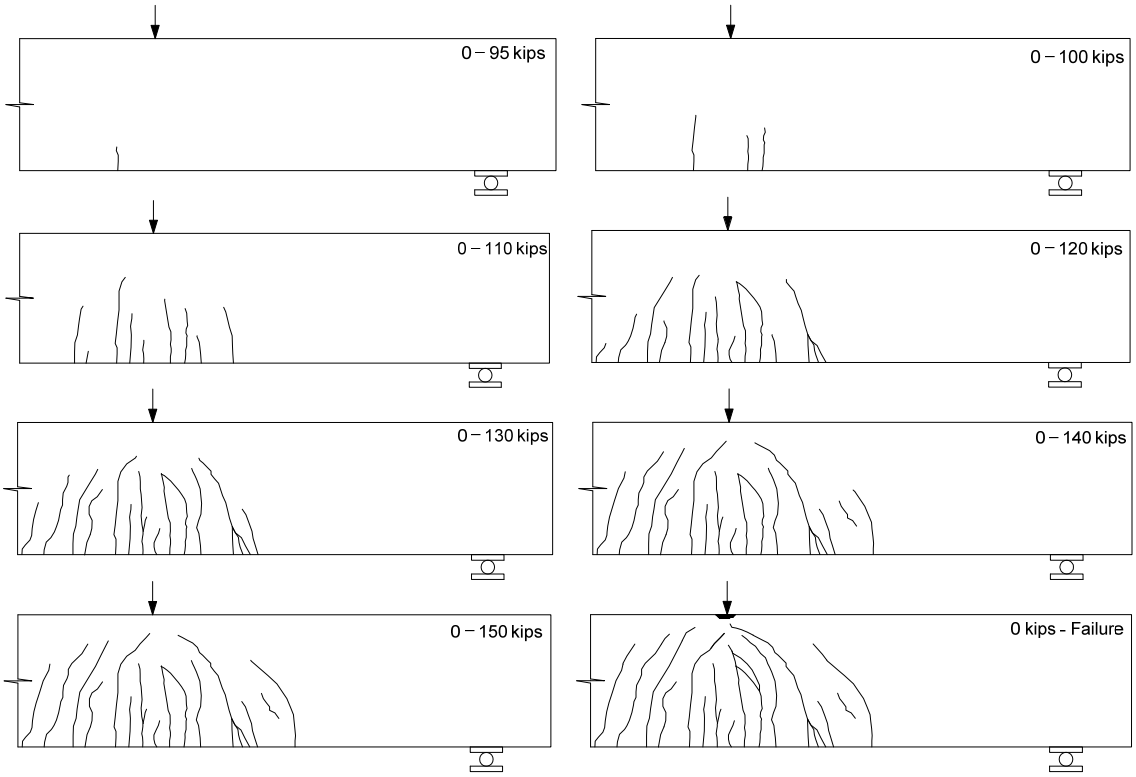

Figure 5.69 Crack pattern 3 – SFRPC#2

(a)

(b)

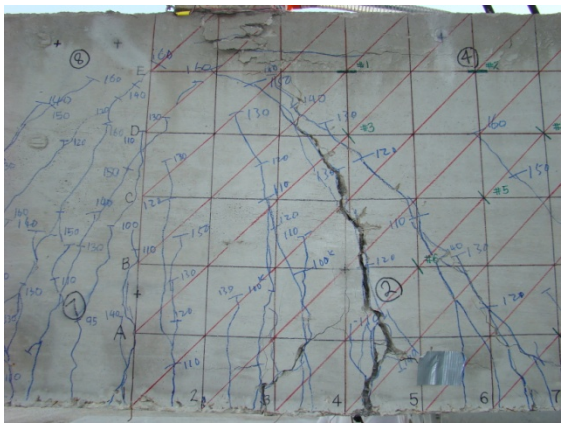

(c) (d)

Figure 5.70 Typical photos during test for 3 – SFRPC#2; (a) Prior to failure; (b) At failure; (c) Fiber pull-out; (d) Flexural crack

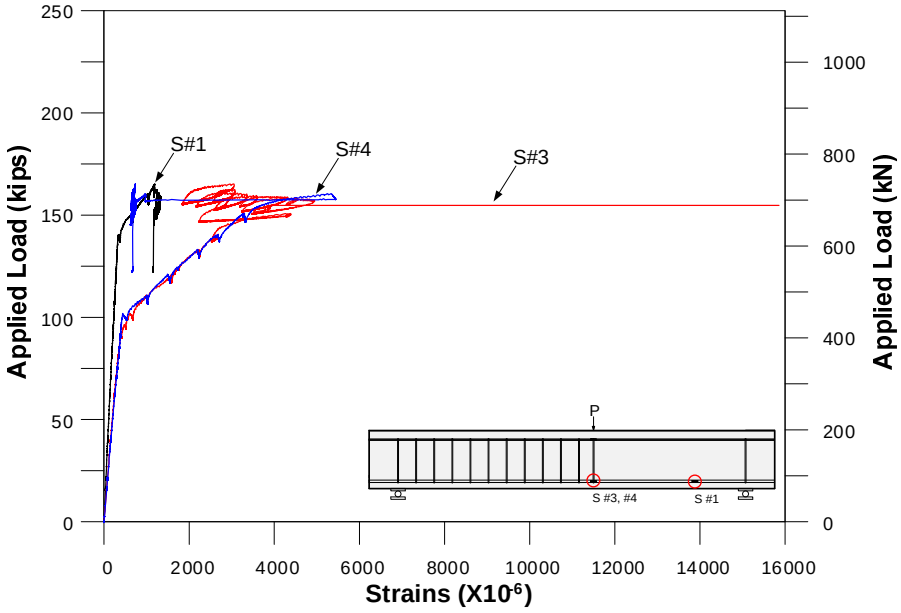

Figure 5.71 Strains in longitudinal reinforcements – 3 – SFRPC#2

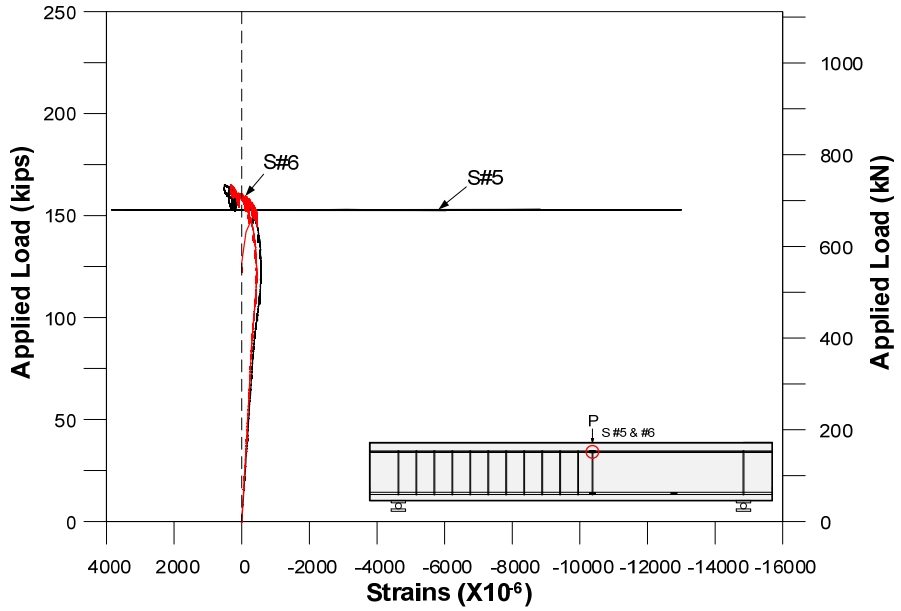

Figure 5.72 Strains in compression reinforcement – 3 – SFRPC#2

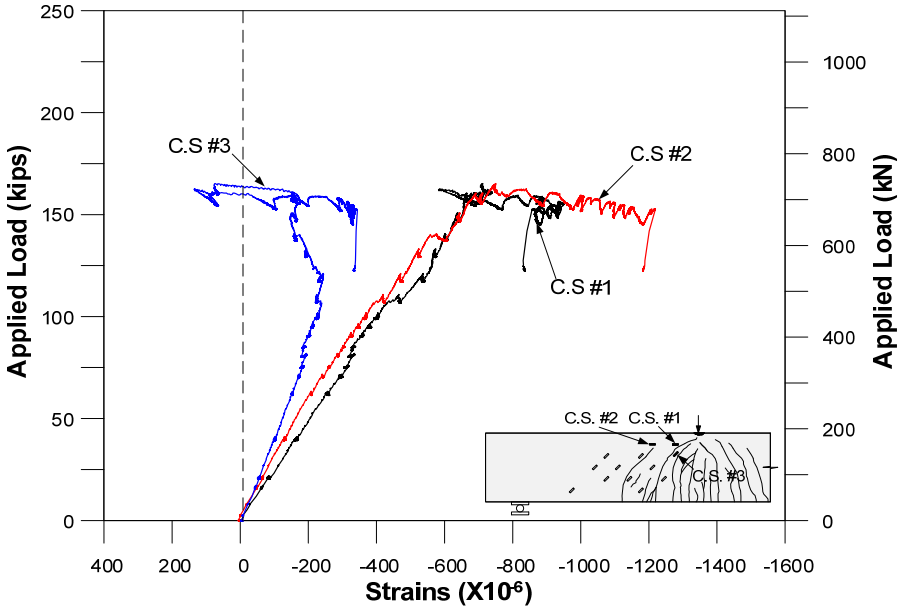

(a)

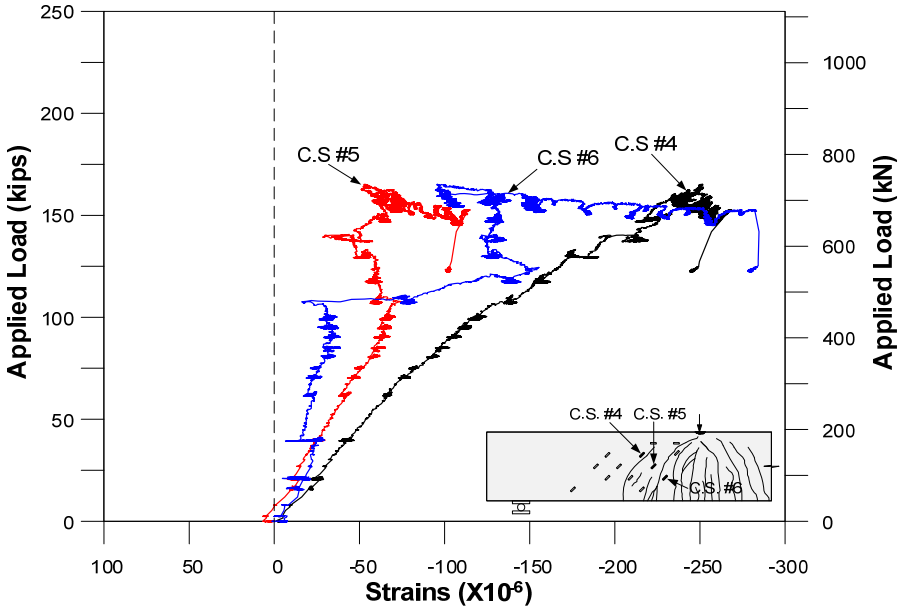

(b)

Figure 5.73 Concrete surface strains – 3 – SFRPC#2; (a) Concrete surface strains set #1; (b) Concrete surface strains set #2

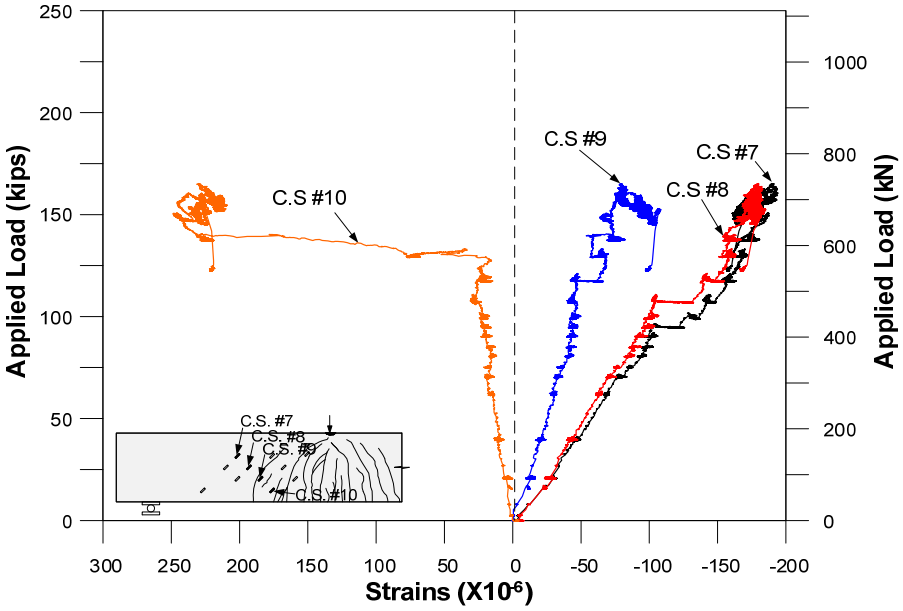

(a)

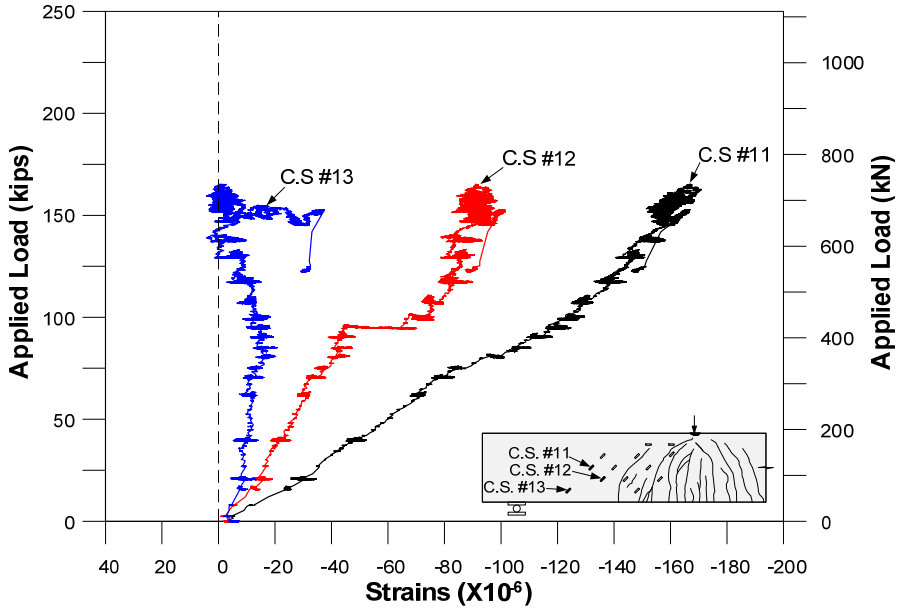

(b)

Figure 5.74 Concrete surface strains – 3 – SFRPC#2; (a) Concrete surface strains set #3; (b) Concrete surface strains set #4

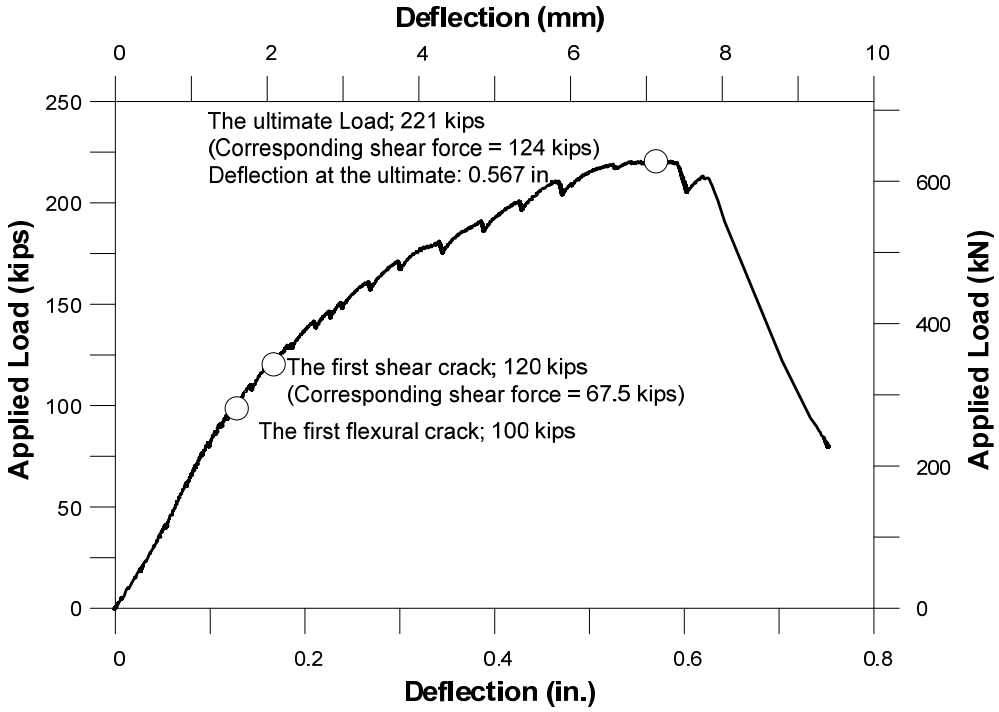

Figure 5.75 Load versus deflection response for 3 – SFRPC#3

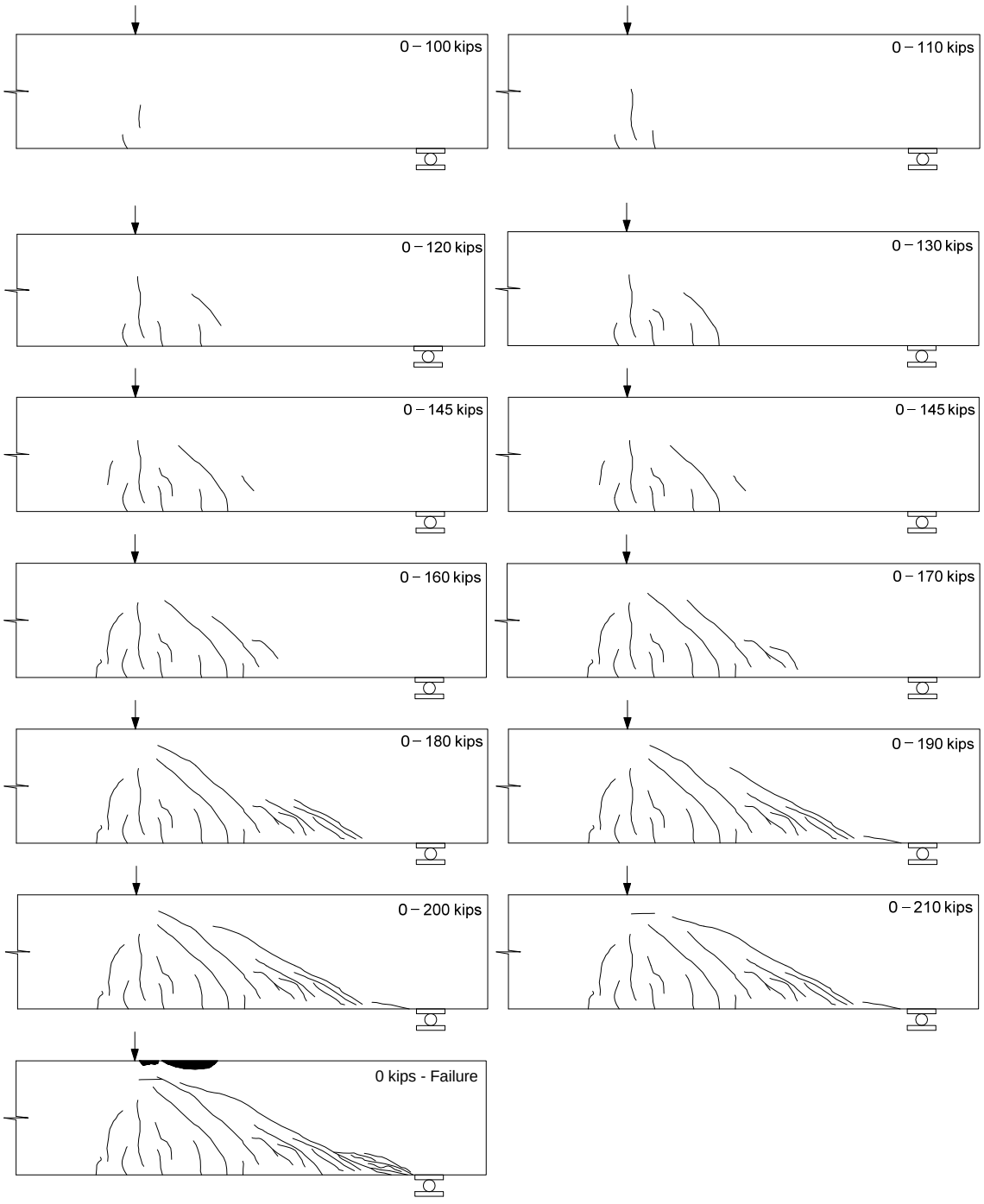

Figure 5.76 Crack pattern for 3 – SFRPC#3

(a)

(b)

(c) (d)

Figure 5.77 Typical photos during test for 3 – SFRPC#3; (a) Prior to failure; (b) At failure; (c) Compression zone prior to failure; (d) Concrete crushing in compression zone

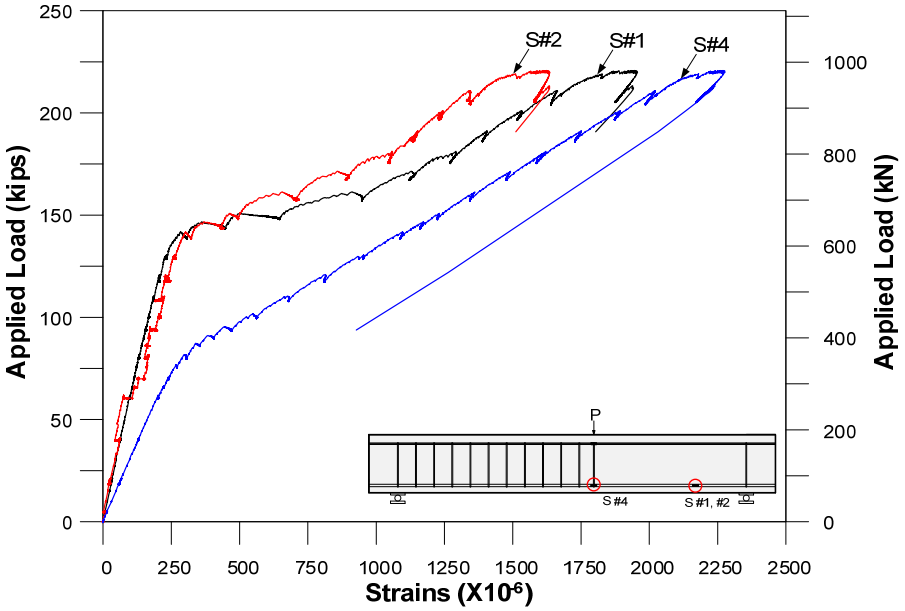

Figure 5.78 Strains in longitudinal reinforcements – 3 – SFRPC#3

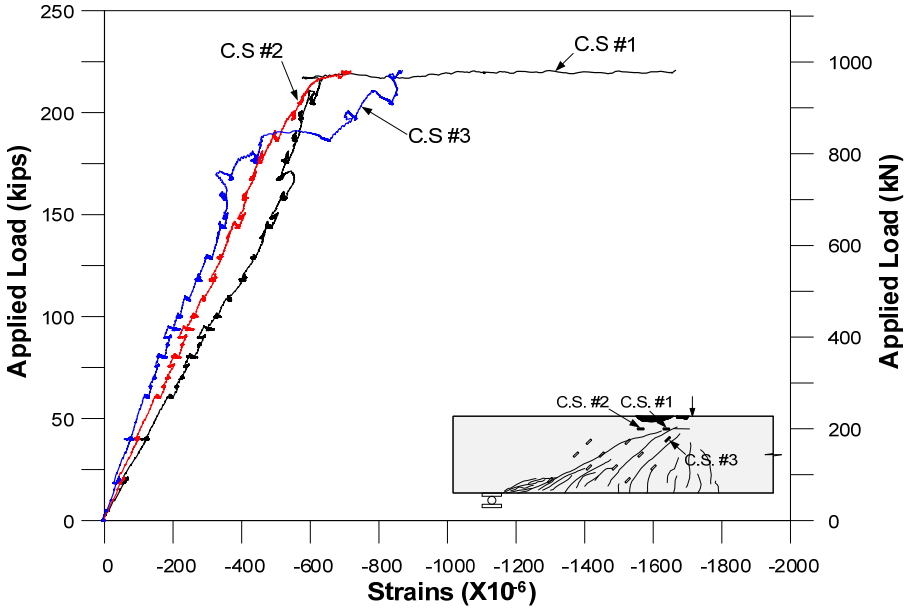

(a)

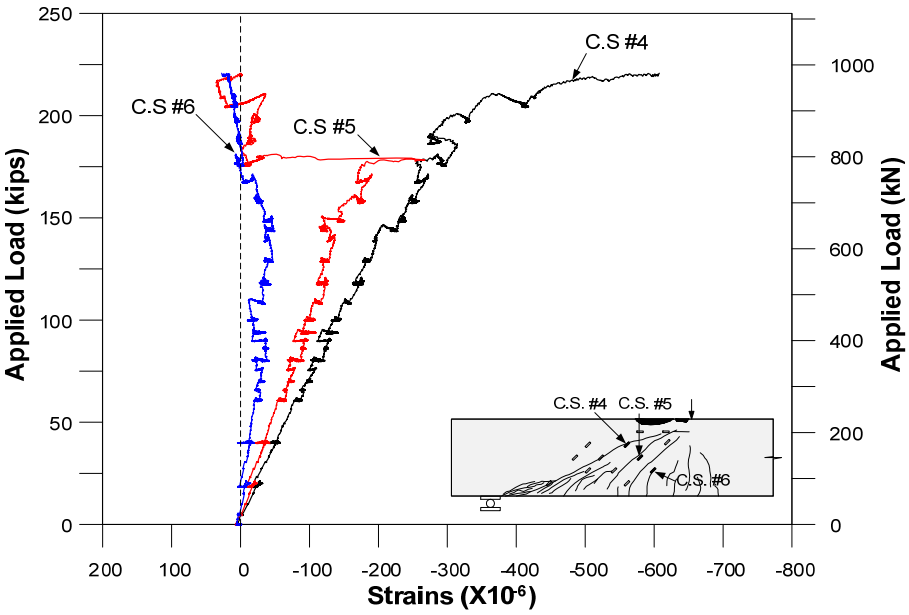

(b)

Figure 5.79 Concrete surface strains – 3 – SFRPC#3; (a) Concrete surface strains set #1; (b) Concrete surface strains set #2

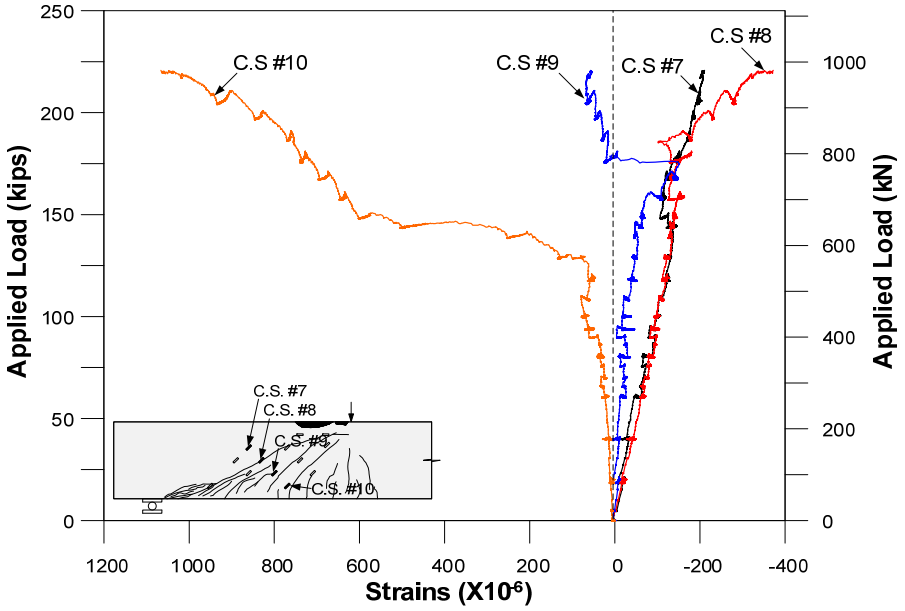

(a)

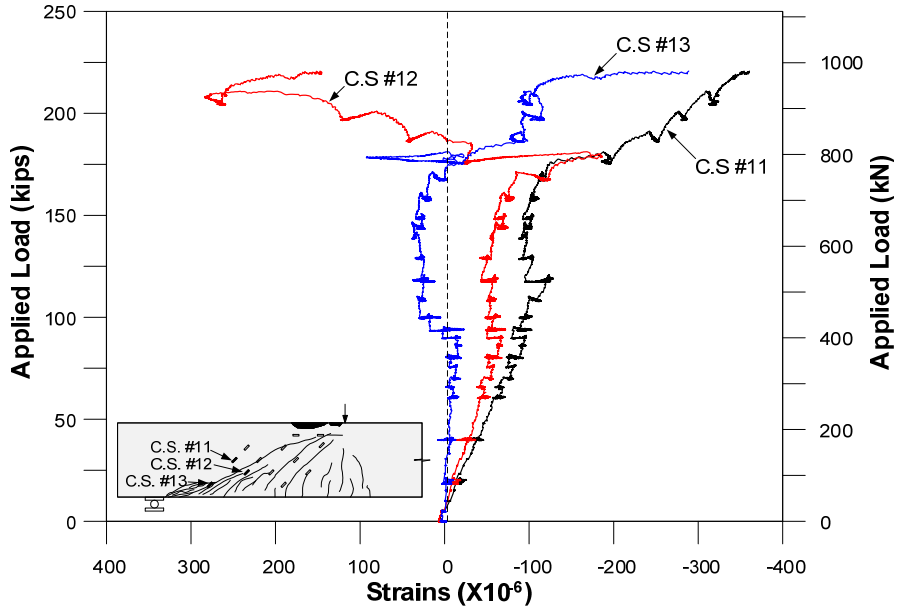

(b)

Figure 5.80 Concrete surface strains – 3 – SFRPC#3; (a) Concrete surface strains set #3; (b) Concrete surface strains set #4

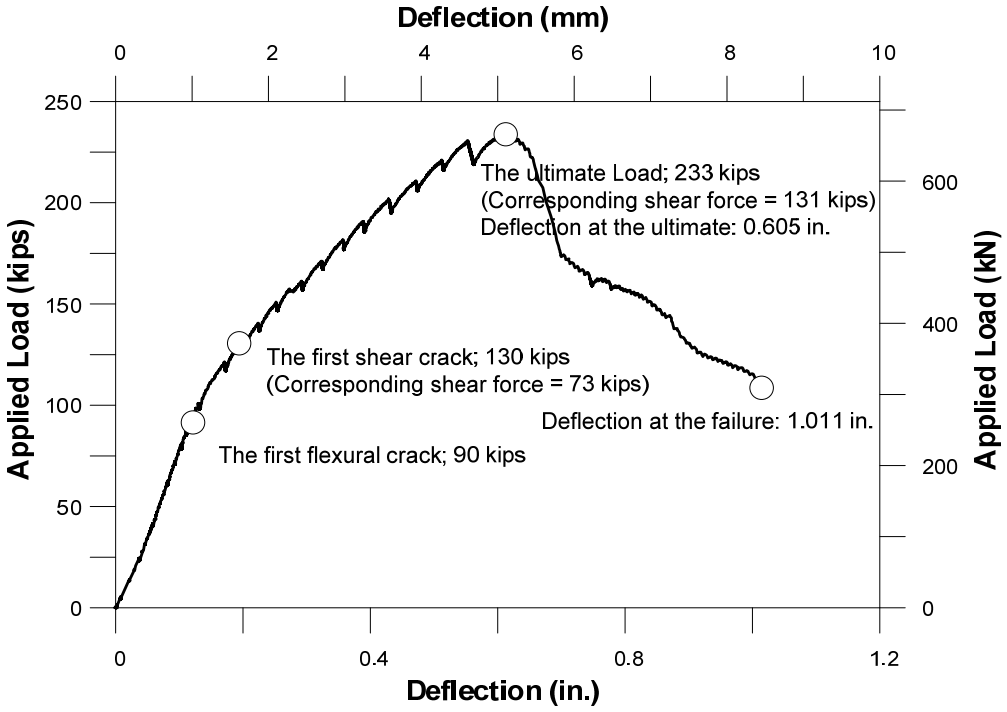

Figure 5.81 Load versus deflection response for 3 – SFRPC#4

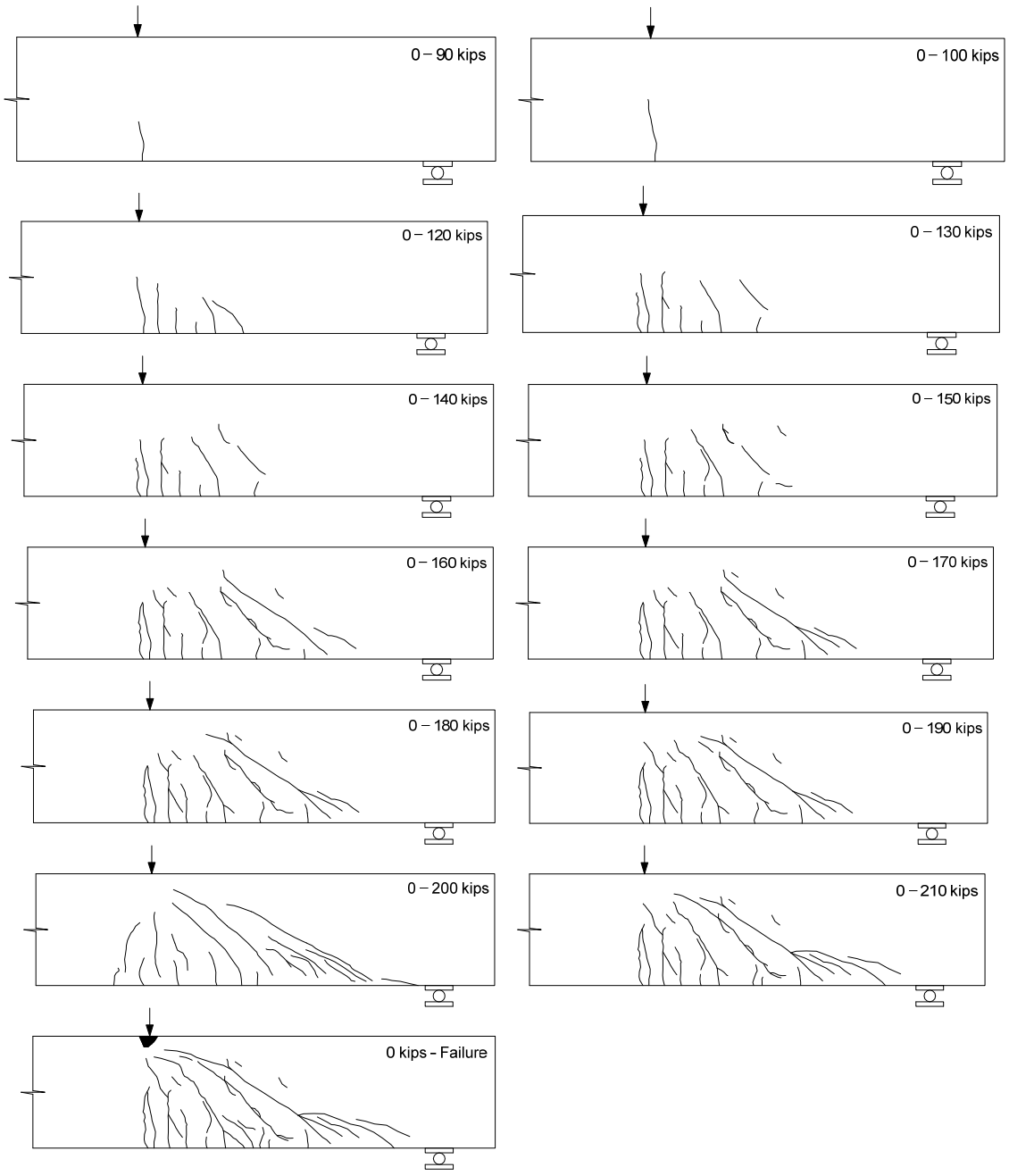

Figure 5.82 Crack pattern for 3 – SFRPC#4

(a)

(b)

(c)

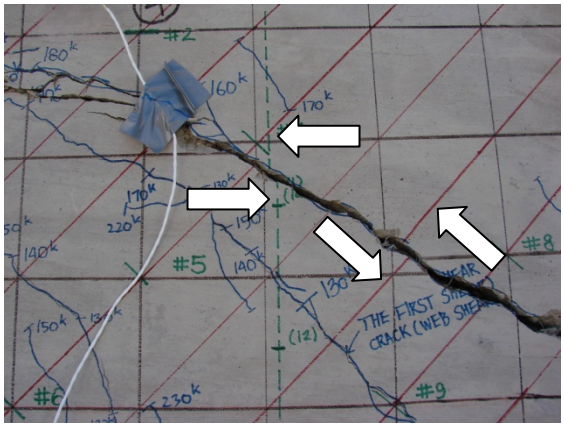

(d)

Figure 5.83 Typical photos during test for 3 – SFRPC#4; (a) Prior to failure; (b) At failure; (c) Concrete crushing in compression zone; (d) Sliding after crushing of concrete in compression zone

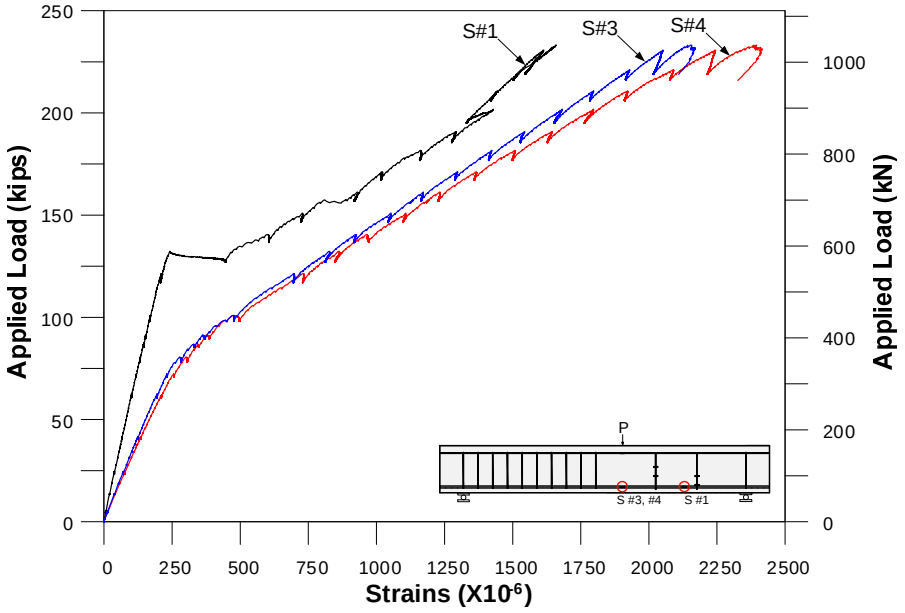

Figure 5.84 Strains in longitudinal reinforcements – 3 – SFRPC#4

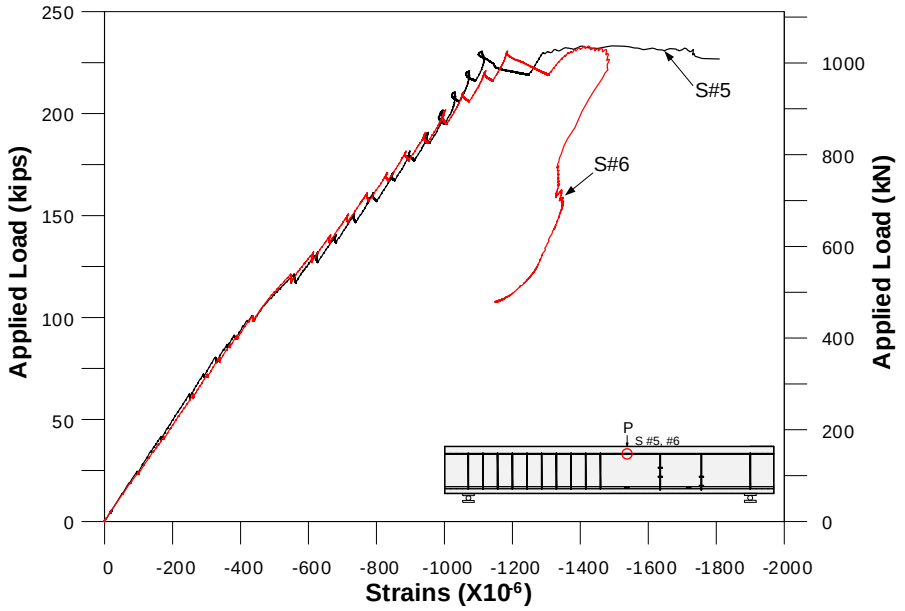

Figure 5.85 Strains in compression reinforcement – 3 – SFRPC#4

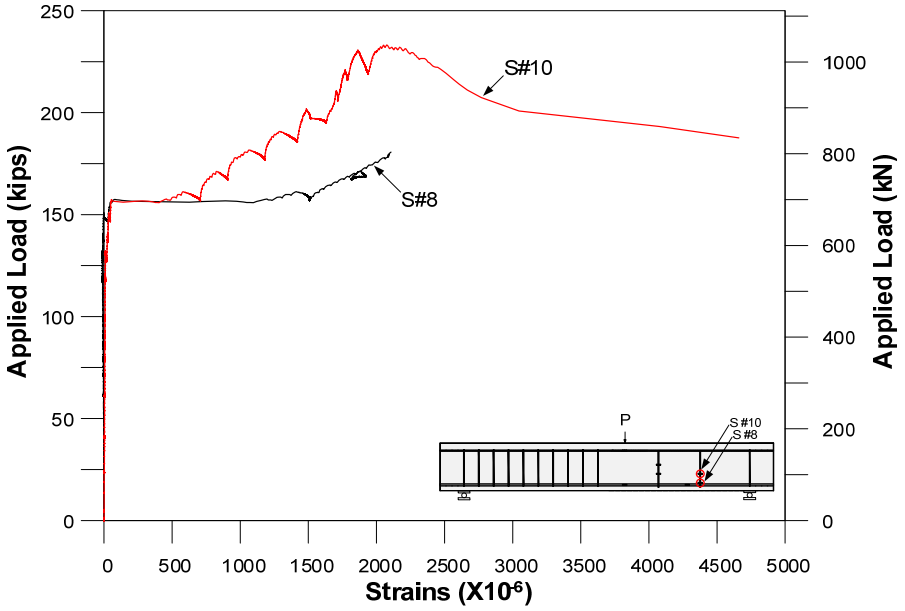

(a)

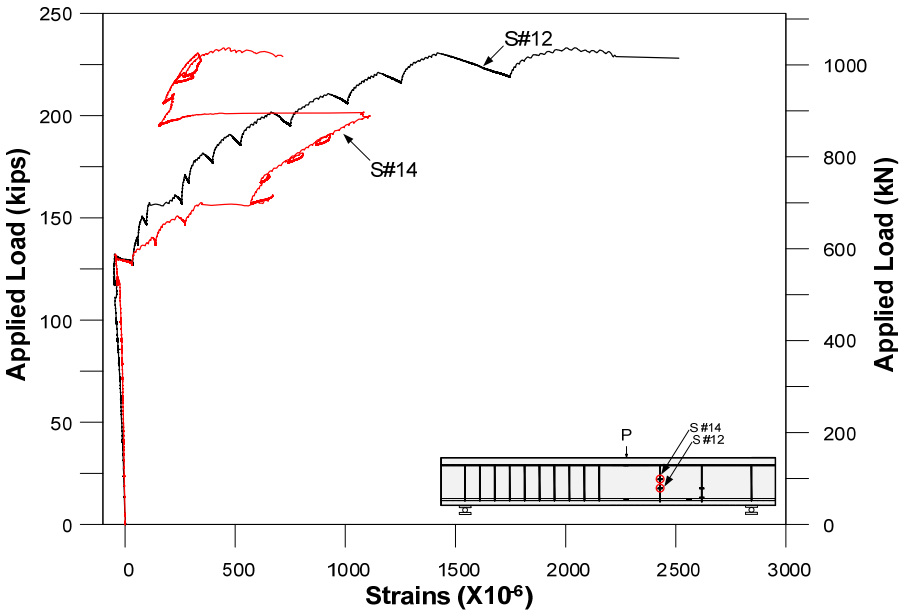

(b)

Figure 5.86 Strains in stirrups – 3 – SFRPC#4; (a) Strains in stirrup #1; (b) Strains in stirrup #2

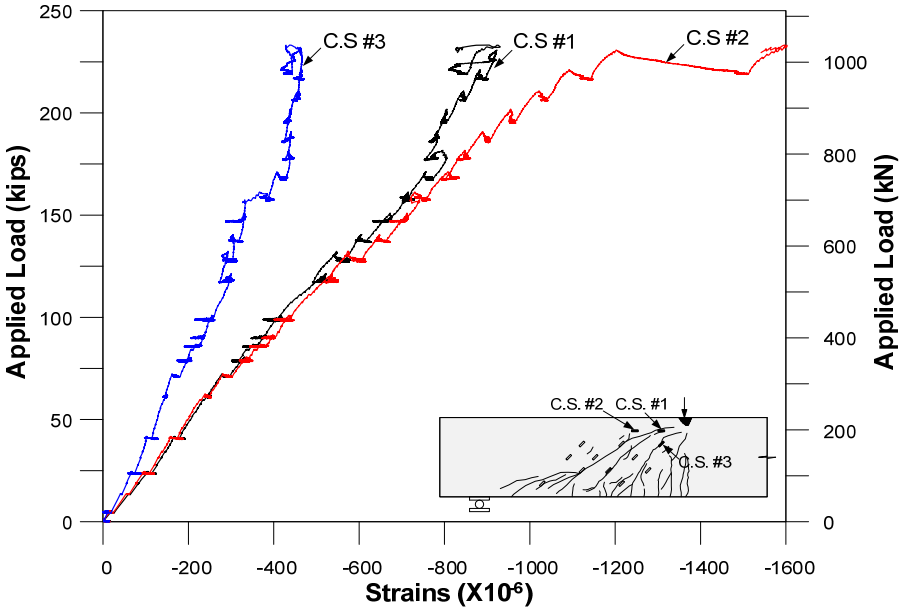

(a)

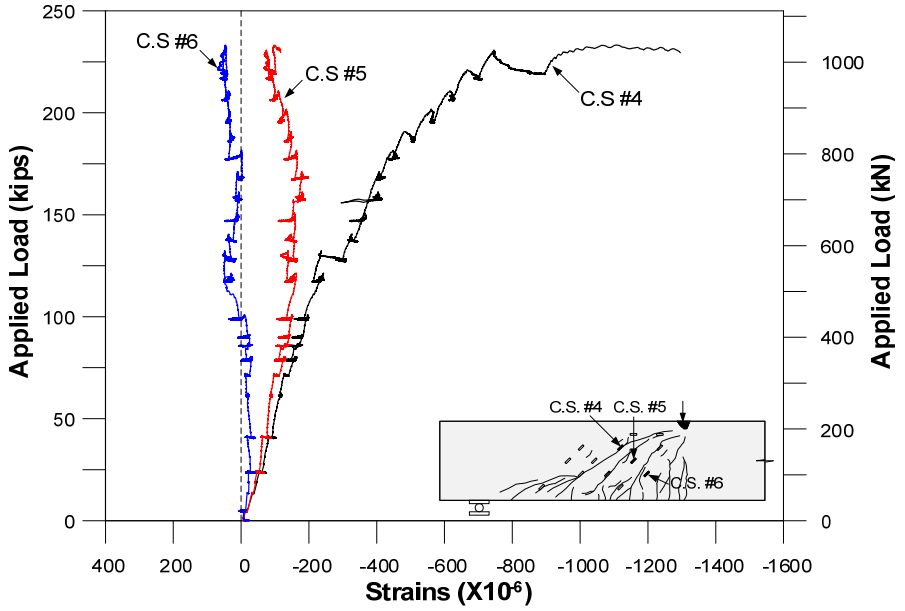

(b)

Figure 5.87 Concrete surface strains – 3 – SFRPC#4; (a) Concrete surface strains set #1; (b) Concrete surface strains set #2

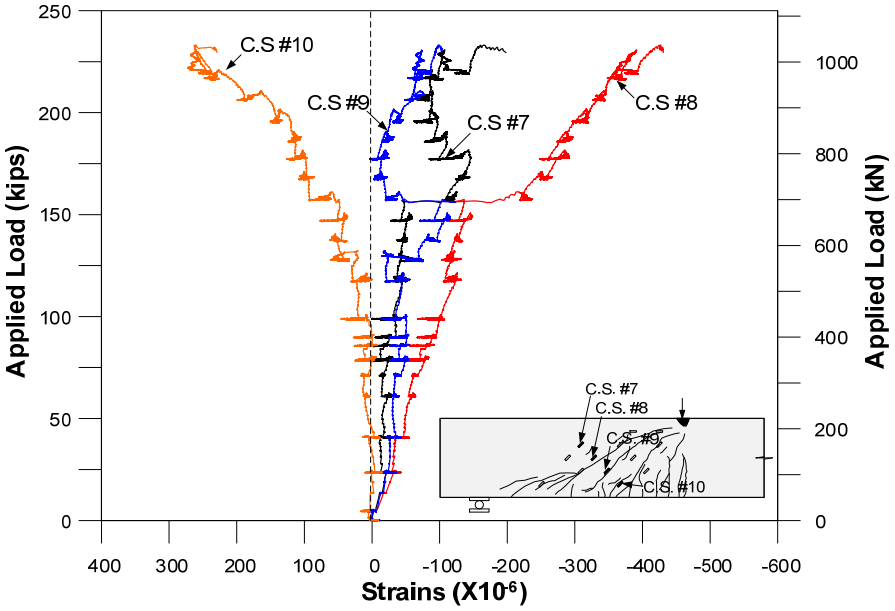

(a)

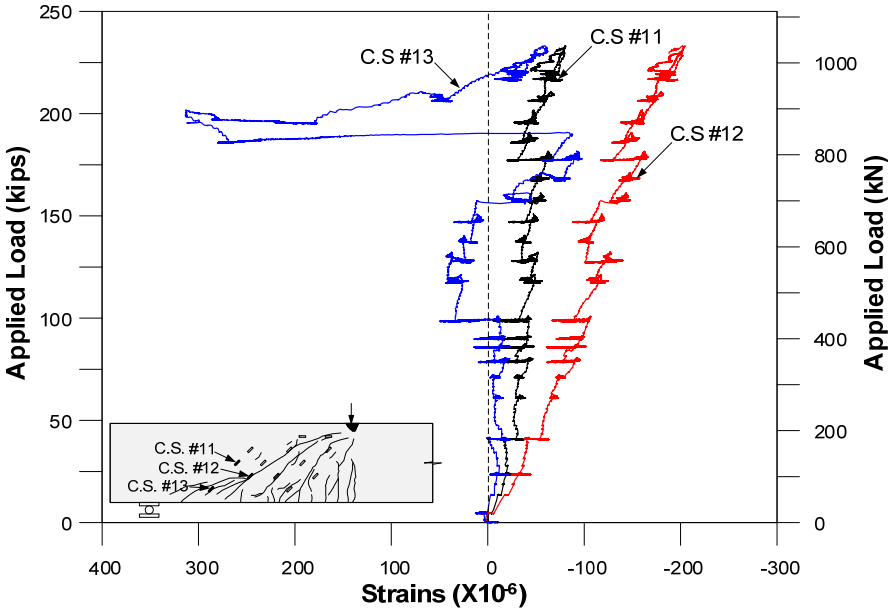

(b)

Figure 5.88 Concrete surface strains – 3 – SFRPC#4; (a) Concrete surface strains set #3; (b) Concrete surface strains set #4

CHAPTER 6

SPECIAL TOPIC – ACOUSTIC EMISSION

6.1 General

One of the most revealing ways to understand actual shear resistance and the corresponding failure mechanism is to visualize the failure process through the initiation and propagation of micro- and macro-cracks in the beams. This can be realized through the use of the Acoustic Emission (AE) technique. AE technique, which is one of the popular nondestructive evaluation methods (NDE), is generally applied to assess internal damages, such as micro-cracks in the material. By definition, acoustic emissions are that "the class of phenomena whereby transient elastic waves are generated by the rapid release of energy from localized sources within a material or the transient waves so generated" (ASTM E 1316-09a, 2009). AE is recognized as a nondestructive monitoring technique that is based on the detection of a transient sound wave that is generated by a short and rapid release of energy. This rapid energy release manifests itself in the form of a characteristic responds to an applied stress (ASTM E 1316-09a, 2009). The principle of AE is illustrated in Figure 6.1. AE is generally made by a piezoelectric material, which converts physical signals to electrical signals. AE are able to determine the location of a flaw and the extent of the damage by analyzing the time of flight of the stress wave and amplitude of the signal (Promboon, 2000). The AE

technique is extensively adopted in the aerospace and pressure vessel industries as well as health monitoring and damage evaluation of concrete structures (e.g., Ohtsu et al., 2002 and Colombo et al., 2003). In this study, it is believed that AE technique would provide valuable information regarding the initiation and propagation of cracks, which are the key parameters to reveal the shear resistance failure mechanism.

6.2 Previous Studies on AE

6.2.1 Definition and Terminology

This section will introduce terminologies that are often mentioned in AE.

AE amplitude (Peak)

The AE amplitude in AE can be defined as "The peak voltage of the largest excursion attained by the signal waveform from an emission event" (ASTM E1316-09a, 2009). The peak amplitude is the highest point of signal in the waveform, and is usually reported in a form of decibels (dB). To convert voltage to decibel, the following equation is used;

$$A = 20\log\left(\frac{V}{V_{ref}}\right) \qquad [6.1]$$

where A is the amplitude in decibels, V is the voltage of the peak excursion, and V_{ref} is the reference voltage, typically $1\mu V$ (voltage generated by 1 mbar pressure of the face of sensor).

Duration

The definition of the duration in AE can be defined as “The time between AE signal start and AE signal end” (ASTM E1316-09a, 2009). It is the time between the first and last threshold crossing and is typically displayed in microseconds.

Energy, acoustic emission signal

The definition of the energy, acoustic emission signal in AE can be defined as “The energy contained in an acoustic emission signal, which is evaluated as the integral of the volt-squared function over time” (ASTM E1316-09a, 2009).

Event (emission event)

The definition of the event in AE can be defined as “A local material change giving rise to acoustic emission” (ASTM E1316-09a, 2009). The event count is the number obtained by counting each discerned acoustic emission event once. In other words, an emission source will be counted once though the source is capture from various AE sensors.

Hit

The definition of the hit in AE can be defined as “The detection and measurement of an AE signal on a channel” (ASTM E1316-09a, 2009). When a signal induced from any physical damage is generated, the signal will be captured by each sensor and the numbers of signals will be counted as a hit.

Location, computed

The definition of the location in AE can be defined as “A source location method based on algorithmic analysis of the difference in arrival times among sensors” (ASTM E1316-09a, 2009).

Signal strength

The definition of the signal strength in AE can be defined as “The measured area of the rectified AE signals with units proportional to volt-sec” (ASTM E1316-09a, 2009).

6.2.2 AE Data Analysis

6.2.2.1 AE Source Location

The location of an AE source can be usually key information for the damage assessment during evaluation. For identifying the location, multiple AE sensors are required. As hits are recorded by each sensor, the source can be located by knowing the velocity of the wave in the material and the difference in hit arrival times among the sensors. The source location technique assumes that the velocity of the AE waves is constant in a material. The schematic view of the way how to find a location of damage is presented in Figure 6.2. To identify a location of an event in planar, at least three AE sensors are required, in addition, accurate arrival times must be available.

6.2.2.2 Amplitude versus Applied Load

The plot of amplitude versus applied load is commonly used in many AE applications (Carey, 2008). The correlation plot shows the types of damage and different failure mechanism at a certain loading stage. The level of the amplitude represents damage, as shown in Figure 6.3. For example, fiber breakage and breaking can be represented by amplitudes of 60 dB and 80 dB respectively.

6.2.2.3 Cumulative Signal Strength

When damage occurs in a structure under a certain level of stress, there will be energy released. Part of that energy is transformed into acoustic emission, therefore, the energy or signal strength of the hit should be directly related to the severity of the damage. The cumulative signal strength can be extracted from each sensor meaning more damage occurs close to a sensor, which generally shows a higher cumulative signal strength.

6.2.2.4 Amplitude versus Duration Time

The plot of amplitude versus log duration can be useful for determining whether or not AE data is genuine. The genuine data generally creates a banded shape while the nongenuine hits appear in the area outside of the band as shown in Figure 6.4.

6.2.2.5 Kaiser and Felicity Effects

The Kaiser effect is defined as “the absence of detectable acoustic emission at a fixed sensitivity level, until previously applied stress levels are exceeded.” (ASTM E 1316a-09, 2009). It is possible for an existing defect to not expand or propagate until the former stress level is exceeded, thus, no acoustic emission is generated normally. The presence of the Kaiser effect indicates good integrity in a material or structure. On the other hand, the Felicity effect is described as “the presence of detectable acoustic emission at a fixed predetermined sensitivity level at stress levels below previously applied stress” (ASTM E1316-09a, 2009). Unlike the Kaiser effect, a material or structure generates emission during a steady holding load or reloading before reaching the previous maximum stress. The Felicity effect can be observed by applying constant loads and watching if the emissions continue to occur. The presence of the Felicity effect indicates substantial and/or critical structural defects.

6.2.3 Application of AE

The advanced technique, acoustic emission (AE), has been successfully used in health monitoring and damage evaluation in the aerospace and pressure vessel industries as well as in civil engineering structures, such as concrete structures. It is worth review of all the applications of AE, but this section will only describe its application to concrete structures.

Hearn and Shield (1997) applied AE techniques to conventionally reinforced and prestressed concrete beams to observe initiation and propagation of cracks induced by bending stress. The beams were loaded in a cyclic pattern and the Kaiser and Felicity effects for concrete members were investigated. Their test results clearly indicated that the observed formation or propagation of cracks in concrete was preceded by a significant increase in AE activity rate. AE activity could be a viable method to identify initiation and/or propagation of cracks in concrete members. The source location of these cracks also could be accurately determined within a few centimeters of error, which can be eliminated by increasing the number of AE sensors.

Ohtsu, et al., (2002) exploited concepts of *Load ratio* and *Calm ratio* for assessment of damage. The load ratio is defined as the load at the onset of AE activity in the subsequent loading divided by the previous load. The calm ratio is described as the number of cumulative AE activities during the unloading divided by the total AE activity during the last loading cycle up to the maximum load. In practice, damage assessment is proposed to classify the damage levels, shown in Figure 6.5. As can be seen in Figure 6.5, cracks with wider (> 0.5 mm) Crack Mouth Opening Displacement (CMOD) belong to the “Heavy damage” category, which is the upper-left portion of the classification graph, in contrast, less than 0.1 mm of crack with was categorized as the “Minor damage”, which is the lower-right portion.

Colombo, et al. (2003) used a concept of “b-value”, which is derived using relationship of followed equations;

$$\log_{10} N = a - b' A_{dB} \quad [6.2]$$

$$b = b' \times 20 \quad [6.3]$$

where N is the incremental frequency (i.e., the number of events with magnitudes), a is empirical constants, and A_{dB} is the peak-amplitude of the AE events in decibels. The b-value analysis is based on a relationship between the frequency and amplitude of events. For example, micro-cracks generate multiple events with less amplitude while macro-crack generates few events at much greater amplitude. This could then be used as an alternative way to process and interpret data recorded during a local AE monitoring. The b-value can be obtained from the log frequency – magnitude graph, which was plotted and their linear trend calculated using the least-squares method of fitting a curve, and its slope represented the b-values with multiplying by 20. An example of a b-value is graphed in Figure 6.6. Colombo et al. (2003) had tested a reinforced concrete beam designed to represent a concrete bridge and the damage occurred and the development of the crack and its opening was investigated visually and by AE. By comparing numerical values from the AE and the appearance of cracks on the beams, some quantitative considerations were drawn and are summarized in Table 6.2. They concluded that the b-value correlated with the fracture process of the concrete and to the degree of localization of the damage, and it could be used to interpret data obtained by a "local monitoring" of concrete bridges.

Acoustic emission techniques were employed to investigate the process of fracture formation in large and shear-critical reinforced concrete beams and to gain improved insight into the mechanisms of shear failure (Katsaga et al. 2007). The authors used large sensor arrays (24 sensors) to observe fracture processes throughout the load history as well as smaller and more concentrated sensor arrays to reveal complex spatial and temporal fracture development. From the experimental study, the visible cracks at the surface of the concrete beams closely corresponded to the AE event locations, as shown in Figure 6.6. In addition, the AE events revealed crack distributions inside the beam that were not identified by surface inspection. Studying the rate of AE activities and their corresponding locations allowed for the investigation of the "spatial" and "temporal" micro-crack development and of the different stages of shear fracture propagation, as illustrated in Figure 6.7 and 6.8. The loading stage A in the Figure 6.8 represented the initiation of a few micro-cracks, and the stage B represented the micro-cracks started to nucleated. The stage C and D represented the initiation of macro-cracks and these propagations. It should be noted that the initiation of the macro-crack showed the higher numbers of AE hits compared to these propagations.

The AE technique was applied to steel fiber reinforced concrete (SFRC) as well. Hauweart et al. (1999) applied the AE technique to recognize the first cracking strength in SFRC. In fact, it is difficult to capture the moment when the first crack initiates by observing the load versus deflection curve especially for SFRC with high contents of steel fibers since the load versus deflection curve may be nonlinear when the first crack

developed. To distinguish the linear and nonlinear phases of the curve can be problem of the scale of the curve (e.g., a curve appears to be linear but it becomes nonlinear when the scale is enlarged a certain point). To overcome this issue, the authors applied AE sensors to capture the first cracking strength of SFRC and its goal was successfully attained. AE technique was confirmed with another NDE technique called “Ultrasonic.” They revealed that the number of events in the low frequency range will increase when micro-cracks initiated and for macro-cracks, the number of events in the high frequency range of the AE spectrum will increase. The moment of initiation of those cracks was confirmed by the fact that the velocity and energy of propagation dropped when it met discontinuity due to those cracks.

Soulioti et al. (2009) had employed AE to SFRC to investigate the AE activity (hit) and fracture mode. They conducted the third – point bending test with varying fiber contents from a 0% to a 1.5% volume fraction. They observed that AE activities increased as the fiber content increased, as can be seen in Figure 6.9. It is clearly seen that the AE activity increased after reaching the peak strength in SFRC since SFRC showed a residual strength obtained from the fiber pull-out mechanism, which does not existed in plain concrete. They also investigated the fracture mode in SFRC using parameters in AE such as RA value and average frequency, which are defined as the ratio of the rise time to the waveform amplitude and the number of threshold crossings (counts) divided by the duration of signal, respectively. They revealed that lower RA values indicate more tensile fracture events and higher values indicate more shear cracks. They

recommended an RA of 2000 $\mu s/V$ indicates tension while an RA of 4000 $\mu s/V$ indicates shear. In addition, they concluded that the shift from higher to lower values of average frequency indicated the shift of the cracking mode from tensile to shear, which correspond to an average frequency ranging from 60 kHz to 35 kHz respectively.

6.3 Experimental Program

AE is applied throughout all phases of the study. Since the acoustic emission data showed locations of the events in real time, the technique was used to recognize the location and the initial of crack during testing, i.e., the locations of events were focused to check cracks during tests.

6.3.1 AE Sensor and Coordinate

Seven R30S AE sensors, which have a resonance frequency of 300 kHz, were attached on the north face of the beams with a selected coordinate. Due to the size of the beams and the limited number of the sensors, the short shear span was targeted for AE analysis. As mentioned previously, at least three sensors were required in a 2-D planar such that the optimized coordinate was selected; as mapping regions connecting three sensors, the targeted span could be covered sufficiently. It should be noted that three sensors are a minimum numbers of sensors to capture the location of events such that more numbers of sensors generally provide more accurate locations of events. Detailed information regarding the coordinates of the AE sensors is provided in Table 6.1 and

Figure 6.10. For consistent analysis, the same coordinates were employed throughout all beams.

6.3.2 Instrumentation of AE Sensor

AE sensors were attached on the beams at the specific locations as followed procedure; the surfaces where AE sensor would be mounted were cleaned with a soft rag to remove dust, and then cleaned again with a wet rag. A dry rag finalized the cleaning. After cleaning, hot glue was applied to the bottom part of a sensor, and then mounted on the cleaned surface. The sensor was held in place, so it would not slide until the sensor was mounted perfectly. A small strip of duct tape was used to provide additional restraint to the sensor to protect it from damage induced by falling if enough sufficient restraint was not provided by the glue. Typical photos of AE sensor instrumentation is shown in Figure 6.11. Carey (2007) studied hot glue as a coupling material, which was used to remove the air gap between AE sensor and surface enabling that the wave transmits without diffusion, and concluded that the hot glue is suitable to transmit elastic waves. As shown in Figure 6.12, each sensor was connected to a pre-amplifier, which is generally necessary since the voltage from the piezoelectric material is low. The pre-amplifier has the ability to not only amplify a signal but also filter out noise, which could be characterized with low value of amplitude. The noise level was set as 40dB meaning any signal below 40dB was not recorded. The pre-amplifiers were connected to the AE data acquisition system so called micro DISP^{TM} manufactured by the Mistra group such that all parameters from the AE sensors were automatically

recorded and some parameters such as hits, location of events, and waveforms, were visible by data analysis software in real time. The real time visible data analysis system helped identify the locations of initiated cracks during tests. Prior to testing, a pencil lead break was done to figure out the wave velocity for PC and SFRPC, which is essential to identify an accurate location of events. The PC and SFRPC beams showed the same wave velocity; the wave velocity was determined to be 1.10×10^5 ft/s. The collection of data from Vishay DAQ (e.g., load, deflection, strains for concrete surface and rebar, etc) and AE DAQ started at the same time so that they were synchronized in post analysis with time.

6.4 Experimental Results

6.4.1 The First and Second Phases

Figure 6.13 and Figure 6.14 show the locations of events in 1 – PC and 1 – SFRPC beams, respectively. The events detected by AE sensors indicate the occurrence of micro-cracking, which is the consequence of internal stresses. Compared the Figure 6.13 and 6.14, the number of AE events in SFRPC beam was significantly greater than that in PC beam, which indicates that more section underwent to resist load in SFRPC beam. It has an agreement with the crack pattern; SFPRC beam showed the multiple shear cracks while PC beam exhibited single shear crack. In addition, it is interesting to note that the location of number of AE events in SFRPC beam gradually shifted from the loading point towards the supports, which can be represented by number of red dots in the Figure. This shift can show the force transfer process as load increased.

Therefore, the load was transferred from the loading point to the support after the initiation of the shear crack, which created internal damage along the path.

In the second phase, 2 – PC#1 and 2 – PC#2 beams showed similar location of events pattern with the 1 – PC#1 beam. However, 2 – PC#3 beam showed more events above the first shear crack similar to the 1 – SFRPC beam. It should be noted that 2 – PC#3 beam showed higher the ultimate strength; the normalized shear strength was $5.2\sqrt{f'_c}$. By observing the AE data, the higher applied load could be induced by the load transfer mechanism, which was observed in the 1 – SFRPC beam; the load was transferred through the strut lying above the shear crack. Since the load was transferred from the loading point to the support directly, there were internal damages, which could be represented by events, in the uncracked section above the shear crack. Thus, the enhanced shear strength could be postulated by this load transfer mechanism. Therefore, even in PC beam, the enhancement of the shear strength might be expected if the load would be transferred from the loading point to the supports directly through the uncracked section for any reason. In the SFRPC beams, 2 – SFRPC#1 and 2 – SFRPC#3 beams showed less amount of number of events than 1 – SFPRC beam. That might be because of the not-well controlled the quality of steel fibers as stated in Chapter 3 and 5. The glued bundle steel fibers were not well resolved such that it prevented well distribution of fibers, and it was shown in AE data by fewer amounts of events. Nevertheless, most of events occurred above the shear crack in 2 – SFRPC#3 beam, and the locations of events were shifted close to the supports while load

increased, which could conclude that the load transfer mechanism in 1 – SFRPC and 2 – SFRPC beams was equivalent.

6.4.2 The Third Phase

Detail AE analysis was conducted in the third phase study. The graphs of duration versus amplitude, amplitude versus applied load, number of hit versus applied, and location of events varying loading stages were plotted. Each plot will be discussed in the following section.

6.4.2.1 Duration versus Amplitude

As stated earlier, the plot of duration versus amplitude could represent genuine data by shaping a type of band. The Figure 6.27, 6.28, and 6.29 show the duration versus amplitude plots for the beams in the third phase. The Y-axis represents duration, which is in log scale, and the X-axis is amplitude in units of decibels. Most of the data generally shaped a band. Some of the data was imprinted out of the band rage; most of non-genuine data points were scattered in the upper portion of the shape, which means that non-genuine data was induced by mechanical rubbing (see Figure 6.4). It is possible that the non-genuine data was generated by the bearing plates at the loading point mostly since sensor number #4 and #8 were installed close to the loading point. However, as can be seen in Figure 6.27, 6.28, and 6.29, AE data points generally showed the band shaped pattern, thus, it can be said that the data was valid in the most part. In consequence, the data was genuine to analyze.

6.4.2.2 Amplitude versus Applied Load with Time

As mentioned previously, there is an intimate relationship between amplitude and the level of damage (see Figure 6.3); higher amplitude generally indicates severe damage. Therefore, the amplitude may provide useful information regarding the assessment of internal damage. The plots of amplitude versus applied load with testing time are presented in Figure 6.30, 6.31, and 6.32. By observing the graph for 3 – PC#1 beam (Figure 6.30 (a)), the amplitude was little above 80 dB when the first visible flexural crack initiated. However, it showed 100 dB at 100 kips, where the first shear crack developed. In the PC beam, a shear crack may generate a high level of energy release, as consequence, higher amplitude and more number of hits exhibited. It has an agreement with the observed the crack pattern; a first flexural crack had narrow and short crack width and length, respectively compared to the first shear crack. Compared with PC beam, first of all, it is interesting to note that there were more number of hits with higher amplitude, higher than 80 dB, prior to the first visible crack in the 3 – SFRPC#1 beam as can be seen in Figure 6.30 (b). It can be said that there might be internal damage before the crack was observed on the surface. However, unlike with PC beam, the damage was not able to be visible since steel fibers took a role as load resistance. This pattern was also observed in other SFRPC beams as well (see Figure 6.31 and 6.32). In addition, this can be evidence that SFRC could need more energy in order to have same level of damage, such as initiation and propagation of cracks, compared to PC. As consequence, the initiation and propagation rate of crack could be delayed in SFRPC beams. In addition, 0.5% volume fraction of fibers could be

sufficient to delay the initiation of macro-crack and its propagation rate since SFRPC beams with 0.75% and 0.50% volume fraction of steel fibers showed the similar pattern.

Unlikely the PC beam, flexural and shear cracks were not distinguishable only by observing its amplitude; flexural crack showed less level of amplitude compared to the shear crack in 3 – PC beam. It might imply that damage induced between fibers and matrix such as de-bonding and fiber pull-out was intended to affect the level of energy release regardless of the types of cracks. Consequently, amplitude is possibly not a suitable parameter to identify the type of crack for SFRC material.

The 3 – SFRPC#3 and SFRPC#4 beams, which contained a 0.5% volume fraction of fibers, exhibited a similar pattern of loading versus amplitude compared to 3 – SFRPC#1 beam (V_f = 0.75%) except that more hits with higher amplitudes (> 80 dB). It was observed prior to the first visible flexural crack, as shown in Figure 6.31 (b) and 6.32. This might be because single fiber would create the high level of energy release induced by severe damage since less numbers of fibers were added. In addition, high amplitude existed when the load was constant. This can be assumed that the fiber pull-out mechanism was in progress at that moment as well.

6.4.2.3 Numbers of Hits versus Time with Applied Load

The plots of the numbers of hits versus time with applied load are presented in Figure 6.33, 6.34, and 6.35. It is clearly seen that each peak for the hit was well

matched with an increase in load. More hits were generated by shear cracks than flexural cracks. This is valid in either PC or SFRPC beams. This is true because shear crack is normally wider and longer than a flexural crack. As expected, the numbers of hits in SFRPC beams were much greater than the PC beams due to inclusion fibers.

In 3 – PC beam, fewer numbers of hits occurred when the first flexural crack was developed, and then the hits showed a sudden jump when the first shear crack developed. The AE data reflected a trend; the damage induced by shear is more severe than flexural. At a loading of 140 kips, a huge jump in the number of hits was observed. This is due to the fact that cracks along the longitudinal reinforcements occurred as well as web shear crack began to propagate and widen. These damage processes increased the number of hits at the loading stage.

In 3 – SFRPC#1 beam, more hits, over 7000 (3 – PC#1 showed approximately 1000 hits at the flexural crack), were observed even before the flexural crack was visible. This also can be evidence that resistance from the steel fibers was ongoing before the first crack became visible. While the load increased the number of hits increased. The SFRPC beams with a 0.5% volume fraction of steel fibers (3 – SFRCP#3 and #4) showed similar hit patterns to that of the specimen with a 0.75% volume fraction of steel fibers (3 – SFRPC#1).

6.4.2.4 Location Plots

The plots of source location allow seeing the initiation and propagation as well as location of internal damage. A micro-crack and/or macro-crack on the concrete surface are/is difficult to distinguish visibly, especially in large scale specimen. By using the AE information, a limited region could be focused to find a crack during test.

The location plot for 3 – PC#1 beam is shown in Figure 6.36. At 90 kips, some events were observed under the loading point that was possible induced by mechanical noise (e.g., at the bearing plate). This is associated with the plot of duration versus amplitude as stated previously. At 100 kips, where the first web shear crack occurred, many events occurred adjacent to the web shear crack.

The location plots for 3 – SFRPC#1 beam is shown in Figure 6.38 and 6.39. At 100 kips, when the first visible flexural crack occurred, events were observed under the loading point. In fact, the locations of events do not well match with the actual location of crack. It should be mentioned that the coordinate of the AE sensors was designed to attain AE information in the shear span such that a flexural crack might not be captured properly due to limited number of sensors. At 140 kips, where the first visible web shear crack occurred, many events occurred near the web shear crack. It is important to note that many events occurred above the web shear crack while load increased even though significant damage was not observed on the surface. In addition, the uncracked section was almost covered by events at the failure. That implies that stresses were

redistributed along the beam section, and by observing distribution of events, the AE data supports the direct load transfer mechanism, which was observed during the test as well. The strut lying above the shear crack in the uncracked section could be created above the web shear crack, which matches the data from the concrete surface strains mentioned in Chapter 5.

The beam with a 0.75% volume fraction of steel fiber and a 0.2% of longitudinal tensile reinforcement ratio, 3 – SFRPC#2, showed less events at the middle of the short shear span. That is because the beam was governed by flexure rather than shear.

The 3 – SFRPC#3 beam, which had a 0.5% volume fraction of fibers, already indicated some events in the short shear span when the first flexural crack occurred. It could be assumed that, as stated, internal damage occurred even though it was not visible on the surface. Similar to 3 – SFRPC#1 beam, events were spread throughout the uncracked section at failure. Comparing the 3 – SFPRC#3 and #4 beams, it should be noted that less events were observed in 3 – SFRPC#4 beams, which contained 0.5% volume fraction of steel fibers as well as No. 3 stirrups with 21 in. spacing in the short shear span. It can be explained that stirrups played a role in the resistance of stresses once cracks occurred, and AE sensor might not be able to capture stresses in the rebars. These have an agreement with strain gauge data mentioned in Chapter 5.

AE data also revealed that more energy was dissipated in the SFRPC beams than the PC beam by observing distribution of events. The inclusion of steel fibers in the concrete caused energy to be dispersed effectively along the beam section, which can be represented by location plots. This agrees with the crack observation; SFRPC beams had more cracks than the PC beam. In addition, more events were observed above the shear crack, even though no significant crack were observed, which could indicate that the load was transferred through the strut located at the above the shear crack. This is also well matched with concrete surface strain profiles, which are presented in Chapter 5.

Table 6.1 Coordinates of AE sensors

ID for sensors	X-position (in.)	Y-position (inches)
#2	8	8
#3	30	4
#4	14	22
#5	42	16
#6	48	6
#7	-4	6
#8	-6	22

Table 6.2 “b-value” quantitative results (Colombo et. al., 2003)

b-value ranges	Damage assessments
1.0 < b-value < 1.2	Implies that the channel is very near to a large crack, i.e., macro-cracks are forming
1.2 < b-value < 1.7	Uniformly distributed cracking, i.e., macro-cracks are constant
b-value > 1.7	Microcracs are dominant or macrocracks are opening

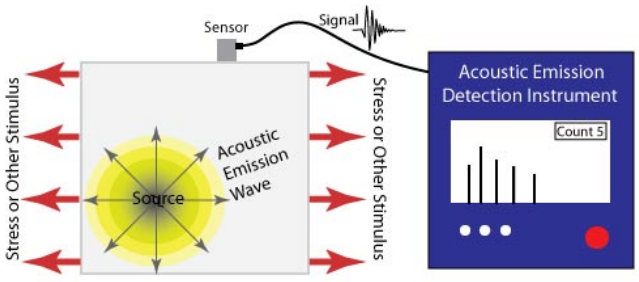

Figure 6.1 Schematic view of AE (http://www.ndt-ed.org)

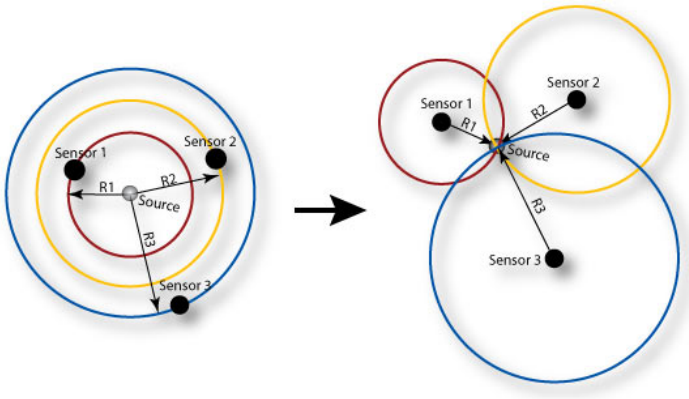

Figure 6.2 Schematic view of the way how to find a location of event (http://www.ndt-ed.org)

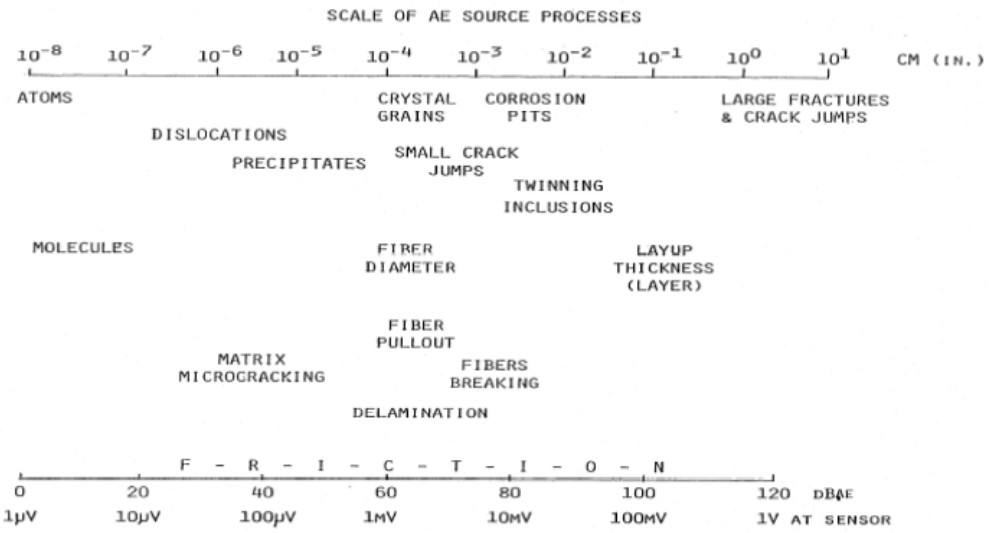

Figure 6.3 A relationship between amplitude and corresponding damage

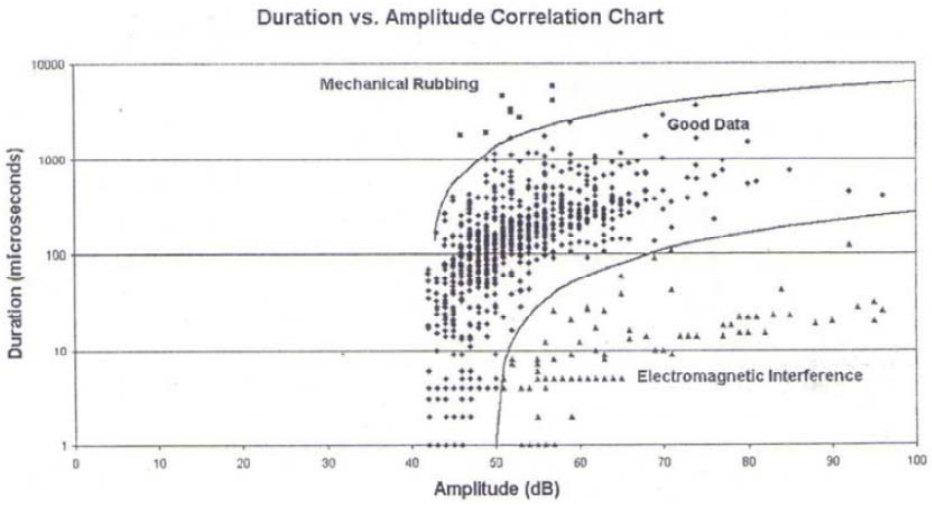

Figure 6.4 Amplitude versus duration plot showing genuine data and two types of nongenuie data (Harvey, 2001)

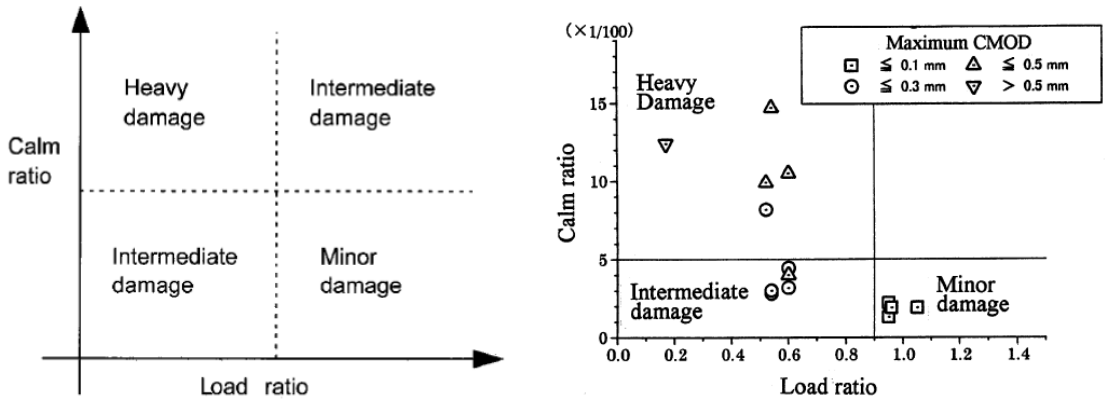

(a) (b)

Figure 6.5 Damage assessment using Calm and Load ratios (Ohtsu et. al. 2002); (a) Classification of damages by two ratios; (b) Classification of AE data obtained from test

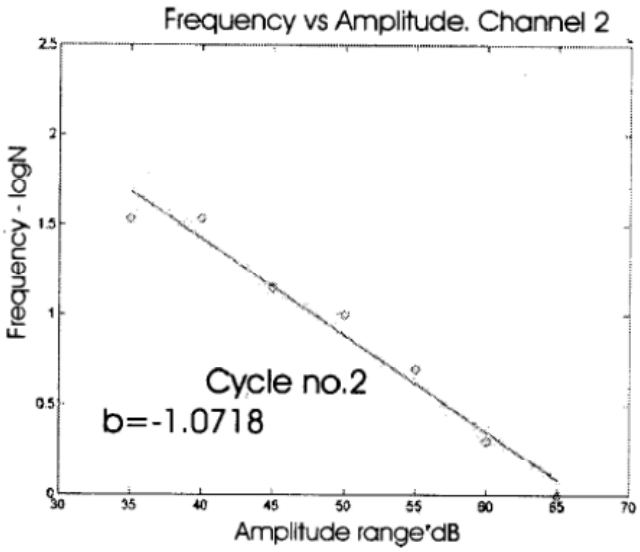

Figure 6.6 Example of calculation for b-value (Colombo, et al. 2005)

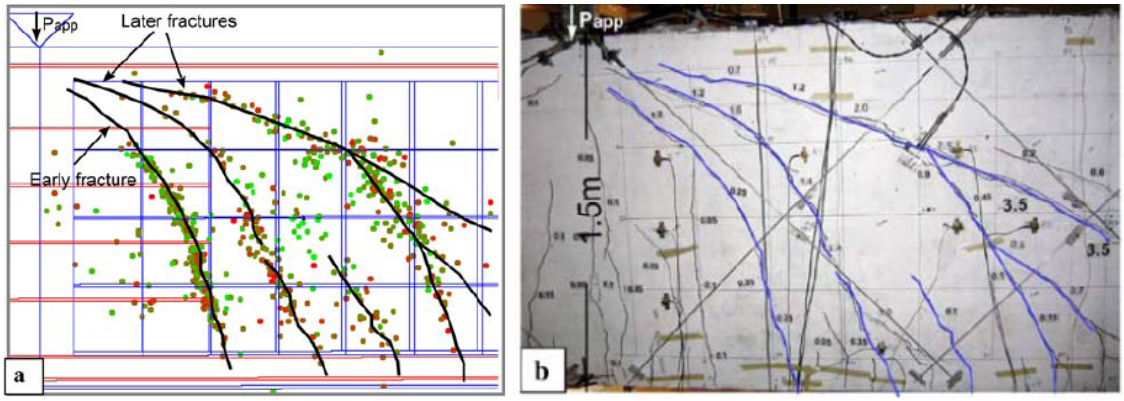

(a) (b)

Figure 6.7 Comparison location of AE event and visible surface cracks (Katsaga et. al. 2007); (a) Source locations of AE events; (b) photos of beam during test

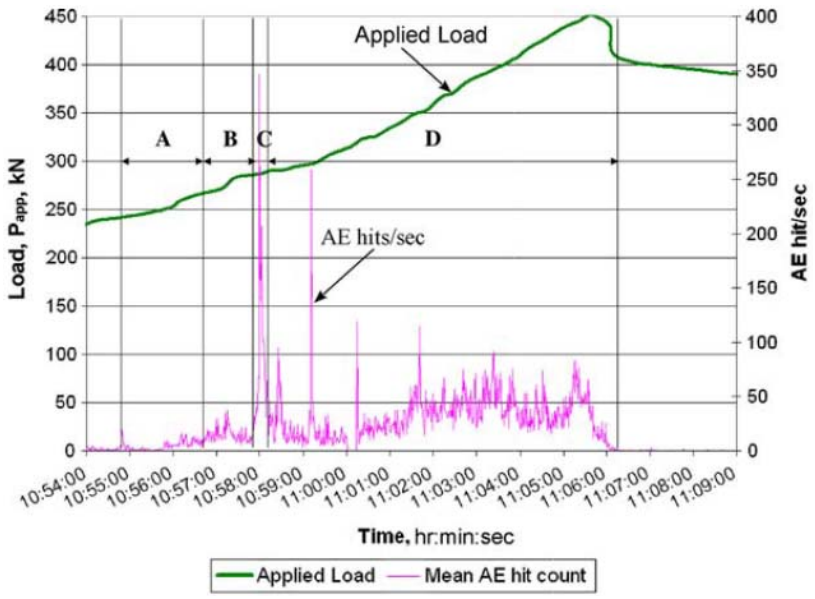

Figure 6.8 Load and AE rate versus time for loading step (Katsaga et. al. 2007)

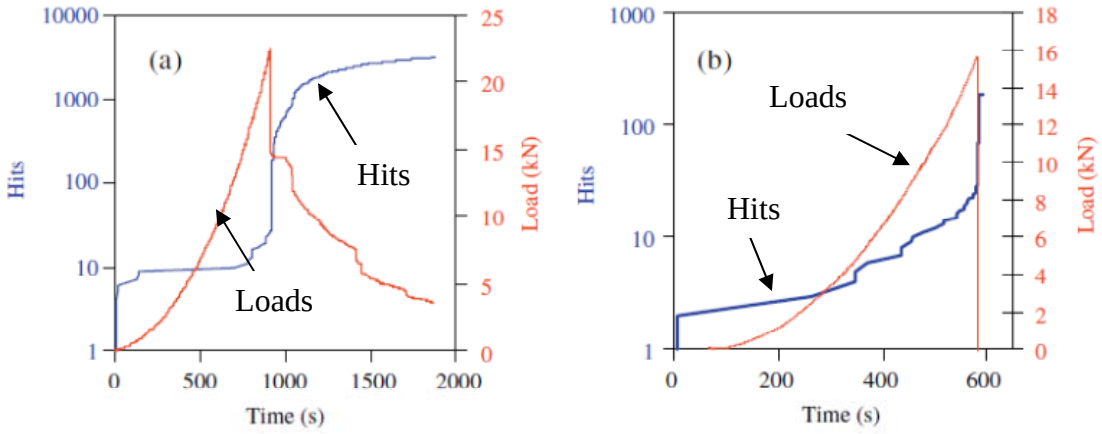

(a) (b)

Figure 6.9 Load versus hit history for beams (Soulioti et al. 2009); (a) SFRC beam with 1.5% volume fraction; (b) Plain concrete

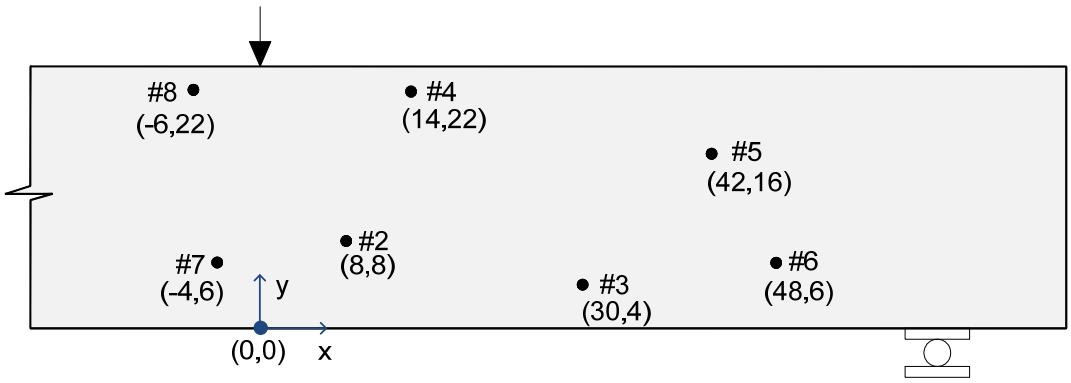

Figure 6.10 Coordinate of AE sensors

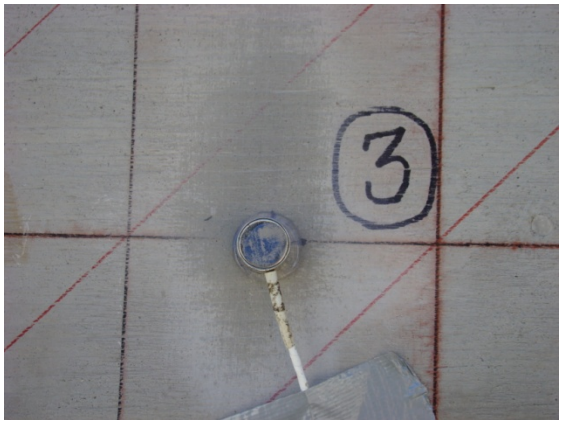

Figure 6.11 AE sensor instrumentation

(a) (b)

Figure 6.12 AE DAQ system; (a) pre-amplifier; (b) AE DAQ system

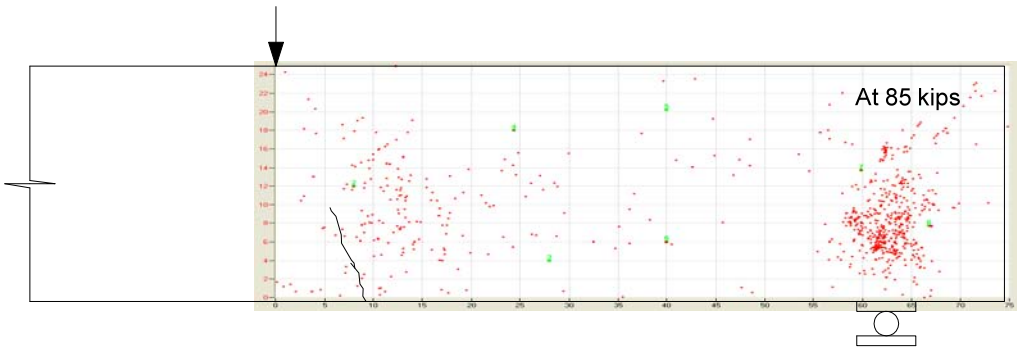

(a)

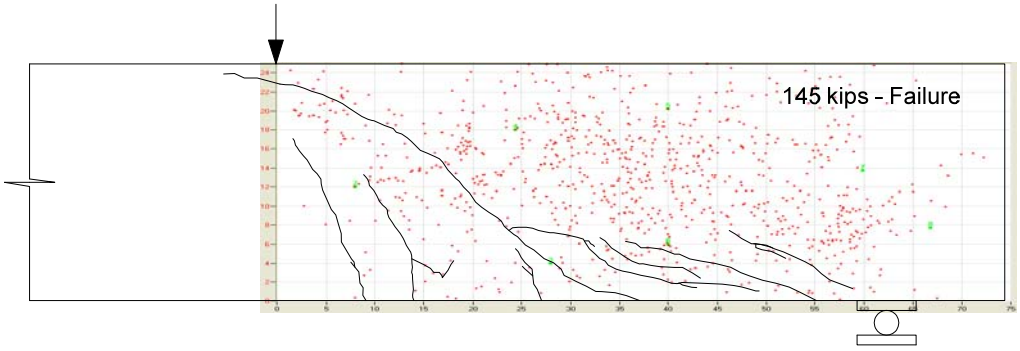

(b)

Figure 6.13 Locations of events in 1 – PC beam; (a) Load at 85 kips; (b) Load at 145 kips to failure

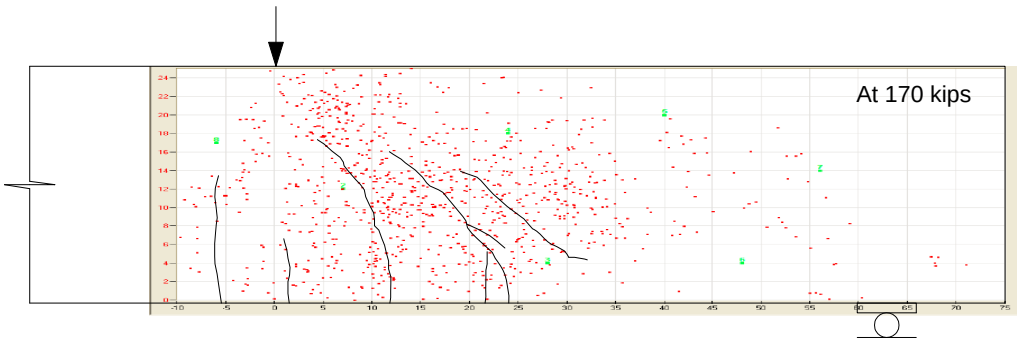

(a)

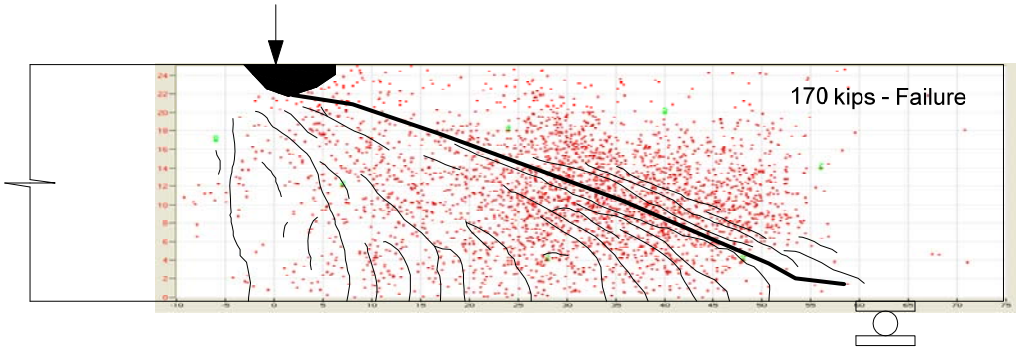

(b)

Figure 6.14 Locations of events in 1 – SFRPC beam; (a) Load at 170 kips; (b) Load at 170 kips to failure

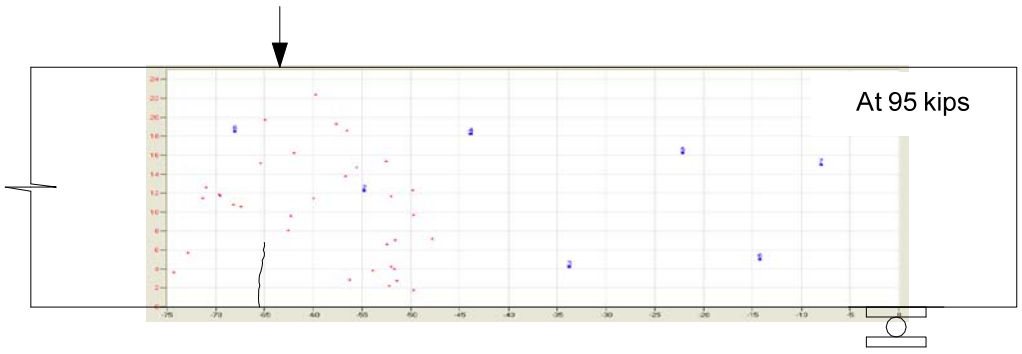

(a)

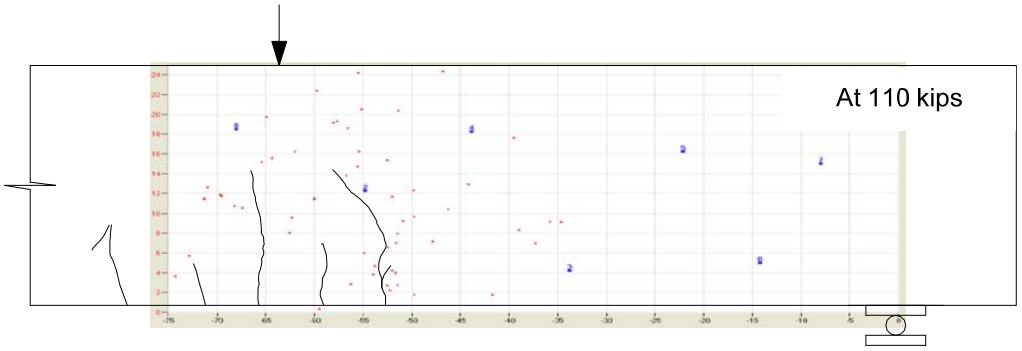

(b)

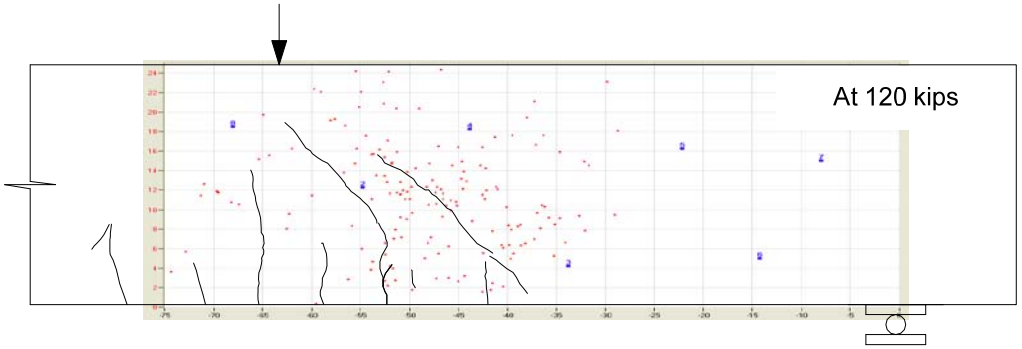

(c)

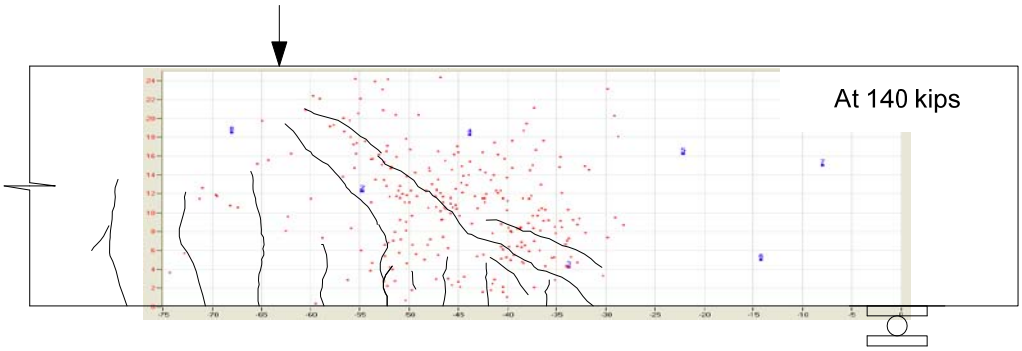

(d)

Figure 6.15 Locations of events in 2 – PC#1 beam at loadings from 95 kips to 140 kips; (a) Load at 95 kips; (b) Load at 110 kips; (c) Load at 120 kips; (d) Load at 140 kips

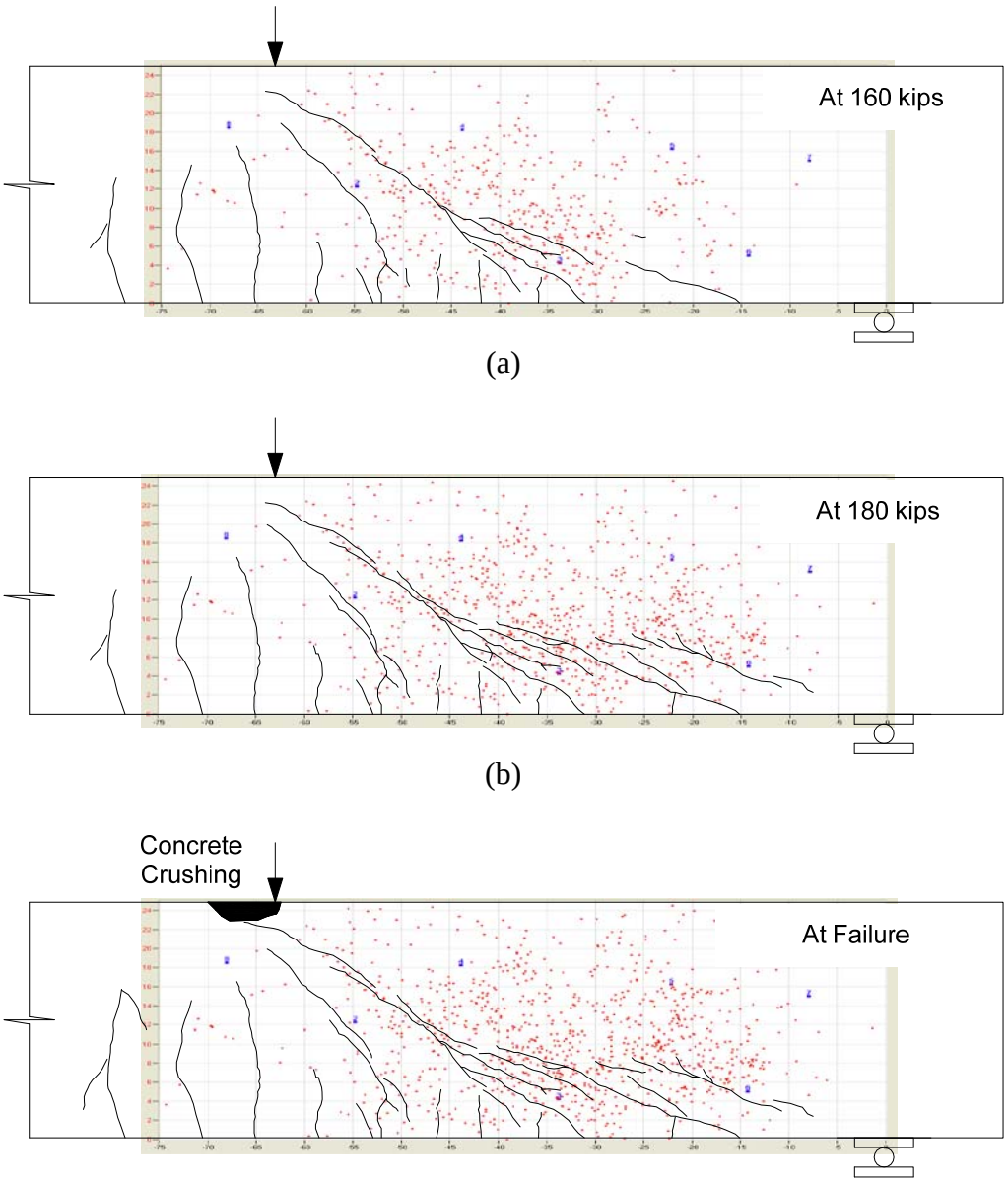

Figure 6.16 Locations of events in 2 – PC#1 beam at loadings from 160 kips to failure; (a) Load at 160 kips; (b) Load at 180 kips; (c) Load at failure

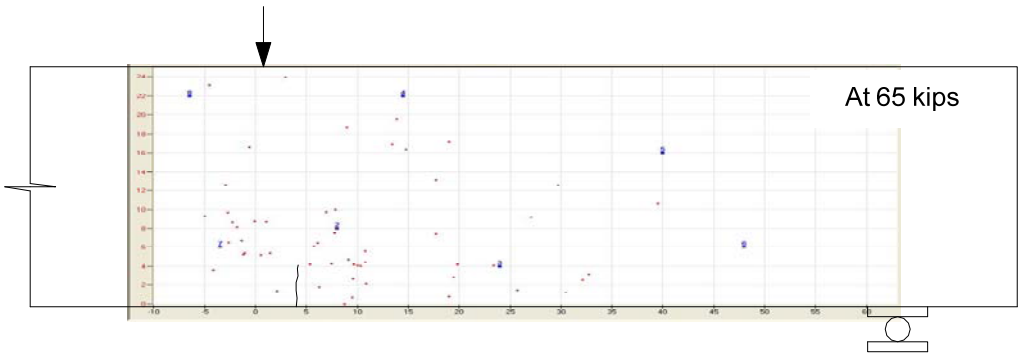

(a)

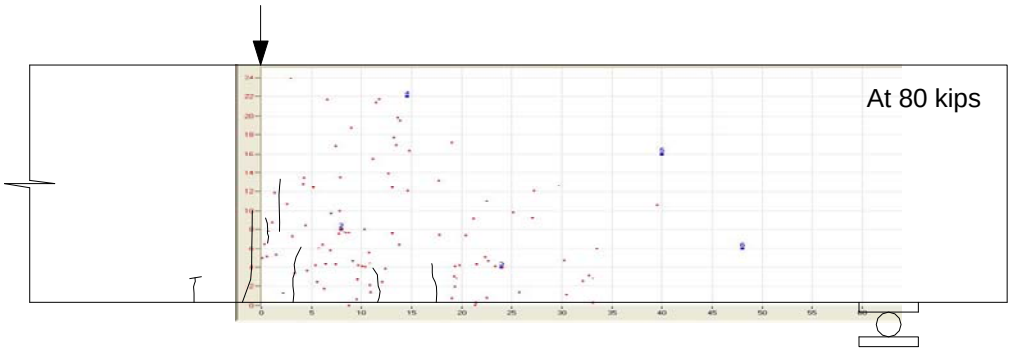

(b)

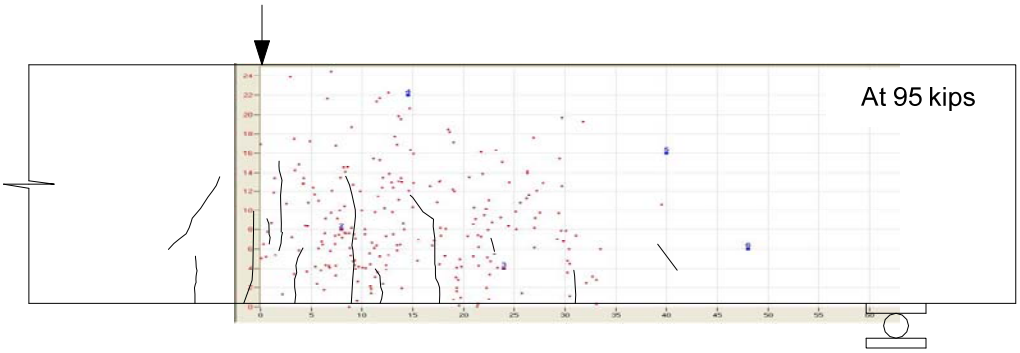

(c)

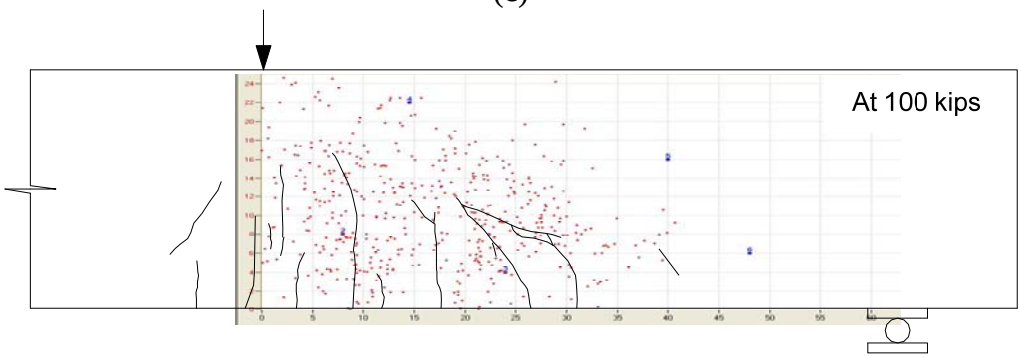

(d)

Figure 6.17 Locations of events in 2 – PC#2 beam at loadings from 65 kips to 100 kips; (a) Load at 65 kips; (b) Load at 80 kips; (c) Load at 95 kips; (d) Load at 100 kips

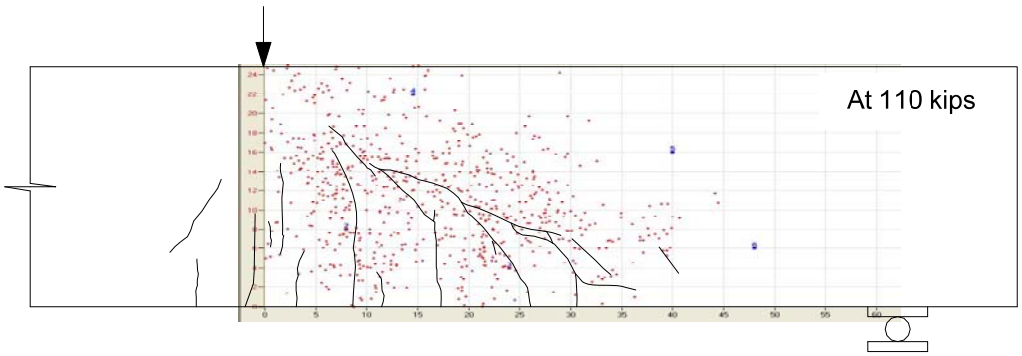

(a)

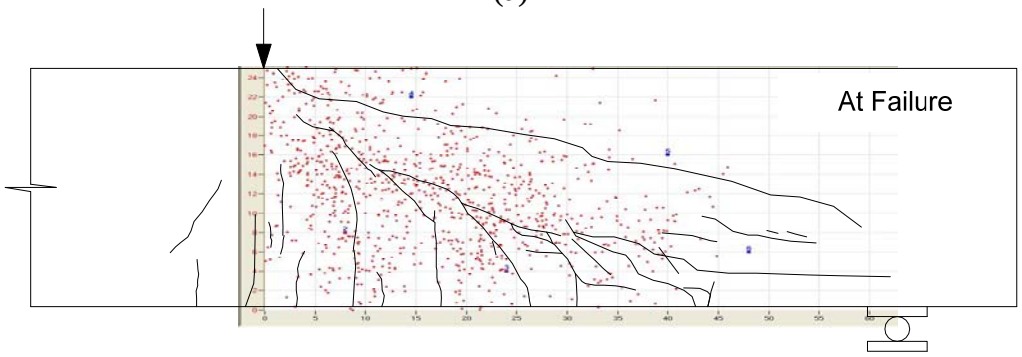

(b)

Figure 6.18 Locations of events in 2 – PC#2 beam at loadings from 110 kips to failure; (a) Load at 110 kips; (b) Load at failure

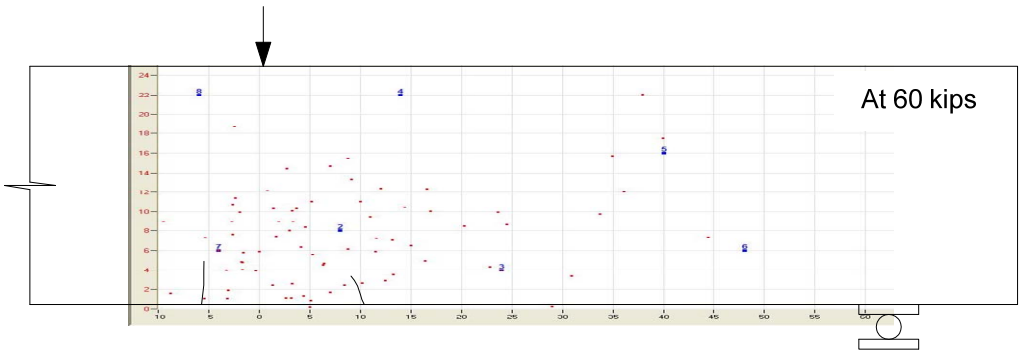

(a)

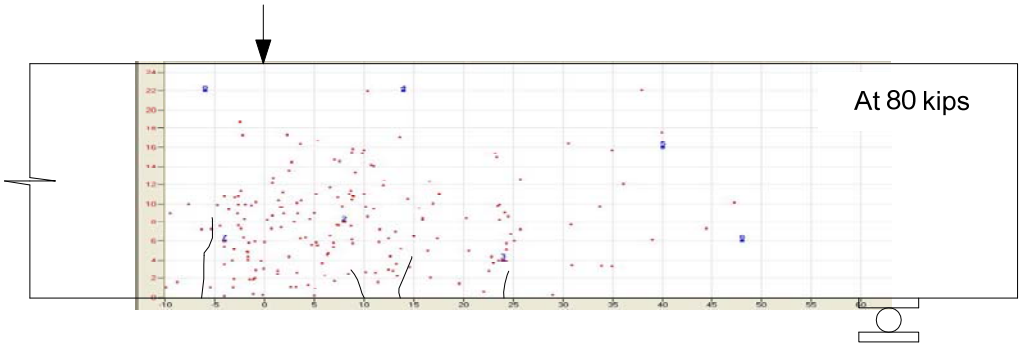

(b)

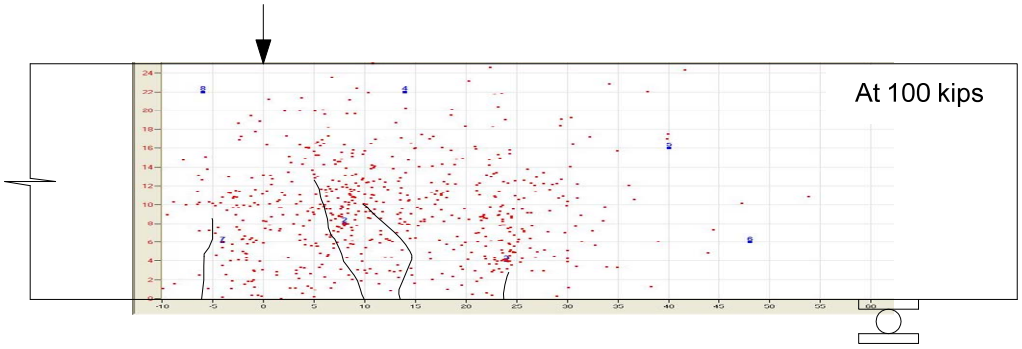

(c)

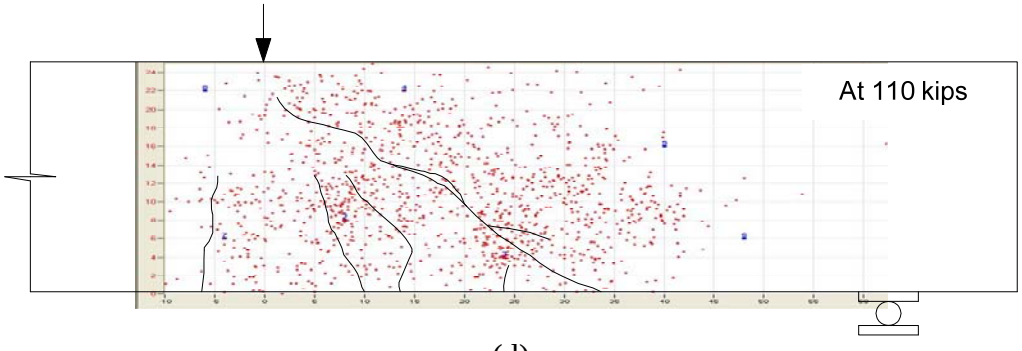

(d)

Figure 6.19 Locations of events in 2 – PC#3 beam at loadings from 60 kips to 110 kips; (a) Load at 60 kips; (b) Load at 80 kips; (c) Load at 100 kips; (d) Load at 110 kips

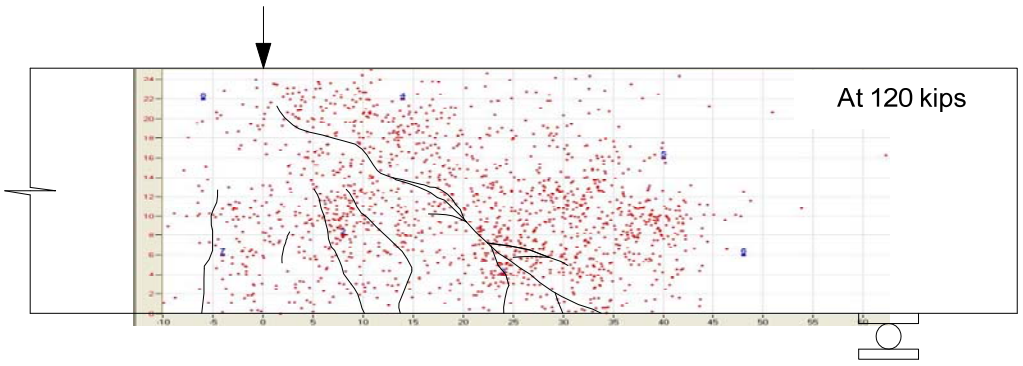

(a)

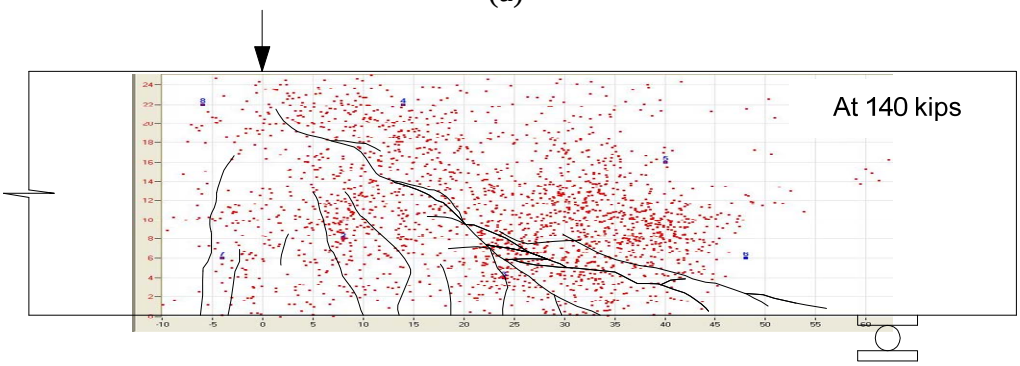

(b)

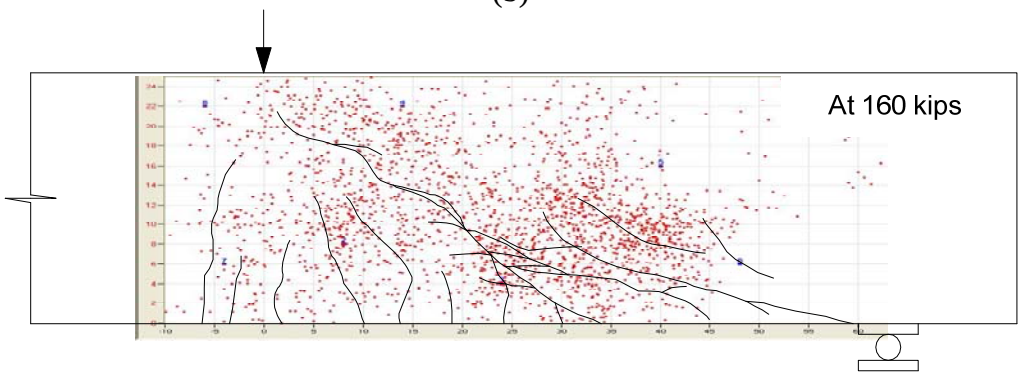

(c)

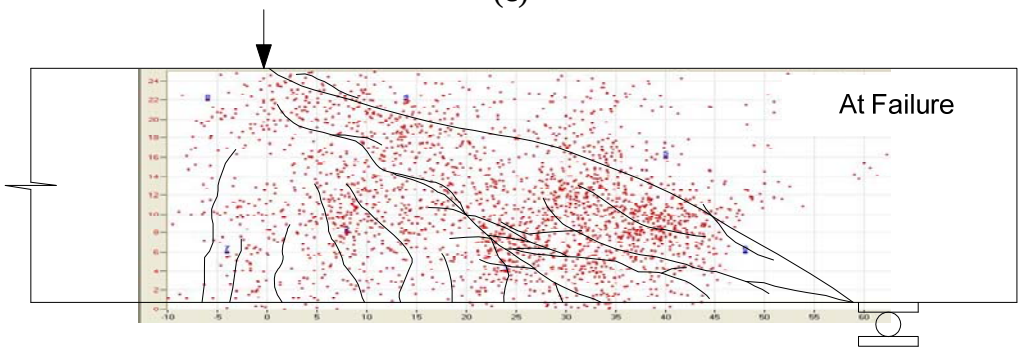

(d)

Figure 6.20 Locations of events in 2 – PC#3 beam at loadings from 120 kips to failure; (a) Load at 120 kips; (b) Load at 140 kips; (c) Load at 160 kips; (d) Load at failure

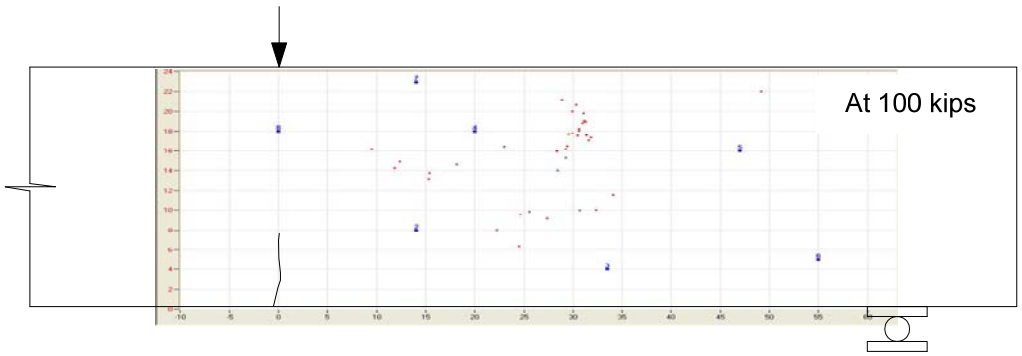

(a)

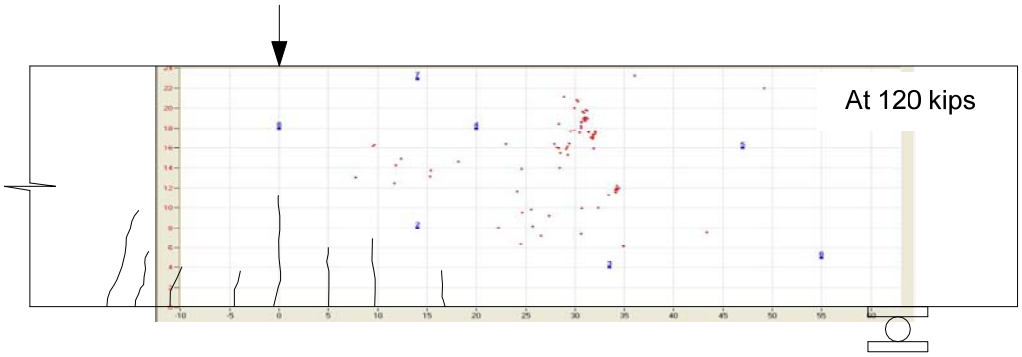

(b)

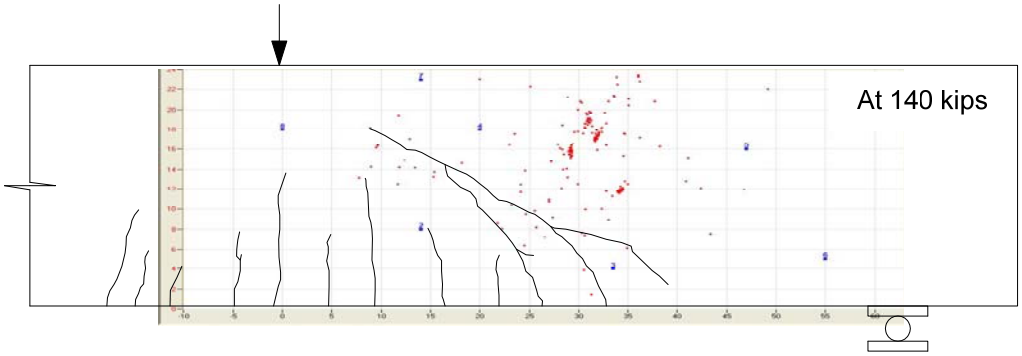

(c)

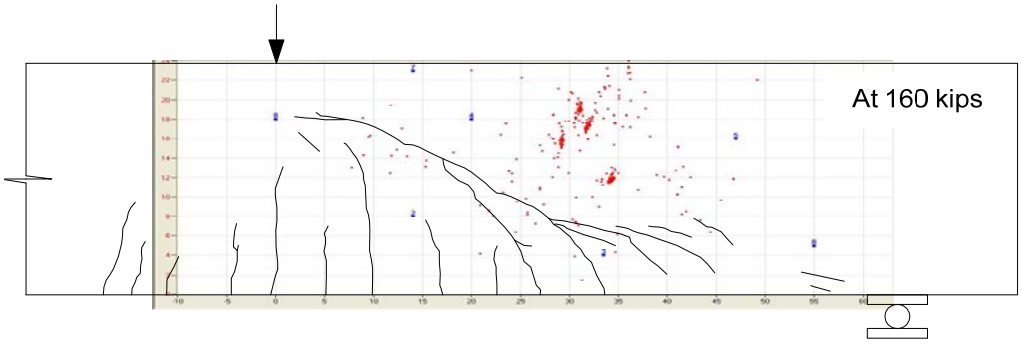

(d)

Figure 6.21 Locations of events in 2 – SFRPC#1 beam at loadings from 100 kips to 160 kips; (a) Load at 100 kips; (b) Load at 120 kips; (c) Load at 140 kips; (d) Load at 160 kips

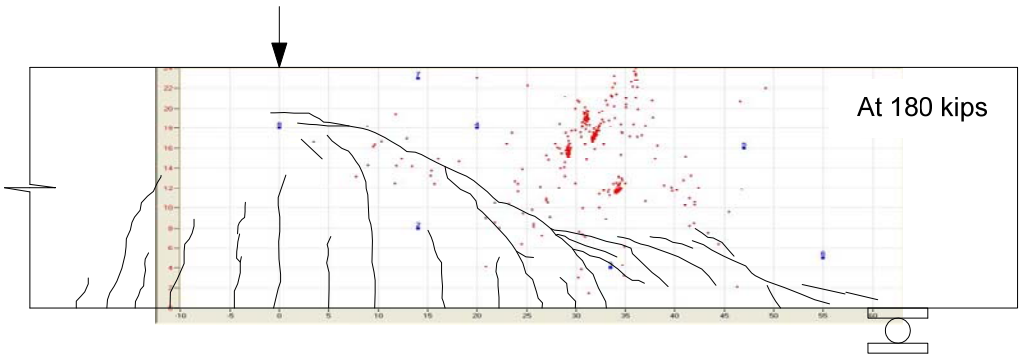

(a)

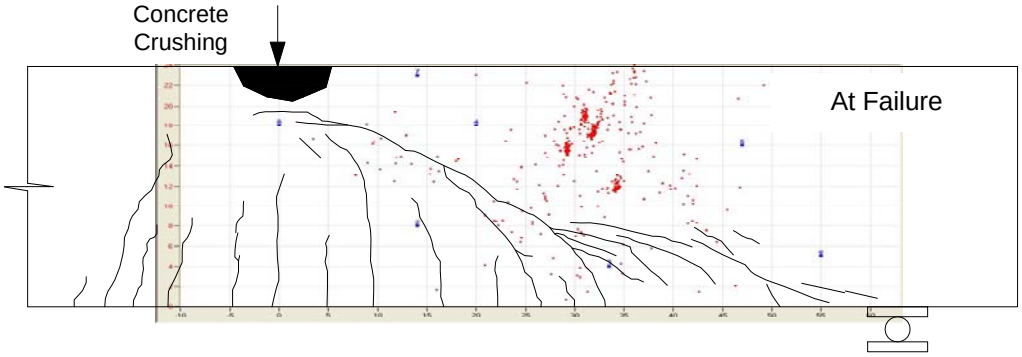

(b)

Figure 6.22 Locations of events in 2 – SFRPC#1 beam at loadings from 180 kips to failure; (a) Load at 180 kips; (b) Load at failure

(a)

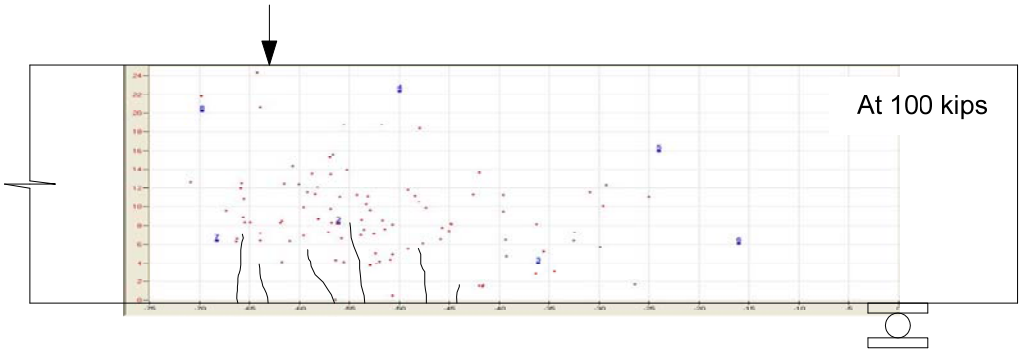

(b)

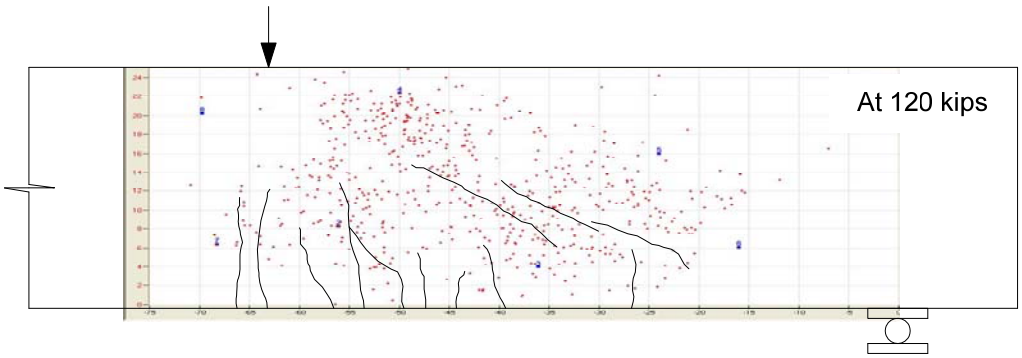

(c)

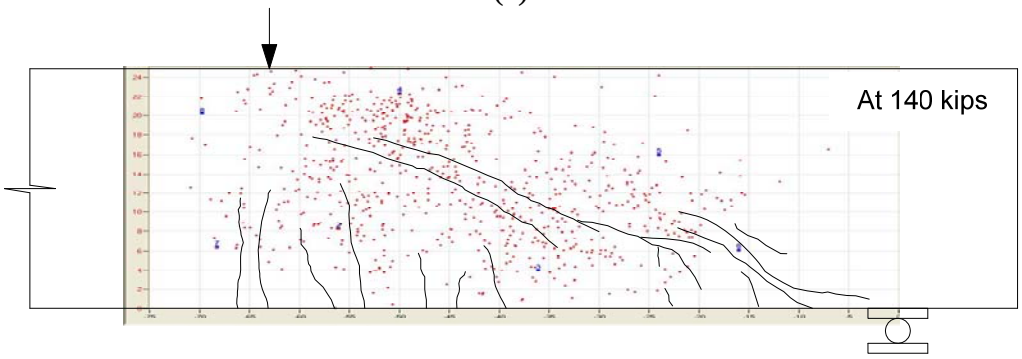

(d)

Figure 6.23 Locations of events in 2 – SFRPC#2 beam at loadings from 70 kips to 140 kips; (a) Load at 70 kips; (b) Load at 100 kips; (c) Load at 120 kips; (d) Load at 140 kips

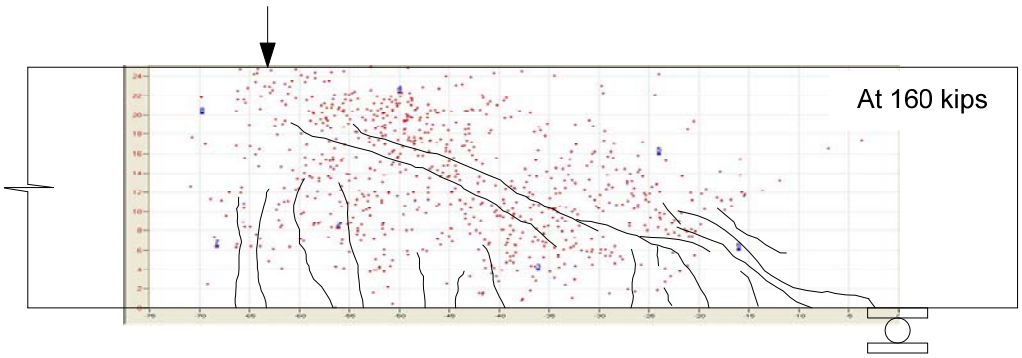

(a)

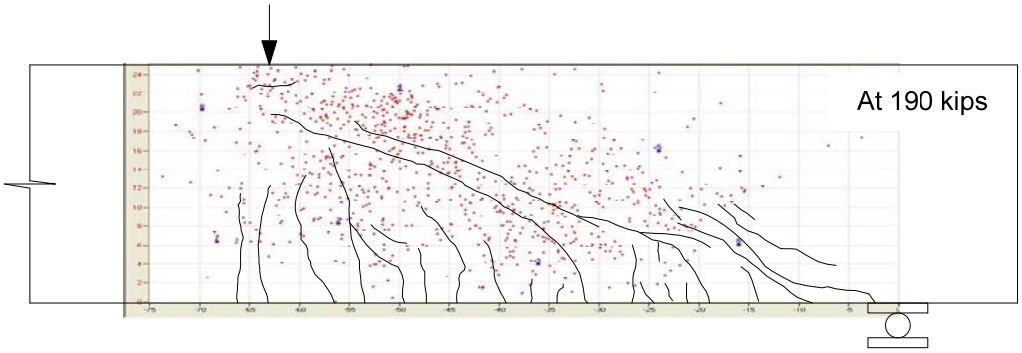

(b)

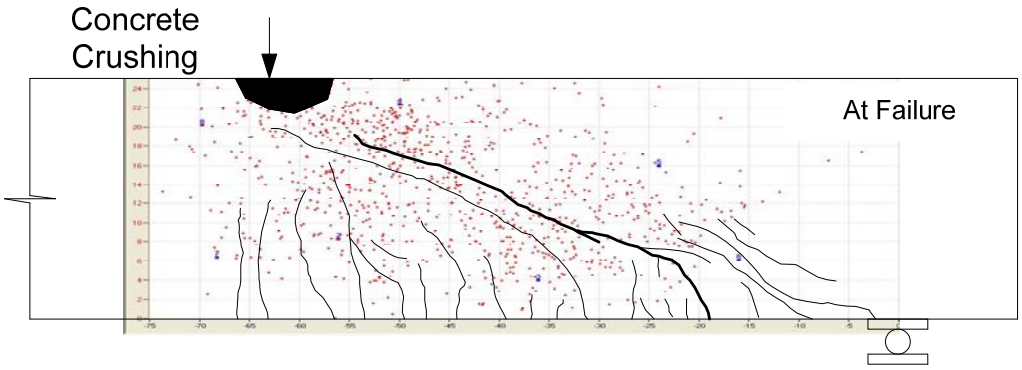

(c)

Figure 6.24 Locations of events in 2 – SFRPC#2 beam at loadings from 160 kips to failure; (a) Load at 160 kips; (b) Load at 190 kips; (c) Load at failure

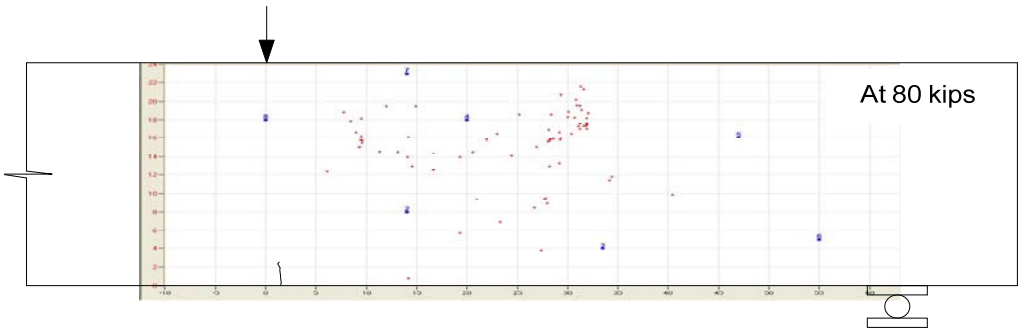

(a)

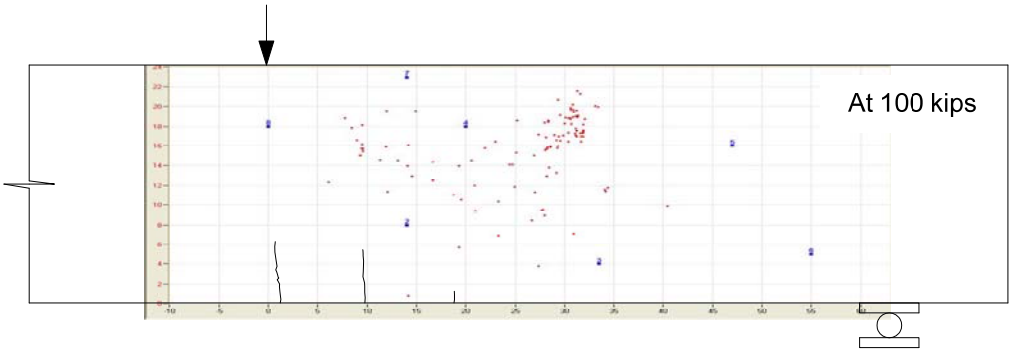

(b)

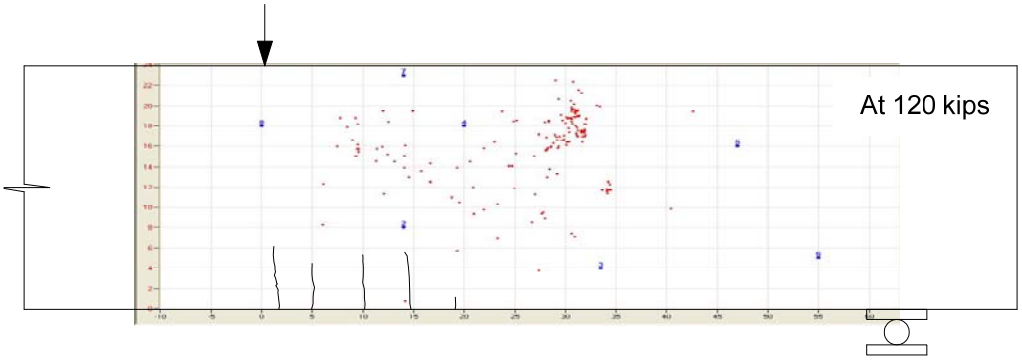

(c)

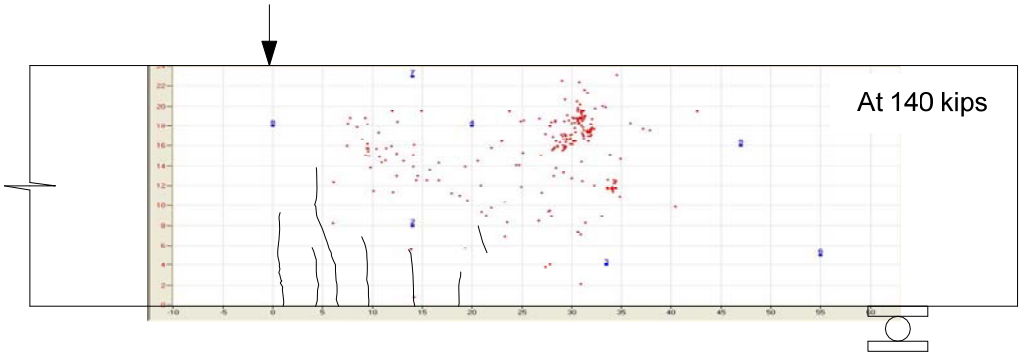

(d)

Figure 6.25 Locations of events in 2 – SFRPC#3 beam at loadings from 80 kips to 140 kips; (a) Load at 80 kips; (b) Load at 100 kips; (c) Load at 120 kips; (d) Load at 140 kips

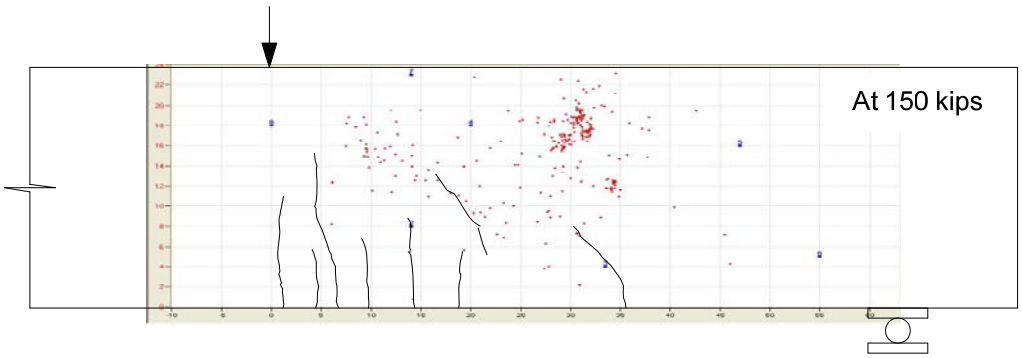

(a)

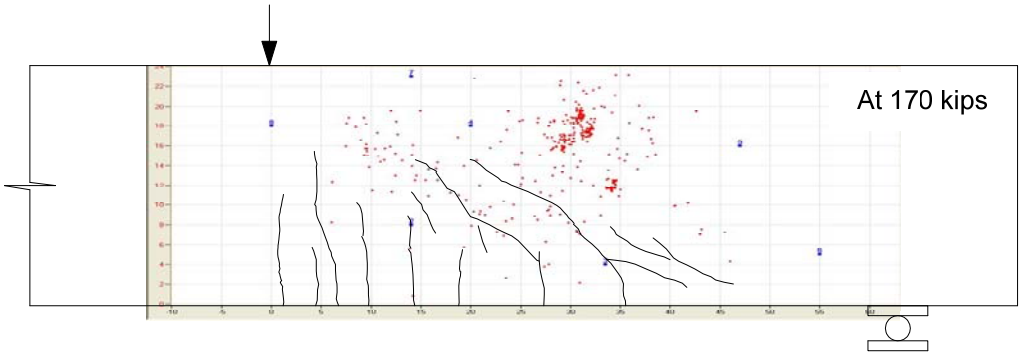

(b)

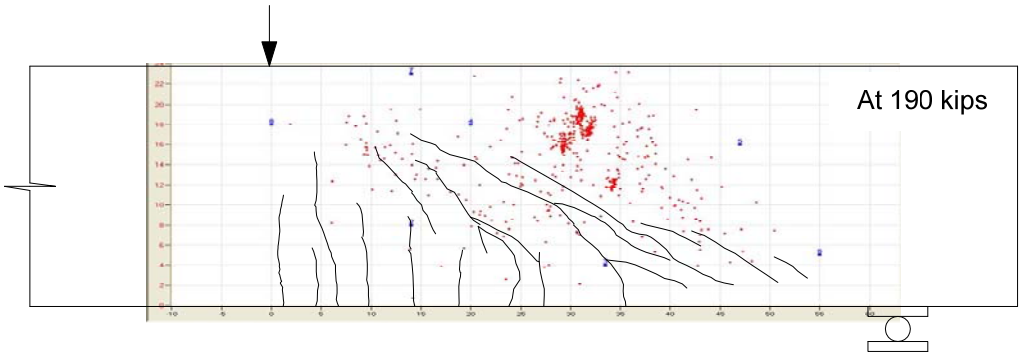

(c)

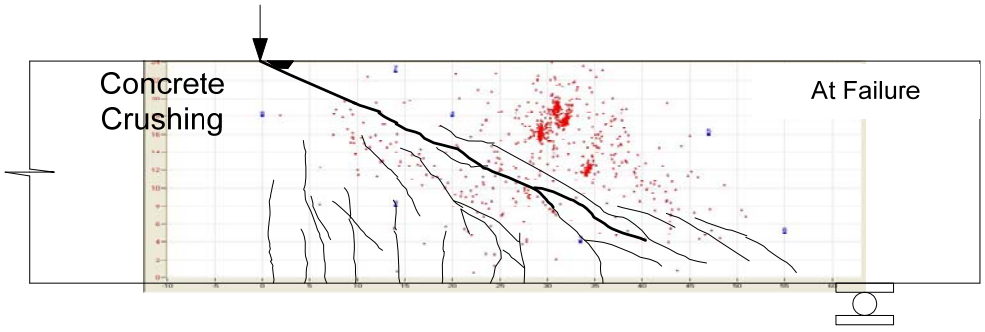

(d)

Figure 6.26 Locations of events in 2 – SFRPC#3 beam at loadings from 150 kips to failure; (a) Load at 150 kips; (b) Load at 170 kips; (c) Load at 190 kips; (d) Load at failure

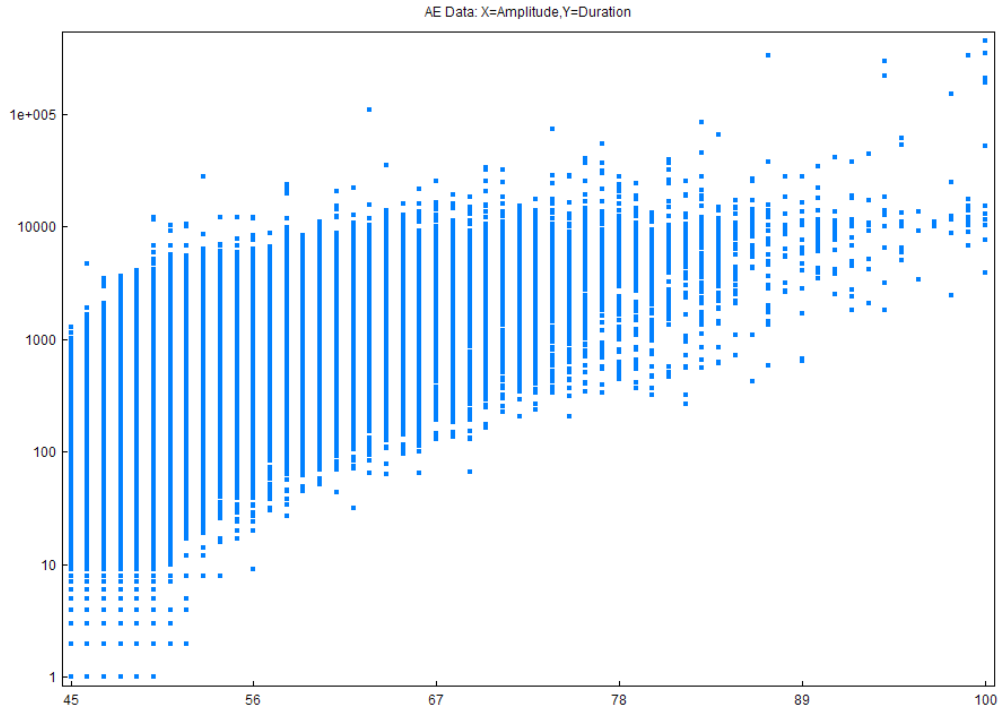

(a)

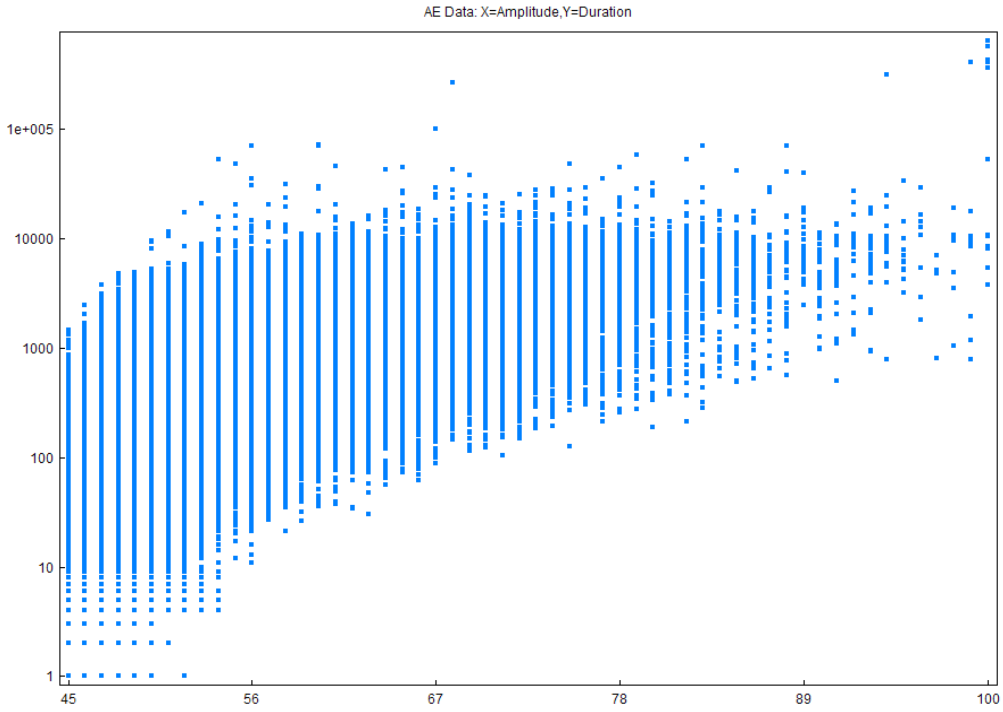

(b)

Figure 6.27 Duration versus amplitude for 3 – PC#1 and 3 – SFRPC#1 beams; (a) 3 – PC#1; (b) 3 – SFRPC#1

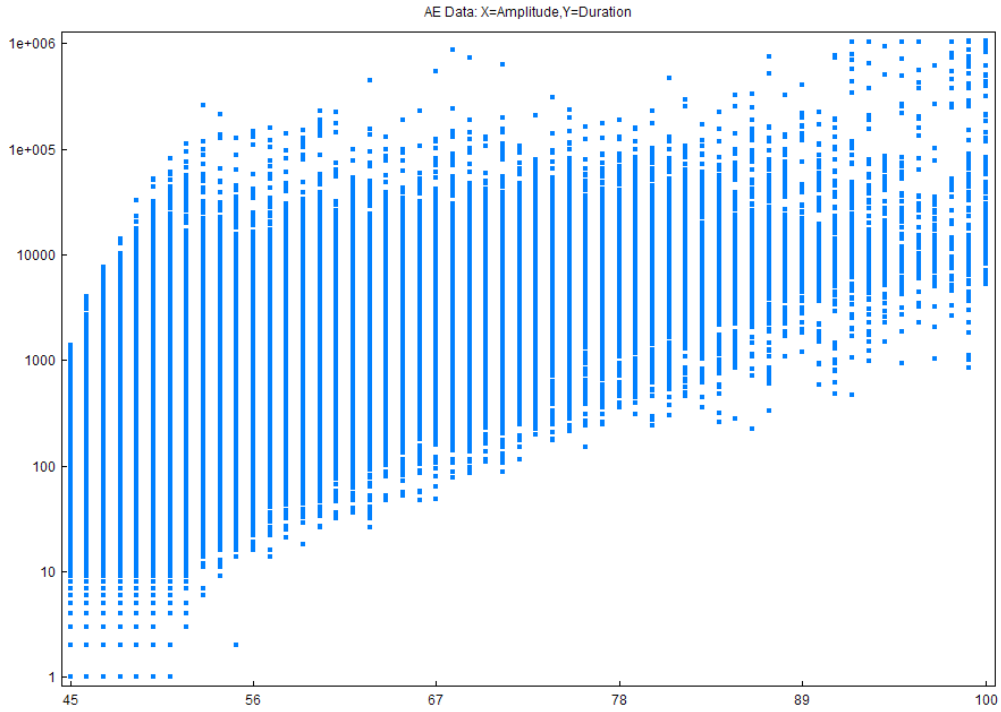

(a)

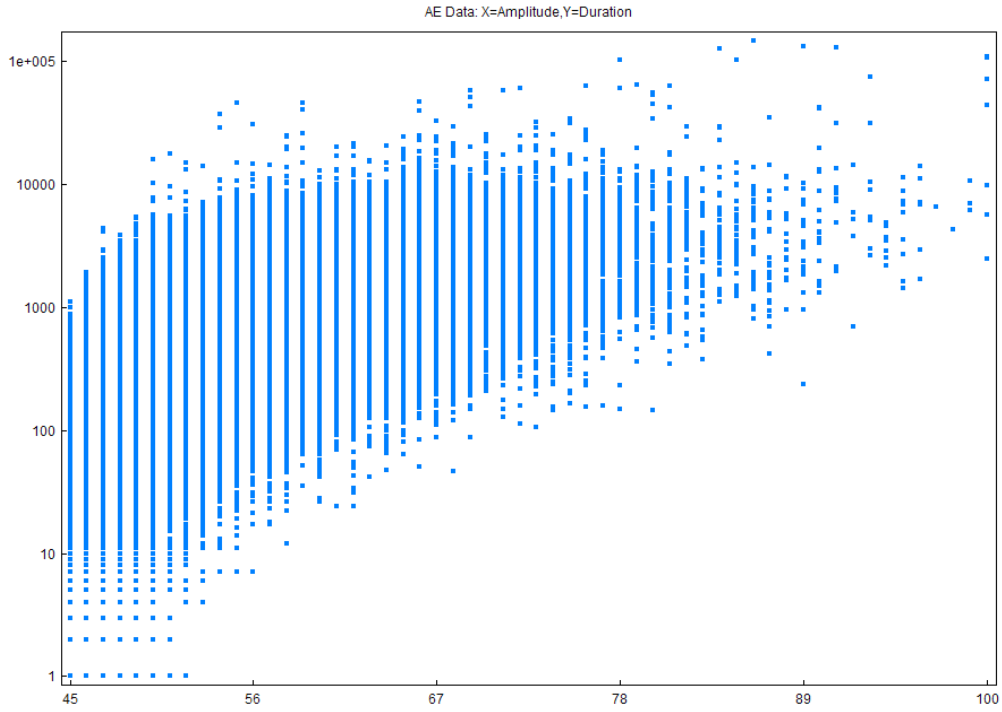

(b)

Figure 6.28 Duration versus amplitude for 3 – SFRPC#2 and 3 – SFRPC#3 beams; (a) 3 – SFRPC#2; (b) 3 – SFRPC#3

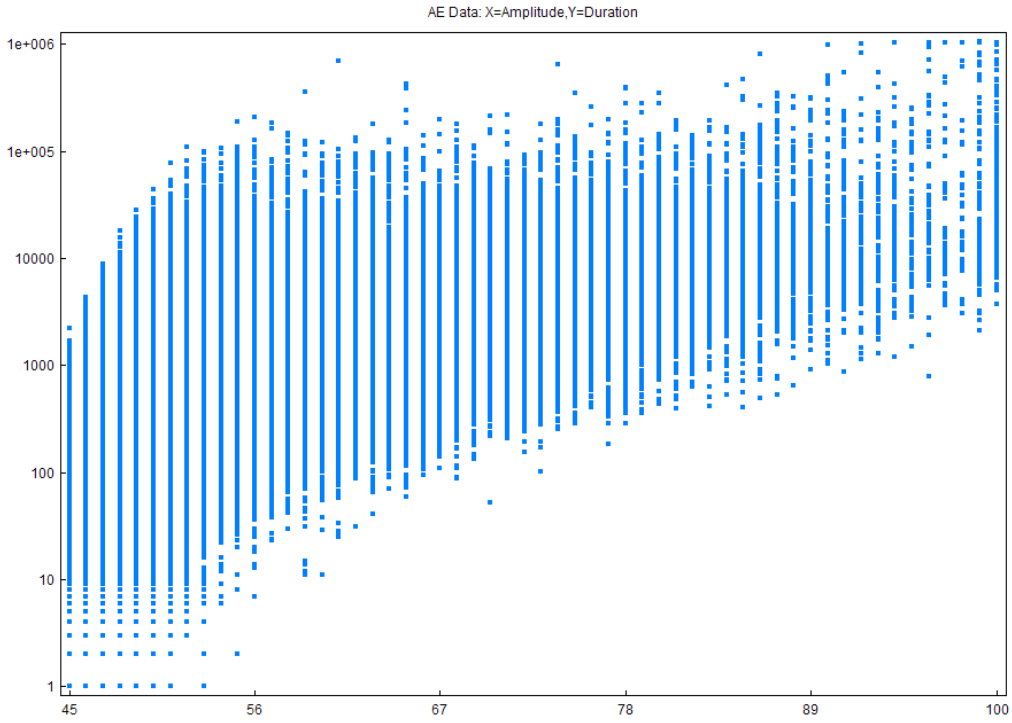

Figure 6.29 Duration versus amplitude for 3 – SFRPC#4 beam

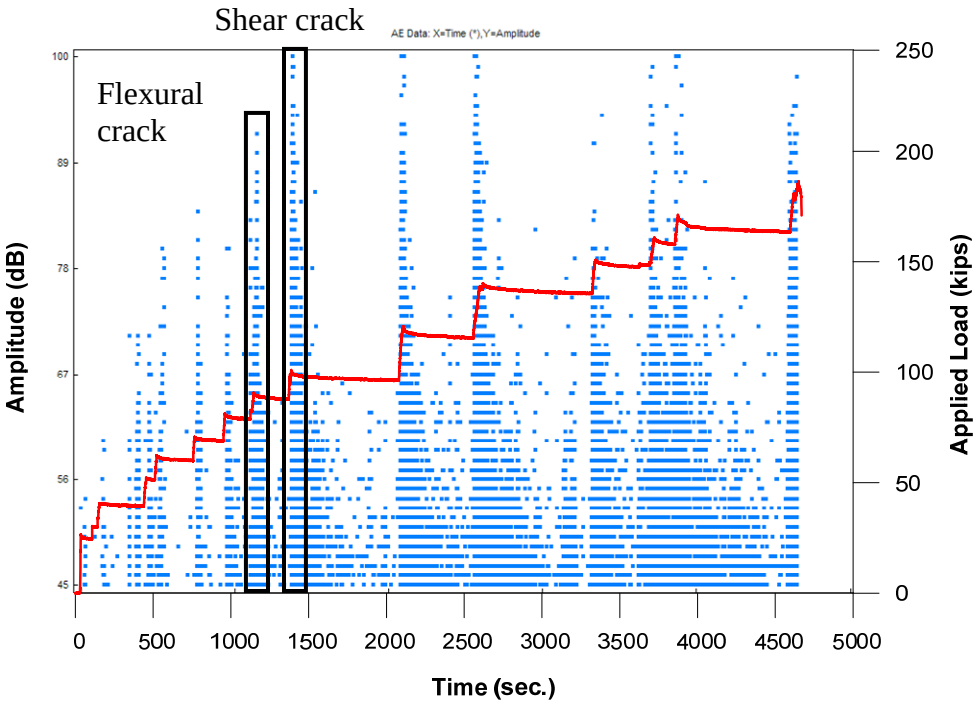

(a)

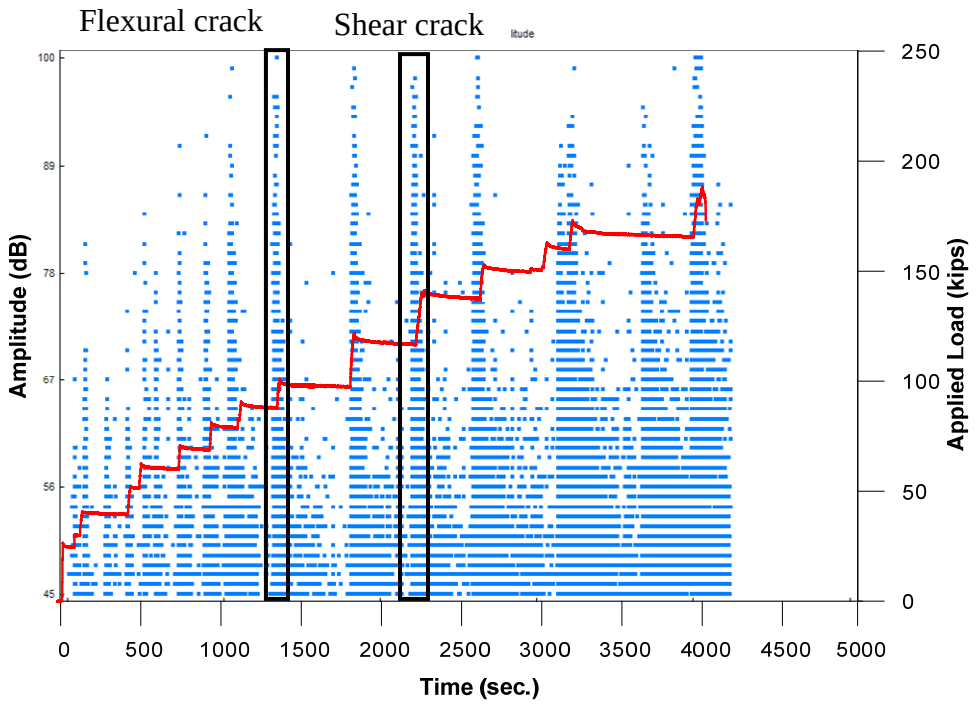

(b)

Figure 6.30 Amplitude versus applied load versus time for 3 – PC#1 and 3 – SFRPC#1 beams; (a) 3 – PC#1; (b) 3 – SFRPC#1

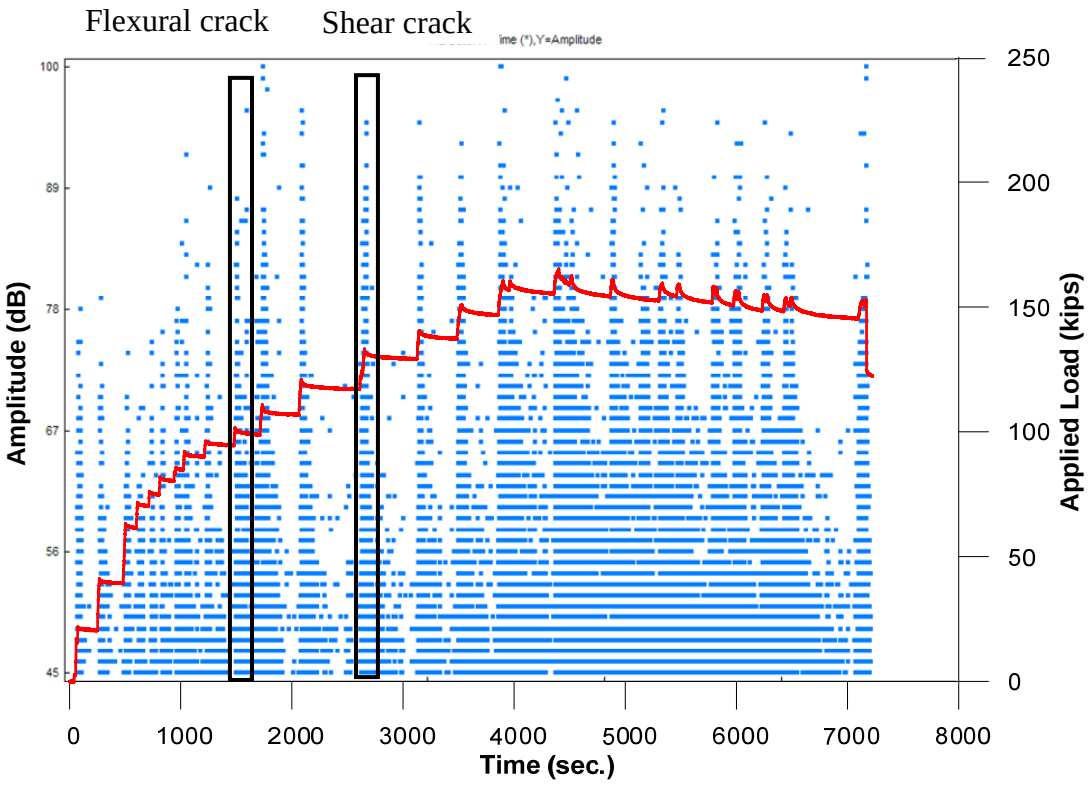

(a)

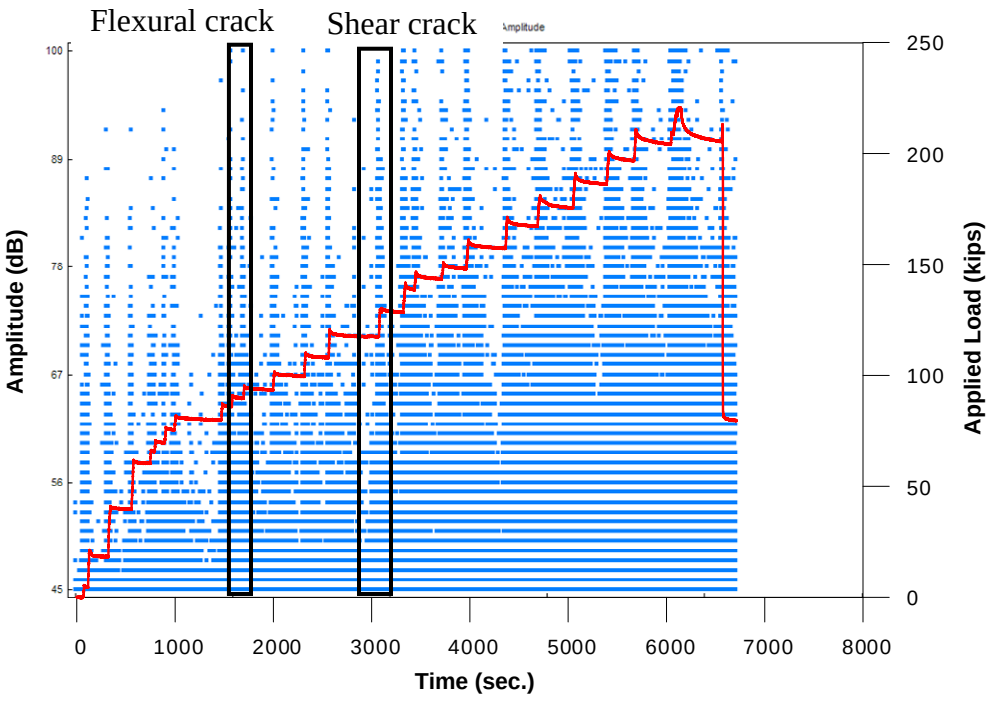

(b)

Figure 6.31 Amplitude versus applied load versus time for 3 – SFRPC#2 and 3 – SFRPC#3 beams; (a) 3 – SFRPC#2; (b) 3 – SFRPC#3

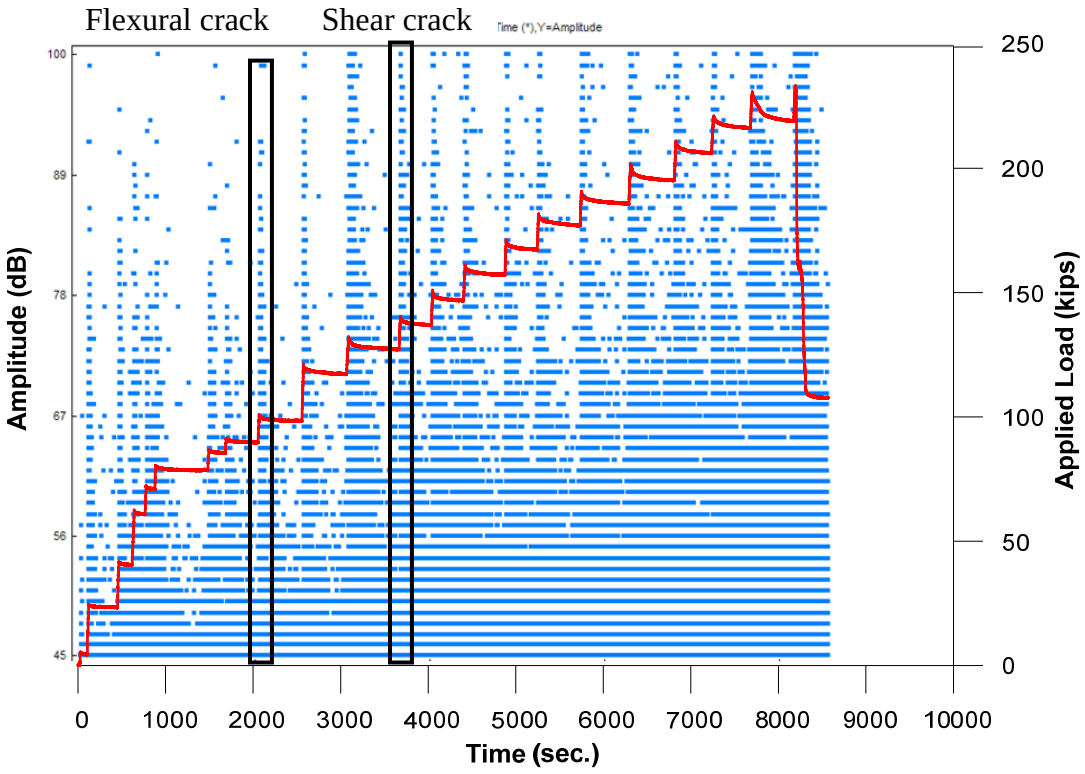

Figure 6.32 Amplitude versus applied load versus time for 3 – SFRPC#4 beam

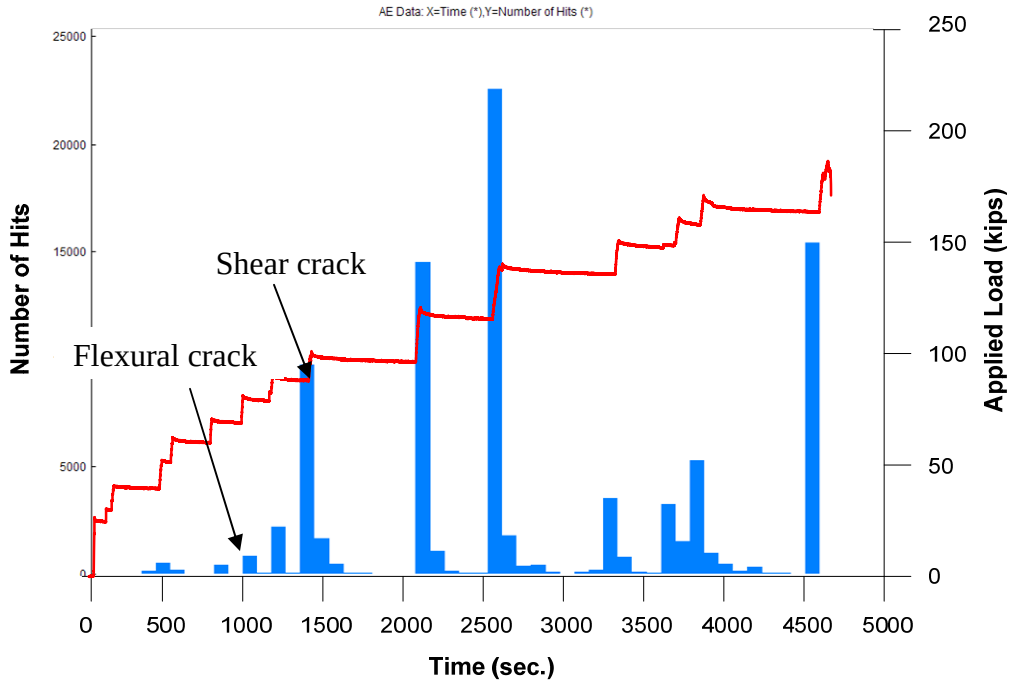

(a)

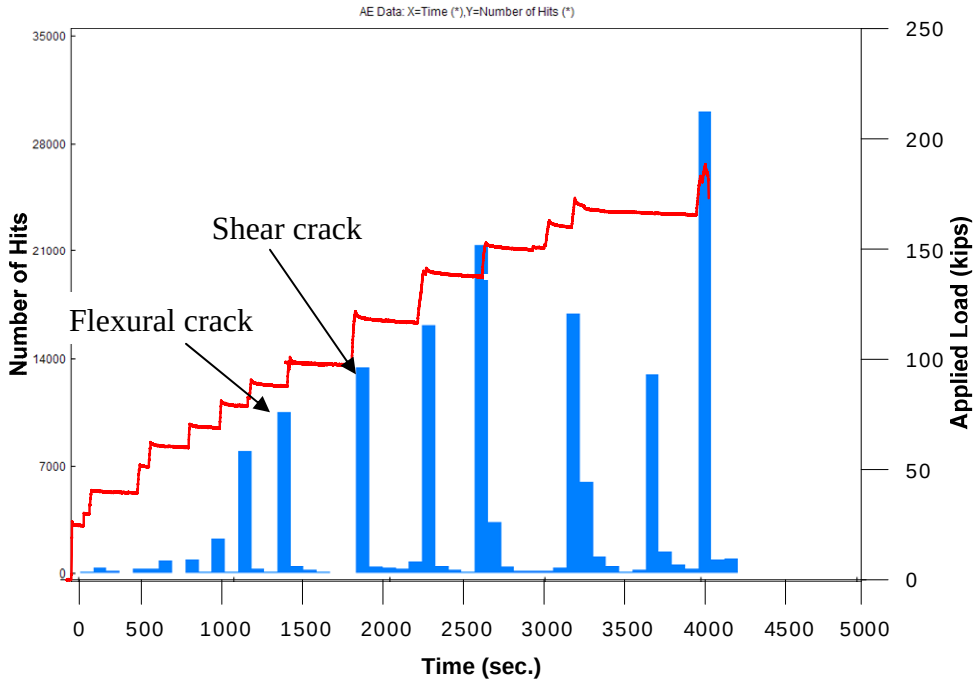

(b)

Figure 6.33 Number of hits versus applied load versus time for 3 – PC#1 and 3 – SFRPC#1 beams; (a) 3 – PC#1; (b) 3 – SFRPC#1

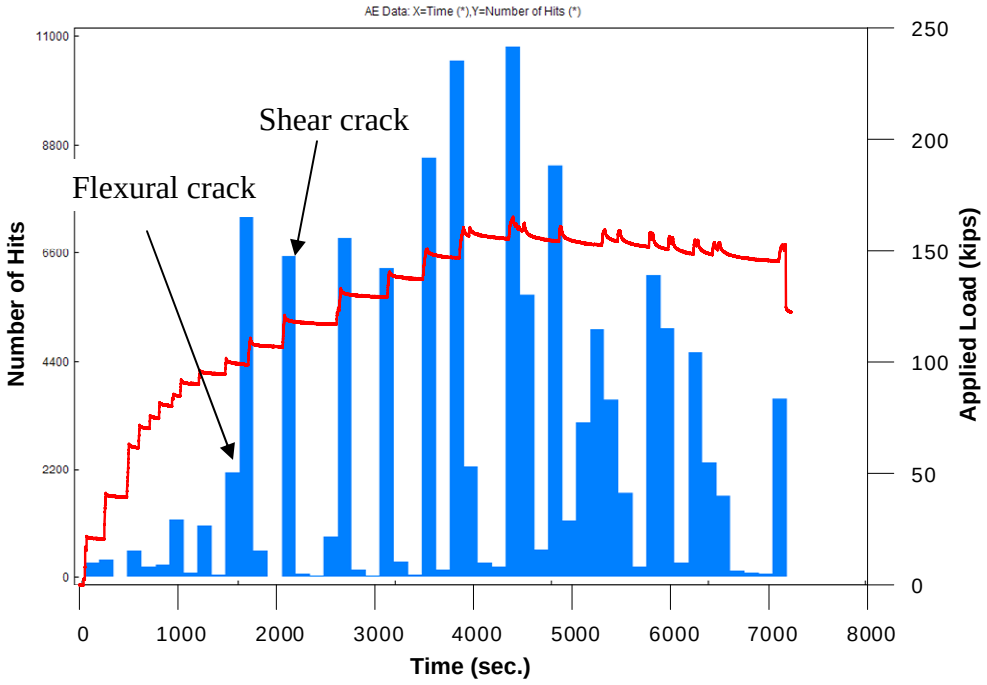

(a)

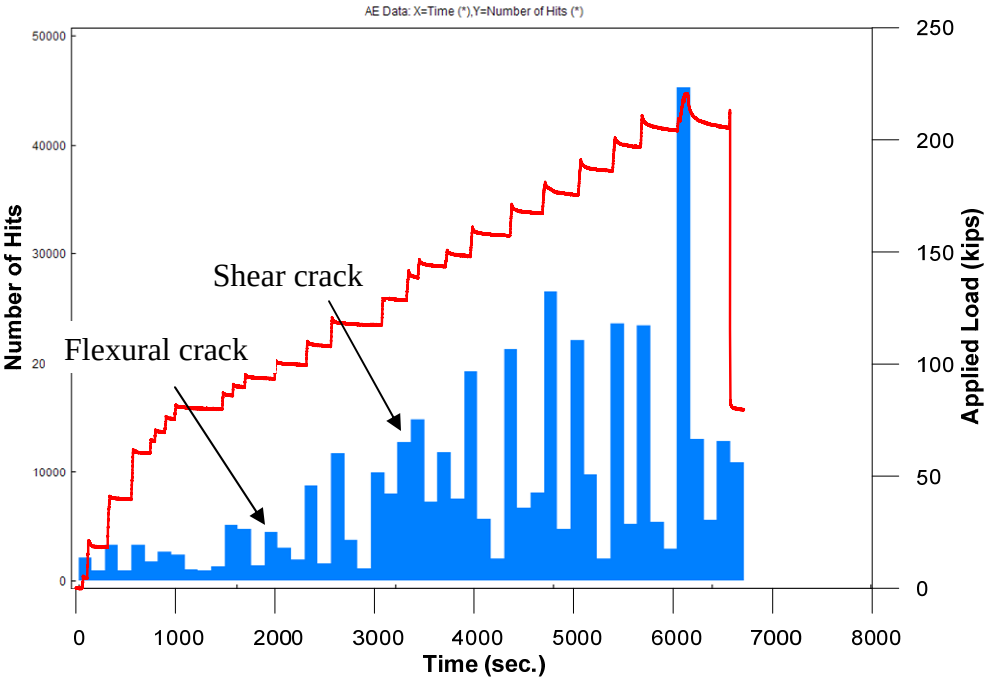

(b)

Figure 6.34 Number of hits versus applied load versus time for 3 – SFRPC#2 and 3 – SFRPC#3 beams; (a) 3 – SFRPC#2; (b) 3 – SFRPC#3

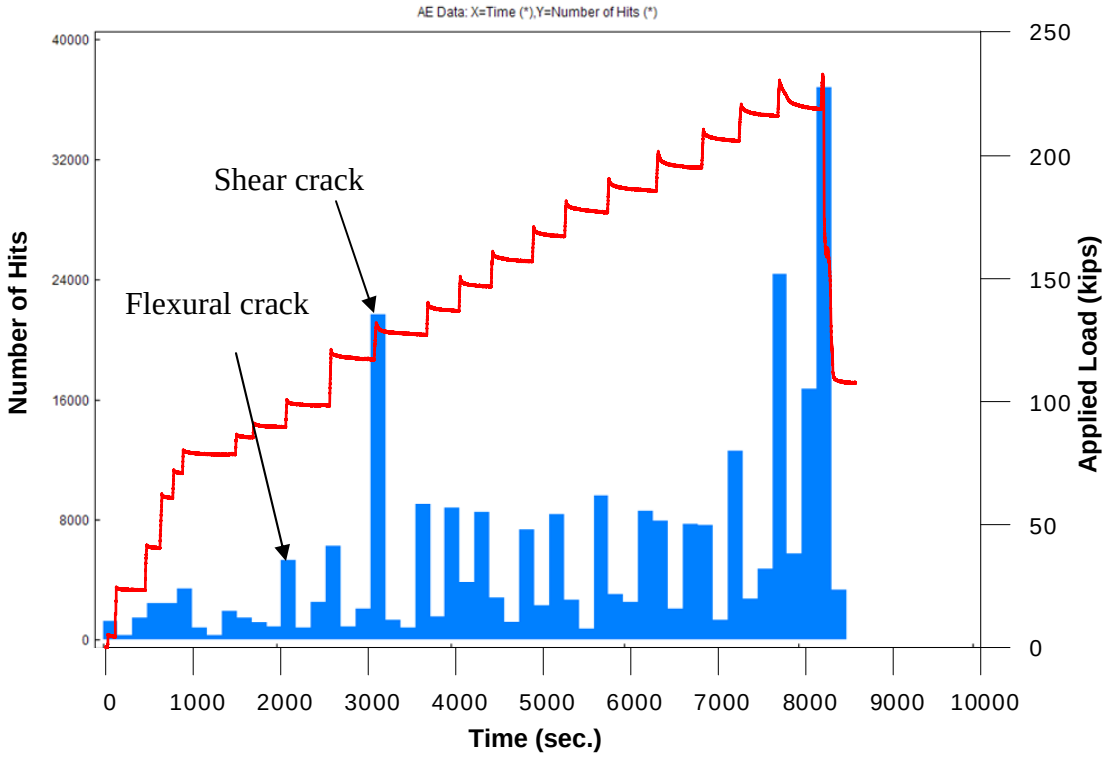

Figure 6.35 Number of hits versus applied load versus time for 3 – SFRPC#4 beams

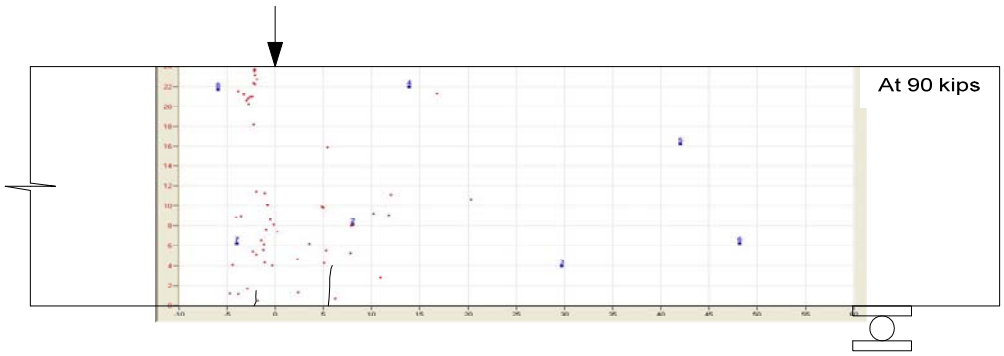

(a)

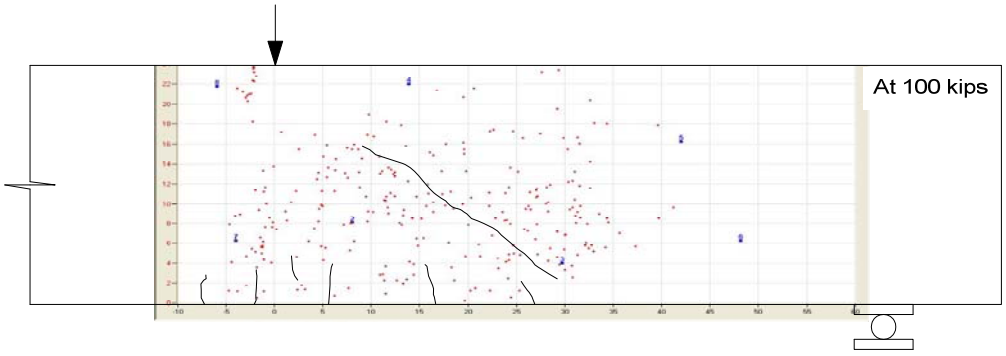

(b)

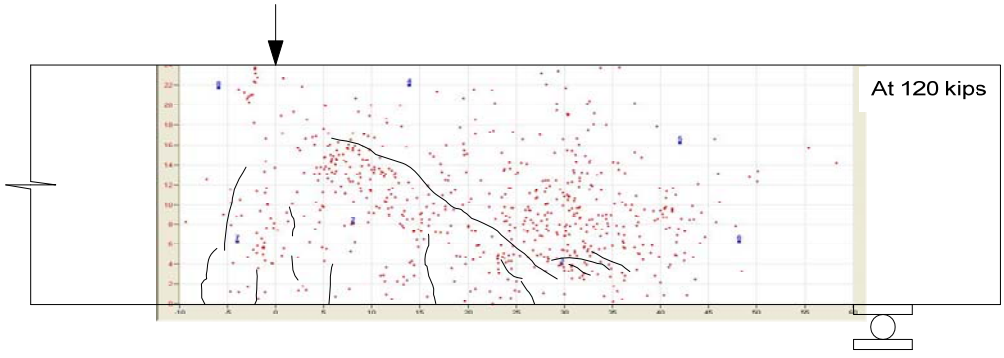

(c)

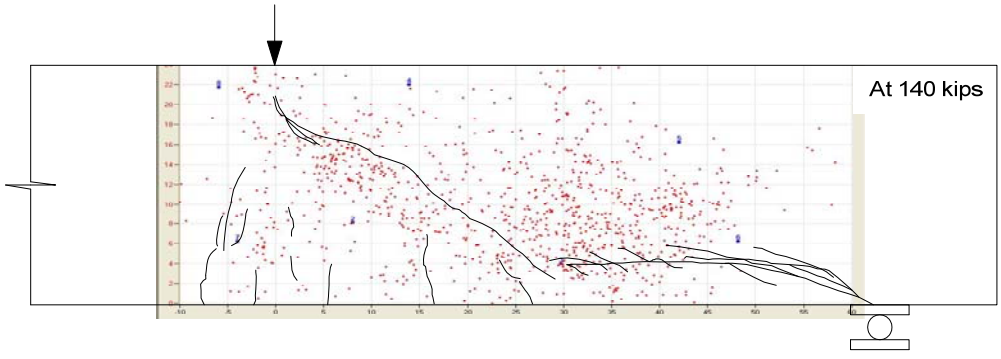

(d)

Figure 6.36 Locations of events in 3 – PC#1 beam at loadings from 90 kips to 140 kips; (a) Load at 90 kips; (b) Load at 100 kips; (c) Load at 120 kips; (d) Load at 140 kips

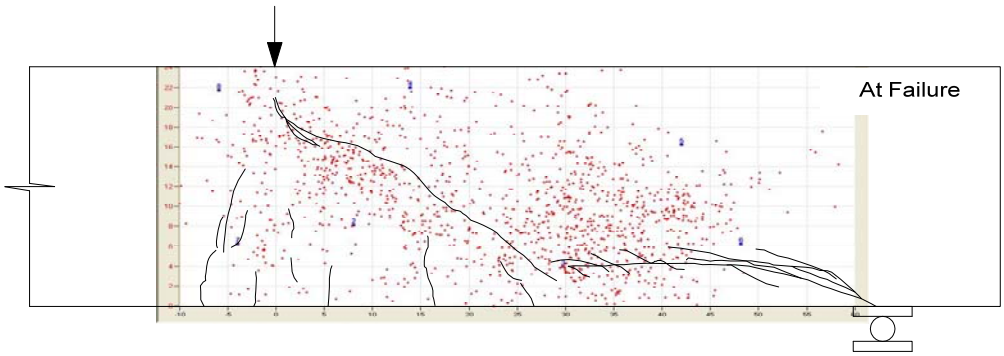

Figure 6.37 Locations of events in 3 – PC#1 beam at failure

(a)

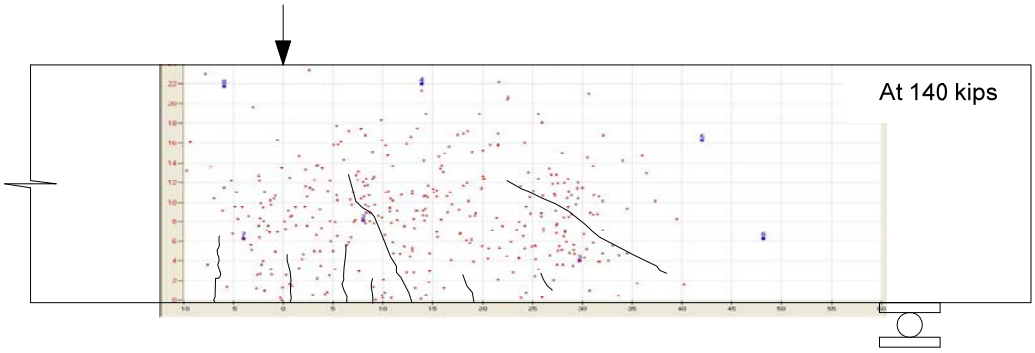

(b)

Figure 6.38 Locations of events in 3 – SFRPC#1 beam at loadings 100 kips and 140 kips; (a) Load at 100 kips; (b) Load at 140 kips

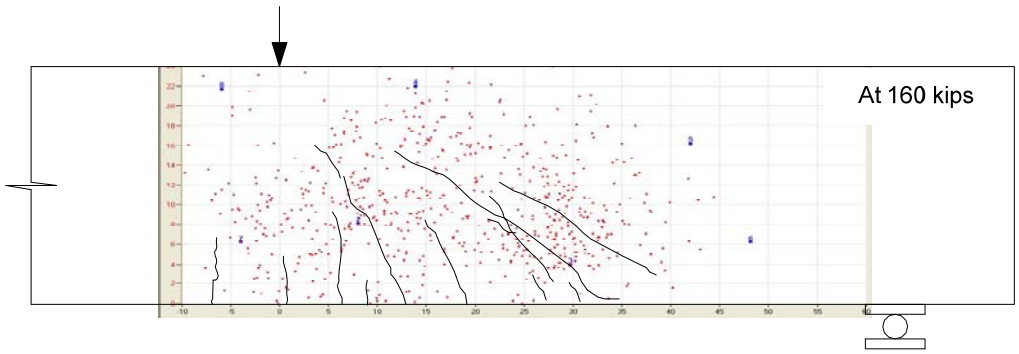

(a)

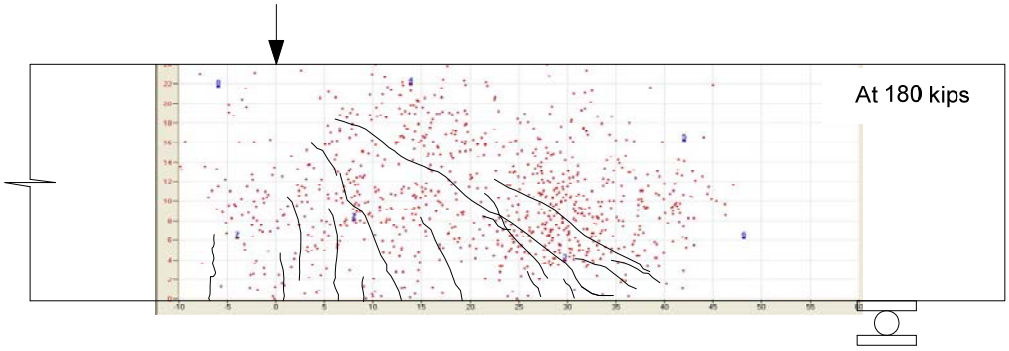

(b)

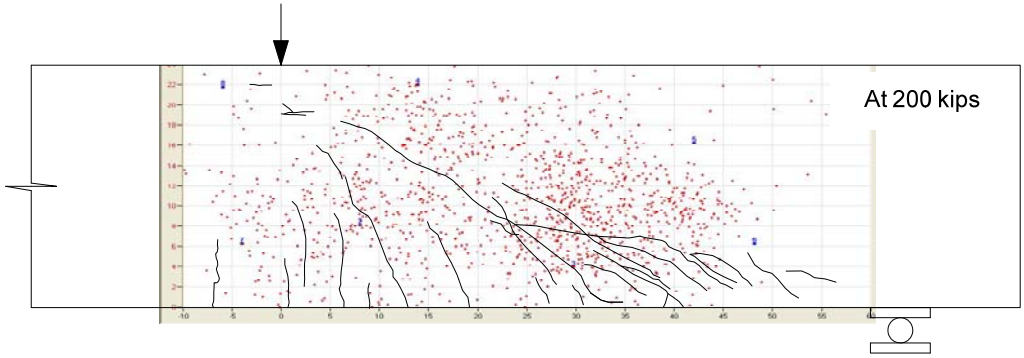

(c)

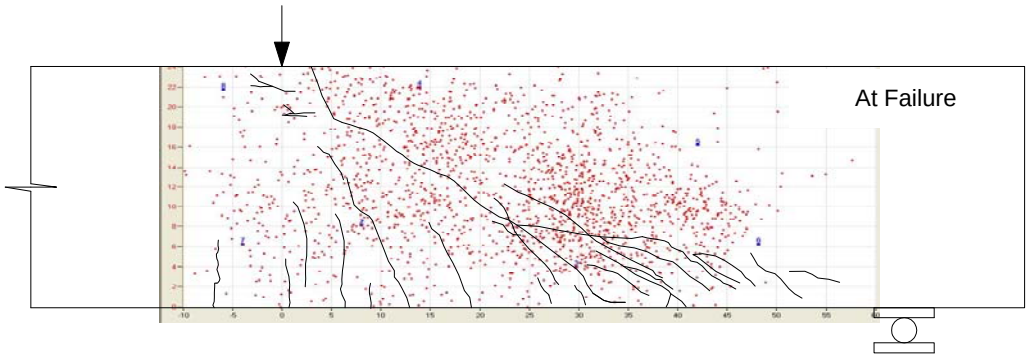

(d)

Figure 6.39 Locations of events in 3 – SFRPC#1 beam at loadings from 160 kips to failure; (a) Load at 160 kips; (b) Load at 180 kips; (c) Load at 200 kips; (d) At failure

(a)

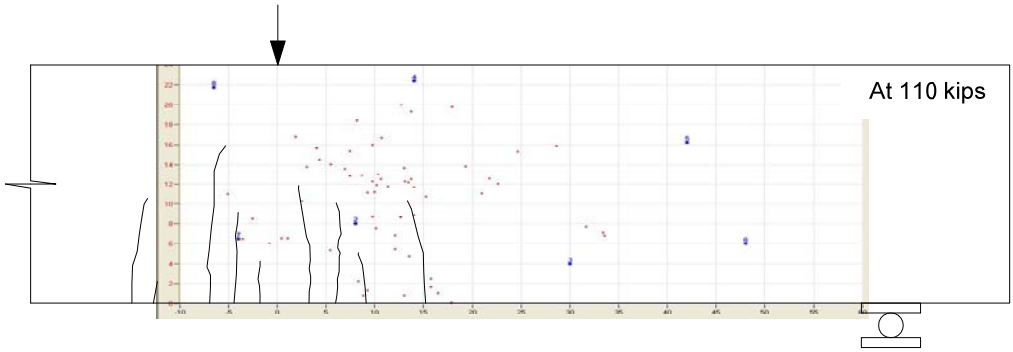

(b)

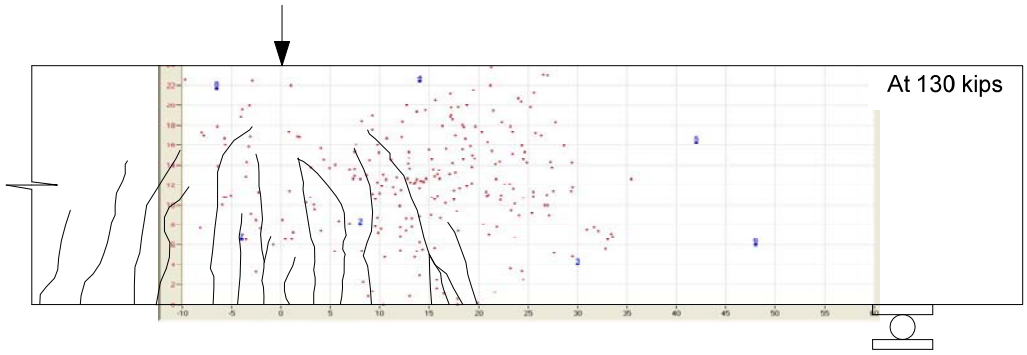

(c)

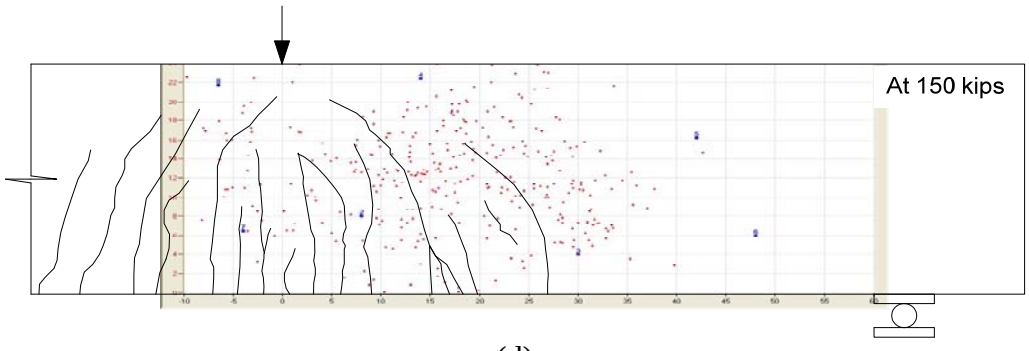

(d)

Figure 6.40 Locations of events in 3 – SFRPC#2 beam at loadings from 95 kips to 150 kips; (a) Load at 95 kips; (b) Load at 110 kips; (c) Load at 130 kips; (d) Load at 150 kips

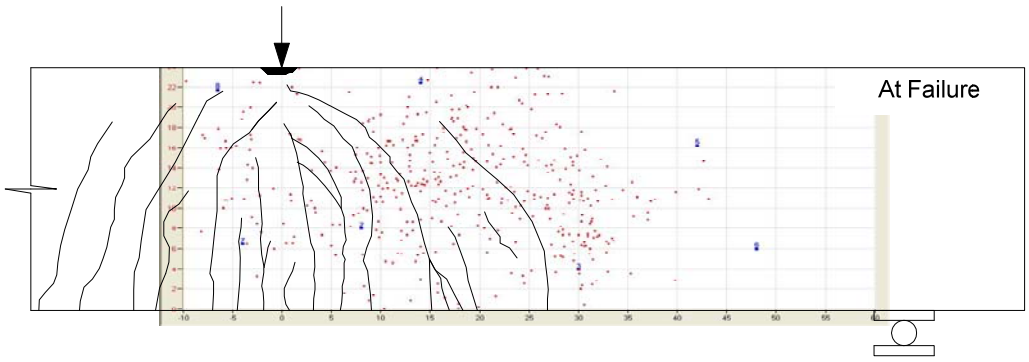

Figure 6.41 Locations of events in 3 – SFRPC#2 beam at failure

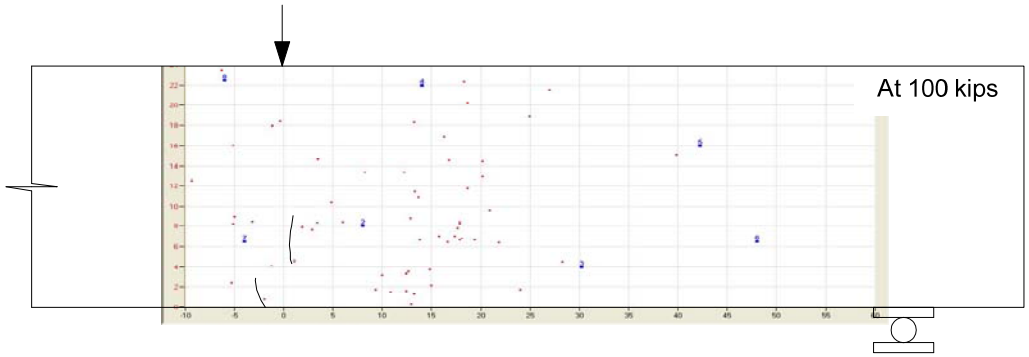

(a)

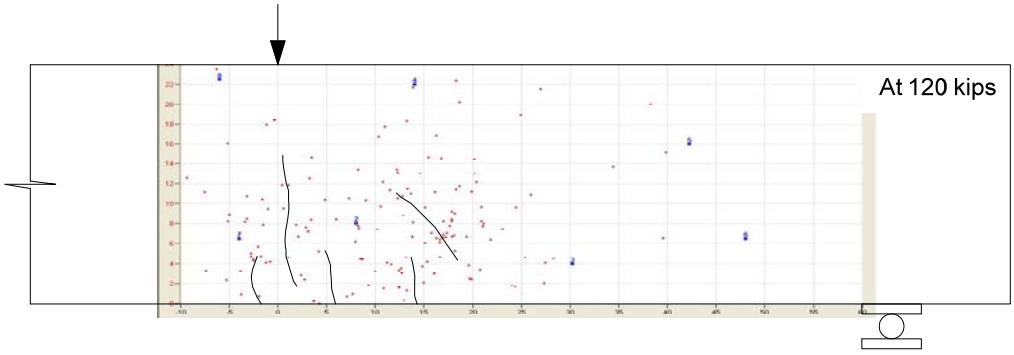

(b)

Figure 6.42 Locations of events in 3 – SFRPC#3 beam at loadings 100 kips and 120 kips; (a) Load at 100 kips; (b) Load at 120 kips

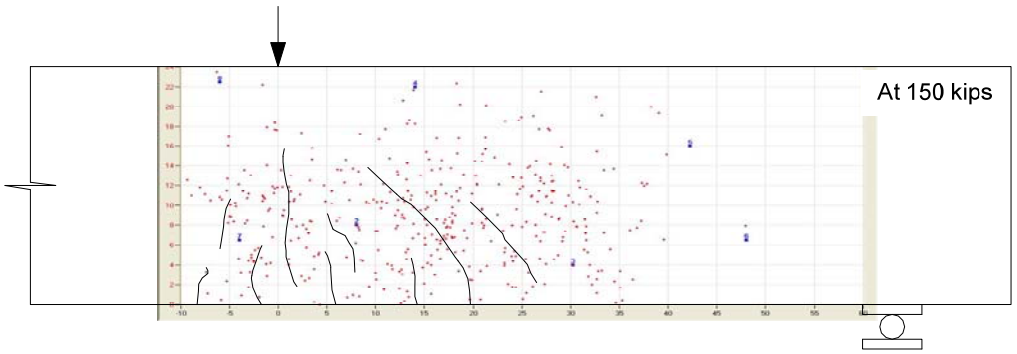

(a)

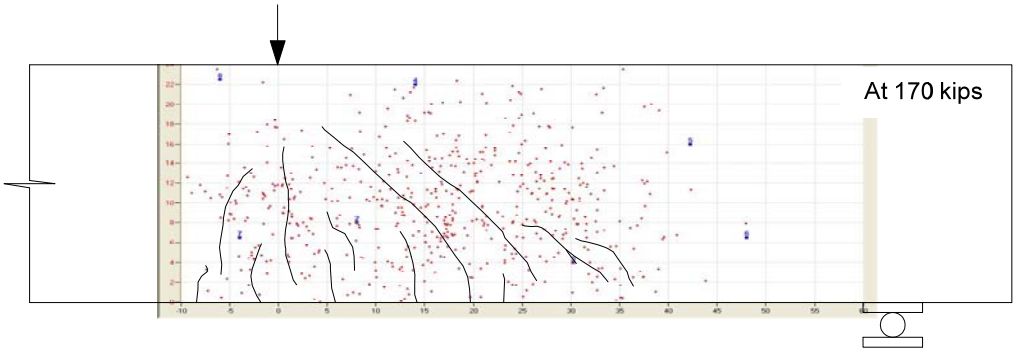

(b)

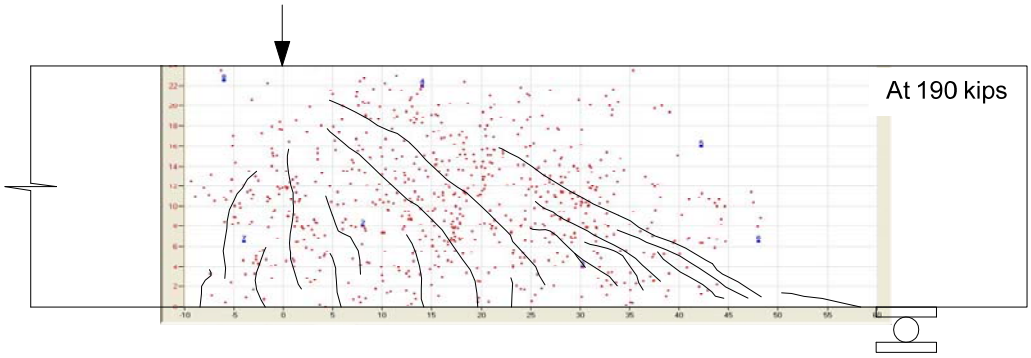

(c)

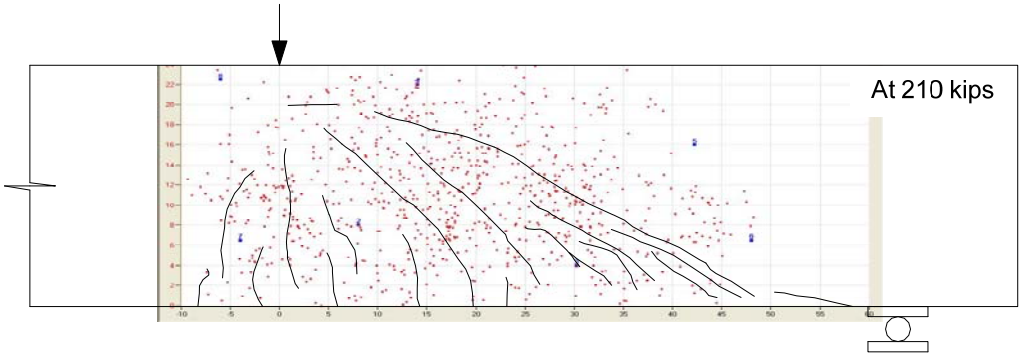

(d)

Figure 6.43 Locations of events in 3 – SFRPC#3 beam at loadings from 150 kips to 210 kips; (a) Load at 150 kips; (b) Load at 170 kips; (c) Load at 190 kips; (d) Load at 210 kips

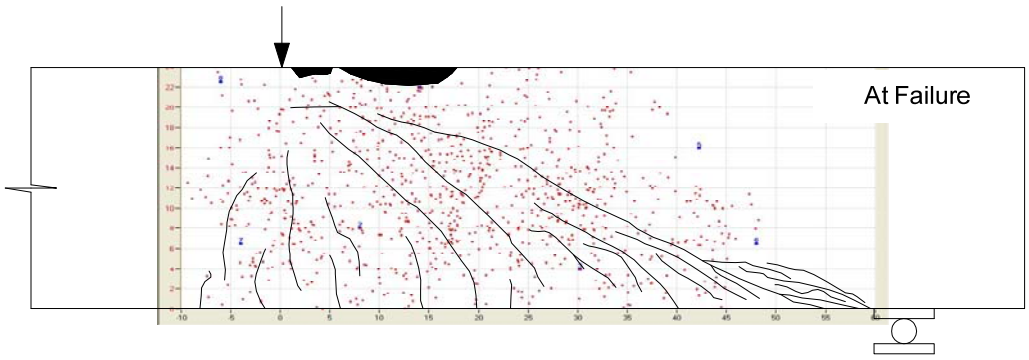

Figure 6.44 Locations of events in 3 – SFRPC#3 beam at failure

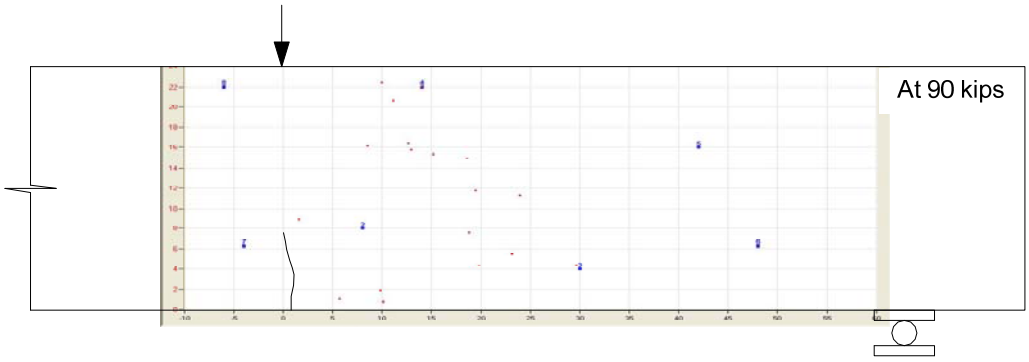

(a)

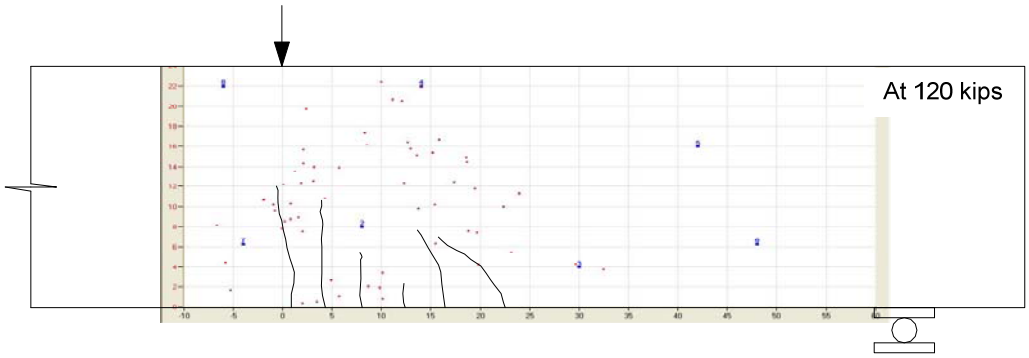

(b)

Figure 6.45 Locations of events in 3 – SFRPC#4 beam at loadings 90 kips and 120 kips; (a) Load at 90 kips; (b) Load at 120 kips

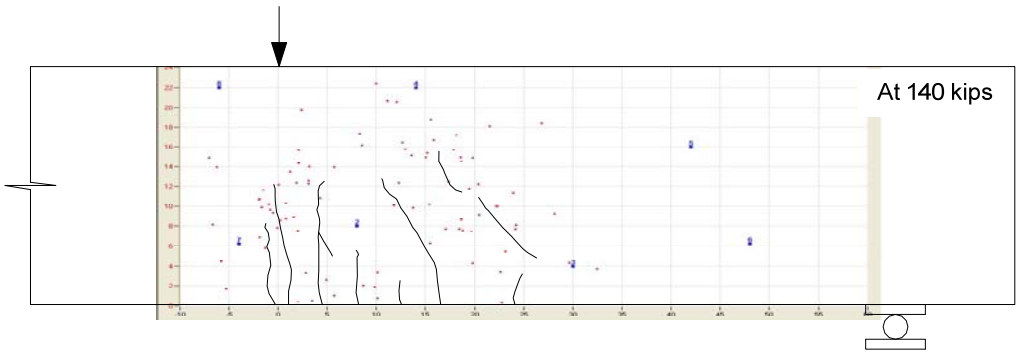

(a)

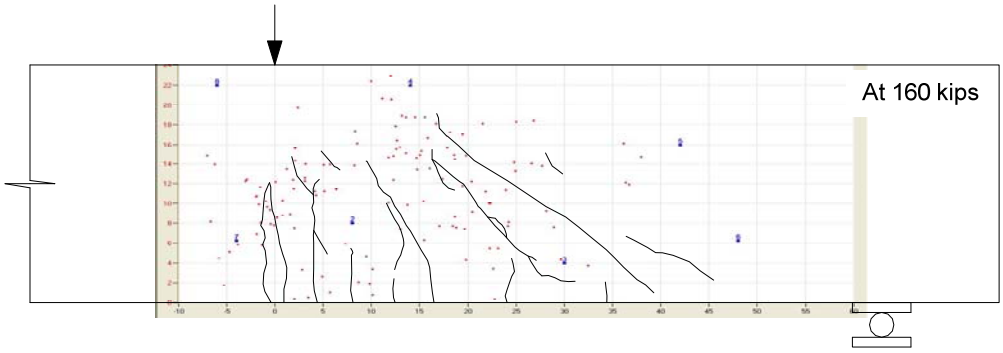

(b)

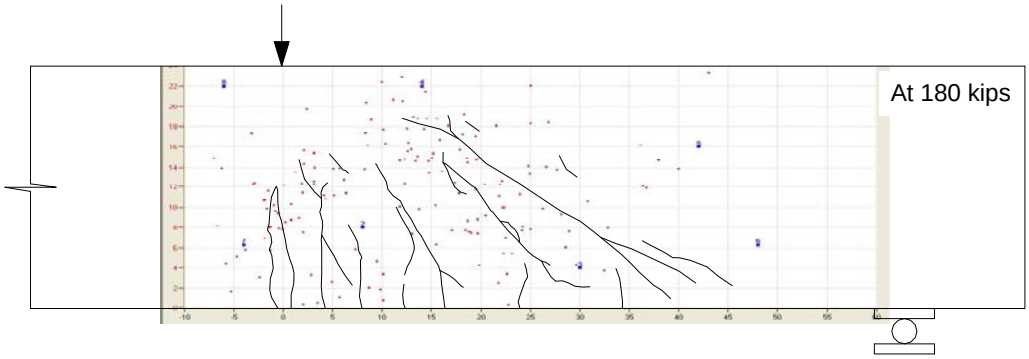

(c)

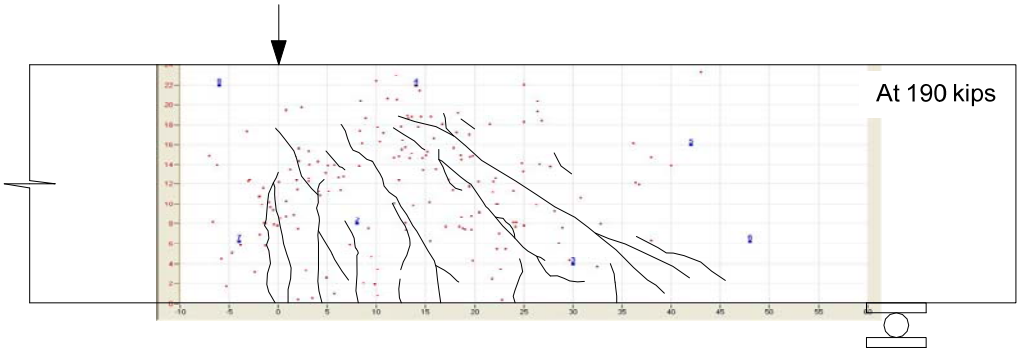

(d)

Figure 6.46 Locations of events in 3 – SFRPC#4 beam at loadings from 140 kips to 190 kips; (a) Load at 140 kips; (b) Load at 160 kips; (c) Load at 180 kips; (d) Load at 190 kips

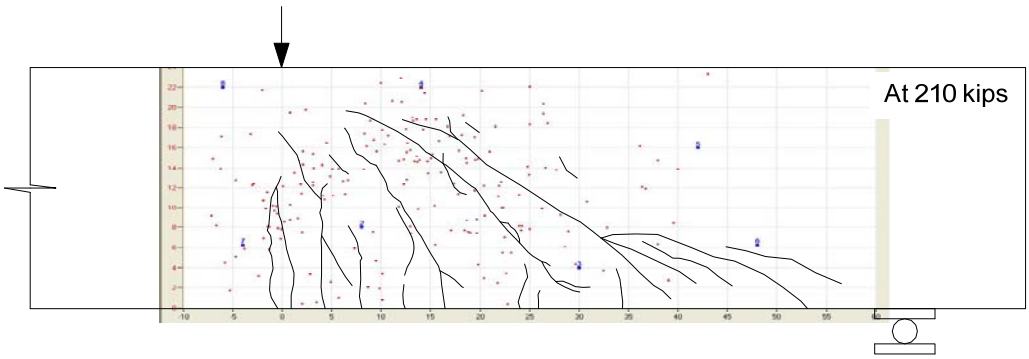

(a)

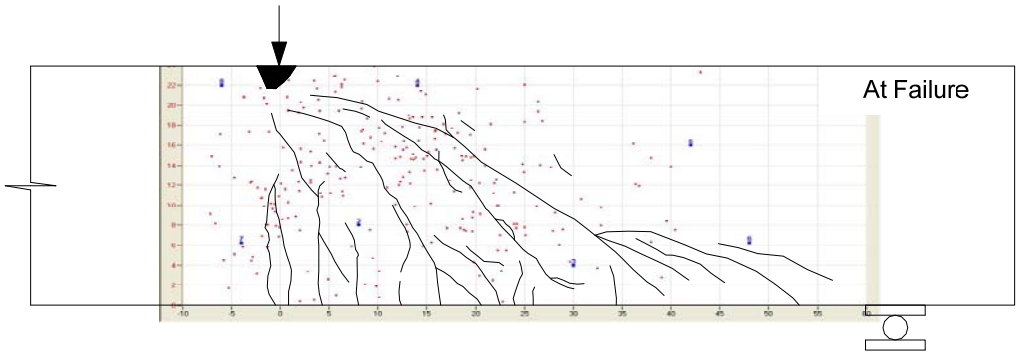

(b)

Figure 6.47 Locations of events in 3 – SFRPC#4 beam at loadings from 210 kips to failure; (a) Load at 210 kips; (b) At failure

CHAPTER 7

ANALYSIS OF EXPERIMENTAL RESULTS

7.1 Shear Stress and Normalized Shear Stress

The shear stress , v_u, resisted by the tested beams can be calculated based on the applied load (P), the span of beams (l), the shear span (a), width of beams (b), and effective depth (d) as follows;

$$v_u = \frac{P(l-a)}{l \cdot bd} \qquad [7.1]$$

In addition, the normalized shear stress can be calculated as the shear stress (v_u) calculated based on Eq. [7.1] divided by square root of compressive strength of concrete (f_c'), $v_u / \sqrt{f_c'}$ (psi).

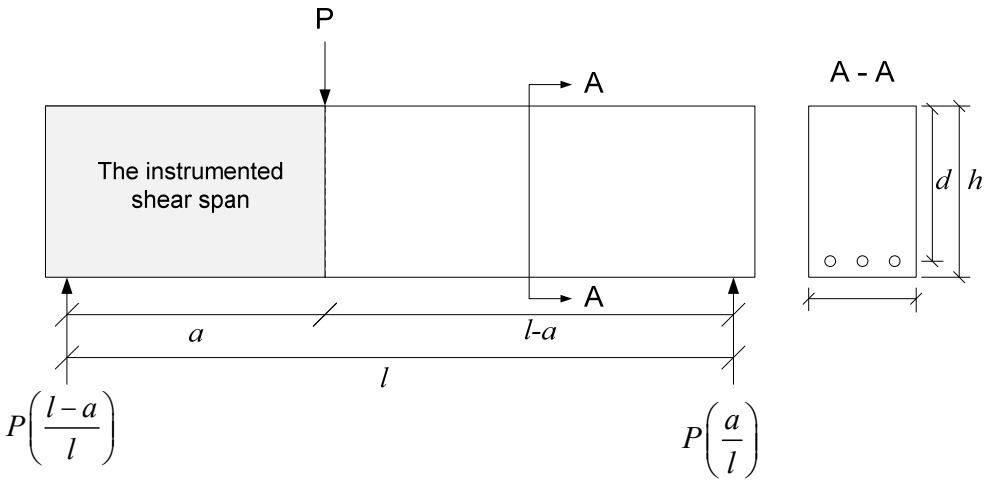

Figure 7.1 Shear forces in tested beams

7.1.1 The shear Stress and Normalized Shear Stress at the First Shear Crack

The first shear cracks were developed at applied load of 110 kips and 170 kips for the first phase specimens, 1 – PC and SFPRC beams, respectively. These are corresponding to shear stresses of 179 psi and 277 psi and normalized shear stresses of $1.9\sqrt{f'_c}$ and $2.9\sqrt{f'_c}$, respectively. The SFPRC beam showed 55% increased the first shear crack strength compared to its counterpart, PC beam. The comparison of load versus deflection response between PC and SFRPC beams is shown in Figure 7.2.

In the second phase, the shear stresses at the first shear crack for two PC beams, 2 – PC#2 and #3, without stirrups in short the shear span were 167 psi and 184 psi, which are corresponding to normalized shear stresses of $2.4\sqrt{f'_c}$ and $2.7\sqrt{f'_c}$, and for PC beam with minimum stirrups, 2 – PC#1, was 176 psi and $2.6\sqrt{f'_c}$ of shear stress and normalized shear stress, respectively. It should be noted that 2 – PC#1, which contained the minimum shear reinforcement showed almost similar the first shear cracking strength compared to 2 – PC#2 and #3. Thus, it can be said that the stirrups were not effective to increase the first shear cracking strength. It was also shown in strain gauges data on the stirrups, i.e., the strains on the stirrups increased after the first shear crack occurred. Unlikely with PC beams, the delay of first shear crack was observed in SFRPC beams in the second phase; the applied loads were 140, 120, and 150 kips at the first crack for the 2 – SFPRC#1(V_f = 0.75%), #2 (V_f = 0.50%), and #3 (V_f = 0.75%), which are corresponding to shear stresses of 234, 201, and 251 psi and normalized shear stresses of $3.2\sqrt{f'_c}$, $3.3\sqrt{f'_c}$, and $3.5\sqrt{f'_c}$, respectively. It is of interest to note that there was no significant different between 0.75% (2 – SFRPC#1 and #3) and 0.50% (2 – SFRPC#2) volume fractions in terms of the first cracking strength. Compared to 2 – PC#3 beams, which showed the highest the first shear cracking load

among PC beams, 2 – SFRPC#1, #2, and #3 beams showed 27%, 10%, and 40% increased the first shear crack strength. It should be noted that ACI 318-08 states that the steel fibers cannot be used as the alternative shear reinforcement when the shear stress exceeds $Ø2\sqrt{f'_c}$ (ACI 318-08 Section 11.4.6.1 (f) *"... V_u not greater than* $\phi 2\sqrt{f'_c}\, b_w d$*"*). However, as can be seen in Figure 7.3, the shear force in SFRPC beams even at the first shear crack much higher than the ACI requirement. In addition, the nominal shear strength calculated ACI 318-08 code for 2 – PC#1 beam is 78 kips, corresponding to the load of 128 kips. This shear strength is even lower than the first shear cracking strength for 2 – SFRPC#1 and #3 beams (V_f = 0.75%), and little higher than that of 2 – SFRPC#2 beam (V_f = 0.50%). As consequence, the criterion is too conservative.

The PC beam in the third phase had the first shear crack at 100 kips of applied load, which is corresponding to shear stress and normalized shear stress of 167 psi and $2.2\sqrt{f'_c}$, respectively, while the SFRPC beams had shear stress and normalized shear stress of 234 psi and $3.4\sqrt{f'_c}$ for 3 – SFRPC#1 (V_f = 0.75%) and 201 psi and $2.8\sqrt{f'_c}$ for 3 – SFRPC#3 (V_f =0.50%), respectively. For the 3 – SFPRC#4 beam, which contained 0.50% volume fraction of steel fibers and No. 3-stirrups with 21 in. spacing as shear reinforcement, the first shear crack stress and corresponding normalized shear stress are 218 psi and $3.0\sqrt{f'_c}$, respectively. Also as shown in Figure 7.4, the first shear cracking loads for SFRPC beams regardless of the amount of steel fibers in the third phase were beyond the maximum limitation required by ACI building code such that ACI code limitation on the maximum shear force is conservative based on this experiment results.

The inclusion of steel fibers was an effective means to improve the first shear crack resistance. Therefore, SFRPC beams will exhibit better structural performance under service loading,

especially when cracks are expected. The crack-free sections will mitigate the problems of fatigue of reinforcement, greater deflection due to reduced moment of inertia, as well as corrosion. The first shear cracking and ultimate strengths of all beams are listed in Table 7.1.

7.1.2 The Shear Stress and Normalized Shear Stress at the Ultimate

The 1 – PC beam was failed at 146 kips of the applied load, which is corresponding to the 238 psi and $2.5\sqrt{f'_c}$ of the shear stress and the normalized shear stress, respectively. While 1 – SFRPC beam was failed at 327 kips of the applied load, which is corresponding to the 533 psi and $5.6\sqrt{f'_c}$. The shear strength of the SFRPC beam was 124% higher compared to the PC beam. In addition, it should be noted that the ultimate strength of PC beam was even less than the first shear cracking strength of SFRPC beam, i.e., the ultimate shear strength of PC beam was 238 psi and the first shear cracking strength of SFRPC beam was 277 psi.

In the second phase, the shear stresses at the ultimate for two PC beams, 2 – PC#2 and #3, without stirrups were 335 psi and 362 psi, which are corresponding to $4.9\sqrt{f'_c}$ and $5.2\sqrt{f'_c}$ of the normalized shear stresses. 2 – PC#1, which contained No. 3 stirrups with 21 in. spacing in the short shear span, showed 377 psi and $5.5\sqrt{f'_c}$ of shear stress and normalized shear stress, respectively. While SFRPC #1 (V_f = 0.75%), #2 (V_f = 0.50%), #3 (V_f = 0.75%)beams showed 353 psi, 333 psi, and 385 psi of shear stresses and $4.9\sqrt{f'_c}$, $5.4\sqrt{f'_c}$, and $5.3\sqrt{f'_c}$ of normalized shear stresses at the ultimate.

In the third phase, it should be mentioned that the discussion regarding to the shear behavior of 3 – SFRPC#2 beam is excluded here since the 3 – SFRPC#2 beam showed flexural failure. The

shear stress at the ultimate for 3 – PC beam was 311 psi and the normalized shear stress was $4.1\sqrt{f'_c}$. While the shear stresses of 3 – SFRPC#1 (V_f = 0.75%), 3 – SFRPC#3 (V_f = 0.50%), and 3 – SFRPC#4 (V_f = 0.50% + stirrups) were 403 psi, 370 psi and 390 psi, which are corresponding to the normalized shear stresses of $5.6\sqrt{f'_c}$, $5.3\sqrt{f'_c}$, and $5.4\sqrt{f'_c}$, respectively. The 3 – SFRPC beam#1 showed 30%, 9%, and 3% increases of shear strength compared to 3 – PC, 3 – SFRPC#3, and 3 – SFRPC#4 beams. It is of interest to note that 3 – SFRPC#4 beam (V_f = 0.50% + No. 3 stirrups spacing 21 in.) showed the normalized shear stress of $5.4\sqrt{f'_c}$, which is lower than 3 – SFRPC#1, $5.6\sqrt{f'_c}$.

Table 7.1 Summary of test results

Phase	Beam	At first shear crack			At the ultimate		
		Applied load (kips)	**Shear stress (psi)**	**Normalized shear stress** $\left(v_u / \sqrt{f'_c}\right)$	**Applied load (kips)**	**Shear stress (psi)**	**Normalized shear stress** $\left(v_u / \sqrt{f'_c}\right)$
1st	PC	110	179	1.9	146	238	2.5
	SFRPC	170	277	2.9	327	533	5.6
2nd	PC#1	105	171	2.5	225	377	5.5
	PC#2	100	163	2.4	200	335	4.9
	PC#3	110	179	2.6	216	362	5.2
	SFRPC#1 (V_f = 0.75%)	140	228	3.2	211	353	4.9
	SFRPC#2 (V_f = 0.50%)	120	195	3.2	199	333	5.4
	SFRPC#3 (V_f = 0.75%)	150	244	3.4	230	385	5.3
3rd	PC	100	163	2.1	186	311	4.1
	SFRPC#1 (V_f = 0.75%)	140	228	3.1	241	403	5.6
	SFRPC#2 (V_f = 0.75%)	120	195	2.7	165	276	3.8
	SFRPC#3 (V_f = 0.50%)	120	195	2.8	221	370	5.3
	SFRPC#4 (V_f = 0.50% + Stirrups)	130	212	3.0	233	390	5.4

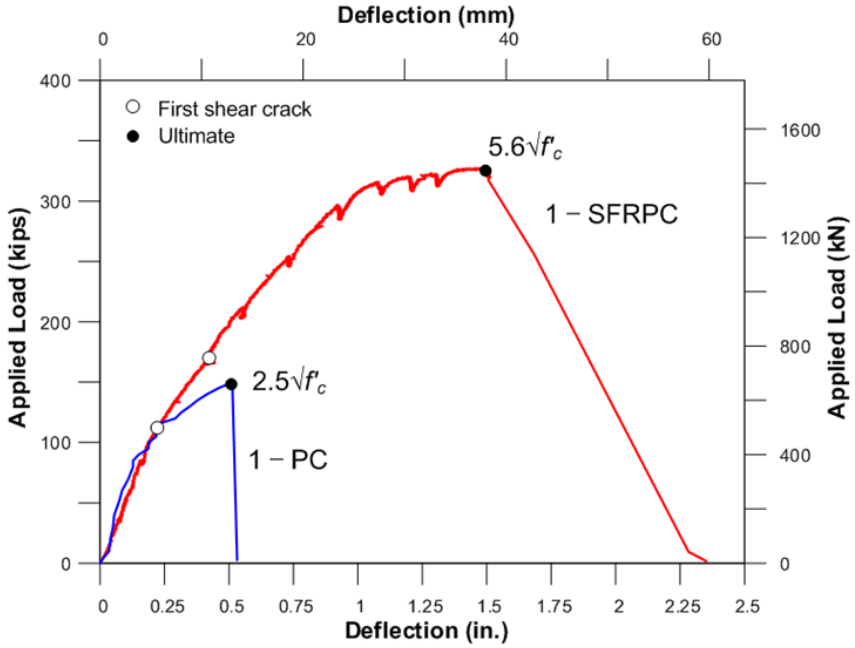

Figure 7.2 Load versus deflection responses for beams in the first phase

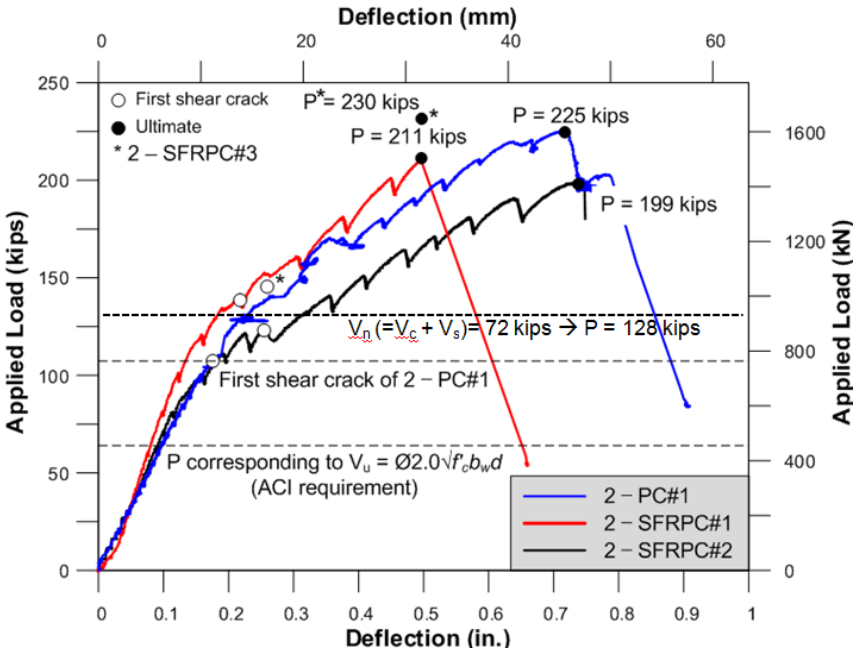

Figure 7.3 Load versus deflection responses for beams in the second phase

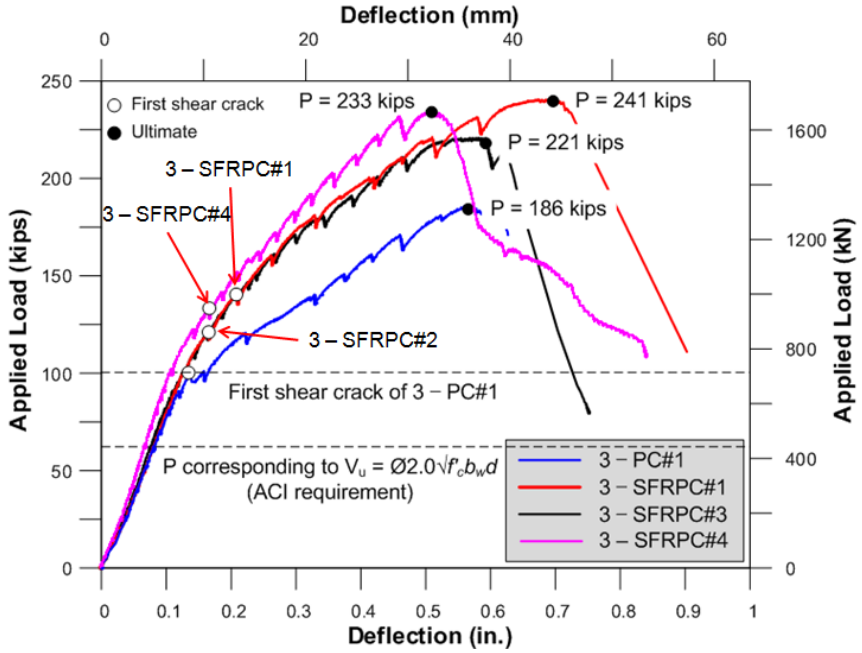

Figure 7.4 Load versus deflection responses for beams in the third phase

7.2 Failure Modes

Diagonal tension failure is more often seen (in addition to the flexural-shear failure) in prestressed concrete beams due to the enhanced flexural resistance by the pre-compression.

The diagonal tension failure was observed in 1 – PC beam. The critical shear crack initiated from mid-depth of the beam, and then rapidly propagated towards loading point. The tip of the crack eventually extended deep into the compression zone, leading to a very small compression zone. Thus, the contribution of the shear resistance coming from the compression zone would be negligible. Finally the beam was failed due to the diagonal crack. This specimen had the lowest shear strength, in terms of normalized shear stress, among all tested beams in this study. 1 – SFRPC beam was failed due to the splitting of the compression strut and instability of the crushed compression zone. Unlikely PC beam, the shear crack propagated toward the loading

point, but the rate was slower and the propagation was stopped under the loading point creating relatively larger area of the compression zone. Figure 7.5 shows the failures of beams in the first phase. By observing the results, the failure modes of PC and SFRPC were clearly different.

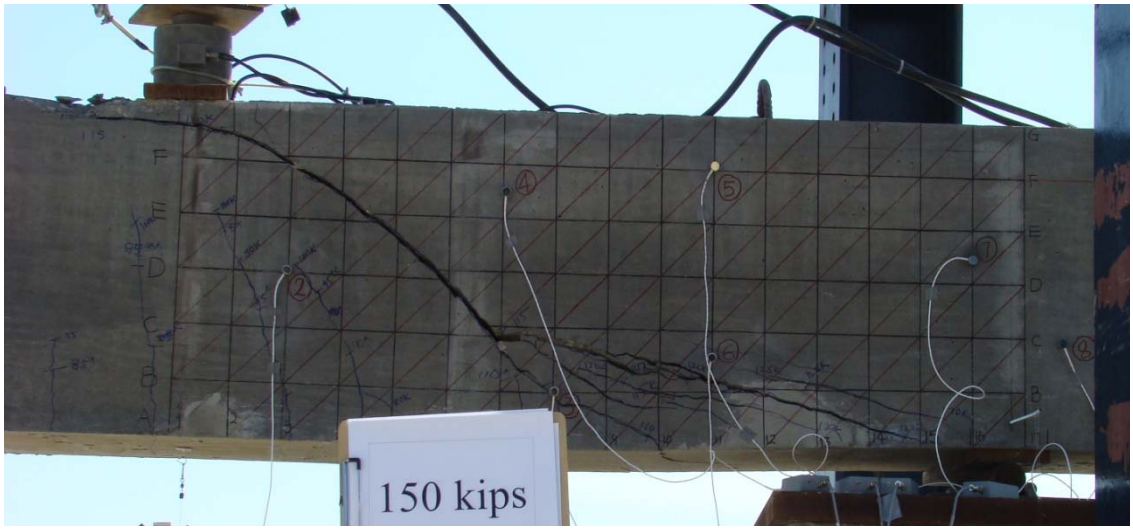

(a)

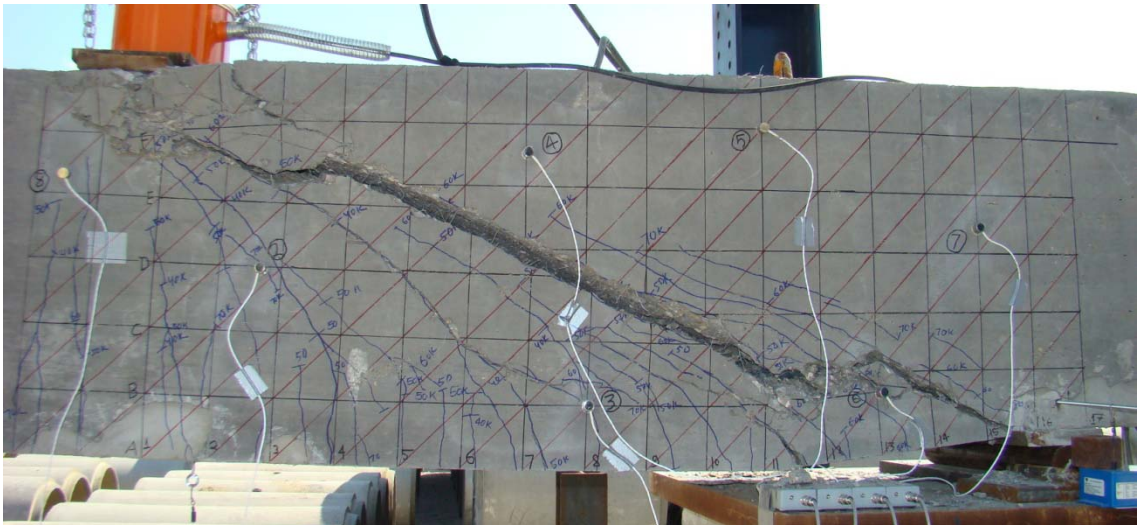

(b)

Figure 7.5 Failure of beams in the first phase; (a) 1 – PC; (b) 1 – SFRPC

Figure 7.6 shows the failures of PC beams in the second phase. 2 – PC#1 (No. 3 stirrups with spacing of 14 in.) failed due to the crushing of concrete in the compression zone. While 2 – PC#2

and #3 beam were failed due to the splitting of the compression strut. The failure modes of 2 – PC#2 and #3 were similar with 1 – SFRPC beam. It should be noted that 2 – PC#2 and #3 beams showed the larger depth of the compression zone prior to the failure (similar with 1 – SFRPC beam). Therefore, the compression zone was able to create the load transfer mechanism, i.e., the load was transferring through the compression strut. The SFRPC beams, regardless of fibers content, in the second phase failed due to the crushing of concrete in the compression zone. Figure 7.4 shows the failure of the SFRPC beams. The SFRPC beams showed the crushing of concrete prior to the failure. It could be said that the SFRPC beams had the similar load transfer mechanism with PC beams, however, the compression zone was crushed in the SFRPC beams prior to the splitting of the compression strut. Figure 7.8 and 7.9 show the failure of the beams in the third phase. 1 – PC beam showed very brittle failure. The compression zone was crushed such that the instability of the compression zone was led to fail. Most of SFRPC beams showed similar failure mode regardless of fiber contents. The concrete crushing in the compression zone led to fail. However, 3 – SFRPC#2 beam, which had less amount of longitudinal tensile rebars, was failed due to flexure. It can be evidence that the inclusion of steel fibers could change the failure from shear to flexure.

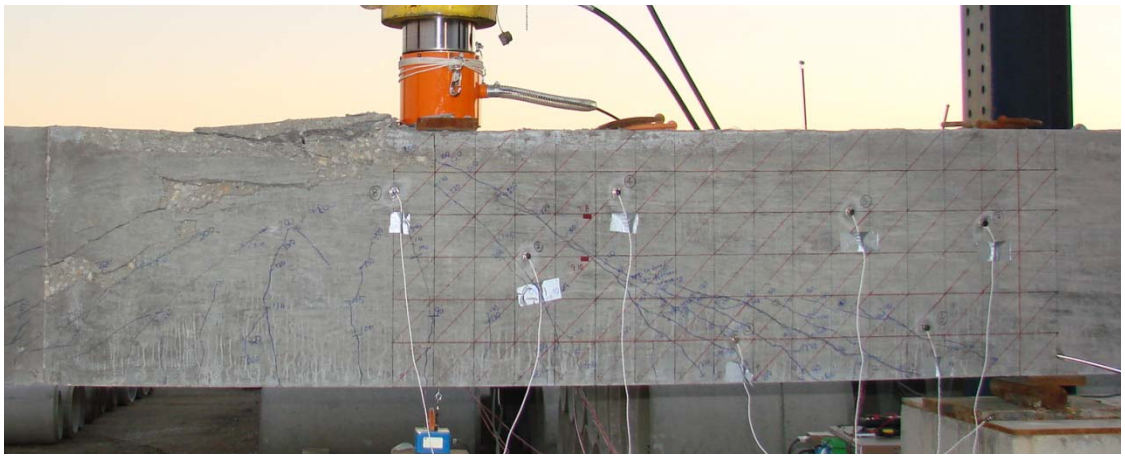

(a)

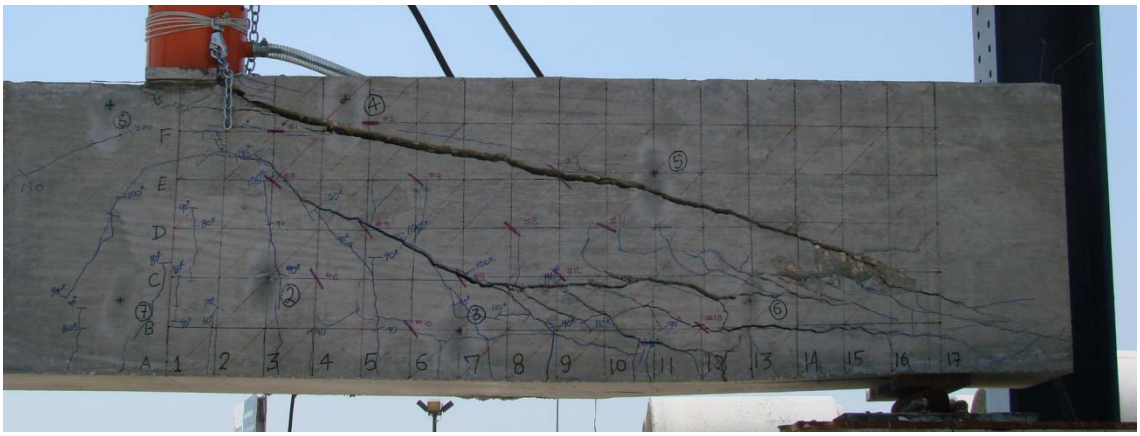

(b)

(c)

Figure 7.6 Failure of PC beams in the second phase; (a) 2 – PC#1; (b) 2 –PC#2; (c) 2 – PC#3

(a)

(b)

(c)

Figure 7.7 Failure of SFRPC beams in the second phase; (a) 2 – SFRPC#1; (b) 2 –SFRPC#2; (c) 2 – SFRPC#3

(a)

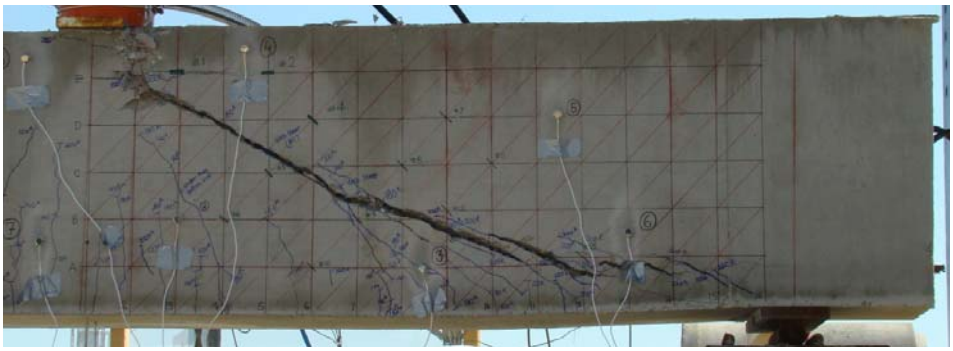

(b)

(d)

Figure 7.8 Failure of beams in the third phase; (a) 3 –PC#1; (b) 3 –SFRPC#1; (c) 3 – SFRPC#3

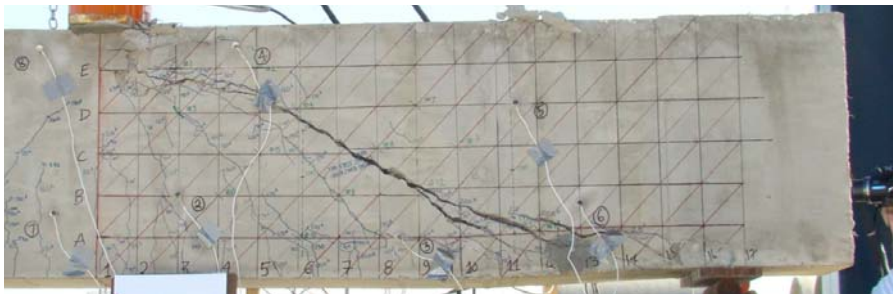

Figure 7.9 Failure of 3 – SFRPC#4 beams in the third phase

7.3 Failure Mechanism

7.3.1 The Direct Load Transfer Mechanism in RC

As discussed in the previous section, most of SFRPC beams were failed due to either the splitting of the compression strut and the crushing of concrete in the compression zone. The failure mode is generally observed in the direct load transfer mechanism, i.e., the load is transferring from the loading point to the support through the compression strut. The mechanism was originally proposed by Drucker (1961). The direct load transfer mechanism, which is based on the theory of the plasticity, indicates that the applied load is carried directly by the inclined compressive struts and the tie, which can be represented by the flexural reinforcement. The schematic view of this model is shown in Figure 7.10. The theory assumes that the concrete cannot take any tension, and the complete debonding between the concrete and the flexural reinforcement occurs.

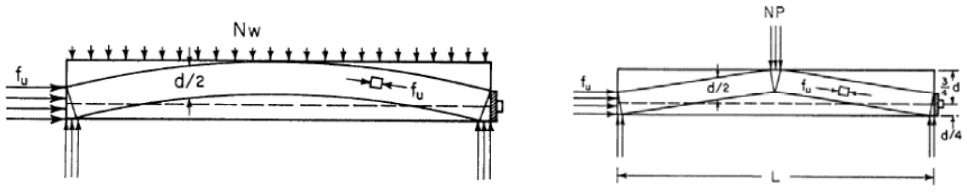

(a) (b)

Figure 7.10 Arch or strut action for load transfer in plain concrete beams (Drucker, 1961); (a) Uniformly distributed load; (b) Concentrated load

However, as point out by Muttoni and Ruiz (2008), the predicted strength of the concrete beam based on this direct load transfer mechanism overestimates its strength as compared to the experiment results, especially for the slender beams. The primary reason why the model leads to unsafe design for the slender RC beams is that any inclined crack that propagates into the imaginary compression strut will destroy the strength of the compression strut. This phenomenon is less significant for smaller value of the shear span to effective depth ratio, which can be classified as deep beam. However, it becomes more critical for the slender beam in which shear span to the depth ratio ranges from 2.5 to 4.0 (Muttoni and Ruiz, 2008). They used the beams (the shear span to the depth ratio equals to 2.77) tested by Leonhardt and Walther to explain this mechanism as shown in Figure 7.11. They found that specimen, EA1, only reached 50% of its strength estimated according to the direct load transfer mechanism, while specimen, EB1, reached 86%. The specimen BP2, in which the cracking control reinforcement was used in the compression zone, attained a full strength since the opening of crack in the compression zone was limited due the reinforcement. This was mainly due to the less interference to the compression strut by the shear crack when the smooth bars were used to minimize the bond and cracks. They also mentioned that the concrete beam could sustain a stress (not collapse) even though a critical shear existed in theoretical compression strut if the width of crack could be limited by any reinforcement in the compression region.

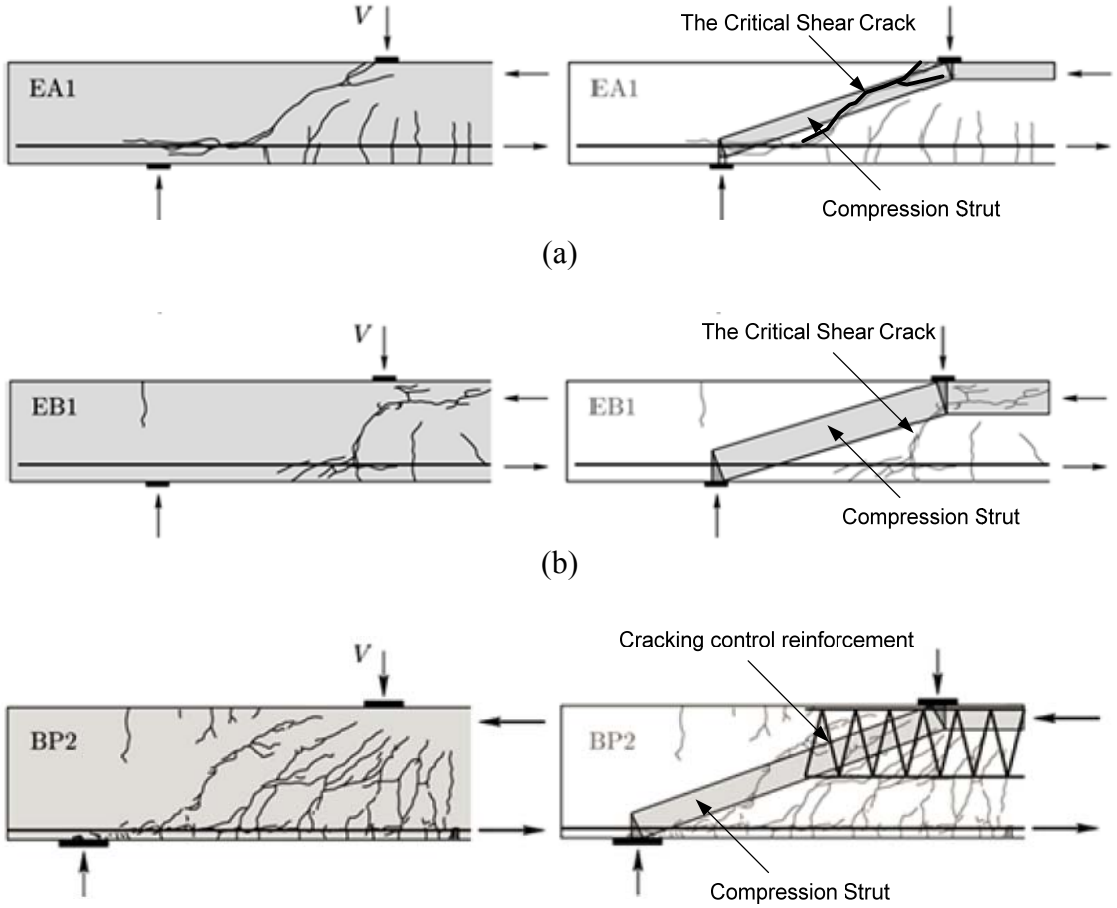

Figure 7.11 Influence of crack pattern in shear strength of concrete beams (reproduce Muttoni and Ruiz, 2008); (a) Specimen EA1 (deformed bars) by Leonhardt and Walther; (b) Speicmen EB1 (smooth bars) by Leonhardt and Walther; (c) Specimen BP2 (cracking control reinforcement) by Muttoni and Ruiz

They proposed the *critical shear crack theory*, which assumes that the direct load transfer mechanism is a valid force transfer path even though the shear crack propagates into the theoretical compression strut since the aggregate interlocking would be activated to prevent the failure of the cracked strut.

7.3.2 The Direct Load Transfer Mechanism in SFRPC

7.3.2.1 Aggregate Interlocking

Currently, it is believed that the shear resistance of a concrete beam without shear reinforcement is primarily originated from three components after the initiation of the shear crack: aggregate interlocking, compression zone, and dowel action of longitudinal reinforcement. It has been assumed that the aggregate interlocking is the primary component contributing the shear resistance (Fenwick and Paulay, 1968). In addition, Vecchio and Collins (1986) developed the Modified Compression Field Theory (MCFT). In this theory, they proposed the following equation to estimate the shear resistance of the aggregate interlocking.

$$\frac{v_{ci}}{\sqrt{f'_c}} = \frac{0.18}{0.31 + \frac{24w}{a_g + 16}} \qquad (MPa, mm) \qquad [7.2]$$

where, v_{ci} is the aggregate interlock shear capacity at a crack, f'_c is the compressive strength of concrete (MPa), w is the crack width (mm), a_g is the maximum aggregate size (mm). Figure 7.12 shows the normalized concrete strength induced by aggregate interlocking varying the crack width. It should be noted that the strength drops to 50% and 20% of its full strength when the crack widths reaches 0.35 mm and 1.30 mm. Figure 7.13 shows the measured crack widths of the shear cracks for beams is the third phase. The beams resisted more loads after the width of cracks were wider, thus, the contribution of aggregate interlocking was minimized. In addition, the critical shear crack theory mentioned above could not be valid as well since the theory relies on the aggregate interlocking resistance as main shear resistance.

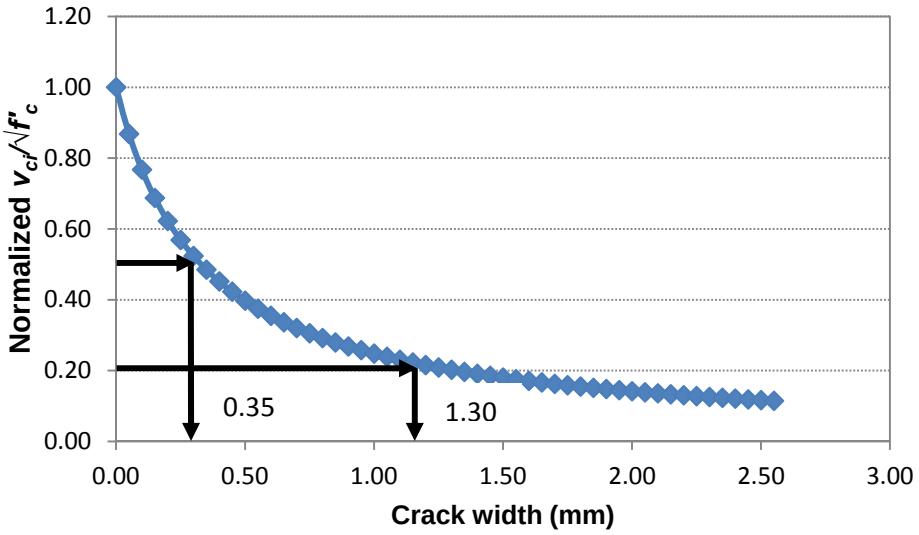

Figure 7.12 Normalized shear resistance induced by the aggregate interlocking varying crack width

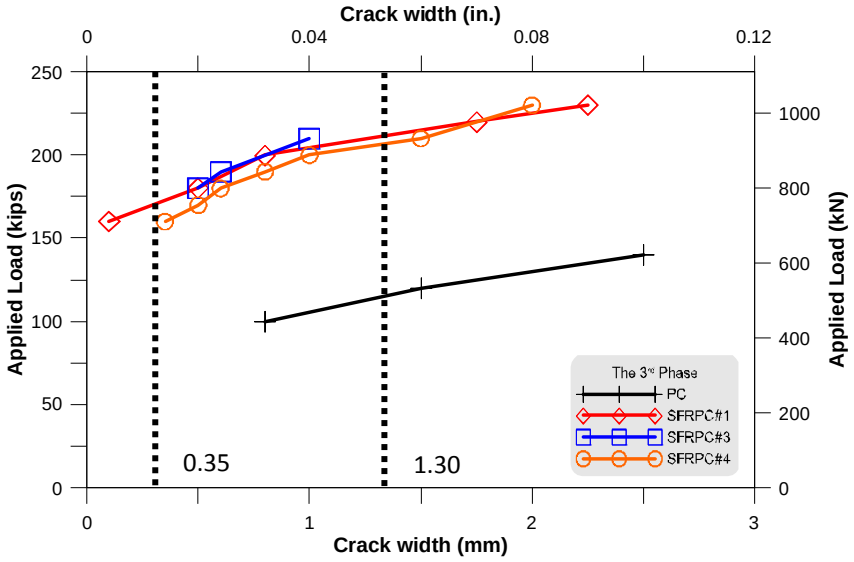

Figure 7.13 Crack widths of the shear cracks for beams in the third phase

In addition, the contribution of the aggregate interlocking is criticized (e.g. Kotsovos, 1998) since it conflicts with the fundamental concrete properties: a crack develops when the maximum tensile stress exceeds its strength, propagates in the direction of the maximum principle compressive stress, and opens in the orthogonal direction such that the friction along the cracked

surface cannot be activated. Moreover the concrete is a brittle material such that it is characterized by a complete and immediate loss of load-carrying capacity as soon as macro-cracking occurs (Kotsovos and Michelis, 1996 and Kotsovos, 2007).

7.3.2.2 Compression Force Path Theory (CFP)

Another shear transfer mechanism, proposed by Kotsovos (1998), introduces the concept of the *compressive force path* theory. In his theory, the ultimate shear resistance of reinforced concrete beam without shear reinforcement is provided by the region of the path along which the compressive force is transmitted to the supports. The schematic view of the illustration is shown in Figure 7.14. The load could not transmit through the cracked section such that the load should transfer through the crack-free region, i.e., the uncracked section. It is assumed that the aggregate interlocking could transmit force since it was not reliable because of the previously mentioned reasons. Therefore, all the forces, including axial and shear, would be transferred through the uncracked section.

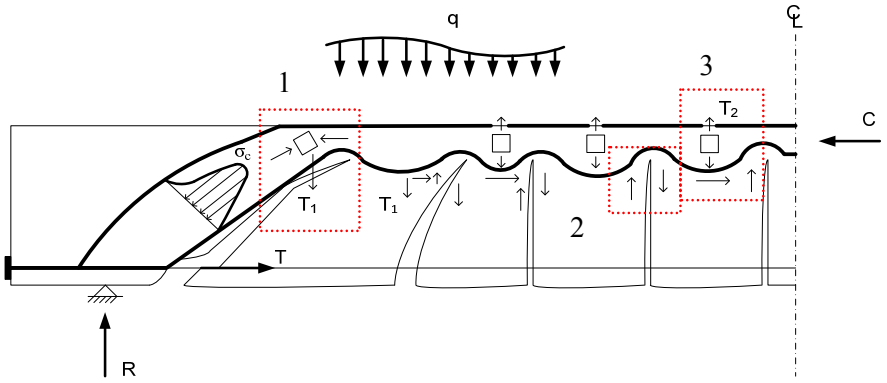

Figure 7.14 Compressive force path for RC (Kotsovos and Pavlović, 1999)

The possible failure would occur at zone 1, 2 and 3. In the zone 1, where the direction of the path is changed, there would be a tensile stress resultant, as indicated in T_1, which tends to separate

the upper part of the compression path from the remainder of the beam. In the zone 2, where crack and uncrakced concrete are interfaced, there would be moment difference if the longitudinal tensile rebars were not completely debonded. As illustrated in Figure 7.15, the moment (ΔM) would be balanced with shear force, V, and level arm, *a* (*Va*). Therefore, the shear force will disrupt the compression zone, which can lead to failure of the beam. In the zone 3, tensile stress resultant, which induced by the compression force due to bending moment, could lead to fail the beam. It should be noted that the diagonal shear crack generally propagates toward the loading point rapidly, as result, the deep penetration of the shear crack into the compression zone and/or path creates smaller area of the compression zone and/or path. However, he claimed that even though the area of the compression zone, which is a key parameter to resist forces, is reduced, the smaller area of the compression zone could be effective to resist load due to the triaxiality of the stress conditions at the ultimate limit state. It should be noted that the compression stress induced by vertical applied load exists such that the strength in the compression zone increase, i.e., the biaxial stress condition increase its strength compared to the uniaxial stress condition as can be seen Figure 7.16.

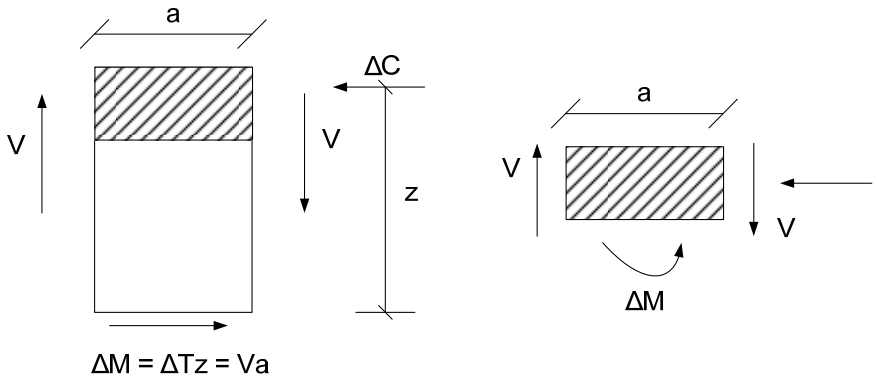

Figure 7.15 State of stress under bond force (Kotsovos and Pavlović, 1999)

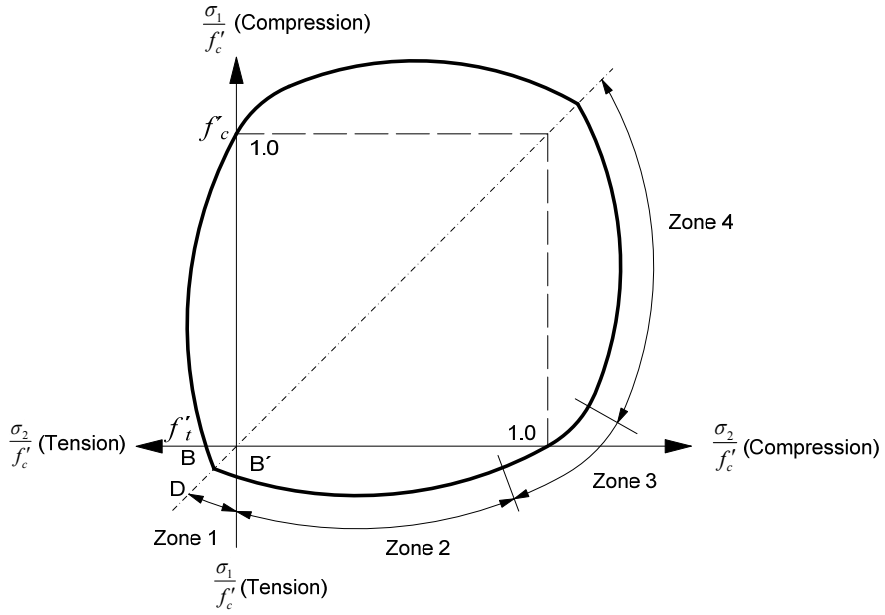

Figure 7.16 Strength of unreinforced concrete subjected to biaxial stresses (Wight and MacGregor, 2009)

This theory was possibly well matched to explain the load transfer mechanism in SFRPC beams. As recalled, most of SFRPC beams through all phases failed due to either crushing of concrete in the compression zone or splitting of the strut. In addition, strains measured on the concrete surface showed higher value above the shear crack, while showed either closed to 0 or tension below the shear crack. Figure 7.17 shows selected concrete surface strain profiles. As can be seen in Figure 7.16 (a), C.S#6 showed increased strain when the first shear crack occurred. On the other hand, C.S.#7 and C.S.#8 showed almost no strain changes. In fact, the strain gauge value may not reflect the actual stress value on the surface since the stain gauges placed with 45° angle with respect to the beam axis. However, the data is still worth to observe since it could provide information of load flow. This strain profile pattern is also shown in C.S.#9, C.S.#10, and C.S.#11 as well as 3 – SFRPC#1 beam shown in Figure 7.17 (b). It could be evidence that the load transferred along the compressive force path, which was located above the shear crack.

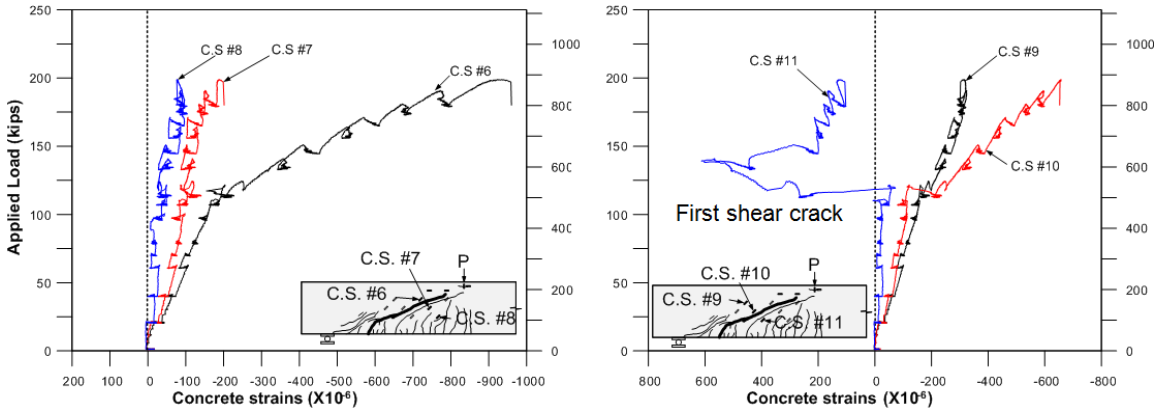

(a)

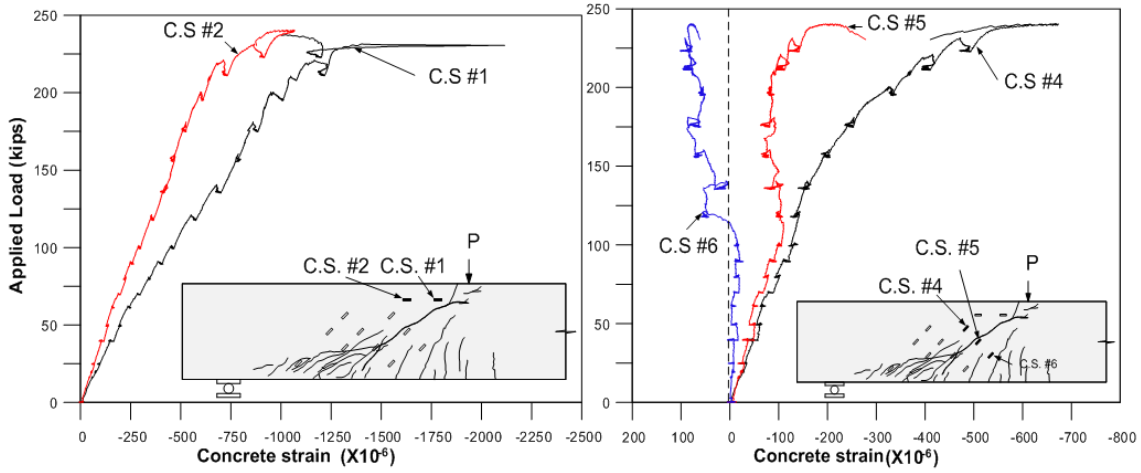

(b)

Figure 7.17 Selected concrete surface strain gauge profiles; (a) 2 – SFRPC#2 beam; (b) 3 – SFRPC#1 beam

In addition to the concrete surface strain profile, AE results support this compression force path. As can be seen in Figure 7.18, a few numbers of AE events occurred in the black dashed line, which was possible compression force path, at the first shear crack. However, at the failure stage, significant numbers of AE events were appeared. This implies that there were a lot of internal damages in the band, in other words, the load was transferred through the band.

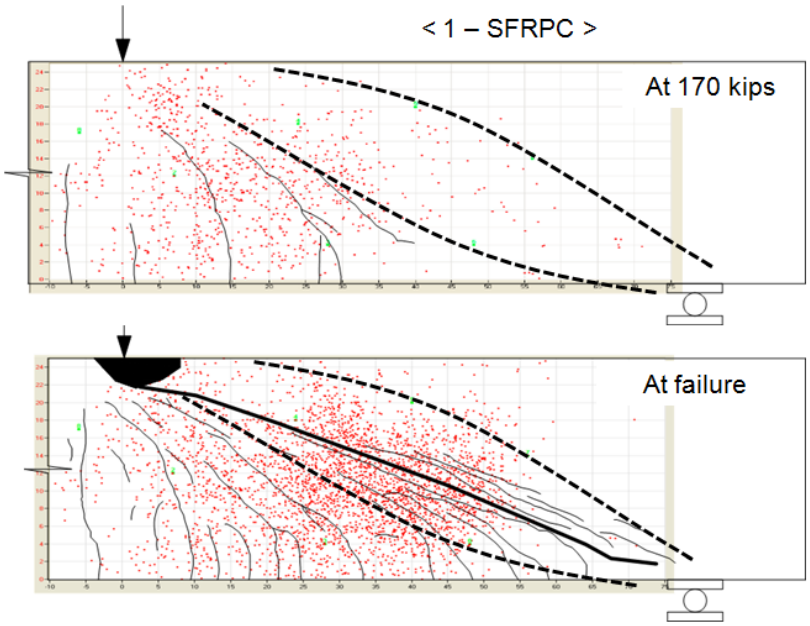

(a)

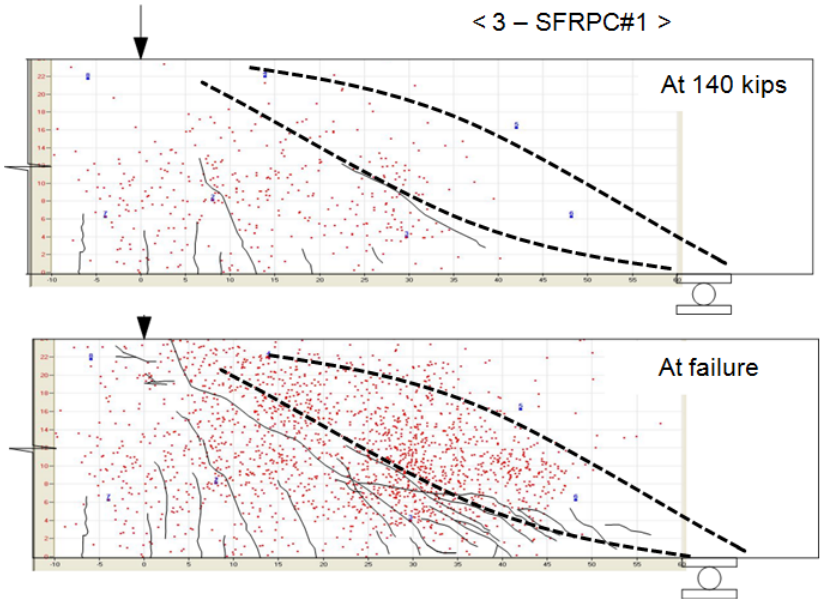

(b)

Figure 7.18 Comparison of locations of AE events at the first shear crack and failure; (a) 1 – SFRPC beam; (b) 3 – SFRPC#1 beam

7.3.2.3 Depth of the Compression Zone

As mentioned previously, the role of the compression zone is primary in the compression force path. It should be pointed out that smaller area of compression zone does not mean that the compression zone could not resist larger force. However, the capacity of the compression zone is normally underestimated since it is occasionally considered as the uniaxial stress condition. It was observed that SFRPC beams had relatively deeper depth of compression zone compared to PC beams. 1 – PC beam showed less 2 in. depth of the compression zone, while 1 – SFRPC beam had approximately 4 in. depth of the compression zone. Most of SFRPC beams showed 3 in. to 4 in. depths of the compression zone. It might be able to create deeper depths of the compressions in the SFRPC beams with two parameters, which were induced by steel fibers: delaying of the crack propagation rates and increase of the first cracking strength. As illustrated in Figure 7.18, SFRPC showed the delay of the first and critical shear cracks. Figure 7.19 (a) shows the crack propagation at 140 kips, where the first shear crack occurred in the SFRPC beam. For 1 – PC#1 beam, the tip of crack was under the loading point, in contrast, the first shear crack just occurred in 3 – SFRPC#1 beam. Even at the lower applied load, the tip of the crack in PC beam was closed to the loading point compared to the SFRPC beam as can be seen in Figure 7.19 (b). That is because the crack propagation rate was delayed by the fiber bridge effect. Therefore, higher load was generally required for cracks to propagate in the SFRPC beams. It should be mentioned for SFRPC beams that when the tip of crack reached under loading, higher biaxial compressive stresses existed in the compression zone; vertically and horizontally. The vertical compression was induced by the applied load directly and the horizontal compression was induced by the flexural bending stress. As stated previously, the concrete strength is

enhanced under biaxial stresses. In addition, the crack propagation angle becomes flatter under this condition as illustrated in Figure 7.20.

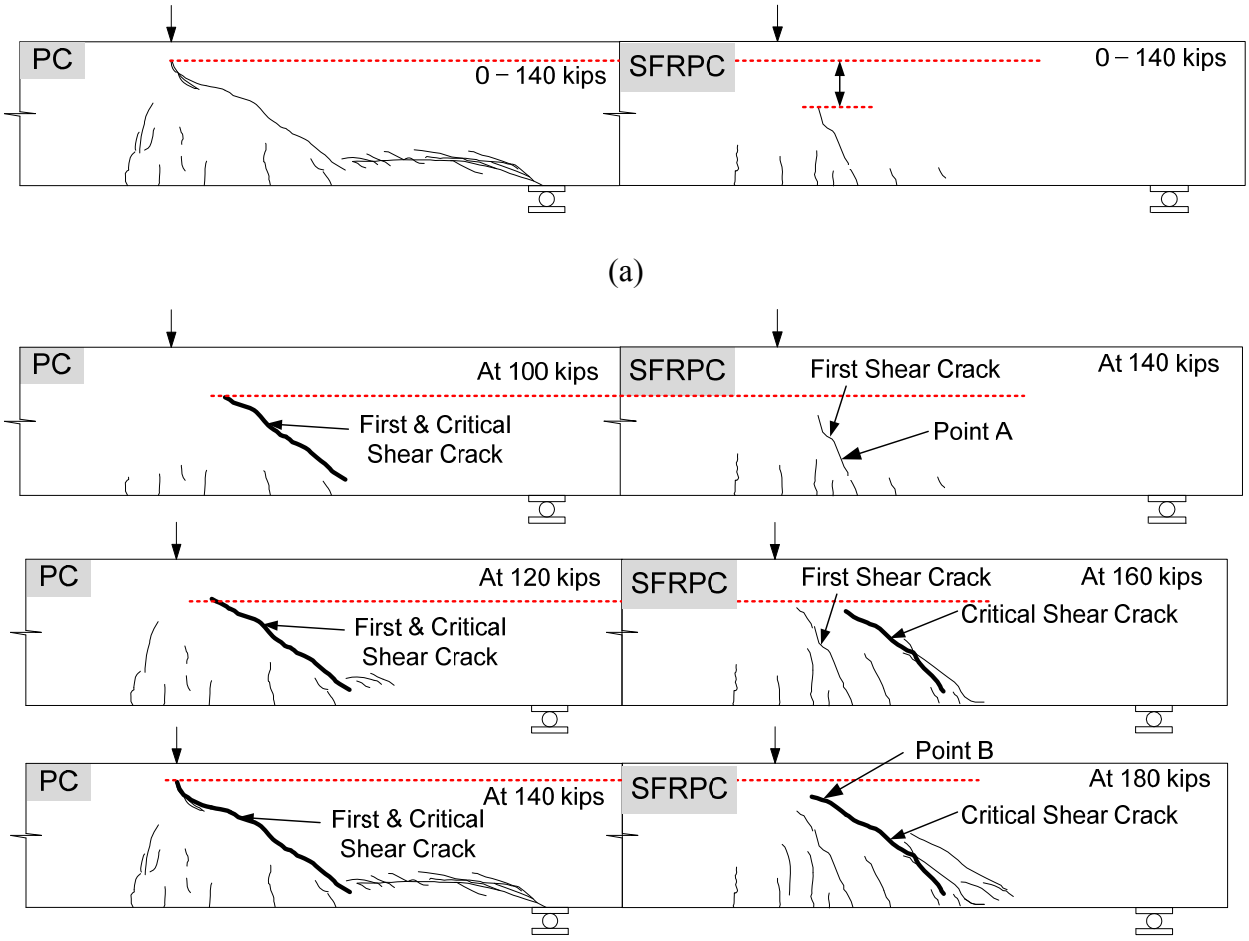

Figure 7.19 Comparison of the rates of the crack propagation between 3 – PC and SFRPC#1; (a) Comparison with the same load; (b) Comparison of the rate after the first crack;

It should be mentioned about the "Pole" in Figure 7.20. The pole is a point of the circle representative the intersection of a line parallel to a known plane and passing by its representative point on the circle. For example, a line parallel to the horizontal plane and passing by point XX intersects the circle at the pole.

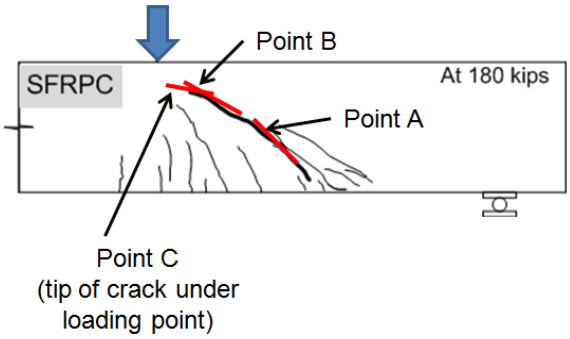

(a)

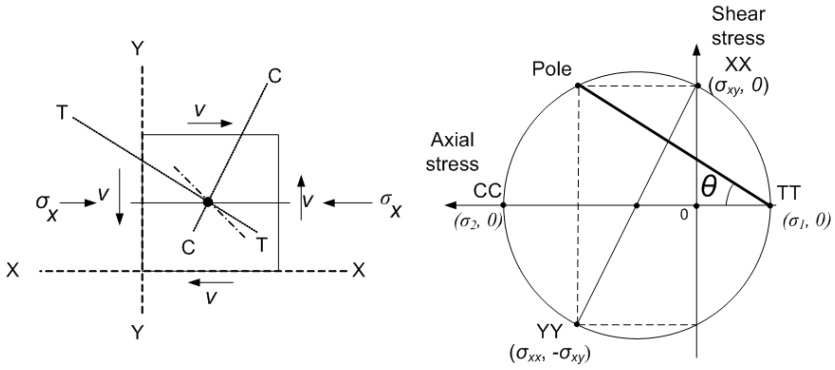

(b)

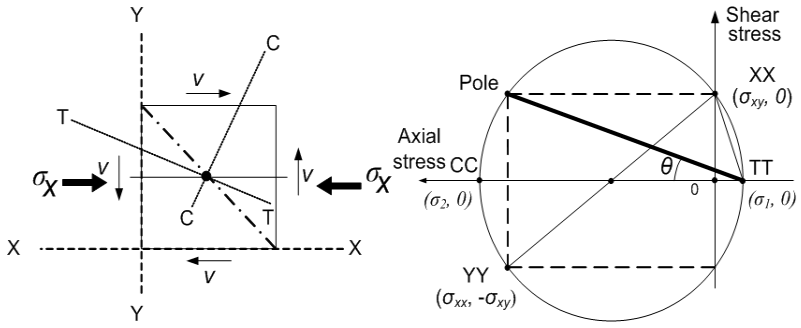

(c)

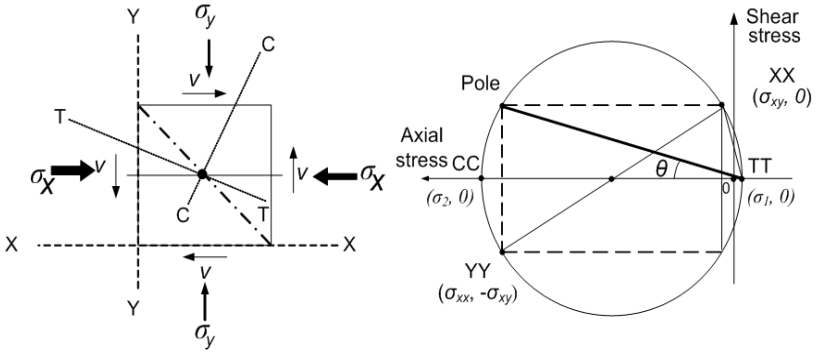

(d)

Figure 7.20 Representative stress states and Mohr's circles; (a) Location of each point; (b) Point A; (c) Point B; (c) Point C

The pole has the following interesting property: any line passing by the pole and another point of the circle parallel to the plane of the element represented by that point, i.e., the line joining pole to point TT in Figure 7.20 gives the actual direction of the TT plane, which the angle θ could represent.

The angle θ is less than 45° due to the prestressing force at point A (see Figure 7.20 (b)), where the first shear crack occurred. When it propagated toward the loading point, which can be representative by point B in the Figure 7.20, it would experience higher horizontal compressive stress due to higher flexural bending stress. As can be seen in Figure 7.20 (c), the angle θ becomes flatter such that the crack propagation angle also becomes flatter. In addition, the principal tensile stress is reduced. At point C, where is under the loading point, vertical compression force would be added by the applied load directly. As can be seen in Figure 7.20 (d), the propagation angle becomes much flatter, and the principal tensile stress is close to zero. That was shown during the tests; the crack propagation was stopped under the loading point such that it never passed through the loading point, unlike PC beams, in all of SFRPC beams. As consequences, relatively deeper compression zone can be created in the SFRPC beams.

CHAPTER 8

SUMMARY AND CONCLUSIONS

8.1 Summary

8.1.1 Experimental Program and Results

This experimental program presented in this dissertation consists of two parts: 1) Development of the material scale test to evaluate shear behavior of Steel Fiber Reinforced Concrete (SFRC) and 2) Study the shear behavior of large-scale Steel Fiber Reinforced Prestressed Concrete (SFPRC) beams without stirrups. For the first part, various existing test methods were analyzed by finite element analysis to evaluate their adequacy as a suitable shear material test based on the findings, a modified Iosipescu test method was developed. Although it was possibly to create pure shear stress state at the specimen, it was necessary to provide reinforcement since the test was essentially a beam-type test such that a premature flexural failure could occur before the intended shear failure occurs. A total seven different types of reinforcement details were attempted. It is shown that a nearly pure shear failure could be achieved by the proposed test specimen.

For the large-scale tests, a total of thirteen simply-supported SFPRC beams were tested up to failure under monotonically increased concentrated load. All beams had a

prestress level at 380 psi to 377 psi and a shear span to effective depth ratio of 3.0. The tested beams contained moderate to high ratio of the longitudinal reinforcement to prevent premature flexural failure. The steel fibers used in this study had double-hooked end shape. The steel fibers used in the first and second phases of the large-scale tests, which were manufactured by Bekaert Corporation, had an aspect ratio of 80 and a tensile strength of 160 ksi. The steel fibers used in the third phase of the large-scale tests, which were manufactured by Maccaferri Inc., had an aspect ratio of 67 and a tensile strength of 159 ksi. 0.75% volume fraction of the steel fibers was used in the specimens in the first phase, and both 0.50% and 0.75% volume fractions of the steel fibers were used in the specimens in the second and third phases. In the second phase, to compare conventionally reinforced PC and SFPRC beams, one of PC beams contained the minimum required area of stirrups (No. 3 stirrups @ 14 in. spacing) calculated based on ACI Code. In addition, to observe the effects of compression reinforcement on the shear strength, Specimen 2–SFRPC#3 beam contained 0.94% of the compressive reinforcement ratio. In the third phase, to investigate the failure mode of regularly reinforced SFRPC beam without stirrups, Specimen 3–SFRPC#2 contained 0.29% of the longitudinal reinforcement ratio. Specimen 3–SFRPC#4 contained the 0.5% volume fraction of steel fibers and small amount of conventional stirrups at a spacing of 21 in. as the shear reinforcement. In the third phase study, the advanced non-destructive evaluation method, Acoustic Emission sensors, were applied and analyzed to assess the damage in the concrete beams. In general, the SFRPC beams showed better shear behaviors in terms of higher first cracking strength and ultimate strength, as well as

ductility. The normalized shear stresses at the first shear crack ranged from 1.9 and $2.6\sqrt{f'_c}$ for the PC beams, while it ranged from 2.8 to $3.2\sqrt{f'_c}$ for the SFRPC beams with 0.50% volume fraction of fibers and from 3.1 to $3.4\sqrt{f'_c}$ for the SFRPC beams with 0.75% volume fraction of fibers. Specimen 3–SFPRC#2 beams (V_f = 0.75%), which contained the 0.29% longitudinal tensile reinforcement and no stirrups, failed in flexure rather than shear. This result indicated that the inclusion of steel fibers could change the failure mode from shear to flexure. At the ultimate, PC beams showed the normalized shear strength ranging from 2.5 to $5.5\sqrt{f'_c}$, while SFRPC beams (V_f = 0.50%) showed it ranging from 5.3 to $5.4\sqrt{f'_c}$ and it ranged for SFRPC beams (V_f = 0.75%) from 4.9 to $5.6\sqrt{f'_c}$. While the failures of PC beams were typically sudden and explosive, i.e., surface of the concrete popped out, the SFRPC beams gave a warning of gradual crushing of the concrete near the loading point and eventually failed by a ductile manner.

AE analysis showed that shear cracks generated higher amplitude compared to that of the flexural cracks in PC beams, but not much difference was observed in SFRPC beams. SFRPC beams showed more numbers of events which indicated a significant internal stress redistribution, and greater region of concrete in the specimens contributed to the resistance for external forces compared to that of the PC beams. It can be said that the more numbers of events is due to the inclusion of steel fibers.

8.1.2 Load Transfer Mechanism – SFRPC beams

The higher shear strength of the SFRPC beams was essentially due to the fiber bridging effect which delays the first cracking and slows down the propagation rate of the critical shear crack. This leads to a larger compression at the tip of the shear crack due to the bending action, which in turn gradually reduces the angle of the crack when propagating towards to the loading point. The crack tip eventually stops near the loading point due to the combined high bi-axial compressions, which reduce the principal tensile stress and at the same time increase the concrete compressive strength. The rapidly reduced crack angle results in a deeper compression zone which effectively facilitates a direct path to transfer the load from the loading point to the support, through a series of uncrakced concrete region, or the *compression force path*. Due to the shear span to effective depth ratio (3.0) adopted in this study, the direct path was almost a linear strut, which can hardly be formed in conventional concrete with a shear span to depth ratio greater than approximately 2.5. This direct compression transfer path was evidenced by the measured concrete surfaced strains, as well as the suddenly appeared splitting cracks in-between the loading point and support upon failure. It was observed that the failure of the SFRPC beams was always induced by the crushing the compression zone. The relatively larger area of the compression zone (thus the smaller the stress) and the increased concrete strength due to bi-axial compression in the vicinity of the loading point in the SFRPC beams delay the ultimate compression failure of the most critical region along the compression force path, thus enhancing the overall shear-carrying capacity.

8.2 Conclusions

The following major conclusions were drawn from this study:

- By using a proper reinforcement layout to prevent premature flexural failure, the modified Isopesicu test method could be used to serve as a standard test method for evaluating the shear properties of SFRC materials.
- The use of double-hooked end shape steel fibers in volume fraction greater than or equal to 0.50% enhanced not only the ultimate shear strength of an SFRPC beam but also its ductility.
- The minimum volume fraction of the steel fibers, 0.75%, specified by ACI 318-08 or ACI 318-11 is conservative for prestressed concrete. Test results showed that the fiber amount can be reduced to 0.50%, which is corresponding to 67 lb per cubic yard.
- The SFRPC beam with 0.50% volume fraction of steel fibers had shear strength much greater than $2\sqrt{f'_c}b_w d$; in addition even the first shear cracking strengths in SFRPC beams were higher than $2\sqrt{f'_c}b_w d$. As a consequence, both the criteria mentioned in ACI 318-11 Section 11.4.6.1 (f), "*… V_u not greater than $\phi 2\sqrt{f'_c}b_w d$;*.", and Section 5.6.6.2 (a), "*The weight of deformed steel fibers per cubic yard of concrete is greater than or equal to 100 lb.*" (ACI 318-11, 2011) could be relaxed for SFRPC beams. The recommended values and quantity are

$\phi 4\sqrt{f'_c}b_w d$ and 67 pounds of steel fibers per cubic yard of concrete for SFRPC beams with an initial prestress at least 380 psi.

- The performance of an SFRPC beam can be further enhanced by the combination of 0.5% volume fraction of deformed steel fibers with stirrups having a spacing of 21 in.
- Acoustic emission technique can be applied to SFRPC beams to observe overall view of internal damage. It also serves a good tool to observe the force transfer path.
- The compression reinforcement barely affected the shear strength in the SFRPC beams.
- The higher shear strength in SFRPC beams was originated by the fiber bridging effect which delayed the occurrence of the critical shear crack and its propagation rate, which eventually led to a large compression zone and greater concrete compressive strength under high biaxial compressions. This enhanced the strength of the critical region at the load transfer path (i.e., the compression force path), thus increasing the overall shear-carrying capacity.

8.3 Recommendations for Future Work

The following research works are recommended for the future study based on findings from this study.

- Further improvement of reinforcement layouts for the modified Isopesicu test method;
- Increase depth of the beams to investigate the size effect in SFRPC beams;
- Varying prestressing force to investigate the effect of the prestressing force in SFRPC beams;
- Further investigation the combination of stirrups and steel fibers;
- Develop nonlinear finite element models for the large-scale SFRPC beams based on the experimental results;
- Develop analytical and design equations;
- Use 3-D technique in AE to investigate the spatial distributions of internal micro-cracking.

REFERENCES

ACI Committee 318, "Building Code Requirements for Reinforced Concrete and Commentary (ACI318-51)," American Concrete Institute, Detroit. 1951.

ACI Committee 318, "Building Code Requirements for Reinforced Concrete and Commentary (ACI318-08/ACI318R-08)," American Concrete Institute, Detroit. 2008.

ACI Committee 544, "State of the Art Report on Fiber Reinforced Concrete," Report 544-1R-96 (Reapproved 2002)," ACI Committee 544, Fiber Reinforced Concrete, 2002.

ACI Committee 544, "Design Consideration for Steel Fiber Reinforced Concrete," Report ACI 544R-88, American Concrete Institute, Farmington Hill, MI, 1998.

ACI-ASCE Committee 326, "Shear and Diagonal Tension," ACI Journal Proceedings, Vol. 59, No. 3, March, 1962.

Adebar, P., Mindess, S., St.-Pierre, D., and Olund, B., "Shear Tests of Fiber Concrete Beams Without Stirrups," ACI Structural Journal, Vol. 94, No. 1, Jam.-Feb., 1997, pp. 68-76.

Adams, D. F., and Walrath, D. E., "Current Status of the Iosipescu Shear Test Method," Journal of Composite Materials, Vol. 21, June 1987, pp. 494-507.

Anderson, B. G., "Rigid Frame Failures," ACI Journal, Proceedings, Vol. 53, No. 1, Jan. 1957, pp. 625-636.

ASCE-ACI Committee 426, "The Shear Strength of Reinforced Concrete Members," Proceeding ASCE, Journal of the Structural Division, Vol. 99, No. ST6, June, 1973.

ASCE-ACI Committee 445 on Shear and Torsion, "Recent Approaches to Shear Design of Structural Concrete," Journal of Structural Engineering, Vol. 124, No., 12, Dec., 1998, pp1375-1417.

Ashour, S. A., Hasanain, G. S., and Wafa, F. F., "Shear Behavior of High-Strength Fiber Reinforced Concrete Beams," ACI Structural Journal, Vol. 89, No. 2, Mar.-Apr., 1992, pp. 176-184.

ASTM A615 / A615M, "Standard Specification for Deformed and Plain Carbon-Steel Bars for Concrete Reinforcement," ASTM International, West Conshohocken, PA, 2009.

ASTM A820 / A820M-11, “Standard Specification for Steel Fibers for Fiber-Reinforced Concrete,” ASTM International, West Conshohocken, PA, 2011.

ASTM C1609 / C 1609M-010, “Standard Test method for Flexural Performance of Fiber-Reinforced Concrete (Using Beam with Third-Point Loading),” ASTM International, West Conshohocken, PA, 2010, pp 9.

ASTM E1316-06a, “Standard Terminology for Nondestructive Examinations,” ASTM International, West Conshohocken, PA, 2006, pp 33.

ASTM D 5379-05, “Standard Test Method for Shear Properties of Composite Materials by the V-Notched Beam Method,” ASTM International, West Conshohocken, PA, 2005.

Balaguru, P. N. and Shah, P., “Fiber-reinforced cement composites,” 1st edition, McGraw-Hill, Inc., 1992.

Barragán, B., Gettu, R., Agulló, L., and Zerbino, R., “Shear Failure of Steel Fiber-Reinforced Concrete Based on Push-Off Tests,” ACI Materials Journal, Vol. 103, No. 4, July-August, 2006, pp. 251-257.

Baston, G., Jenkins, E., and Spatney, R.,"Steel Fibers as Shear Reinforcement in Beams," ACI Journal, Proceedings, Vol. 69, No.10, Oct., 1972, pp 640-644.

Belghiti, M. M, “ Influence of Steel Fibres on Response of Beam,” Mater thesis, McGill University, 2007.

Bentur, A., and Mindess, S., “Fiber Reinforced Cementitious Composites,” 2nd edition, Taylor & Francis, 2007.

Bentz, E., “Sectional Analysis of Reinforced Concrete Members,” Ph.D Dissertation, University of Toronto, 2000.

Bentz, E., Vecchio, F. J., and Collins, M. P., “Simplified Modified Compression Field Theory for Calculating Shear Strength of Reinforced Concrete Members,” ACI Structural Journal, Vol. 103, No. 4, July-Aug., 2006, pp 614-624.

Bernard, E. S., “Correlations in the Behaviour of Fibre Reinforced Shotcrete Beam and Panel Specimens,” Materials and Structures, 35, 2002, pp.156-164.

Bresler, B., and Pister, K. S., "Strength of Concrete Under Combined Stresses," ACI Journal Proceedings, Vol. 55, No. 9, September., 1958.

Carey, S. A., "Acoustic Emission and Acousto-Ultrasonic Signature Analysis of Failure Mechanisms in Carbon Fiber Reinforced Polymer Materials," Ph.D Dissertation, University of South Carolina, 2008.

Casanova, P. and Rossi, P., "Analysis and Design of Steel Fiber Reinforced Concrete Beams," ACI Structural Journal, Vol. 94, No. 5, Sept.-Oct., 1997, pp 595-602.

Casanova, P., Rossi, P., and Schaller, I., "Can Steel Fibers Replace Transverse Reinforcements in Reinforced Concrete Beams?," ACI Material Journal, Vol. 94, No. 5, September-October, 1997.

Chao, S-.H-., Naaman, A. E., and Parra-Montesinos, G. J., "Bond Behavior of Reinforcing Bars in Tensile Strain-Hardening Fiber-Reinforced Cement Composites," ACI Structural Journal, Vol. 106, No. 6, Nov.-Dec., 2009, pp 897-906.

Chen, W. F., Plasticity in Reinforced Concrete, McGraw-Hill Book Co., New York, 1982.

Cheng, M.-Y., and Parra-Montesino, G. J., "Evaluation of Steel Fiber Reinforcement for Punching Shear Resistance in Slab-Column Connections-Part 1: Monotonically Increased Load," ACI Structural Journal, Vol. 107, No. 1, Jan.-Feb., 2010, pp101-109.

Cho, J.-S., Lundy, J. M., and Chao, S.-H., 2009, "Shear Strength of Steel Fiber Reinforced Prestressed Concrete Beams," ASCE Structures Congress '09, April 30-May 2, 2009, Austin, Texas.

Choi, K-K., Park, H-G., and Wight, J.K., "Shear Strength of Steel Fiber-Reinforced Concrete Beams without Web Reinforcement," ACI Structural Journal, Vol. 104, No. 1, January-February 2007.

Collins, M. P. and Mitchell, D., "A Rational Approach to Shear Design-The 1984 Canadian Code Provision," ACI Journal, Vol. 83, No. 6, Nov., 1986, pp. 925-933.

Colombo, I. S., Main, I. G., and Forde, M. C., "Assessing Damage of Reinforced Concrete Beam Using "b-value" Analysis of Acoustic Emission Signals," Journal of Materials in Civil Engineering, ASCE, Vol. 15, No. 3, June, 2003, pp 280 – 286.

Cucchiara, C., Mendola, L. L., and Papia, M., "Effectiveness of Stirrups and Steel Fibres as Shear Reinforcement," Cement and Concrete Composites, Vol. 26, No. 7, Oct., 2004, pp. 777-786.

Dhonde, H. B., "Steel Fibers and Self-Consolidating Concrete in Prestressed Concrete Beams," Ph.D Dissertation, University of Houston, 2006.

Dinh, H. H., "Shear behavior of Steel Fiber Reinforced Concrete Beams without Stirrup Reinforcement," Ph.D Dissertation, University of Michigan, 2009.

Drucker, D. C., "On Structural Concrete and the Theorems of Limit Analysis," IABSE proceedings, Vol. 21, 1961, pp. 49-59.

Fanella, D. and Naaman, A. E., "Stress-Strain Properties of Fiber Reinforced Mortar in Compression," ACI Journal, Vol. 82, No. 4, July, 1985, pp. 475-483.

Fenwick R. C. and Paulay, T., "Mechanisms of Shear Resistance of Concrete Beams," Journal of Structural Division proceedings, Vol. 94, No. ST10, Oct., 1968, pp. 2325-2350.

Ferguson, P. M., "Some Implications of Recent Diagonal Tension Tests," ACI Journal, Vol. 28, No. 2, Aug., 1956, pp. 157-172.

Gao, J., Sun, W., and Morino, K., "Mechanical Properties of Steel Fiber-reinforced, High-strength, Lightweight Concrete," Cement and Concrete Composite, Vol. 19, 1997, pp. 307-313.

Gostautas, R. S., Ramirez, G., Peterman, R. J., and Meggers, D., "Acoustic Emission Monitoring and Analysis of Glass Fiber-Reinforced Composites Bridge Decks," Journal of Bridge Engineering, ASCE, Nov.-Dec., 2005, pp 713-721.

Gostautas, R. S. and Tamutus, T., "Condition Assessment of Prestressed Concrete Girders from the Lake View Drive Bridge (I-70) Using Acoustic Emission," Western Pennsylvania Transportation Research Forum, June 6, 2007, Pittsburgh, PA.

Hannant, D. J., Fibre Cements and Fibre Concrete, Wiley, Chicester, U.K., 1978.

Hearn, S. W. and Shield, C. K., "Acoustic Emission Monitoring as A Nondestructive Testing Technique in Reinforced Concrete," ACI Materials Journal, Nov.-Dec., 1997, pp 510-519.

Hsu, T. T. C. and Mo, Y. L., "Softening of Concrete in Torsional Members – Theory and Tests," ACI Journals, Vol. 82, No. 3, May 1, 1985, pp.290-303.

Hsu, T. T. C. and Mo, Y. L., Unified theory of reinforced concrete, Wiley & Sons, Ltd., 2010, pp500.

Hofbeck, J. A., Ibrahim, I. O., and Mattock, A. H., "Shear Transfer in Reinforced Concrete," ACI Journal, Vol. 66, No. 2, Feb, 1969, pp. 119-128.

JSCE-SF6, "Method of Test for Shear Strength of Steel Fiber Reinforced Concrete (SFRC)," Japan Society of Civil Engineers, Tokyo, 1990, pp. 67-69.

Iosipescu, N., “New Accurate Procedure for Single Shear Testing of Metals,” Journal of Materials, Vol. 2, No. 3, September, 1967, pp. 537-566.

Iosipescu, N., and Negoita, A., “A New Method for Determining the Pure Shearing Strength of Concrete,” Journal of Concrete Society, 1969, Vol. 3, No. 1, pp. 63.

Kani, G. N. J., “A Rational Theory for the Function of Web Reinforcement,” ACI Journal proceedings, Vol. 66, No. 3, Mar., 1969, pp. 185-197.

Kar, J. N., “Diagonal Cracking in Prestressed Concrete Beams,” Journal of the Structural Division, ASCE, Vol. 94, No. ST1, Proc. Jan., 1968.

Katsaga, T., Sherwood, E. G., Collins, M. P., and Young, R. P., “Acoustic Emission Imaging of Shear Failure in Large Reinforced Concrete Structures,” Journal of Fracture, Vol. 148, June, pp 29-45.

Kim, D., Kim, W., and White, R. N., “Arch Action in Reinforced Concrete Beams – A Rational Prediction of Shear Strength,” ACI Structural Journal, Vol. 96, No. 4, July-Aug., 1999, pp. 586-595.

Kotsovos, M. D., “A Fundamental Explanation of the Behavior of Reinforced Concrete Beams in Flexure Based on the Properties of Concrete Under Multiaxial Stress,” Matériaux et Constructions, Vol. 15, No. 90, 1982, pp. 529-537.

Kotsovos, M. D., “Compressive Force Path Concept: Basis for Reinforced Concrete Ultimate Limit State Design,” ACI Journal, Vol. 85, No. 1, Jan., 1988, pp. 68-75.

Kotsovos, M. D. and Pavlović, Ultimate Limit-State Design of Concrete Structures: A new approach, Thomas Telford, Ltd., 1998.

Kotsovos, M. D. and Lefas, I. D., “Behavior of Reinforced Concrete Beams Designed in Compliance with the Concept of Compressive-Force Path,” ACI Structural Journal, Vol. 87, No. 2, Mar.-Apr., 1990, pp. 127-139.

Kwak, Y.-K, Eberhard, M. O., Kim, W.-S., and Kim, J., “Shear Strength of Steel Fiber-Reinforced Concrete Beams Without Stirrups,” ACI Structural Journal, Vol. 99, No. 4, July-Aug., 2002, pp. 530-538.

Laws, V., “The Efficiency of Fibrous Reinforcement of Brittle Matrices,” Journal of Physics, Vol. 4, No. 1737, 1971, pp. 1737-1746.

Leondardt, Ing. F., “Reducing the Shear Reinforcement in Reinforced Concrete Beams and Slabs,” Magazine of Concrete Research, Vol. 17, No. 53, Dec., 1965, pp. 187-198.

Li, V. C., Ward, R., and Hamza, A. M., “Steel and Synthetic Fibers as Shear Reinforcement,” ACI Material Journal, Vol. 89, No. 5, Sept.-Oct. 1992, pp. 499-508.

Lim, T. Y., Paramasivam, P., and Lee, S. L., “Shear and Moment Capacity of Reinforced Steel-Fibre-Concrete Beams,” Magazine of Concrete Research, Vol. 39, No. 140, Sept., 1987, pp. 148-160.

MacGregor, J. G. and Hanson, J. M., “Proposed Changes in Shear Provisions for Reinforced and Prestressed Concrete Beams,” ACI Journal proceedings, Vol. 66, No. 4., Apr., 1969, pp. 276-288.

MacGregor, J. G., Sozen, M. A., and Siess, C. P., “Strength of Prestressed Concrete Beams with Web Reinforcement,” ACI Journal, Vol. 62, No. 12, Dec., 1965, pp.1503-1519.

Mansur, M. A. and Ong, K. C. G., “Behavior of Reinforced Fiber Concrete Deep Beams in Shear,” ACI Structural Journal, Vol. 88, No. 1, Jan.-Feb., 1991, pp 98-105.

Mansur, M. A., Ong, K. C. G., and Paramasivam, P., “Shear Strength of Fibrous Concrete Beams Without Stirrups,” Journal of Structural Engineering, Vol. 112, No. 9, Sept., 1986, pp. 2066-2079.

Mirsayah, A.A., and Banthia, N.,”Shear Strength of Steel Fiber-Reinforced Concrete,” ACI Material Journal, Vol. 99, No. 5, Sep.-Oct., 2002, pp 473-479.

Muttoni, A. and Ruiz, M. F., “Shear Strength of Members without Transverse Reinforcement as Function of Critical Shear Crack Width,” ACI Structural Journal, Vol. 105, No. 2, Mar.-Apr., 2008, pp. 163-172.

Namman, A. E., “Fiber Reinforced Concrete,” Concrete International, Vol. 7, No. 3, March, pp21-25.

Naaman, A. E., Prestressed Concrete Analysis and Design—Fundamentals, Second Edition, Techno Press 3000, 2004.

Naaman, A. E. and Reinhardt, H. W., “Proposed classification of HPFRC composites based on their tensile response,” Materials and Structures, Vol. 39, June, 2006.

Narayanan, R., and Darwish, I.Y.S., “Use of Steel Fibers as Shear Reinforcement,” ACI Structural Journal, Vol. 83, No. 3, May-June, 1987.

Noghabai, K., “Beams of Fibrous Concrete in Shear and Bending: Experiment and Model,” Journal of Structural Engineering, Vol. 126, No. 2, Feb., 2000, pp. 243-251.

Ohtsu, M., Uchida, M., Okamoto, T., and Yuyama, S., "Damage Assessment of Reinforced Concrete Beams Qualified by Acoustic Emission," ACI Structural Journal, Vol. 99, No. 4, July-Aug., 2002, pp 411-417.

Ouyang, C., Landis, E., and Shah, S. P., "Damage Assessment in Concrete Using Quantitative Acoustic Emission," Journal of Engineering Mechanics, Vol. 117, No. 11, Nov., 1991, pp 2681-2698.

Padmarajaiah, S. K. and Ramaswamy, A., "Behavior of Fiber-Reinforced Prestressed and Reinforced High-Strength Concrete Beams Subjected to Shear," ACI Structural Journal, Vol. 98, No. 5, Sep.-Oct., 2001. pp. 752-761.

Park, P. and Paulay, T., Reinforced Concrete Structures, John Wiley & Sons, Inc., 1975.

Parra-Montesinos, G., "Shear Strength of Beams with Deformed Steel Fibers," Concrete International, Vol. 28, No. 11, Nov., 2006, pp. 57-66.

Pierron, F., and Vautrin, A., "Measurement of the In-Plane Shear Strength of Unidirectional Composites with the Iosipescu Test," Composites Science and Technology, Vol. 57, 1997, pp. 1653-1660.

Promboon, Y., "Acoustic Emission Source Location," Ph.D Dissertation, University of Texas at Austin, 2000.

Ramakrishnan, V., Brandshaug, T., Coyle, W. V., and Schrader, E. K., "A Comparative Evaluation of Concrete Reinforced with Straight Steel Fibers and Fibers with Deformed Ends Glued Together into Bundles," ACI Journal, Vol. 77, No. 3, May, 1980, pp. 135-143.

Ridge, A. R. and Ziehl, P. H., "Evaluation of Strengthened Reinforced Concrete Beams: Cyclic Load Test and Acoustic Emission Methods," ACI Structural Journal, Vol. 103, No. 6, Nov.-Dec., 2006, pp. 832-841.

Rossi, P., "Steel Fiber Reinforced Concretes (SFRC): An Example of French Research," ACI Material Journal, Vol. 91, No. 3, May-June, 1994, pp 273-279.

Saqan, E. I. and Frosch, R. J., "Influence of Flexural Reinforcement on Shear Strength of Prestressed Concrete Beams," ACI Structural Journal, Vol. 106, No. 1, Jan.-Feb., 2009, pp. 60-68.

Shah, S. P. and Rangan, B. V., "Fiber Reinforced Concrete Properties," ACI Journal, Vol. 68, No. 2, Feb., 1971, pp. 126-137.

Sharma, A. K., "Shear Strength of Steel Fiber Reinforced Concrete Beams," ACI Journal, Proceedings, Vol. 83, No. 4, July-Aug., 1986, pp. 624-628.

Sherwood, E.G.,"One-Way Shear Behavior of Large, Lightly-Reinforced Concrete Beams and Slabs," Ph.D Dissertation, University of Toronto, 2008.

Sherwood, E., Lubell, A., Bentz, E. C., and Collins, M. P., "One-Way Shear Strength of Thick Slabs," ACI Structural Journal, Vol. 103, No. 6, Nov.-Dec., 2006, pp. 794-802.

Stevens, N. J., Uzumeri, S. M., and Collins, M. P., "Reinforced Concrete Subjected to Reversed Cyclic Shear – Experiments and Constitutive Model," ACI Structural Journal, Vol. 88, No. 2, Mar.-Apr., 1991, pp 135-146.

Sun, S., "Shear Behavior and Capacity of Large-Scale Prestressed High Strength Concrete Bulb-Tee Girders," Ph.D Dissertation, University of Illinois at Urbaba-Champaign, 2007.

Swamy, R. N., Jones, R., and Chiam, A.T.P., "Influence of Steel Fibers on the Shear Resistance of Lightweight Concrete I-Beams," ACI Structural Journal, Vol. 90, No. 1, Jan.-Feb., 1993, pp 103-114.

Swamy, R. N. and Bahia, H. M., "The Effectiveness of Steel Fibers as Shear Reinforcement," Concrete International, Vol. 7, No. 3, Mar., 1985, pp. 35-40.

Swartz, S. E., and Taha, N. M., "Crack Propagation and Fracture of Plain Concrete Beams Subjected to Shear and Compression," ACI Structural Journal, Vol. 88, No. 2, March-April, 1991. pp. 169-177.

Tan, K. H., Murugappan, K., and Paramasivam, P., "Shear Behavior of Steel Fiber Reinforced Concrete Beams," ACI Structural Journal, Vol. 90, No. 1, Jan.-Feb., 1993, pp. 3-11.

Tan, K. H., Paramasivam, P., and Murugappan, K., "Steel Fiber as Shear Reinforcement in Partially Prestressed Beams," ACI Structural Journal, Vol. 92, No. 6, Nov.-Dec., 1995, pp. 643-652.

Thomas. J. and Ramaswamy, A., "Shear Strength of Prestressed Concrete T-Beams with Steel Fibers over Partial/Full Depth," ACI Structural Journal, Vol. 103, No. 3, May-June, 2006. pp. 427-435.

Tureyen, A. K. and Frosch, R. J., "Concrete Shear Strength: Another Perspective," ACI Structural Journal, Vol. 100, No. 5, Sept.-Oct., 2003, pp. 609-615.

Valle, M., and Büyüköztürk, O., "Behavior of Fiber Reinforced High-Strength Concrete under Direct Shear," ACI Materials Journal, Vol. 90, No. 2, Mar.-Apr., 1993, pp. 122-133.

van Zijl, G. P. A. G., "Improved Mechanical Performance: Shear Behavior of Strain-Hardening Cement-Based Composites (SHCC)," Cement and Concrete Research, V. 37, 2007, pp. 1241-1247.

Vecchio, F. J. and Collins, M. P., "Predicting the Response of Reinforced Concrete Beams Subjected to Shear Using Modified Compression Field Theory," ACI Structural Journal, Vol. 85, No. 3, May-June, 1988, pp. 258-268.

Vecchio, F. J. and Collins, M. P., "The Modified Compression-Field Theory for Reinforced Concrete Elements Subjected to Shear," ACI Journal, Vol. 83, No. 2, Mar., 1986, pp. 219-231.

Wafa, F. F. and Ashour, S. A., "Mechanical Properties of High-Strength Fiber Reinforced Concrete," ACI Material Journal, Vol. 89, No. 5, Sept.-Oct., 1992, pp. 449-455.

Walrath, D. E. and Adams, D. F., "The Iosipescu Shear Test as Applied to Composite Materials," Experimental Mechanics, Vol. 23, No. 1, 1983, pp. 105-110.

Wight, J. K. and MacGregor, J. G., Reinforced concrete: Mechanics and Design, fifth edition, Prentice Hall, 2009.

BIOGRAPHICAL INFORMATION

Jae-Sung Cho graduated with Bachelor degree in Civil Engineering from the Kookimin University in Seoul, Korea in 2002. After graduation, He came to the University of Texas at Arlington (UTA) to have a Master degree. In 2003, he got the Master of Engineering degree with Dr. Abolmaali. Jae-Sung Cho was back to Korea, and had been worked for about 2 years in an engineering consulting firm, AceAll co. Ltd. In January 2007, he came back to UTA and entered the doctoral program in Structural and Applied Mechanics.